Universität Hamburg
DER FORSCHUNG | DER LEHRE | DER BILDUNG

Near-field and stereo far-field X-ray ptychography for in-situ imaging of nanoparticle growth and considerations on radiation damage

---

Dissertation

for the attainment of the degree
doctor rerum naturalium
(Dr. rer. nat.)

submitted by
Sina Röper

Fakultät für Mathematik, Informatik und Naturwissenschaften
Institut für Nanostruktur- und Festkörperphysik
Universität Hamburg

Hamburg
2026

1. Gutachterin:	Prof. Dr. Dorota Koziej
2. Gutachter:	Jun.-Prof. Dr. Peter Modregger
Mitglieder der Prüfungskomission:	Prof. Dr. Dorota Koziej
	Prof. Dr. Christian Schroer
	Jun.-Prof. Dr. Peter Modregger
	Prof. Dr. Lisa Vondung
	Priv.-Doz. Dr. Tobias Kipp
Datum der Disputation:	20.02.2026

Deutsches Elektronen-Synchrotron DESY und Universität Hamburg
Start der Dissertation: 15.03.2021
Abgabe der Dissertation: 09.01.2026

Zusammenfassung

Funktionalität und Eigenschaften von Nanomaterialien hängen stark mit ihrer Größe, Form und Oberfläche zusammen. Die Prozesse und Dynamiken, die zu bestimmten Strukturen und Oberflächen führen, sind in vielen Fällen noch nicht gut verstanden. Dies ist unter anderem auf die Schwierigkeit zurückzuführen, Synthesen in situ oder operando unter relevanten Bedingungen zu beobachten. Mit Röntgenstrahlung können chemische und physikalische Prozesse im Nanobereich studiert werden. Die hohe Eindringtiefe von Röntgenstrahlung in Materie ermöglicht die Untersuchung von Proben in speziellen Probenumgebungen, welche benötigt werden, um beispielsweise hohe Temperaturen oder Drücke zu erzeugen. Ptychographie hat sich in den letzten Jahren zur Methode der Wahl für hochauflösende Röntgenbildgebung entwickelt. Hiermit konnten Auflösungen von unter 10 nm in quantitativen Projektionen erzielt werden. Der quantitative Phasenschub in Ptychographie lässt Rückschlüsse auf die Dicke von Objekten oder auch Einblicke in die Kinetik von Reaktionen zu. Im Rahmen dieser Arbeit wurden fortschrittliche Varianten der Ptychographie mit harter Röntgenstrahlung für in-situ Bildgebung entwickelt und angewendet. Das Verfahren der Stereo-Ptychographie wurde entwickelt und zur Bildgebung an ex-situ Proben und zur in-situ Untersuchung einer galvanischen Austauschreaktion eingesetzt. Hierzu wurden zwei nanofokussierte Röntgenstrahlen über Spiegel abgelenkt, um eine Probe gleichzeitig aus verschiedenen Winkeln zu beleuchten. Ähnlich wie beim menschlichen Sehen führte die Kombination dieser stereoskopischen Ansichten zu einer erheblich verbesserten Tiefenschärfe, die die derzeitigen Grenzen reiner 2D-Bildgebungssysteme übersteigt. Die verbesserte Tiefenauflösung ermöglichte die Entfernung von störenden Objekten aus anderen Schichten aus der Rekonstruktion der untersuchten Nanopartikel über die Grenzen des bisher Möglichen hinaus. Eine hohe laterale und temporale Auflösung konnte dabei erhalten werden. Außerdem wurde Nahfeld Multi-Slice Ptychographie erstmals für in-situ Bildgebung eingesetzt. Die Bildung von Gold-Nanokäfigen durch galvanischen Austausch wurde untersucht. Eine laterale Auflösung besser als 50 nm konnte durch den Einsatz von mehrschichtigen Laue-Linsen erreicht werden. Die hohe numerische Apertur dieser Optiken ermöglichte eine Unterscheidung von Schichten in sogenannten multi-slice Rekonstruktionen, die weniger als 100 µm voneinander entfernt sind. In weiteren Experimenten wurde der Einsatz von Radikalfängern zur Reduzierung von Strahlenschaden in in-situ Studien mit Röntgenstrahlung untersucht. Freie Radikale, die sich in wässriger Lösung bei Bestrahlung mit Röntgenlicht bilden, können Reaktionsverläufe beeinflussen und zu ungewünschten Nebenreaktionen führen. Verschiedene Radikalfänger wurden mittels Kleinwinkelstreuung und Ptychographie hinsichtlich ihrer Fähigkeit diese ungewünschten Nebenreaktionen zu unterdrücken evaluiert.

Abstract

The functionality and properties of nanomaterials are strongly related to their size, shape, and surface. In many cases, the processes and dynamics that lead to certain structures and surfaces are not yet well understood. This is partly due to the difficulty of observing syntheses in situ or operando under relevant conditions. X-rays can be used to study chemical and physical processes at the nanoscale. Their high penetration depth into matter allows samples to be examined in special sample environments, which are needed, for example, to create high temperatures or pressures. In recent years, ptychography has become the method of choice for high-resolution X-ray imaging. It has enabled resolutions of less than 10 nm to be achieved in quantitative projections. The quantitative phase shift in ptychography allows conclusions to be drawn about the thickness of features and provides insights into the kinetics of reactions. As part of this work, advanced variants of ptychography with hard X-rays were developed and applied for in-situ imaging.

The stereo ptychography method was newly developed and used for imaging of ex-situ samples and for in-situ investigation of a galvanic replacement reaction. For this purpose, two nano-focused X-rays are deflected via mirrors to illuminate a sample from different angles simultaneously. Similar to human vision, the combination of these stereoscopic views results in significantly improved in-depth resolution, exceeding the current limitations of pure 2D imaging systems. The improved depth resolution allows the removal of obscuring features from other layers from the reconstruction of the investigated nanoparticles beyond the limits of what was previously possible. High lateral and temporal resolution were maintained in the process.

Additionally, near-field multi-slice ptychography was used for in-situ imaging for the first time. The formation of gold nanocages by galvanic replacement was investigated. A lateral resolution better than 50 nm was achieved by using multilayer Laue lenses. The high numerical aperture of these optics enabled the differentiation of layers in so-called multi-slice reconstructions that are less than 100 µm apart.

In further experiments, the use of radical scavengers to reduce radiation damage in in-situ studies with X-rays was investigated. Free radicals, which form in aqueous solutions when irradiated with X-rays, can influence reaction processes and lead to undesirable side reactions. Various radical scavengers were evaluated using small-angle X-ray scattering and ptychography with regard to their ability to suppress these undesirable side reactions.

Contents

List of Abbreviations

Abbreviations

3PIE	Three-dimensional ptychographical iterative engine
CDI	Coherent diffractive imaging
CRL	Compound refractive lens
DOF	Depth of field
ePIE	Extended ptychographical iterative engine
FFP	Far-field ptychography
FWHM	Full width half maximum
FZP	Fresnel zone plate
GHS	Globally Harmonized System of Classification and Labelling of Chemicals
GRR	Galvanic replacement reaction
Gy	Gray $1\text{Gy} = 1\frac{\text{J}}{\text{kg}}$
KB mirror	Kirkpatrick-Baez mirror
ML-mirror	Multilayer mirror
MLL	Multilayer Laue lens
NFP	Near-field ptychography
OSA	Order sorting aperture
PIE	Ptychographical iterative engine
PtyNAMi	Ptychographic nano-analytical microscope at beamline P06
SAXS	Small angle X-ray scattering
SEM	Scanning electron microscopy
STXM	Scanning transmission X-ray microscopy
TEM	Transmission electron microscopy
WAXS	Wide angle X-ray scattering

1 Introduction

The physical and chemical characteristics of nanoparticles, including their optical, electronic, catalytic, magnetic, and biological properties, depend strongly on their shape, size, and degree of anisotropy [1,2]. Understanding how the morphology of nanoparticles transforms during chemical processes is essential for precisely designing synthesis routes that target specific morphological characteristics. However, the nanoscale size of these particles makes studying their real-time changes difficult.

In-situ imaging allows for the direct observation of nanoparticle formation and transformation. These dynamic processes require excellent spatial resolution and fast image acquisition. Transmission electron microscopy (TEM) provides both of these qualities, making it a valuable tool for visualizing the evolution of nanoparticles in various systems [3–7]. However, TEM is limited in its ability to study reactions under diverse environmental conditions due to the limited penetration depth of electrons in matter. This restricts the range of temperatures and pressures that can be explored, as well as the reaction volume.

In contrast, hard X-ray imaging allows for the investigation of larger sample volumes and more complex environments. Thus, it is an excellent tool for examining the morphological dynamics of nanoparticles under various physical and chemical conditions.

Insights obtained through in-situ X-ray microscopy are of great interest to chemists and materials scientists. However, the method must meet high standards to produce meaningful in-situ imaging data in the following areas:

- **Lateral resolution:** The minimal size of particles and features that can be studied is ultimately limited by the lateral resolution. Single-digit nanometer resolution would bring the method closer to the resolution of electron microscopy and could enable X-ray imaging in research fields like nanoclusters and quantum dots.
- **Depth resolution:** In-situ imaging of chemical reactions can often only be done with special reactors that create the needed reaction environment. Impurities in windows of the reaction containers, dirt or particles in the reaction solution can limit the resolution and interpretability of the captured images. A higher depth resolution can improve the removal of all these obscuring factors from the reconstructed layer of interest.
- **Temporal resolution:** The morphological evolution of nanoparticles can occur relatively quickly. To capture all the relevant intermediate steps and provide an advantage over ex-situ imaging, a high temporal resolution is required.
- **Mitigation of radiation damage:** When ionizing radiation, such as X-rays, interacts with a material it can cause excitation or ionization of the atoms or molecules in the

material and lead to the formation of free radicals. These can influence the studied chemical reactions and alter the outcome. To collect meaningful data, the influence of beam damage must be considered and, ideally, minimized.

These improvements could extend the applicability of hard X-ray imaging to a wider range of sample systems.

This thesis explores advances in ptychographic X-ray imaging for in-situ studies of the morphological evolution of nanoparticles. We will use the galvanic replacement reactions of Cu_2O nanocubes with Au and Pd as model systems. The reactions take place in an aqueous solution, which makes the process prone to radiation damage.

To improve the depth resolution, stereo ptychography was developed. By scanning the sample with two inclined X-ray beams, two perspectives can be acquired in a single scan without rotating the specimen. This enables a high temporal resolution to be maintained and a 3D impression of the sample to be obtained quickly.

Near-field ptychography has the potential to significantly improve temporal resolution. It uses an extended illumination, meaning fewer scan points are required to image a given area. Furthermore, the larger illumination leads to a reduced photon fluence, resulting in a lower dose rate. This could have a positive effect when imaging radiation-sensitive samples.

Finally, we will examine the use of free radical scavengers in the context of in-situ imaging of nanoparticle growth. The increased photon flux brought about by the rise of fourth-generation synchrotrons makes measures to reduce the effect of radiation damage increasingly important.

Structure of this thesis

The thesis is structured into six main chapters. Chapters two to four provide an overview of the theoretical background for this thesis. Chapters five to seven cover the development of stereo ptychography, in-situ near-field ptychography, and the application of free radical scavengers, respectively.

Chapter 2 X-rays – summarizes the X-ray physics relevant to this work.

Chapter 3 Ptychography – covers a description of ptychography and phase retrieval.

Chapter 4 In-situ synthesis – gives an introduction to galvanic replacement reactions as well as radiation damage.

Chapter 5 Stereoscopic ptychography – describes the newly developed stereo ptychography, which significantly improved the depth sensitivity compared to single beam ptychography.

Chapter 6 In-situ near-field ptychography – contains ex-situ and in-situ studies utilizing near-field multi-slice ptychography.

Chapter 7 Radiation damage and use of scavengers for in-situ studies – covers a small angle X-ray scattering and a far-field ptychography series that aims at the reduction of beam damage in in-situ studies using radical scavengers.

2 X-rays

This chapter will give a short introduction to the physics of X-rays. More in depth information can be found in the books by Goodman[8], Jacobsen[9] Als-Nielsen[10], Willmott[11], and Hecht[12].

Wilhelm Conrad Röntgen captured the first image with X-rays in 1895 [13]. Now, over 100 years later, X-ray microscopy is still a field of active research and innovation. X-rays are characterized as electromagnetic radiation with a wavelength between 10 nm and 10 pm. All experiments in this thesis were carried out with hard X-rays at energies between 8.0 keV and 18.0 keV, which corresponds to wavelengths between 155 pm and 69 pm.

2.1 Wave propagation

For X-ray microscopy it is crucial to understand how electromagnetic waves propagate in space. We consider a primary wavefront $\psi_0(x_0, y_0, 0)$ propagating to a downstream point (x, y, z), as shown in Fig. 2.1. Every point of the primary wavefront is a source for a spherical secondary wave with the same frequency and velocity as the primary wave. This is called the Huygens principle.

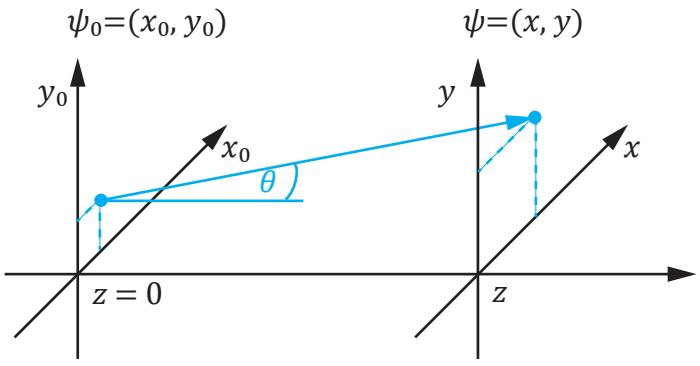

Figure 2.1: Propagation of a wavefront $\psi_0(x_0, y_0)$ to a downstream point (x, y, z).

Fresnel later modified the Huygens principle to account for interference. The secondary waves overlap and interfere downstream of the source. The sum of these spherical wavelets at the

position (x, y, z) then gives the new wavefront $\psi_z(x, y)$ [8]

$$\psi_z(x, y) = \frac{z}{i\lambda} \int\int \psi_0(x_0, y_0) \frac{e^{ikr}}{r^2} \cos\theta dx_0 dy_0, \tag{2.1}$$

where λ is the wavelength, θ is the angle between the propagation direction and the optical axis z, and $k = \frac{2\pi}{\lambda}$. The radius r from the point $(x_0, y_0, 0)$ to (x, y, z) is given by [8]

$$r = \sqrt{z^2 + (x - x_0)^2 + (y - y_0)^2}. \tag{2.2}$$

2.1.1 Fresnel approximation

For long propagation distances, the propagation can be approximated to be paraxial $\cos(\theta \approx 0) \approx 1$. Using the binomial series of the radius given by Eq. 2.2 we get [9]

$$r = z \left(1 + \frac{(x - x_0)^2 + (y - y_0)^2}{2z^2} - \frac{[(x - x_0)^2 + (y - y_0)^2]^2}{8z^4} + \cdots \right). \tag{2.3}$$

If $z^2 \gg [(x - x_0)^2 + (y - y_0)^2]$, the third term and all higher-order terms are negligible and we arrive at [9]

$$r \approx z \left(1 + \frac{(x - x_0)^2 + (y - y_0)^2}{2z^2} \right). \tag{2.4}$$

The Fresnel approximation can be summarized with $\rho = \sqrt{(x - x_0)^2 + (y - y_0)^2}$ representing the transverse distance [9]

$$\frac{2\pi z}{\lambda} \frac{\rho^4}{8z^4} \ll \frac{\pi}{2}. \tag{2.5}$$

In this case, the phase error introduced by neglecting the higher-order terms does not exceed the maximum permitted by the Rayleigh quarter-wave criterion. This states that performance reduction will be modest, if the error of an optical system is below $\lambda/4$, which corresponds to a phase variation of $\pi/4$ [9]. We simplify Eq. 2.1 by applying the Fresnel approximation to $\exp(-ikr)$, using $r \approx z$ for $1/r$, and assuming $\cos(\theta \approx 0) \approx 1$ [8]

$$\psi_z(x, y) = \frac{e^{ikz}}{i\lambda z} \int_{-\infty}^{\infty} \psi_0(x_0, y_0) \exp\left(\frac{ik}{2z} [(x - x_0)^2 + (y - y_0)^2] \right) dx_0 dy_0. \tag{2.6}$$

2.1.2 Fraunhofer approximation

For very long propagation distances the wave propagation can be further simplified, if the Fraunhofer approximation is satisfied [8]

$$z \gg \frac{k(x_0^2 + y_0^2)_{max}}{2}. \tag{2.7}$$

In this case, the term under the integral sign of Eq. 2.6 becomes $\exp(\frac{ik}{2z}[(x - x_0)^2 + (y - y_0)^2]) \approx \exp(\frac{ik}{2z}(x^2 + y^2)) \cdot \exp(-\frac{ik}{z} \cdot (xx_0 + yy_0))$. Since $\exp(\frac{ik}{2z}(x^2 + y^2))$ is independent of the

integral, it can be moved to the front. The propagated wave field is then represented by [8]

$$\psi_z(x,y) = \frac{e^{ikz} \cdot e^{\frac{ik}{2z}(x^2+y^2)}}{i\lambda z} \int\int_{-\infty}^{\infty} \psi_0(x_0,y_0) \exp\left(-\frac{ik}{z}(x \cdot x_0 + y \cdot y_0)\right) dx_0 dy_0. \tag{2.8}$$

If we express x and y with the coordinates in reciprocal space $q_x = \frac{kx}{z}$ and $q_y = \frac{ky}{z}$, we get

$$\begin{aligned} \psi_z(x,y) &= \frac{e^{ikz} \cdot e^{\frac{iz}{2k}(q_x^2+q_y^2)}}{i\lambda z} \int\int_{-\infty}^{\infty} \psi_0(x_0,y_0) \exp(-i(q_x \cdot x_0 + q_y \cdot y_0)) dx_0 dy_0 \\ &= \frac{e^{ikz} \cdot e^{\frac{ik}{2z}(q_x^2+q_y^2)}}{i\lambda z} \cdot \mathcal{F}(\psi_0(x_0,y_0)). \end{aligned} \tag{2.9}$$

Here, the propagated wave field becomes the Fourier transform of the original wave. The prefactor is neglected in most cases as it is irrelevant when only considering relative intensities [9].

2.1.3 Imaging regimes

Based on the Fresnel and Fraunhofer approximations one can define different imaging regimes (see Fig. 2.2). One commonly speaks of the near field when the propagation distance is sufficiently large to fulfill the Fresnel approximation. If the propagation distance satisfies the Fraunhofer approximation, it is considered as in the far field or Fraunhofer regime. The recorded signal on the detector is, in this case, a diffraction pattern which encodes all spatial frequencies. The Fresnel number F, a dimensionless number, is often used to easily categorize the imaging regimes

$$F = \frac{W^2}{\lambda z}, \tag{2.10}$$

where W is the transverse extent (diameter) of the illumination.

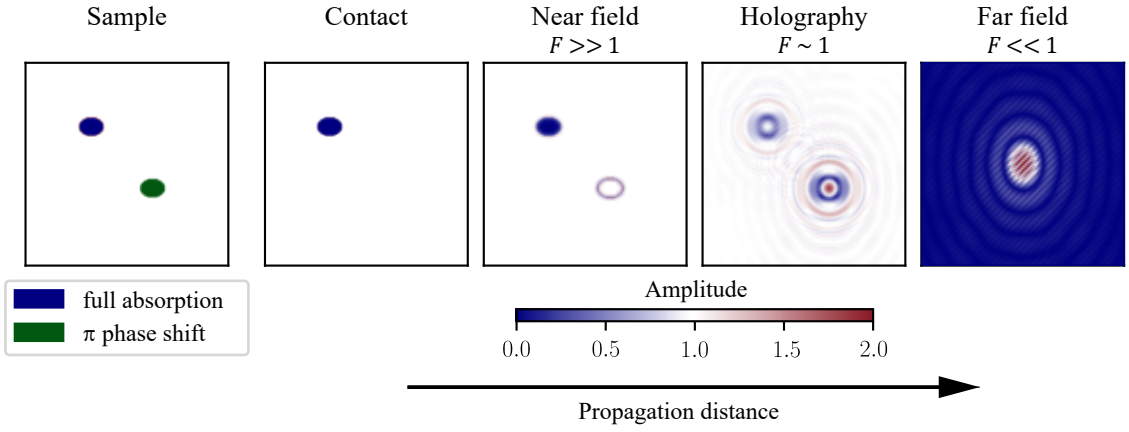

Figure 2.2: A sample consisting of two ellipses, one of them fully absorbing and one phase shifting by π is propagated. Directly behind the sample in the contact regime, only the absorbing ellipse can be detected. As the propagation distance increases, the edge contrast increases in the near field, and interference becomes apparent for lower spatial frequencies with increasing distance. In the far field, for a Fresnel number $F << 1$, the spatial frequencies are completely decoupled.

The contact regime is, as the name suggests, in direct contact with the sample plane. In the contact regime, a real space image of the sample is recorded. Here, only absorption, but no phase contrast is visible (Fig. 2.2). In the near field, for Fresnel numbers higher than one, interference in the form of an enhanced edge contrast becomes apparent. Interference can be observed for scattered waves originating from two points with a lateral distance smaller than the first Fresnel zone radius r_F [14]

$$r_F = \sqrt{\lambda \cdot z}. \tag{2.11}$$

Thus, for small propagation distances z phase contrast is limited to high spatial frequencies. With increasing propagation distance interference fringes begin to form. In the holographic regime, the Fresnel number approaches unity, and the contrast is mixed between real and reciprocal space. The boundary between the near field and the holographic regime is often ill-defined, sometimes, the two terms are used interchangeably. The far field diffraction pattern, for a Fresnel number much less than one, no longer resembles the real-space sample and is a representation of the object in reciprocal space.

Considering a photon energy of 8.0 keV (wavelength $\lambda = 0.155\,\text{nm}$) and an illumination with a diameter of 500 nm, we reach the far field regime for a propagation distance $z \gg 1.61\,\text{mm}$. These parameters resemble the ones used in the stereo ptychography experiments.

2.2 Coherence

(Partial) coherence of the illuminating beam is a prerequisite for the recording of interference patterns and, consequently, a crucial property for ptychographic imaging. It is a measure of the correlation between the phases of waves. A real beam deviates from the so far assumed ideal case of full coherence, where perfect monochromaticity and perfectly uniform propagation in a well-defined direction are assumed. These limitations are described by the temporal and spatial coherence length. [10]

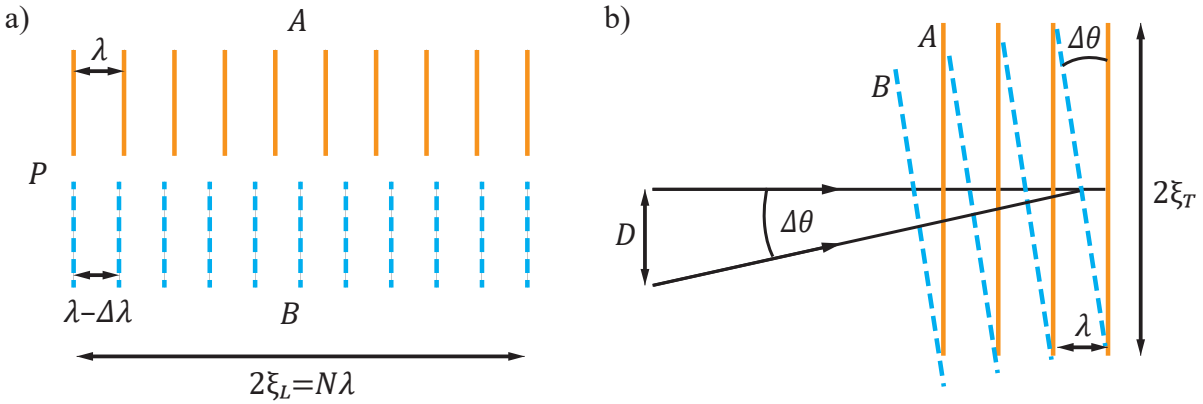

Figure 2.3: a) Longitudinal coherence. b) Transverse coherence.

2.2.1 Longitudinal coherence

Longitudinal coherence, also called temporal coherence, describes the misfit of two waves as they propagate along the same direction, but with slightly different wavelengths. We consider a quasi-monochromatic wave field with a bandwidth of $\Delta\lambda$. The temporal coherence length is then defined as the distance ξ_L two plane waves A and B with slightly different wavelengths λ and $\lambda - \Delta\lambda$ have to travel between being perfectly in phase and being perfectly out of phase (see Fig. 2.3a) [10]:

$$\xi_L = \frac{1}{2}\frac{\lambda^2}{\Delta\lambda}. \tag{2.12}$$

2.2.2 Transverse coherence

Two waves of the same wavelength λ propagating in slightly different directions are described in terms of transverse coherence, also known as spatial coherence. Two waves A and B are emitted from a finite source with height D and propagating with an angular offset of $\Delta\theta$ (Fig. 2.3b). Their spatial coherence length is defined as [10]

$$\xi_T = \frac{1}{2}\frac{\lambda L}{D}, \tag{2.13}$$

where L is the distance between source and imaged object.

2.3 Interaction of X-rays with matter

When passing through matter, X-rays interact with it through different processes. An X-ray photon interacting with an electron can either be absorbed or scattered. The probability of an X-ray photon interacting with an electron is described by the cross section σ of a process. The cross section is dependent on the photon energy. As a result, different effects dominate at different energies, as shown in Fig. 2.4.

Elastic scattering

Elastic scattering is defined as the scattering of an X-ray beam by an atom without any energy transfer. In the classical description, an X-ray wave interacts with an atom, and the electrons start to oscillate in the electric field. This leads to the generation of a secondary electromagnetic wave with the same frequency. The outgoing wave field has a different direction, but the same energy as the incoming wave field. [10]

First, we consider the interaction of X-rays with a free electron. The incident electromagnetic wave causes an oscillatory motion when interacting with a free electron. The electron will move (anti)parallel to the direction of oscillation of the incident electric field, resulting in electromagnetic dipole radiation, an electromagnetic wave of the same frequency is emitted. [11] The antiparallel motion of the electron can be explained using the model of a damped, driven harmonic oscillator. If the electric field oscillates at frequencies higher than the resonance frequency of the electron,

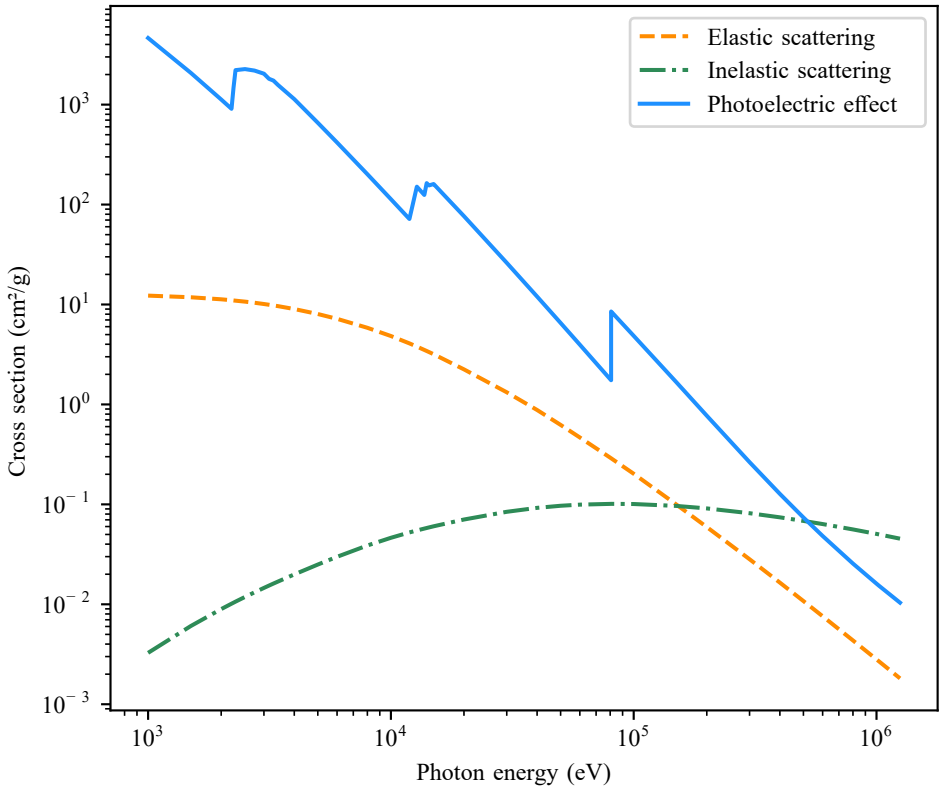

Figure 2.4: Cross sections for the different processes involved when gold is exposed to X-rays of variable photon energy. Data was obtained from the NIST XCOM package [15].

the electron will lack behind, resulting in a phase retardation. Above the resonance frequency, as it is the case for hard X-rays, the motion of the electron approaches an opposite phase from the driving electric field [9].

The Thomson scattering length quantifies the ability of an isolated electron of rest mass m_e to scatter an X-ray

$$r_e = \frac{e^2}{4\pi\epsilon_0 m_e c^2} = 2.82 \cdot 10^{-5}\text{Å}, \tag{2.14}$$

where e is the elementary charge, ϵ_0 the dielectric constant of the vacuum, and $m_e c^2$ can be understood as the rest-mass energy of the electron. r_e is sometimes also referred to as the classical electron radius. [11] The differential Thomson cross section $\frac{d\sigma}{d\Omega}$ for a single free electron is given by [9]

$$\frac{d\sigma}{d\Omega} = \left| -r_e \sqrt{1 - \sin^2\theta \cos^2\phi} \right|^2, \tag{2.15}$$

where θ is the deflection angle, and ϕ is the azimuthal angle. Integrating over all possible polarization directions, yields the total cross section for elastic scattering from a single electron [11]

$$\sigma_T = \frac{8\pi r_e^2}{3}. \tag{2.16}$$

In the next step we will consider scattering by a cloud of electrons instead of a single free electron. The vectorial difference $\overrightarrow{q}$ between an initial wave vector $\overrightarrow{k}$ and a final wave vector $\overrightarrow{k'}$ is given by [11]

$$\overrightarrow{q} = \overrightarrow{k} - \overrightarrow{k'}. \tag{2.17}$$

In the case of elastic scattering $|\overrightarrow{k}| = |\overrightarrow{k'}|$, hence the magnitude of the wave vector transfer q is given based on the scattering angle 2θ by [10]

$$|\overrightarrow{q}| = q = \frac{4\pi}{\lambda} \sin\theta. \tag{2.18}$$

$\overrightarrow{q}$ can be interpreted as the scattering vector and the imparted momentum transfer is given by $\hbar\overrightarrow{q}$, where $\hbar$ is the Planck constant [11]. For a number of electrons in a three-dimensional space, the X-ray amplitude $G(\overrightarrow{q})$ diffracted in direction $\overrightarrow{k'}$ relative to a single free electron at the origin is given by

$$G(\overrightarrow{q}) = \int_{-\infty}^{+\infty} \rho(\overrightarrow{r}) exp(-i\overrightarrow{q} \cdot \overrightarrow{r}) d^3\overrightarrow{r}, \tag{2.19}$$

where $\rho(\overrightarrow{r})$ is the electron density distribution. If $\rho(\overrightarrow{r})$ represents an atom, $G(\overrightarrow{q})$ can be interpreted as the atomic form factor $f_0(\overrightarrow{q})$. [9] It can be seen that the right hand side of Eq. 2.19 is a Fourier transform of the electron density of the scatterer. In the forward direction $q \to 0$, $f_0(\overrightarrow{q} = 0) = Z$, where Z is the atomic number. For $q \to \infty$, the scattered amplitude decays to zero, $f_0(\overrightarrow{q} \to \infty) = 0$. [10]

Inelastic scattering

Beyond the classical description, we consider the incident X-rays to be a beam of photons. Inelastic scattering occurs when kinetic energy is transferred from an incoming photon to an electron. This process is also known as Compton scattering. The scattered photon, due to the energy transfer, has a lower energy than the incoming photon. Consequently, it has a longer wavelength and loses its phase relationship with the incoming photon. The change in wavelength is proportional to the Compton scattering length $\lambda\!\!\!^{-}_C$, which is given by [10]

$$\lambda\!\!\!^{-}_C = \frac{\hbar}{m_e c} = 3.86 \cdot 10^{-3}\text{Å}, \tag{2.20}$$

where $\hbar$ is the Planck constant, m_e the electron mass, and c the speed of light. The Compton effect is dominant at very high X-ray energies ($> 50\,\text{keV}$) and up to moderate γ-ray energies ($\sim 3\,\text{MeV}$).

Photoelectric effect

The photoelectric effect describes the absorption of a photon by an atom inducing the excitation of a bound electron to an unoccupied state, or emission of a photoelectron [11]. The hole created in the inner shell can be filled by an electron from an outer shell, creating a photon of a characteristic energy. This process is called fluorescent X-ray emission. Alternatively, the hole is filled by an

electron from a higher shell, releasing the excess energy through emission of an Auger electron.[10] All experiments in this thesis were performed at a photon energy where the photoelectric effect is dominant.

2.3.1 Complex index of refraction

From the interaction of X-rays with single electrons or atoms, we will now proceed to a more macroscopic view of X-ray interaction with matter. The two relevant phenomena are in this case the refraction of the X-ray beam, which is a shift of the phase of the outgoing beam, and the attenuation, which is a reduction in intensity. Both these effects are summarized in the complex refractive index n for X-rays, which is commonly given by[9]

$$n = 1 - \delta - i\beta. \tag{2.21}$$

The real part describes the refraction of an electromagnetic wave when passing through a material and the imaginary part describes its attenuation. For X-rays the real part of the refractive index is often written as $1 - \delta$ with δ being positive but significantly smaller than unity. δ can be related to the electron density by

$$\delta = \frac{\lambda^2 \rho_e r_e}{2\pi}, \tag{2.22}$$

where λ is the wavelength, ρ_e the electron density, and r_e the classical electron radius. The phase shift ϕ of an electromagnetic wave when passing through a material of thickness d compared to propagation in vacuum is given by

$$\phi = -\frac{2\pi}{\lambda} \int_0^d \delta dz. \tag{2.23}$$

In ptychography, this relationship can be used to calculate the thickness of particles if the material and hence the refractive index is known.

2.4 Small angle X-ray scattering

Small-angle X-ray scattering (SAXS) is a technique used to characterize the nanoscopic heterogeneity of matter. SAXS is based on measuring the intensity of elastically scattered X-rays as a function of the scattering angle. The measured signal represents the scattered intensity as a function of the magnitude of the scattering vector q, which was already introduced in Eq. 2.18. The scattering angle is reciprocally related to the length scales probed in the sample[16]

$$d = \frac{2\pi}{q}. \tag{2.24}$$

In contrast to wide angle X-ray scattering (WAXS), SAXS probes scattering intensity at small angles, which corresponds to larger distances.

Recalling the definition of the amplitude of a scattered wave introduced in Eq. 2.19, we can define the scattering amplitude in a SAXS experiment as following

$$A(\overrightarrow{q}) = \int \Delta\rho(\overrightarrow{r}) exp(-i\overrightarrow{q} \cdot \overrightarrow{r}) d^3\overrightarrow{r}, \tag{2.25}$$

where $\Delta\rho = \rho_p - \rho_s$ is the difference between the scattering length density of the particle ρ_p and the scattering length density of the solvent ρ_s.[17] The intensity over a scattering volume V is then given by[16]

$$I(q) = \frac{1}{V}\left|\int \Delta\rho(\overrightarrow{r}) exp(-i\overrightarrow{q} \cdot \overrightarrow{r}) d^3\overrightarrow{r}\right|^2. \tag{2.26}$$

For a monodisperse system of chaotically tumbling particles, the intensity only depends on the magnitude of $\overrightarrow{q}$ and can be expressed by

$$I(q) = n\Delta\rho^2 V^2 P(q) S(q), \tag{2.27}$$

where n is the number density of particles, V is the volume of a single particle and $P(q)$ the rotationally averaged scattering form factor of the particle and $S(q)$ the structure factor.[16] The scattering form factor $P(q)$ describes the size and shape of the particles. The structure factor $S(q)$ describes the interference between neighboring particles in the sample. Hence, it gives insights into interactions between particles in the sample system. For very dilute systems, $S(q)$ can be approximated by $S(q) \approx 1$.[16]

SAXS can provide information on the size and structure of colloidal nanoparticles, which is encoded in the scattering form factor $P(q)$. The shape of the probed particles is typically determined using prior knowledge of the sample. A primitive particle shape is chosen, in the simplest case a sphere, and its form factor is calculated. The model is then fitted to the experimental data.

If the shape of the particles is unknown, one can still extract information on the radius of gyration R_g of the particle by applying the Guinier approximation. It states that any form factor function can be approximated to a Gaussian function in the small angle limit ($q < 1/R_g$) and in this way enables a size determination independent of the form factor. A prerequisite is that the structure factor $S(q)$ is equal to one. The intensity is in this case given by[17]

$$I(q) = I(0) \exp\left(-\frac{(qR_g)^2}{3}\right). \tag{2.28}$$

The Guinier plot, where $\ln(I(q))$ is plotted against q^2, is widely used to determine the radius of gyration R_g. The scattering intensity in the Guinier plot should be a linear function for any form factor. With the slope of a linear fit of the intensity data R_g can be determined.[17] Fig. 2.5 shows a Guinier fit of an exemplary data set. More detailed introductions to SAXS can be found in the publications by Li[18], Kikhney[17], Jeffries[16], and Gommes[19].

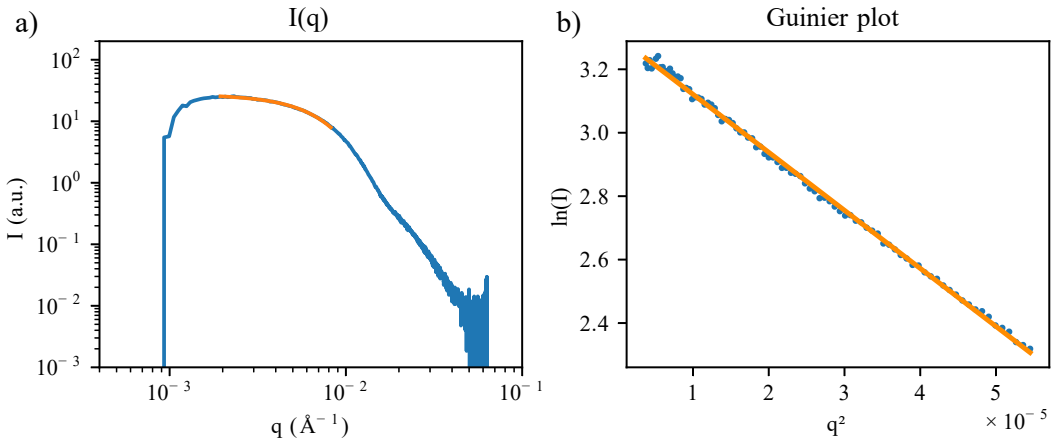

Figure 2.5: Example of a SAXS data set. a) Exemplary SAXS signal of Au nanoparticles recorded after 10 min in the reference measurement at 9.65 keV, described in Sec. 7.2. b) shows the corresponding Guinier plot with the linear fit indicated in orange.

2.5 X-ray optics

Röntgen initially deemed that X-rays can not be focused with lenses [20]. The challenge of focusing X-rays stems from their refractive index being close to one (see Sec. 2.3.1).

In general, lenses for X-rays can be categorized by their working principle. They can work by diffraction, refraction, or reflection. An example for refractive optics are compound refractive lenses (CRL). Due to their relatively low focusing efficiency, refractive lenses are commonly used as a stack of lenses, as shown in Fig. 2.6a. Refractive lenses were in the realm of this thesis only exploited as prefocusing lenses and I will, therefore, not go into more detail about them. Examples for diffractive optics are Multilayer Laue lenses (MLL) and Fresnel zone plates (FZP). Reflective optics are often applied in the form of Kirkpatrick-Baez (KB) mirrors. A general overview about X-ray focusing can be found in a review by Ice *et al.* [21]

Kirkpatrick-Baez mirrors

KB mirrors are, as the name suggests, a reflective optic. Other types of reflective X-ray optics exist, such as Wolter optics, but KB mirrors are the most common type used at synchrotron facilities. A set of two elliptically curved mirrors is illuminated under grazing incidence, where one typically focuses in vertical and the other in horizontal direction [22] (see Fig. 2.6d). An advantage of mirror optics is that they are inherently achromatic and hence an optimal choice for wide-bandpass applications. They can be also employed to suppress higher harmonics of the X-ray beam, since the critical angle for total external reflection is energy dependent. This energy dependence of the critical angle restricts the application of standard KB mirrors to photon energies below ~ 40 keV. Compared to FZPs, MLLs, and CRLs, KB mirrors, especially for high photon energies, are a less compact type of focusing optic. Typically, the working principle of KB mirrors is based on total reflection. But multilayer structures, making use of Bragg conditions,

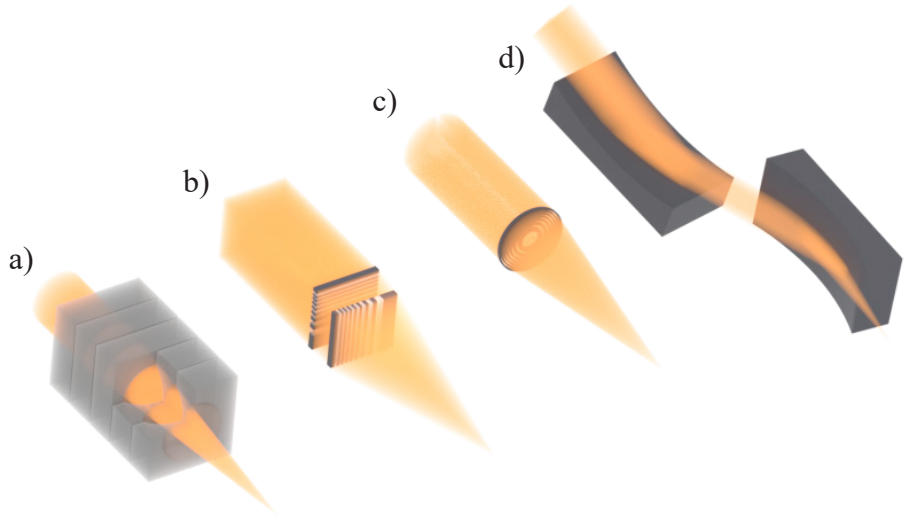

Figure 2.6: Schematic of X-ray lens types. a) Stack of compound refractive lenses. b) Multilayer Laue lenses. c) Fresnel zone plate. d) Kirkpatrick-Baez mirrors. The illustration is not to scale.

can also be employed to achieve higher reflection angles. However, their periodic structure is designed for a specific photon energy with only a small tolerance, which makes them less versatile. Focus sizes down to 7 nm have been realized with advanced KB mirrors, which have a multilayer structure [23]. However, fabrication of such high-performance mirrors is challenging and conventional setups at beam lines create focus sizes of 30 nm to 50 nm at the moment [24,25].

Fresnel zone plates

FZPs are diffractive lenses that work based on a circular grating, shown in Fig. 2.6c. The zones of absorption FZPs alternate between opaque and transparent. Alternatively, phase-shifting FZPs can be employed, where zones alternate between transparent and, ideally, phase-shifting by π. Focusing is for both types achieved through constructive interference in the focal plane. The binary structure of the zone plate leads to a series of diffraction orders. For this reason, Fresnel zone plates create several foci. Typically, the first order focus is selected, and other diffraction orders get blocked by a pinhole, called order sorting aperture.

The width of the outermost (finest) zone of the FZP dr_N defines the achievable focus spot size and the numerical aperture (NA). Assuming the first order focus is selected, the spatial resolution given by the Rayleigh criterion for a FZP is

$$\delta_{FZP} = 1.22 \cdot dr_N. \tag{2.29}$$

Focus sizes below 10 nm have been achieved with FZPs at a photon energy of 9 keV [26]. FZPs are most effective at photon energies below 10 keV, since very high, hard to manufacture, aspect ratios of the structure would be needed at higher energies.

Multilayer Laue lenses

Another type of diffractive optic are MLLs, shown in Fig. 2.6b. Their working principle is similar to that of FZPs, but they are not limited to lower photon energies. MLLs are produced by sputtering alternating layers of two materials with different refractive indices. The structure is then sliced to the desired thickness. This method allows for achieving very high aspect ratios between zone width and thickness.[27] Because of their manufacturing principle, MLLs are only 1D focusing optics. Therefore, a set of two MLLs, one for horizontal and one for vertical focusing, is typically used to create a 2D focal spot. MLLs, like FZPs, create foci of different orders and an order sorting aperture is used to select the first order focus. They offer the highest numerical aperture in the hard X-ray regime. MLLs with a focus size of below 10 nm have been recently employed for hard X-ray near-field ptychography[28].

3 Ptychography

The description of ptychography in this chapter considers far-field ptychography as the default version and specifies differences that have to be considered in the near field regime in Sec. 3.3.

3.1 Ptychographic model

Ptychography combines the strengths of coherent diffractive imaging (CDI) and scanning transmission X-ray microscopy (STXM). In STXM a sample is scanned in the focal plane of an X-ray beam, and the transmitted intensity is recorded. However, the spatial resolution of STXM is inherently limited by the beam size on the sample and scanning of larger areas with a high spatial resolution can be time consuming.

CDI, on the other hand, is a lensless imaging method, in the sense that no objective lens is used. The spatial resolution is in this case not limited by the numerical aperture of an objective lens. The sample is placed downstream of the focus, and a diffraction pattern is captured by a 2D area detector. The detector functions as a virtual lens and the resolution limit is given by the highest scattering angle that can be recorded. CDI has the potential for imaging with single digit nanometer resolution [29]. The forward model of CDI as well as of ptychography is visualized in Fig. 3.1. The wave field after interaction with a sample, for a thin object, is given

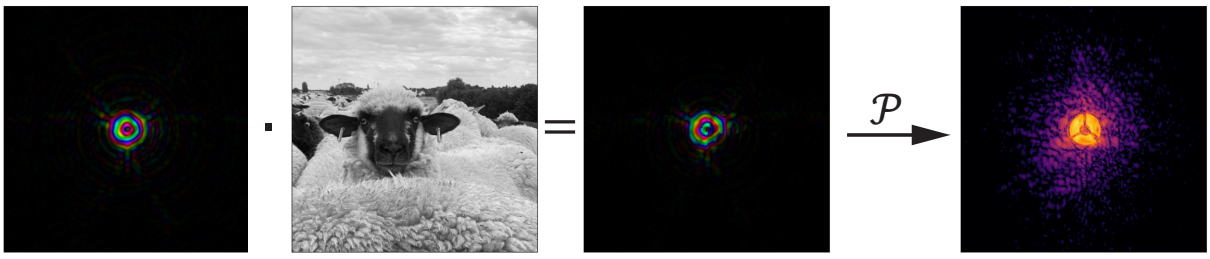

Figure 3.1: Visualization of the forward model of ptychography. The interaction of the probe $P(\mathbf{r})$ with the object $O(\mathbf{r})$, yields the wave field behind the sample $\psi(\mathbf{r}) = P(\mathbf{r}) \cdot O(\mathbf{r})$. The measured signal in the detector plane is the intensity of the propagated exit wave field $\Psi(\mathbf{r})$.

by the multiplication of the illumination function $P(\mathbf{r})$ with the illuminated part of the object function $O(\mathbf{r})$. The convolution of illumination and object in reciprocal space, can be expressed as a simple multiplication in real space. The illumination function and object function are both complex valued, modelling the amplitude and phase of the incoming wave field and of the object

transmission function, respectively. The exit wave field is then propagated to the detector plane. The propagation between sample and detector is modelled with a fast Fourier transform in far field ptychography, while a Fresnel propagator is used in the case of near-field ptychography.

In the detector plane the diffraction pattern is recorded. However, only the intensities of the wave field can be measured. This is the phase problem. The loss of the phases leads to an underdetermined inverse problem. In CDI, support constraints, requiring prior knowledge of the sample, are crucial for a successful phase retrieval.

In ptychography, which is a form of scanning coherent diffractive imaging, such prior knowledge is not required. By scanning the sample with overlapping neighboring scan positions, redundancy in the diffraction data is created, as shown in Fig. 3.2. This method ensures that enough information is acquired to find a unique solution for the object transmission function. An overlap of 60-70% is typically recommend for robust phase retrieval [30].

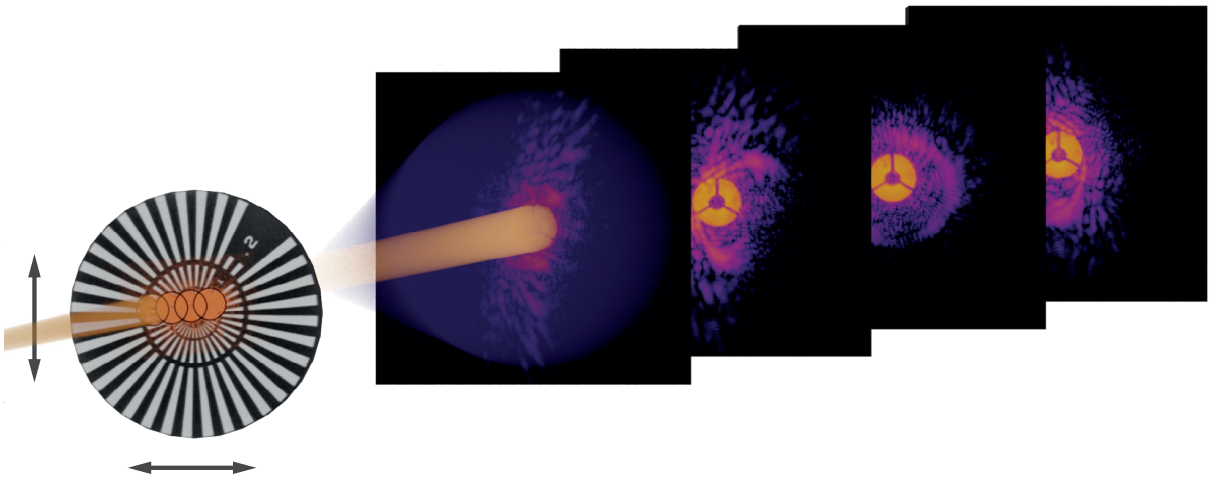

Figure 3.2: Scanning with overlap. A Siemens star test pattern is scanned with overlapping scan positions. The diffraction patterns are recorded in the far field.

The classical ptychographic model assumes the sample under study is optically thin. This requires the projection and the first Born approximation to be met. In other words, the sample is thin enough to disregard propagation effects of the illuminating wave field and secondary scattering. The depth of field describes the thickness limit for an optically thin sample (see Sec. 3.4).

3.2 Multi-slice ptychography

Multi-slice ptychography enables imaging of samples with an extended depth of field. An optically thick sample is virtually sliced in the reconstruction and multiple layers can be recovered this way. The forward model for a sample consisting of two layers, which are separated by a distance greater than the depth of field, is visualized in Fig. 3.3.

The probe $P(\mathbf{r})$ interacts with the first slice O_1 and the exit wave field behind the first slice is then given by $\psi_1(\mathbf{r}) = P(\mathbf{r}) \cdot O_1(\mathbf{r})$. So far, the approach is identical to single slice ptychography,

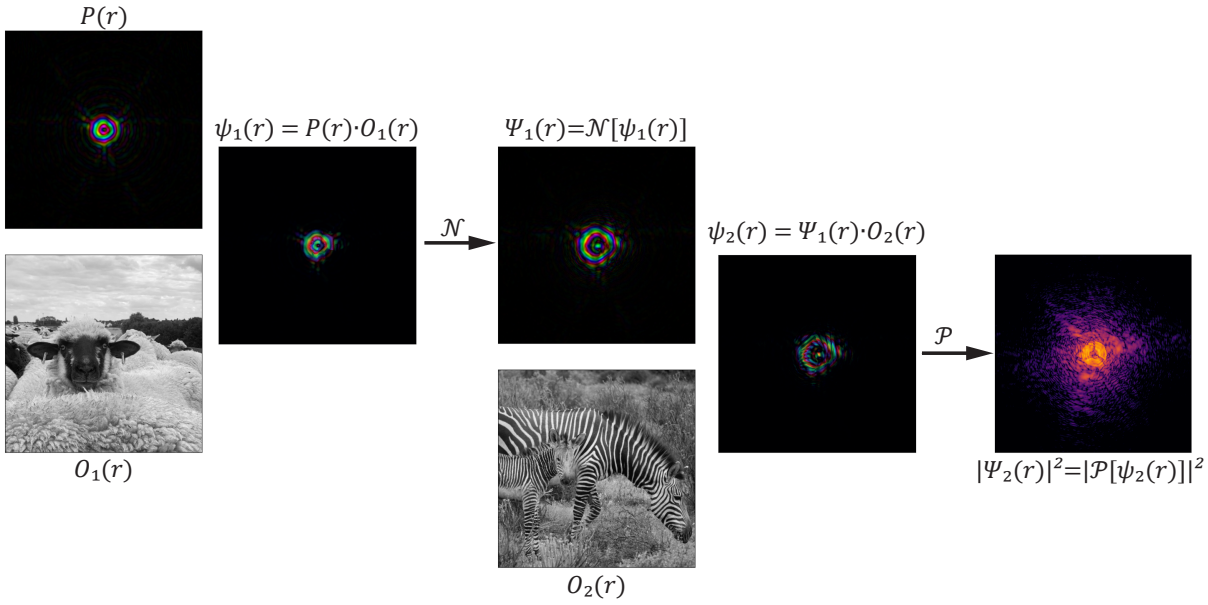

Figure 3.3: Visualization of the forward model of multi-slice ptychography.

but instead of direct propagation to the detector plane, the exit wave field is propagated to the second slice with a Fresnel propagator. The propagated wave field $\Psi_1(\mathbf{r})$ is then multiplied with the second layer O_2. This procedure is repeated until the last slice is reached, then the exit wave field is propagated to the detector plane.

Multi-slice ptychography is not limited to well separated thin layers, but can be also applied to 3D structures that get virtually sliced. In this case, the propagation distance is typically chosen equal to or slightly above the depth of field limit. The thickness of the sample in this way determines the number of slices. With visual light ptychography, the recovery of more than thirty slices of a volumetric sample has been demonstrated [31].

3.3 Near-field ptychography

Like its far-field analog, near-field ptychography (NFP) is based on scanning of the sample with overlapping scan positions. In NFP, the sample is usually positioned farther downstream of the X-ray beam focus to create an extended illumination. A measurement is considered to be in the near-field regime if the Fresnel number is close to or greater than one (see Sec. 2.1.3). The propagation within a sample and between sample and detector is modelled with a Fresnel propagator.

In the recorded near-field diffraction patterns, the spatial frequencies are mixed, but not fully decoupled as it is the case in the far field. The maximum lateral distance between two points for which interference effects can be observed depends on the propagation and is given by the first Fresnel zone radius r_F [14] (see Sec. 2.1.3, Eq. 2.11). When NFP is used for imaging of sparse samples, such as widely spread nanoparticles, the scanning step size should, for this reason, be chosen smaller than the first Fresnel zone radius [32]. This incomplete decoupling of the spatial

frequencies is also the reason for the relaxed spatial coherence requirements that were reported for near-field ptychography [33,34]. Coherence of the illumination over the first Fresnel zone width is in principle sufficient in near field imaging [35].

3.3.1 Fresnel scaling theorem

In near field ptychography, the exit wave field has to be propagated over relatively long distances between sample and detector with a Fresnel propagator. Application of the Fresnel scaling theorem makes NFP reconstructions significantly more efficient. The cone beam geometry is converted to a parallel beam geometry by scaling the pixel size and propagation distance by the magnification. Fig. 3.4 visualizes the cone beam geometry of a near-field experiment.

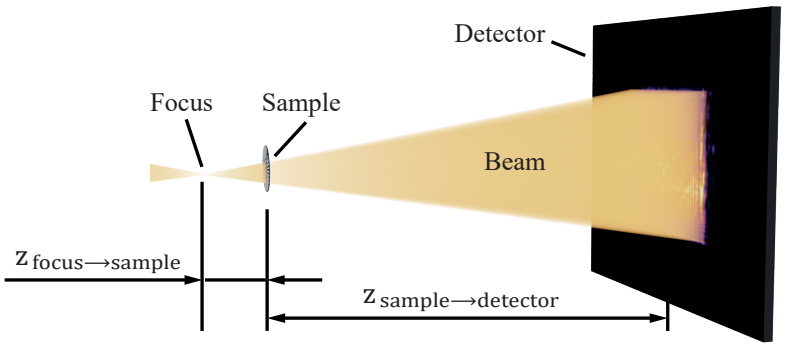

Figure 3.4: Cone beam geometry in near-field imaging.

The magnification M is given by

$$M = 1 + \frac{z_{\text{sample}\to\text{detector}}}{z_{\text{focus}\to\text{sample}}}. \tag{3.1}$$

The pixel size in the sample plane Δx_{sample} can be calculated with the magnification M

$$\Delta x_{\text{sample}} = \frac{\Delta x_{\text{detector}}}{M}, \tag{3.2}$$

where $\Delta x_{\text{detector}}$ is the pixel size of the detector. The effective propagation distance between sample and detector z_{eff} is calculated by

$$z_{\text{eff}} = \frac{z_{\text{sample}\to\text{detector}}}{M}. \tag{3.3}$$

The exact implementation of Fresnel scaling for near-field multi-slice ptychography is described in Sec. 6.2.1.

3.3.2 Structured illumination

Structure in the illuminating beam is generally beneficial for robust reconstruction in ptychography[36,37], and this is even more important in NFP. To facilitate efficient phase recovery, NFP relies on a structured illumination[34,38]. Structure is typically achieved by placing a diffuser, such as sandpaper, in front of the lens.

If a plane wave were used, there would be little diversity in the detected interference pattern apart from a lateral shift (see Fig. 3.5a). Structured illumination, on the other hand, results in greater differences in the detected signal for different scan positions (Fig. 3.5b). As the phase of the illumination is not modelled as a constant over the entire cross section of the beam, this effectively eliminates the problem of zero crossings in the contrast transfer function.

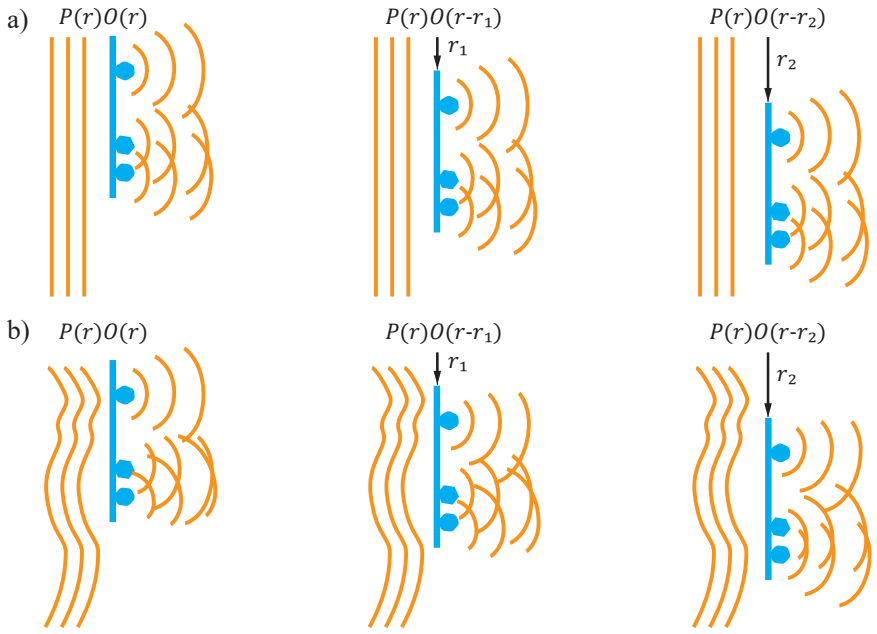

Figure 3.5: Structure in the illumination is crucial to create sufficient diversity in the measured signal. a) The diffraction signal, caused by interaction of a plane wave with a sample (shown in blue), is invariant to small translations of the sample. Only a lateral shift is introduced. b) If the illumination is highly structured, the detected signal exhibits greater differences when the sample is moved transverse to the propagation direction. Figure adapted from[32].

3.4 Spatial resolution

The resolution of a ptychographic reconstruction can be assessed using a resolution target, such as a Siemens star. In this case, the size of the distinguishable features provides an estimate of the resolution. Alternatively, the resolution can be determined based on edge contrast or Fourier ring correlation[39,40], which was used in this thesis.

Theoretical resolution limits for the transversal and depth resolution are given in the following.

Transversal resolution

The achievable lateral resolution δ_r in an optical imaging system, is typically defined by

$$\delta_r = c \cdot \frac{\lambda}{n \sin\theta} = c \cdot \frac{\lambda}{NA}, \tag{3.4}$$

where λ is the wavelength, n the refractive index, θ the scattering angle and $NA = n \sin\theta$ the numerical aperture of the imaging system. The constant c, also called the imaging factor, is 0.5 in the Abbe limit, which specifies the theoretical limit of the ultimate resolvable distance for a perfect imaging system.[41] Another concept is, to define the resolution limit based on how well two closely spaced point-sources are resolved. As formulated by Rayleigh, two point-sources are just resolved when the zero-order diffraction maximum of one diffraction pattern coincides with the first minimum of the other. In this case the constant c is 0.61 [42] and becomes $c = 1.22$ for coherent light [43].

Since ptychography is a lensless imaging method, the detector acts as a virtual lens. Approximating the refractive index with one ($n \approx 1$) and considering only small angles ($\sin\theta \approx \theta$), as it is generally valid for far-field ptychography, the numerical aperture of the detector NA_{detector} is given by

$$NA_{\text{detector}} = n \sin\theta \approx \theta \tag{3.5}$$

with

$$\theta = \tan\left(\frac{N \cdot \Delta x_{\text{detector}}}{2 \cdot z_{\text{sample}\to\text{detector}}}\right) \approx \frac{N \cdot \Delta x_{\text{detector}}}{2 \cdot z_{\text{sample}\to\text{detector}}}, \tag{3.6}$$

where N is the number of pixel rows or columns of the detector, $\Delta x_{detector}$ is the detector pixel size and $z_{sample\to detector}$ the propagation distance between sample and detector (see Fig. 3.6). If we now plug Eq. 3.5 into Eq. 3.4 with $c = 0.5$, we arrive at

$$\delta_r = \frac{\lambda z_{\text{sample}\to\text{detector}}}{N \Delta x_{\text{detector}}}, \tag{3.7}$$

which is also the definition of the pixel size in the sample plane in far-field ptychography. The highest scattering angle, at which a signal is detected, sets the limit for the achievable resolution in far-field ptychography. An additional requirement for a successful ptychographic reconstruction is that the sampling of the diffraction pattern fulfills the Nyquist criterion, which states that the sampling interval (detector pixel size) should be no larger than half the bandwidth (separation between speckle maxima) [11].

In near-field ptychography the transversal resolution is ultimately limited by the size of the secondary source and the pixel size in the sample plane. The pixel size in the sample plane is here given by the detector pixel size divided by the magnification (see Sec. 3.3.1). Practically, the available coherent photon flux, stability of the measurement system, and other factors often degrade the spatial resolution.

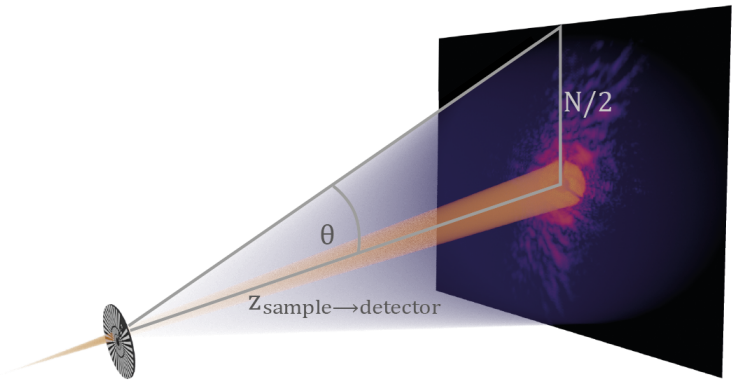

Figure 3.6: In far-field ptychography, the detector can be considered as a virtual lens. The highest detected scattering angle represents the opening angle of the virtual lens.

Depth of field

The depth of field (DOF) is defined as the maximum longitudinal distance between two objects to appear sharp in a captured image. The depth of field can be used analogous to the depth of focus in lens-based imaging. For multiple slices to be distinguishable in multi-slice ptychography, the thickness of the object must exceed the DOF. Further, the DOF determines the minimum thickness of individual slices. The DOF is commonly defined based on the lateral resolution δ_r and the wavelength λ with a constant c

$$\mathrm{DOF} = c \cdot \frac{\delta_r^2}{\lambda}. \tag{3.8}$$

The constant c is reported to be between 1.0 and 5.2 [44–46]. In far-field ptychography, the value of c is commonly set to 5.2, as it was determined by Tsai *et al.* [46] For near-field ptychography, Stockmar *et al.* defined c as $c = 1.0$ [44]. Hu *et al.* define the depth resolution for near-field multi-slice ptychography as

$$\mathrm{DOF} = \frac{\delta_r \cdot (z_1 + z_2)}{D}, \tag{3.9}$$

where $z_1 + z_2$ is the propagation distance between the focus of the cone beam and the detector and D is the beam diameter on the detector [47].

3.5 Phase retrieval

The overlapping scan positions in ptychography provide the possibility to solve the phase problem. Maiden and Rodenburg were the first to successfully reconstruct an X-ray ptychogram using their ptychographic iterative engine (PIE) [48], which initially required a defined illumination function. Since then, other algorithms to recover the phase have been introduced, such as difference map and maximum likelihood refinement [49,50].

All reconstructions shown in this thesis were achieved using the extended ptychographical iterative engine [30] and its variant for optically thick samples – the three-dimensional ptychographical iterative engine [51].

The reconstruction algorithms are described as they would be applied to far-field ptychography. In the case of near field ptychography, a Fresnel propagator has to be used for the propagation between the sample plane and the detector plane.

3.5.1 Extended ptychographical iterative engine

The extended ptychographical iterative engine (ePIE) [30] was the first engine for ptychographic reconstructions with probe recovery, which was an extension of PIE [48].

The reconstruction process is illustrated in Fig. 3.7. The algorithm runs sequentially through the recorded diffraction patterns and updates the probe and the illuminated part of the object in each sub-iteration.

An initial guess of the object O and the probe P is used to determine an exit wavefront. $\mathbf{r}$ and $\mathbf{u}$ are real-space and reciprocal-space coordinate vectors.

$$\psi_j(\mathbf{r}) = O_j(\mathbf{r}) \cdot P_j(r - \mathbf{R}_{s(j)}), \tag{3.10}$$

where j is the index of the diffraction pattern and $\mathbf{R}_{s(j)}$ a vector describing the relative shift between the object and probe before recording the intensity of the j-th diffraction pattern. This wavefront is then propagated to the detector plane, where the measured amplitude $\sqrt{I_{s(j)}}$ replaces the amplitude of the wavefront guess

$$\Psi'_j(\mathbf{u}) = \sqrt{I_{s(j)}(\mathbf{u})}\frac{\mathcal{F}[\psi_j(\mathbf{r})]}{|\mathcal{F}[\psi_j(\mathbf{r})]|}. \tag{3.11}$$

The updated wavefront is then back-propagated to the sample plane. Here, the object and probe get updated. The object update is defined as following

$$O_{j+1}(\mathbf{r}) = O_j(\mathbf{r}) + \alpha\frac{P_j^*(r - \mathbf{R}_{s(j)})}{|P_j(r - \mathbf{R}_{s(j)})|^2_{max}}(\psi'_j(\mathbf{r}) - \psi_j(\mathbf{r})), \tag{3.12}$$

where α is a constant to adjust the step-size of the update and can have any value between $\alpha = 0$ and $\alpha = 1$. The probe update is defined analogously

$$P_{j+1}(\mathbf{r}) = P_j(\mathbf{r}) + \beta\frac{O_j^*(\mathbf{r})}{|O_j(\mathbf{r})|^2_{max}}(\psi'_j(\mathbf{r}) - \psi_j(\mathbf{r})). \tag{3.13}$$

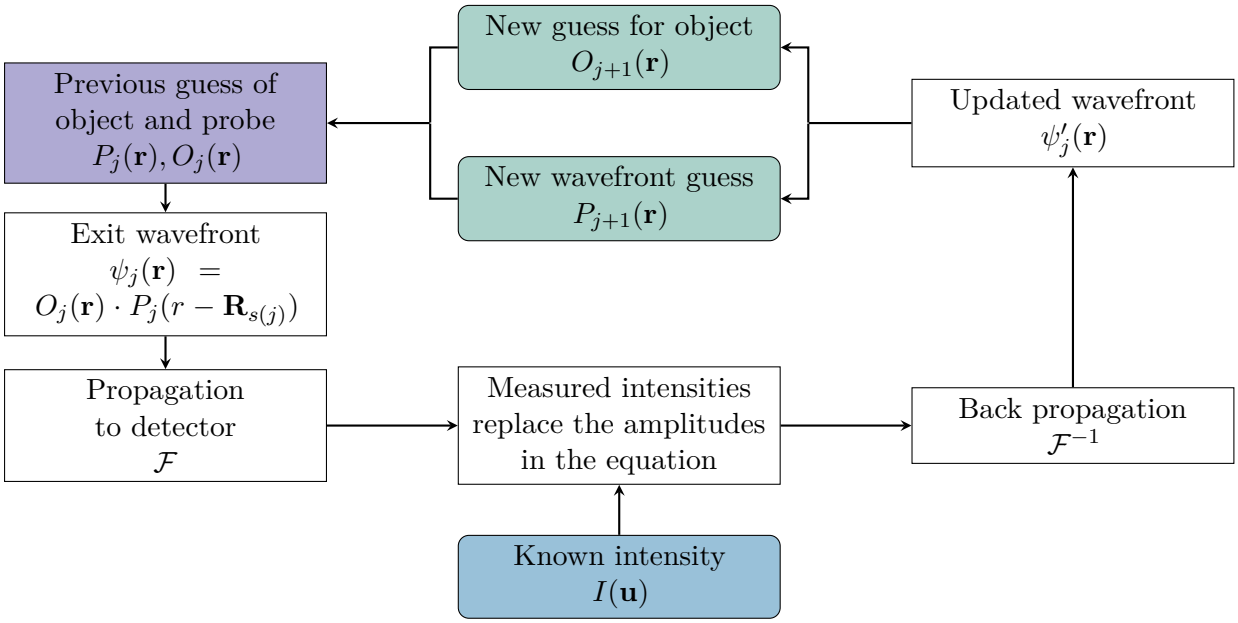

Figure 3.7: Extended ptychographic iterative engine (ePIE)

The diffraction patterns get processed in a random order. For this reason, reconstruction results and their error can vary slightly. The reconstruction error is calculated as

$$E_{\Psi} = \frac{\sum_j \sum_{\mathbf{u}} |\sqrt{I_j(\mathbf{u})} - \Psi_j(\mathbf{u})||^2}{\sum_j \sum_{\mathbf{u}} I_j(\mathbf{u})}. \tag{3.14}$$

As a stopping criterion either a certain error value or a maximum number of iterations can be defined. In this work, most reconstructions were run for 1000 iterations.

3.5.2 Three-dimensional ptychographical iterative engine

The three-dimensional ptychographical iterative engine (3PIE) enables reconstruction of several object slices of an optically thick object [51]. 3PIE can be seen as an extension of ePIE and thus follows the same principle (see Fig. 3.8). Initial guesses for the probe and the objects (slices) have to be created. The exit wavefront of the first slice is calculated and then propagated over a distance Δ_{z1} to the next slice

$$\psi_{e,1,j}(\mathbf{r}) = O_{1,j}(\mathbf{r}) \cdot P_j(r - \mathbf{R}_{s(j)}), \tag{3.15}$$

$$\psi_{i,2,j}(\mathbf{r}) = \mathcal{N}_{\Delta_{z1}}(\psi_{e,1,j}(\mathbf{r})). \tag{3.16}$$

The index e is used for exit wavefronts and the index i for incoming wavefronts. Then, the exit wavefield of the second object is calculated by multiplying the propagated exit wavefront of the first slice by the second slice

$$\psi_{e,2,j}(\mathbf{r}) = O_{2,j}(\mathbf{r}) \cdot \psi_{i,2,j}(\mathbf{r}). \tag{3.17}$$

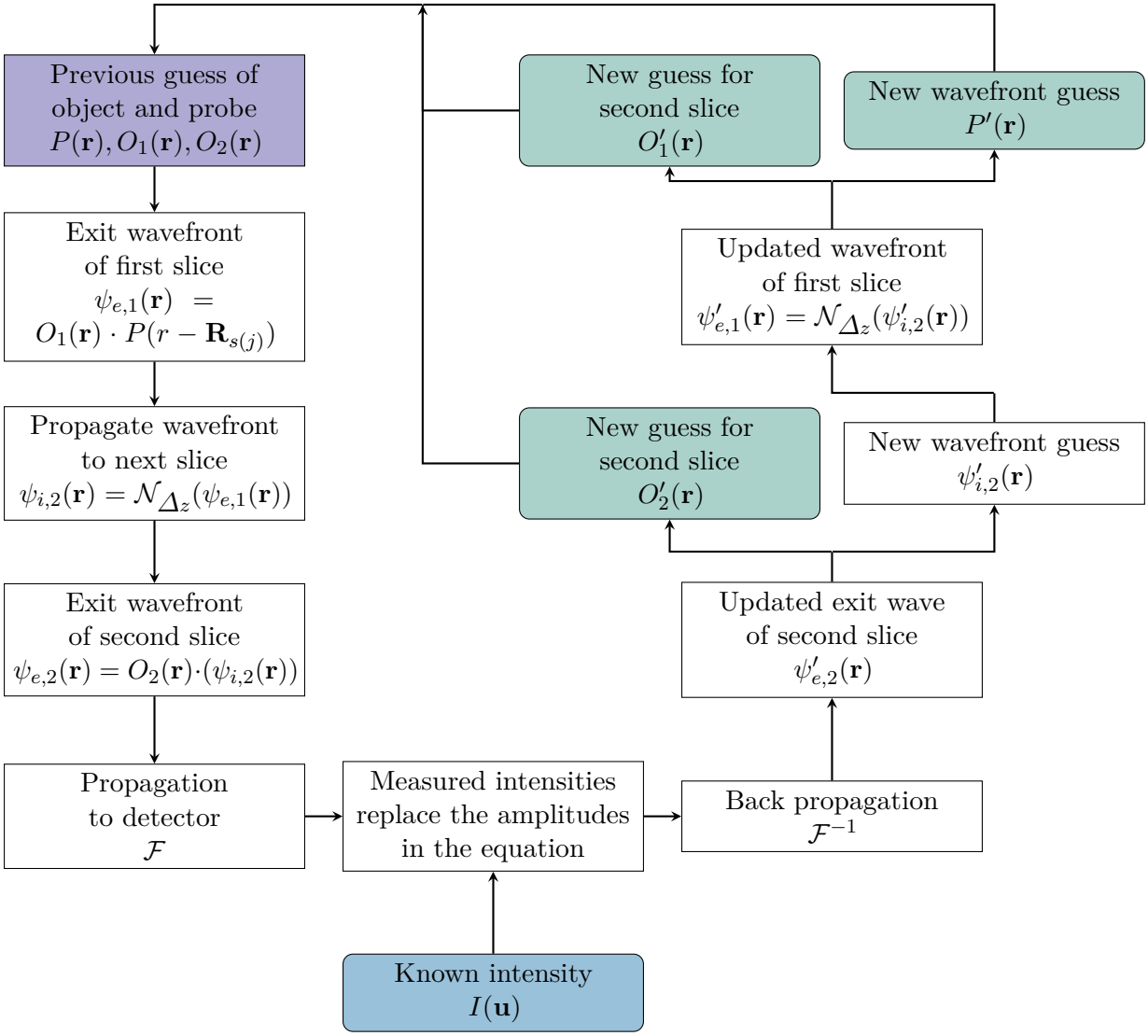

Figure 3.8: Ptychographical iterative engine for three dimensions (3PIE) at the example of a two-slice system.

This step is repeated until the last (N-th) slice is reached. Then, the wavefront is propagated to the detector plane, and the amplitudes get updated with the measured intensities

$$\Psi_j(\mathbf{u}) = \mathcal{F}[O_{N,j} \cdot \mathcal{N}_{\Delta_{zN-1}}[O_{N-1,j} \cdots \mathcal{N}_{\Delta_{z2}}[O_{2,j} \cdot \mathcal{N}_{\Delta_{z1}}[O_{1,j} \cdot P_j(r - \mathbf{R}_{s(j)})]]]], \tag{3.18}$$

$$\Psi'_j(\mathbf{u}) = \sqrt{I_{s(j)}(\mathbf{u})} \frac{\Psi_j(\mathbf{u})}{|\Psi_j(\mathbf{u})|}. \tag{3.19}$$

The wavefront is then propagated back to the last slice and the guess for the N-th slice and the incoming wavefront of the N-th slice get updated

$$O_{N,j+1}(\mathbf{r}) = O_{N,j}(\mathbf{r}) + \alpha \frac{\psi^*_{i,N,j}}{|\psi_{i,N,j}|^2_{max}} (\psi'_{e,N,j}(\mathbf{r}) - \psi_{e,N,j}(\mathbf{r})), \tag{3.20}$$

$$\psi'_{i,N,j} = \psi_{i,N,j} + \beta \frac{O^*_{N,j}(\mathbf{r})}{|O_{N,j}(\mathbf{r})|^2_{max}} (\psi'_{e,N,j}(\mathbf{r}) - \psi_{e,N,j}(\mathbf{r})). \tag{3.21}$$

The updated wavefield is then propagated to the $(N-1)$-slice

$$\psi'_{e,N-1,j}(\mathbf{r}) = \mathcal{N}^{-1}_{\Delta_{zN-1}}(\psi'_{i,N,j}(\mathbf{r})). \tag{3.22}$$

The $(N-1)$-slice and the incoming wavefield are updated. Subsequently, all slices get updated until the first slice is reached, where the first slice and probe get updated. In the next sub-iteration the next diffraction pattern is processed.

In near-field multi-slice ptychography, in contrast to far-field multi-slice ptychography, the propagation between slices is modeled with the Fresnel scaling theorem. Hence, the pixel size differs for every slice. Additionally, the propagation between last slice and detector is performed with a Fresnel propagator instead of a Fourier transform.

4 In-situ synthesis

This chapter provides a brief theoretical background on the galvanic replacement reaction of copper(I) oxide with gold and palladium, which is studied in situ in this thesis. Additionally, the chapter presents an overview of X-ray radiation-induced damage in in-situ studies.

4.1 Galvanic replacement reaction

Galvanic replacement reactions (GRRs) are a redox process in which one metal or metal oxide undergoes oxidation by ions of another metal possessing a higher electrochemical potential. In other words, a metal or metal oxide gets replaced by a more noble metal. GRRs, in principle, can be understood as a corrosion process. GRRs, if used intentionally, provide a relatively simple pathway to synthesize hollow nanoparticles [52]. The initial particles, in this thesis Cu_2O nanocubes, act as a reactive template and over the realm of the reaction get gradually oxidized and dissolve. At the same time, the more noble metal ions, here Pd^{2+} and Au^{3+}, from the solution get reduced and grow on the outer surface of the template.

The half reactions and standard reduction potentials E^0_{red} for the galvanic replacement reactions of Cu_2O with Au and Pd are given by [53]

$$\begin{aligned} AuCl_4^- + 3e^- &\rightarrow Au^0 + 4Cl^- \qquad & E^0_{red} &= 0.99\,V \text{ vs standard hydrogen electrode} \\ PdCl_4^{2-} + 2e^- &\rightarrow Pd^0 + 4Cl^- \qquad & E^0_{red} &= 0.59\,V \text{ vs standard hydrogen electrode} \\ Cu_2O + 2H^+ &\rightarrow 2Cu^{2+} + H_2O \qquad & E^0_{red} &= 0.13\,V \text{ vs standard hydrogen electrode} \end{aligned}$$

Unlike in GRRs of two metals, e.g. Ag and Au, the oxidation of Cu_2O involves hydrogen ions. This makes the GRR of Cu_2O with Au or Pd pH-dependent [53].

The overall reaction equation of Cu_2O with Au is given by [54]

$$1.5Cu_2O_{(s)} + AuCl^-_{4(aq)} + 3H^+_{(aq)} \rightarrow 3Cu^{2+}_{(aq)} + Au^0_{(s)} + 4Cl^-_{(aq)} + 1.5H_2O$$

and for the GRR of Cu_2O with Pd by [53]

$$Cu_2O_{(s)} + PdCl^{2-}_{4(aq)} + 2H^+_{(aq)} \rightarrow 2Cu^{2+}_{(aq)} + Pd^0_{(s)} + 4Cl^-_{(aq)} + H_2O$$

The GRR has been described by a mechanism similar to pinhole corrosion [52,55], shown in Fig. 4.1a.

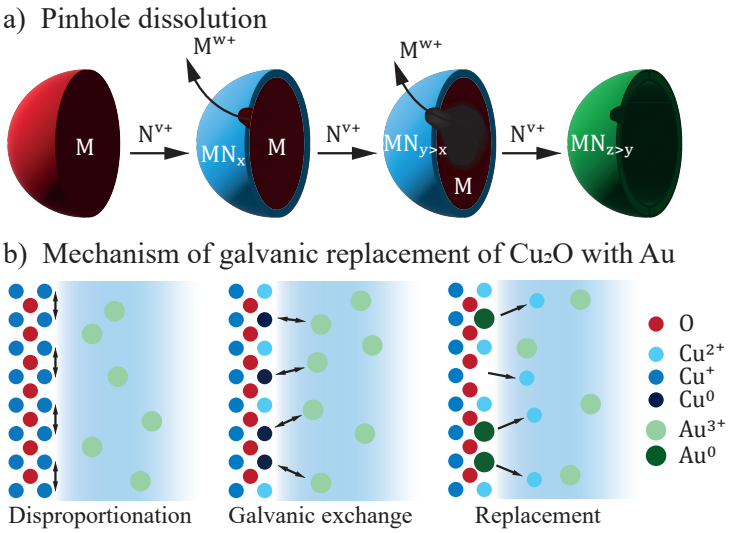

Figure 4.1: Mechanism of the galvanic replacement reaction. a) Visualization of a galvanic replacement reaction following a pinhole corrosion like process. A particle of metal M is exposed to ions of a nobler metal N^{v+} in solution. A shell forms around the initial particle, which is an alloy MN_x of the initial metal M and the nobler metal N. The less noble metal M dissolves into solution (M^{w+}) through pinholes forming in the shell. At later stages, the less noble metal M may be gradually removed from the alloy ($MN_{z>x}$). Adapted from [55]. b) Mechanism of the galvanic replacement of Cu_2O with Au as it was proposed by Lowe and Coridan. The surface disproportionates, resulting in Cu and CuO on the surface. Cu and $AuCl_4^-$ from the solution get exchanged, resulting in a surface of Au and CuO. Adapted from [54].

The first stage of the reaction is characterized by an alloying process, where a thin layer of the introduced metal grows on the template particle. Through diffusion processes, an alloy of both metals forms on the template surface. Later stages of the reaction are characterized by dealloying when the metal with a lower reduction potential is selectively removed from the alloyed shell [55–58].

Specifically, for the galvanic replacement reaction of Cu_2O with Au, Lowe and Coridian propose that the GRR starts with a surface disproportionation, forming Cu and CuO (Fig. 4.1b). Then, the Cu and dissolved $AuCl_4^-$ undergo a galvanic exchange, resulting in a surface of CuO and Au. Further deposition of Au is limited until the CuO is etched by the acid in solution. [54]

4.2 Radiation damage

Conducting experiments in situ allows to observe reactions as they occur and gain valuable insights. These insights may include identifying intermediate products or observing the morphological evolution of particles. However, it is crucial to recognize that the observation itself can influence the outcome. To detect a signal, the X-rays must interact with the studied material. In the used X-ray energy range (8 keV to 18 keV), the dominant part of this interaction is governed by the photoelectric effect. Photoelectric absorption causes excitation or ionization of atoms or molecules of the irradiated substance and can lead to the emission of photoelectrons. These

electrons and radical species, which can form in a process following the ionization or excitation of the material, can impact the reaction chemistry. In some cases, the influence of X-rays might be negligible, in others, it might dominate the reaction pathway. Whether this is called beam damage or radiolytic synthesis depends on the observer's aim and perspective.

The following section will provide an introduction to hydrolysis and influencing parameters in X-ray experiments. A broader overview of radiation damage in X-ray experiments can be found in a publication by Bras *et al.*[59]

4.2.1 Dose

The dose of ionizing radiation quantifies the energy absorbed in a unit mass of material. Gray (Gy) is the unit of dose, which is defined as the absorption of one joule of radiation energy per kilogram of material ($1\,\mathrm{Gy}{=}1\,\mathrm{J\,kg^{-1}}$). The absorbed dose D, which is measured in Gray, is not to be confused with the dose equivalent H, which is measured in Sievert. The absorbed dose is a physical quantity, whereas the dose equivalent H is used to measure a biological effect. Hence, the relevant unit when discussing beam damage in chemical systems is Gray.

In X-ray imaging the dose D can be calculated with

$$D = \frac{\mu}{\rho} \Phi_0 E N_{illu} \left(\frac{\mathrm{J}}{\mathrm{kg}} = \mathrm{Gy} \right), \tag{4.1}$$

where μ is the linear absorption coefficient, ρ the mass density, Φ_0 the incident photon fluence (photons per area), E the photon energy, and N_{illu} the number of illuminations of a given area.

The dose rate is another important measure, which quantifies the absorbed radiation per unit time and is often given in μGy/h.

4.2.2 Hydrolysis

When ionizing radiation, in the realm of this thesis X-rays, interacts with water, radicals and other highly reactive species are formed.

$$\mathrm{H_2O} \xrightarrow{\mathrm{h}\nu} \mathrm{e^-_{(aq)}}, \mathrm{H^+}, \mathrm{H\cdot}, \mathrm{OH\cdot}, \mathrm{H_2O_2}, \mathrm{H_2}$$

This process is called Hydrolysis. Hydrolysis is a multi-step process, which is based on ionization and excitation of water molecules (Fig. 4.2). At pH 7 the radiolytic yields of the radicals elementary species per 100 eV absorbed are $G(e^-_{(\mathrm{aq})}) = 2.7$, $G(\mathrm{H\cdot}) = 0.55$, and $G(\mathrm{HO\cdot}) = 2.8$ (where $G = 1$ corresponds to $9 \times 10^{-5}\,\mathrm{mol/(L \cdot kGy)}$)[61].

Solvated electrons and hydrogen radicals are both highly reducing agents, while the hydroxyl radical is of highly oxidizing nature. They can react with metal ions in the following manner[62]

$$\begin{aligned} \mathrm{M^+ + e^-_{(aq)}} &\rightarrow \mathrm{M^0} \\ \mathrm{M^+ + H\cdot} &\rightarrow \mathrm{M^0 + H^+} \\ \mathrm{M^+ + OH\cdot} &\rightarrow \mathrm{M^{2+} + OH^-} \end{aligned}$$

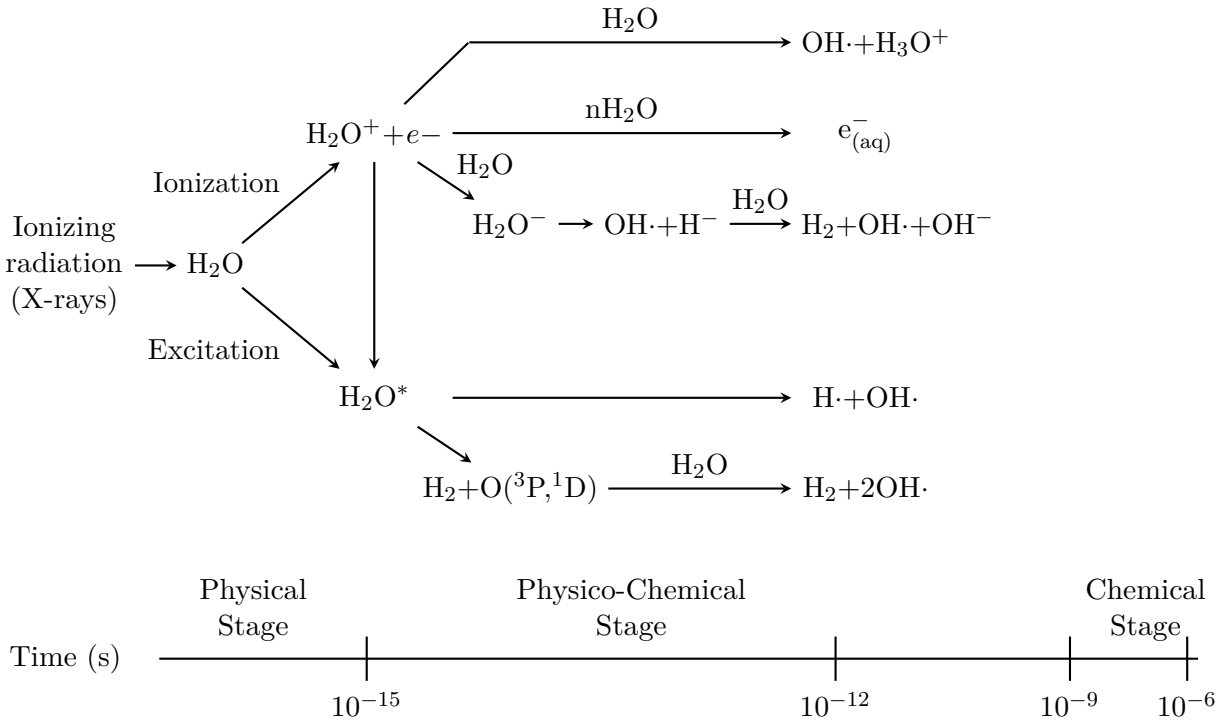

Figure 4.2: Process of hydrolysis (adapted from [60]).

The direct reduction of metal ions by solvated electrons or hydrogen radicals may influence the yield of the elementary metal in in-situ imaging experiments of galvanic replacement reactions.

4.2.3 Synthesis parameters influenced by nanofocused X-ray beams

Apart from hydrolysis, which is especially relevant for reactions in aqueous solutions, X-rays can also affect the reaction in other ways. The following list only mentions the most relevant parameters.

Temperature

The absorption of X-rays, or for that matter any electromagnetic radiation, can cause a localized increase in temperature [63–65]. The temperature change by a nanofocused X-ray beam can be more than 10 K for a very short time frame [64,65]. This is particularly relevant for samples in a vacuum environment, as is often the case for cryocooled samples, where heat dissipation is poor. In principle, a locally elevated temperature in an in-situ study of a chemical reaction could affect the synthesis, e.g. lead to a higher reaction rate. However, since the reactions studied in this thesis take place at a liquid-solid interface, heat conductivity and dissipation are quite good and any potential temperature increase should be insignificant.

pH

The interaction of a reaction system with X-rays can lead to a change of the pH. Radiolysis products can cause an acidification of the reaction solution [59]. Depending on the reaction that is studied, this change in pH level can result in a shift in the reaction equilibrium. Laanait *et al.* showed that X-rays can significantly shift the equilibrium in dissolution at the calcite/water interface through acidification [66]. However, in our case the total volume of the reaction solution is high compared to the irradiated volume. Therefore, diffusion is likely to reduce this acidification before it has a significant impact.

Water evaporation

It has been found that X-rays can lead to increased evaporation at the water-air-interface. In a closed capillary, the water vapor is reversibly condensed during pauses in irradiation. Weon *et al.* suggested that this phenomenon is caused by the reduction of the surface tension due to photoionization. [67] In an open system, such as the in-situ reaction cell used in this work, water vapor may diffuse away before condensation. But the illuminated spot is relatively far away from the water-air-interface and the total volume of the reaction solution of more than 1 mL is high compared to the irradiated volume, so that this effect is probably insignificant.

Excitation and ionization of reactants

Beyond hydrolysis, X-rays can also cause direct ionization and excitation of the reactants. The majority of studies neglects the direct interaction of reactants with X-rays and interaction with radical species formed by hydrolysis are listed as the cause of the radiolytic synthesis with X-rays or γ-rays [68–71]. But especially at higher photon energies the cross section for absorption of water decreases significantly, while even at 100 keV absorption is still dominant for copper(I) oxide, gold, and palladium [15]. The low concentration of the metal precursor in solution, coupled with the relatively high absorption in water at photon energies around 10 keV, likely permits the neglect of this effect. However, it may need to be reconsidered for experiments involving significantly higher X-ray energies or higher concentrations of the metal precursor.

4.2.4 Radiolytic synthesis of noble metal nanoparticles

A synthesis of particles caused by high energy radiation, such as X- and γ-rays or electron and ion beams, is called radiolytic synthesis. The irradiated solvent in this case acts as a reductant or more precisely solvated electrons, free radicals and other reducing species formed in the solvent through irradiation [68]. The creation of these species in aqueous solutions is covered in Sec. 4.2.2. Radiolytic synthesis of nanoparticles have been reported for a wide range of noble metals and their alloys, including gold [71–74] and palladium [75–77].

The use of γ-rays for radiolytic synthesis is well documented, as is the use of synchrotron radiation [73,74,78]. However, the latter is utilized less frequently. The interactions of X-rays and

γ-rays with matter relevant to radiation damage, namely the photoelectric effect and the Compton effect, are the same. However, the probability of certain interactions is energy dependent and for γ-rays of very high energies, pair production needs to be additionally considered. But for commonly used γ-ray sources, ^{60}Co and ^{137}Co[79], the photon energy is below the threshold for significant influence of pair production and Compton scattering is dominant for most materials[15].

In the radiolytic synthesis of metal nanoparticles in aqueous solution hydrolysis products, primarily solvated electrons and hydrogen radicals, reduce dissolved metal precursors.

$$\mathrm{M^{n+}} + \mathrm{ne^-_{(aq)}} \rightarrow \mathrm{M^0}$$
$$\mathrm{M^{n+}} + \mathrm{nH\cdot} \rightarrow \mathrm{M^0} + \mathrm{nH^+}$$

These neutral M^0 atoms in the next step dimerize when encountering or being associated with M^+ ions.

$$\mathrm{M^0} + \mathrm{M^0} \rightarrow \mathrm{M_2^0}$$
$$\mathrm{M^0} + \mathrm{M^+} \rightarrow \mathrm{M_2^+}$$

Charged dimers M_2^+ may be reduced. Further association with unreduced ions or charged clusters will drive the particle growth.[70]

A high dose rate was reported to favor the formation of more nucleation centers and lead to particles with a narrow size distribution, whereas lower dose rates lead to bigger particles[71]. The dose rate can also influence whether alloys (high dose) or core-shell particles (low dose) are obtained in radiolytic synthesis of bimetallic particles.[80] Generally, the dose rates in X-ray experiments at synchrotron radiation facilities are significantly higher than in most described experiments with γ-rays. Rates of less than 5 kGy/h are considered low, while the dose rates in the X-ray experiments in this thesis were significantly higher, between 1 kGy/s in near-field ptychography and 5 MGy/s in far-field ptychography.

The yield of particles can be increased by the addition of hole scavengers. The hydroxyl radical $OH\cdot$ has a strong oxidative potential and can cause unfavorable oxidation of metal ions. Secondary alcohols, such as propan-2-ol, can be used to scavenge hydroxyl radicals. While propan-2-ol was reported to increase the yield of particles in experiments with γ-rays, Wang *et al.* reported a negative effect on the yield in a synchrotron experiment with a white X-ray beam (6.5 keV to 30 keV, centered around 12.5 keV)[73].

4.2.5 Experimental parameters influencing radiation damage

The choice of some experimental parameters can significantly impact the degree of radiation damage. The following lists some of the most important parameters relevant to in situ X-ray imaging.

Dose and dose rate

As the dose quantifies the absorbed energy, it is plausible that higher doses cause stronger radiation damage. However, while the relationship between dose and radiation damage is well described in the field of protein crystallography, systematic studies are lacking for in-situ studies on chemical reactions. In the field of radiolytic synthesis, dependencies between dose and dose rate and the shape, quantity and size of particles have been found [70,71]. Higher dose and higher dose rate lead to more, but smaller particles [71]. However, most of these experiments are carried out at much lower doses and dose rates than the ones we encounter in synchrotron experiments.

X-ray energy

At higher X-ray energies, the absorption is generally lower, while the phase shift does not decay at the same rate. Therefore, it would be a reasonable hypothesis that beam damage is lower at higher photon energies. Whether this hypothesis is correct, will be evaluated in the following.

Björling *et al.* simulated the concentration of reactive species (H_2O_2, H_2, $H\cdot$, $OH\cdot$) for the same photon flux at 24 keV and 800 eV. They found that the concentration of all species was more than one order of magnitude higher at 800 eV. The model included diffusion and recombination reactions [81]. However, the intensity of the detected signal would not be the same considering the same photon flux at 800 eV and 24 keV. Therefore, one would in most cases either adjust the photon flux or the exposure time to achieve a similar dose independent of the used photon energy. To answer the question of whether higher photon energies reduce beam damage, further research comparing concentrations at different photon energies with a constant dose would be needed.

Another interesting aspect when considering the influence of photon energies was covered by Sanishvili *et al.* They studied the effect of beam size and photon energy in protein crystallography [82]. As these samples are in most cases cryocooled, the main remaining contributor to beam damage is from photoelectrons, which are generated by the interaction of sample and X-ray. At higher X-ray energies, the energy of the generated photoelectrons is higher, and their flight path length is longer. As a result, at higher energies, most of the damage occurs farther away from the incident beam and is distributed over a larger area. [59,82]. Building on this idea, Dickerson and Garman sought an optimal X-ray energy, considering the lower efficiency of X-ray detectors at higher photon energies [83].

Because of the decreasing coherent flux and the decreasing efficiency of most focusing optics at high X-ray energies as well as the lack of suitable CdTe-detectors at most beamlines, it is at the moment in most cases not feasible to achieve high-resolution coherent diffractive imaging at photon energies above 30 keV.

Additionally, when considering the galvanic replacement reaction specifically, one should take into account that the radiolytic synthesis of noble metal nanoparticles is often carried out at even higher energies with γ-rays of a photon energy, where Compton scattering is dominant.

Beam size

Considering a constant photon flux, the X-ray beam size is directly coupled to the photon fluence on the sample. In this way, it has also an impact on the dose and dose rate as these are considered per kilogram. Further, diffusion effects play a role for the concentration of free radical species and the likelihood of recombination events. Björling *et al.* reported, based on simulations of different beam sizes, that concentrations increase as the beam is focused, albeit to a lesser extent than the flux density. This effect was partly offset by diffusion and the nonlinear kinetics of the decay reactions.[81]

Other parameters

Beyond the parameters listed above, the degree of beam damage highly depends on the studied reaction and concentration of precursor in the solution. Reactions in organic solvents, which are less susceptible to radiolysis, might be less prone to beam damage than reactions in aqueous solution. The reaction temperature might be relevant as it affects the diffusion rate and thus potential recombination of radical species. Madsen *et al.* reported a dependence of ambient water temperature and the survival probability of hydrated electrons[84]. The pH of the solution effects the yield of radical species and in this way also impacts radiation damage[71].

5 Stereoscopic ptychography

This chapter presents the first demonstration of hard X-ray stereo ptychography, a technique that utilizes two angled beams to scan a specimen simultaneously. The results shown in this chapter are part of the publications "Stereo hard X-ray ptychography"[85] and "Hard X-ray stereo ptychography with multi-slicing"[86]. Additionally, the application of stereo ptychography for in-situ imaging of a galvanic replacement reaction is presented.

Andreas Schropp came up with the initial idea for stereo ptychography. I then developed the concept and the experimental setup for stereo X-ray ptychography with support from Andreas Schropp. Further, I investigated the capabilities and limitations of stereo X-ray ptychography. As the principal investigator, I led the two beamtimes that these results are based on.

The experiments were planned and carried out together with Sarah-Alexandra Hussak, Karolina Stachnik, Dorota Koziej, Mattias Åstrand, Ulrich Vogt, Caterina Carus, Martin Seyrich, Johannes Hagemann, Christian G. Schroer, and Andreas Schropp. Mattias Åstrand manufactured the Fresnel zone plates. The initial algorithm for the separation of two distinct layers was developed by Caterina Carus and Johannes Dora, and adapted by me. The ptychographic reconstructions and layer separation analysis were done by me. I prepared the manuscript for both publications, together with Andreas Schropp in case of the paper "Stereo hard X-ray ptychography". All authors reviewed the original manuscripts for the publications.

The parameters of the synthesis were optimized for in-situ imaging beforehand by Sarah-Alexandra Hussak and Christoph Kruck. In addition to the beamtime participants of the ex-situ experiment, Christoph Kruck and Jenna Cathrin Fischer supported the in-situ experiment. I developed the method to remove obscuring particles based on stereo pairs, which was applied on the in-situ data, and carried out the complete data analysis.

5.1 Introduction

Compared to TEM, hard X-ray microscopy can be used with larger, thicker samples due to its greater penetration depth. This is particularly important for in-situ imaging of chemical reactions, which often requires special reactors to produce the necessary reaction environment. Furthermore, hard X-ray microscopy can provide morphological insights that go beyond pure two-dimensional imaging. It is a powerful method for determining the three-dimensional structure of a sample.

Thus far, most imaging techniques require a full rotation of the sample, to obtain a three-dimensional impression. Different 3D ptychographic imaging experiments have been carried out in tomographic and laminographic scanning mode [87–89]. Alternatively, 3D information of a sample can also be obtained by multi-slice ptychography. In this case, the depth information is extracted from just a 2D scan, which requires that variations in the illumination function are sufficiently large such that different sample layers can be separated from each other [46,51,90]. This also enables imaging of optically thick samples.

However, depth information in multi-slice ptychography can only be obtained for samples thicker than the depth of field of the imaging system [90,91]. Acquisition of multiple projections can overcome this limitation. This was achieved with sequential stereoscopic X-ray ptychography by rotation of the sample [92–94]. A separation in multi-slice reconstruction of slices thinner than the depth of field of the imaging system was demonstrated using nine scans of the sample tilted by 1° around four axes [95,96].

The need for rotation of the sample, however, increases the necessary scan time. The simultaneous acquisition of multiple projections of a sample is particularly valuable for in-situ or operando studies, where a high temporal resolution is crucial. For single shot ptychography, multi-slicing was realized with multiple inclined laser beams [97,98]. The simultaneous measurement of multiple projections with hard X-rays was accomplished with a resolution in the micrometer range [99–102]. In the field of high-resolution X-ray microscopy, stereoscopic or multi-projection X-ray imaging was demonstrated for coherent diffractive imaging at X-ray free electron lasers [103–106]. At synchrotron sources, simultaneous microscopy of multiple projections was shown for propagation-based phase-contrast imaging [105], differential phase imaging [107], and holotomography [108].

Another option to speed up the acquisition of volumetric ptychographic data sets is the use of multi-beam ptychography [109–113], which in principle could be combined with a rotation of the sample.

The simultaneous acquisition of multiple X-ray ptychographic projections has not been demonstrated so far. Our experiment is the first of its kind in this regard and makes use of the qualities of hard X-ray ptychography to offer the potential for a lateral resolution of 10 nm [114,115]. Meanwhile, it is suitable for a variety of samples ranging from bacteria [114,116] to in-situ studies of chemical systems [117–119].

5.2 Principle

Similar to human vision, multiple perspectives of a sample can provide a considerably improved 3D depth perception. In the presented case, the stereoscopic X-ray impression is created by two separate nanofocused X-ray beams that illuminate a sample with a certain angular offset. The beams are produced by a set of X-ray optics, as illustrated in Fig. 5.1. The direct, middle beam facilitates the alignment of the setup.

The focal length of the Fresnel zone plates (FZPs) and the optimal reflection angle of the small multilayer (ML) mirrors are chosen such that the three beams overlap close to the focal

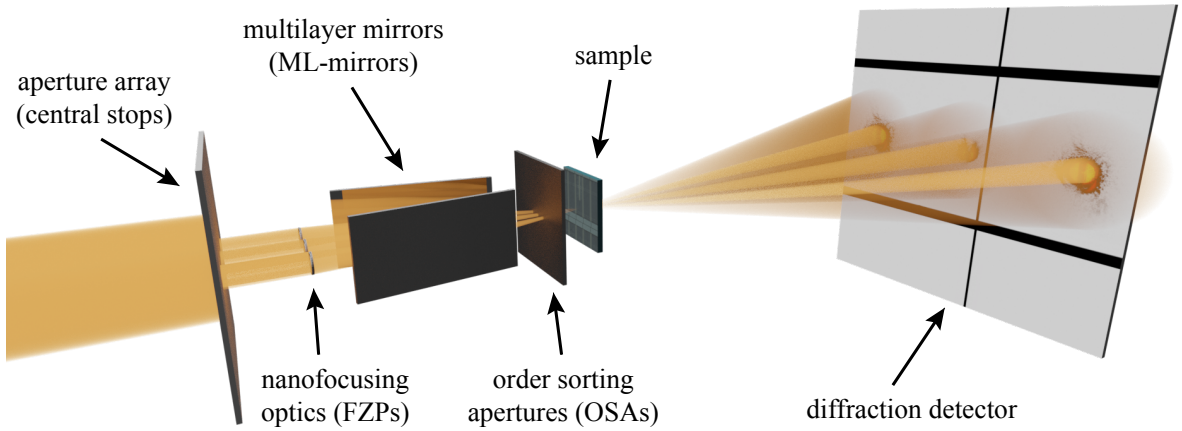

Figure 5.1: Schematic of the stereoscopic X-ray imaging setup. Three beams are formed by an aperture array that includes central stops and are then focused by a set of Fresnel zone plates (FZPs). The outer two beams are subsequently deflected by two multilayer-mirrors (ML-mirrors). The beams get cleaned from other diffraction orders by a set of pinholes (OSAs), placed between the mirrors and the sample. The sample is positioned in the intersection point of the beams and the diffraction pattern is recorded in the far field. Reprinted from [85].

plane of the FZP optics. By positioning a diffraction detector in the far-field regime of the imaging system, three individual ptychographic data sets can be recorded at the same time, each capturing a distinct view of the sample. The strongest stereoscopic effect can be expected from the outermost two beams, because of the maximum deflection angle, but in practice any two-beam combination from the setup can be used for stereoscopic vision.

5.2.1 Experimental setup

The stereoscopic microscope is mainly based on a set of FZPs and flat ML-mirrors. The ML-mirrors had a length of 12 mm, which is small enough for them to be positioned between the FZPs and the focal plane of the optics (see Fig. 5.2). The three nanobeams were created by introducing first an array of apertures with integrated central beam stops that are required to block the zeroth order of the FZPs. The gold central stops had a diameter of 25 µm and a thickness of 40 µm. Subsequently, the three separate parts of the X-ray beam were focused by a set of FZPs. They were laterally displaced in the horizontal direction by 500 µm, meaning that the individual beams can be considered as mutually incoherent. The FZPs were fabricated out of gold via a direct-write electron-beam lithography process followed by electroplating [120,121], with a diameter of $D = 74.9\,\mu\text{m}$ and an outermost zone width of $dr_N = 60\,\text{nm}$. The small W/Si-ML-mirrors were produced by AXO DRESDEN GmbH, Germany with alternating layers of tungsten and silicon with a period thickness of 6.4 nm. A mask with order sorting apertures (OSAs) was positioned between the mirrors and the sample to filter out all undesired diffraction orders of the FZPs. The mask was made out of a 50 µm thick tungsten foil. Individual apertures had a diameter of 17.5 µm.

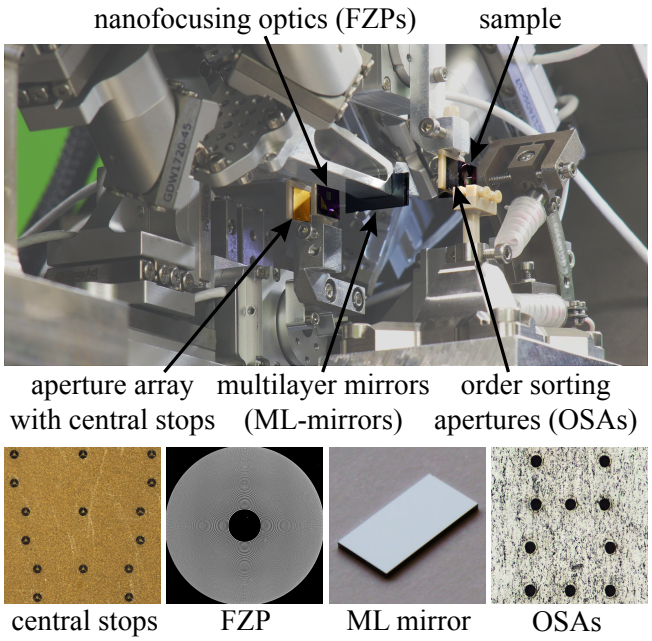

Figure 5.2: Photo of the stereo setup implemented into PtyNAMi, highlighting the different X-ray optics used, namely: an array of central stops, the FZPs for X-ray focusing, the ML mirrors to deflect the X-ray beams and an array of OSAs to clean the focused beam from undesired diffraction orders of the FZPs. Reprinted from [85].

The different X-ray optics were implemented into the ptychographic nano-analytical microscope (PtyNAMi) [122]. This instrument at beamline P06 at PETRA III (DESY Hamburg, Germany) provides all degrees of freedom to align the optics with the required positioning stability and accuracy. Due to rather strong space constraints, as shown in Fig. 5.2, the optics were implemented using a compact set of different stages and hexapods (SmarAct GmbH, Germany) for their precise alignment.

In this experiment, the X-ray photon energy was set to $E = 8.0\,\mathrm{keV}$ by a silicon channel-cut monochromator. At this energy, we expected a diffraction-limited beam spot from the FZPs of $d = 1.22 dr_N \approx 73\,\mathrm{nm}$ at a focal length of $f_1 = Ddr_N/\lambda = 29\,\mathrm{mm}$. The ML-mirrors had a maximum reflectance of $R = 80\,\%$ at the Bragg angle of $\vartheta = 0.75°$. Hence, the deflection angle of a single mirrored beam was $\theta = 2\vartheta = 1.5°$ with respect to the forward direction and the maximum viewing angle between the two outermost nanobeams was therefore $2\theta = 3.0°$.

We observed three separated beams on the detector at a distance of $L = 2.0\,\mathrm{m}$ from the sample, as indicated in Fig. 5.3. The distance between the sample and the detector was measured using a tape measure. The diffraction patterns were recorded by an Eiger X 4M photon-counting detector (DECTRIS AG, Switzerland) with a pixel size of 75 µm positioned at the end of an evacuated flight tube. The separation between the different beams was sufficiently large so that each signal could be analyzed individually and the spurious diffraction signal from a neighboring beam could be neglected. More specifically, 712 pixels between two beams correspond to a distance of 53.4 mm on the detector, or an angle of 1.53°, which is very close to the theoretically expected

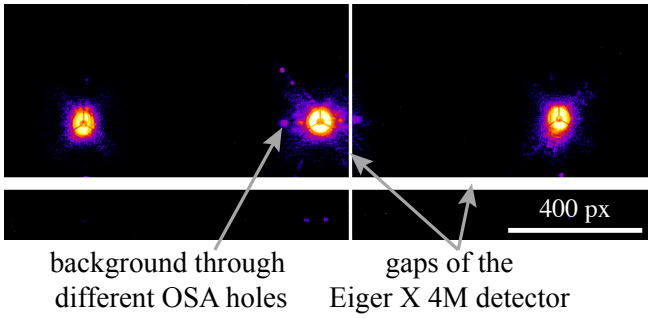

Figure 5.3: Three distinct far-field diffraction patterns, measured simultaneously on the Eiger X 4M detector at $L = 2\,\mathrm{m}$ distance from the sample. Reprinted from [85].

value of $\theta = 1.5°$. To accommodate all three beams on the detector, it has to be positioned closer to the sample than in single-beam ptychography. This leads to a lower sampling of the diffraction patterns and, depending on the size of the illumination, may reduce the reconstruction quality. In the present case, the stereographic data were reconstructed with an upsampling factor of 2 to mitigate this effect of a slightly reduced data sampling in reciprocal space [123].

The spatial resolution is limited by the maximum scattering angle that can be cropped out from the detector image for each individual diffraction pattern. In the current stereo-imaging geometry, using in addition the central third beam, this yields an area on the detector of about 512×512 pixels for each of the individual nanofocused X-ray beams. It guarantees that there is no overlap between adjacent diffraction patterns on the detector. At the chosen exposure times and cropping areas, we did not observe a significant crosstalk between the different nanofocused X-ray beams. The individual ptychograms can therefore be treated like normal single-beam scans without compromising reconstruction accuracy. Without the central X-ray beam and if the detector size is sufficiently large, the cropping area could in principle be increased, thereby further enhancing the maximum achievable spatial resolution for the different stereoscopic perspectives. A photon-counting detector with a large detection area can ensure a high signal-to-noise ratio and detection efficiency also at high scattering angles. The inclination angle of 1.5° for the two outermost beams on the detector is negligible as it is associated with a reduction in the horizontal size of the detection area of only 0.03 % compared to the perpendicular geometry.

Setting up the stereo X-ray microscope requires a precise alignment of the X-ray optics such that the different nanobeams overlap in the sample plane and is therefore more time consuming than in a comparable single-beam experiment. Here, the standard configuration of PtyNAMi could be employed to a large extent, thereby reducing setup time to a minimum. However, optimization of the setup or ideally a dedicated endstation would allow to reduce the additional time needed. The X-ray beam, provided by PETRA III, was quite stable throughout the experiment and we did not experience any increased influence of X-ray beam instabilities on the reconstruction quality. If a comparable setup would be used at, e.g. X-ray free-electron lasers, one would have to re-evaluate any instability effects.

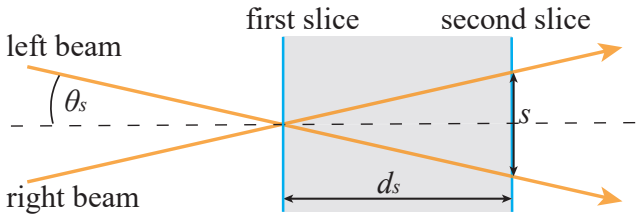

Figure 5.4: Schematic of the two deflected beams passing through two slices of a sample. The angle between the two beams is $2\theta_s$, the shift between the two beams in the second slice s, and the distance between the slices d_s. To see a difference of the layers in depth the shift s has to be greater than the lateral resolution δ. Reprinted from [85].

5.2.2 Depth Resolution

Stereoscopic ptychography allows for a visual depth resolution well below the limits of conventional ptychography. Unlike multi-slice ptychography, the depth resolution in stereoscopic ptychography does not rely on propagation effects of the illuminating wave field. The depth resolution in stereo imaging is defined using ray tracing of the beams through the sample (see Fig. 5.4).

The limit is defined based on s, the minimal transverse shift required of the two beams with respect to each other, as $s > \delta$ with $s = 2d_s \cdot \tan(\theta_s)$, where θ_s is the deflection angle of a single beam of the stereo setup. For small angles between the deflected beams, the minimal slice distance can be defined as

$$d_s > \frac{\delta}{2\theta_s}, \tag{5.1}$$

where d_s defines the axial resolution. This definition is in good agreement with the depth resolution defined by Duarte *et al.* for stereoscopic coherent diffractive imaging $d_s = \delta/(\tan\theta_1 + \tan\theta_2)$, where θ_1 and θ_2 are the angles of the deflected beams with respect to the optical axis [103].

5.3 Stereo ptychography

The logic structure of an STM32H753VIT6 microcontroller (STMicroelectronics, Switzerland) with an Arm Cortex-M7 core was used as the sample for the first experimental demonstration of stereo ptychography. Microchips are produced layer-wise by lithography techniques and, hence, have a three-dimensional structure, which can be well observed with stereoscopic microscopy. The microchip was scanned over a quadratic area of 30 µm × 30 µm in 100 × 100 steps, whereby an additional random jitter of up to 30 % of the step size was added to the nominal positions in order to prevent scanning on a perfect 2D grid in ptychography [124]. The mean step size was therefore 300 nm and, additionally, optical interferometers tracked the sample position for every scan point. The non-deflected central beam defined the optical axis of the microscope and considerably facilitated the alignment of all optical components.

Fig. 5.5 shows the reconstructed ptychographic image of the microchip obtained using the diffraction patterns only from the central beam. The size of the reconstructed illumination function indicates that the sample was not scanned in the focal plane of the optics but rather at

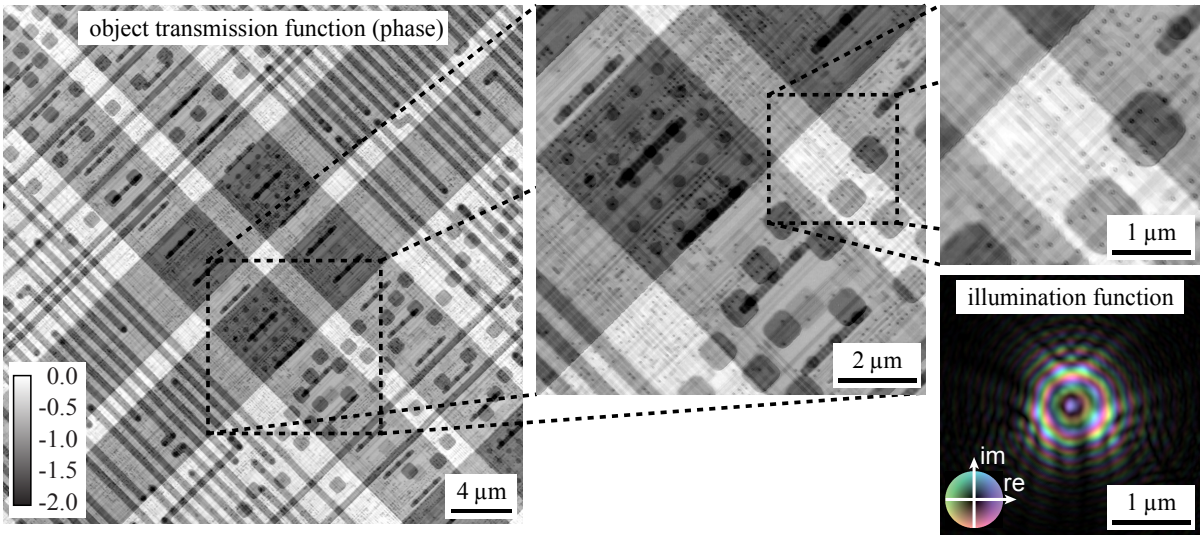

Figure 5.5: Ptychographic reconstruction of the microchip sample using the central beam only. It highlights the large field of view of 30 µm and the high spatial resolution of around 14 nm, with fine structural details shown in the magnified areas. Phase shifts of the object transmission function are given in radians whereas the amplitude and phase of the complex-valued illumination function are encoded by brightness and hue, respectively (see insets). Reprinted from [85].

a distance of 0.5 mm upstream. This permitted to perform the ptychographic scan with a larger step size due to the extended illuminating wave field.

The focus size of the optics was determined to about 70 nm (FWHM) by numerically propagating the retrieved complex-valued illumination function into the focal plane of the optics. The depth of focus of the FZP optics is given by $d_o = \lambda/(2NA^2) \approx 50\,\mu\text{m}$ in this case. However, in ptychography neither the lateral nor the axial resolution are limited by the optics but rather by the maximum diffraction angles at which a significant diffraction signal can be measured [45]. Here, the spatial resolution in the 2D ptychographic image was determined by Fourier-ring correlation to $\delta = 14\,\text{nm}$ (details can be found in the appendix Fig. B.1), which considerably improves also the axial resolution in this single-view ptychographic scan to below $d_p \approx 7\,\mu\text{m}$ using Eq. 3.8 with the constant c given by $c = 5.2$.

The same region was scanned with the left and right nanofocused beams at the same time. Due to their inclination angle of maximum 1.5°, the resulting reconstructed objects exhibit subtle lateral shifts of certain features encoding their position in the layered microchip electronics' structure. From the perspective of the X-ray beams, we speak of "left" and "right" nanobeam or view, depending on whether the signal originates from the left or right side of the incident X-ray beam.

First, the different nanobeams were characterized by ptychography and the result is summarized in Fig. 5.6. The ptychograms of the three nanobeams were separately reconstructed with in-house software, which is based on the ePIE algorithm [30]. The reconstructions were run with 900 iterations of the ePIE engine followed by 100 iterations of a parallel update scheme [125].

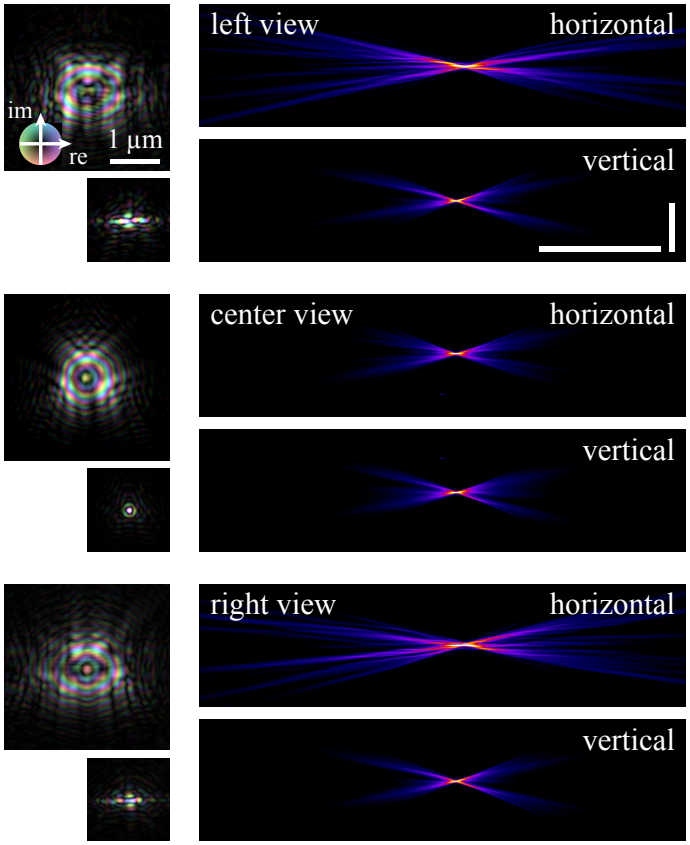

Figure 5.6: Characterization of the three nanofocused X-ray beams. The complex-valued illumination functions of the three beams in the sample plane are shown on the left side of the figure. Smaller images below indicate the wave field in the focal plane of the FZP optics. The corresponding beam caustics in horizontal and vertical direction are summarized on the right side. Scale bars in the caustic images refer to 5 mm in the respective beam direction and 5 µm in the lateral coordinate, either the horizontal or vertical direction. Reprinted from [85].

With this method, the individual sub-beams and respective projections of the sample were recovered. Since the diffraction patterns of each beam are well separated, a disentanglement, as it is necessary in multi-beam ptychography where the diffraction patterns of the beams overlap, is not needed. The total computation time is therefore comparable to the reconstruction of three single-beam ptychograms. Parallel reconstruction of the three projections on different computing nodes would even allow for reconstruction at the same speed as a single-beam ptychogram. Afterwards, the horizontal and vertical offsets between the projections were determined with the phase cross correlation function of the python library scikit-image [126]. The offset of 13 pixels in vertical and 62 pixels in horizontal direction were corrected by translation of the individual projections.

As expected, comparing the beam caustics of the deflected (left and right) beams and the direct (center) beam shows that the ML-mirrors mainly alter the horizontally deflected nanofocused beams in the horizontal direction. The complex wave fields of these nanobeams exhibit a pronounced astigmatism, shifting the horizontal focus by about 400 µm further downstream. These imperfections of the illuminating beams could cause difficulties for imaging techniques

that in some cases rely on an ideal illumination, such as inline holography [127,128]. However, the performance of ptychography does not depend on perfect focusing conditions, since the illumination function is recovered during phase retrieval, and the imaging performance does not degrade as long as the beam size is not increased beyond the limits required for an optimal sampling of the diffraction patterns.

The reconstructions of the microchip sample scanned with the inclined beams, alongside the anaglyph of the two perspectives, are shown in Fig. 5.7. The anaglyph image of the aligned reconstructions allows a clear distinction between several of these layers in the sample (see Fig. 5.7). From the cross section of the microchip (see Fig. 5.8) one can see that larger structures, which appear farther back in the anaglyph, are thicker and farther spaced than smaller structures which appear closer in the anaglyph. This depth perception is, as anticipated, based on the direction of the beams passing through the sample. The beams were traversing the sample from the substrate side to the side with conductor paths. Smaller features, embedded deeper in the microchip, were downstream, whereas thick conductor paths were upstream. The total thickness of the logical structure of the microchip was 3.8 µm with layer distances between 1.1 µm and less than 0.1 µm.

The resolution of the reconstructions, determined by Fourier-ring correlations, is 10 nm for the left beam and 12 nm for the right beam (for details see appendix Fig. B.1). Therefore, as a conservative estimate of the spatial resolution in the single ptychographic reconstructions, we use the size of two pixels $\delta = 16.2\,\text{nm}$ and, hence, a 3D perception due to the stereoscopic effect is given for features that are separated in depth by $d_\text{s} \approx 300\,\text{nm}$ using Eq. 5.1. This value is significantly lower than the minimal separation distance of layers in conventional multi-slice reconstructions, which would require a distance of $d_\text{p} \approx 9\,\mu\text{m}$ according to Eq. 3.8 with the constant c given by $c = 5.2$. Therefore, the use of stereoscopic ptychography with a viewing angle of 3.0° improves the thickness limit for a depth impression of the sample in this case by more than one order of magnitude, allowing us to visually separate the different layers of the logic structures of the microchip.

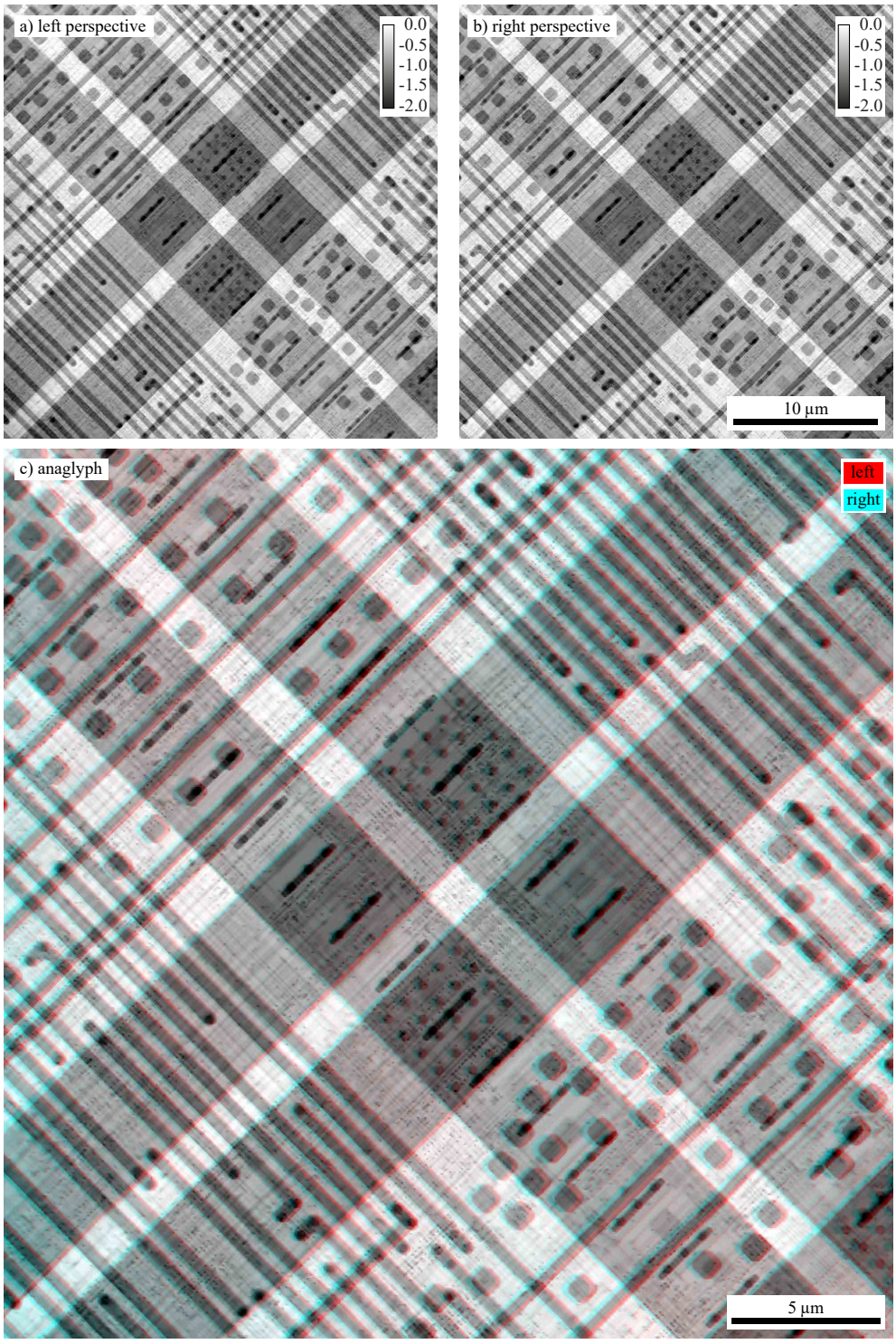

Figure 5.7: Reconstructions of a stereoscopic scan of an STM32H753VIT6 microcontroller. a) shows the phase reconstructions of the sample scanned with the deflected left beam. b) is the result of scanning with the right beam at an angle of 3.0° with respect to the left beam. The anaglyph of the two projections is shown in c). Reprinted from [85].

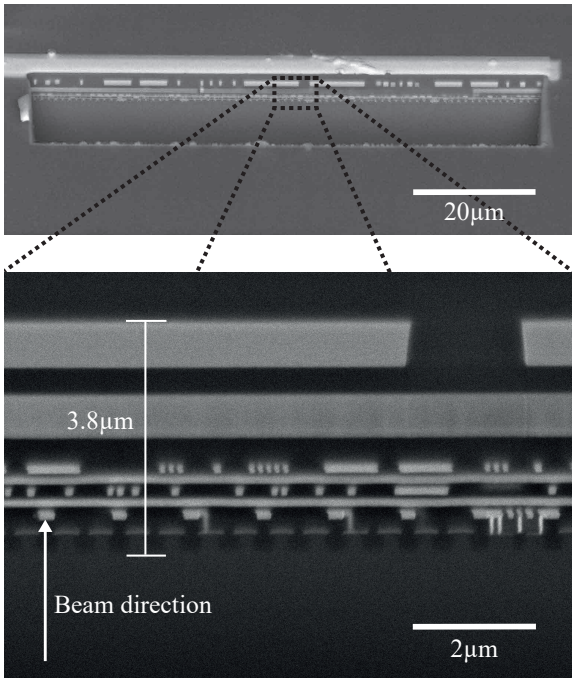

Figure 5.8: Cross section of the microchip imaged with a scanning electron microscope after preparation with a focused ion beam. The X-ray beams were passing through the sample from the small features to the larger ones. The total thickness of the conductor path structures of the chip is 3.8 µm. The FIB-SEM image was taken by Satishkumar Kulkarni from the DESY Nanolab. Reprinted from [85].

5.4 Layer recovery in stereo X-ray ptychography

We demonstrate the potential of stereo X-ray ptychography to quantitatively separate tightly connected layers at the example of another specimen with a less complex layer structure. In this case, we use a silicon nitride membrane of 200 nm thickness with Au nanoparticles with a diameter of 250 nm on one side and an FZP on the other side. Here, the scanned part of the FZP acts as a sample structure and not as a focusing optic. In Fig. 5.9a a schematic drawing of the sample is shown.

This sample was scanned over an area of 4 µm × 8 µm in 20 × 40 steps, with an additional random jitter of up to 30 % of the step size. The exposure time per scan point was 0.1 s. The left and right projection were reconstructed separately with 800 iterations of the ePIE algorithm [30] followed by 200 iterations of a parallel update scheme [125]. Position refinement was used starting at iteration 650 [129]. The reconstructions were mutually aligned with a vertical shift of 186.5 px and a horizontal shift of 156.5 px and cropped to a size of 550 px × 900 px (4.4 µm × 7.3 µm) for the slice separation. The spatial resolution for both projections, determined by Fourier ring correlation, is 13 nm (for details see appendix Fig. B.2). Similar to the microchip sample, we therefore estimate limits in depth resolution of approximately $\delta_s \approx 300\,\text{nm}$.

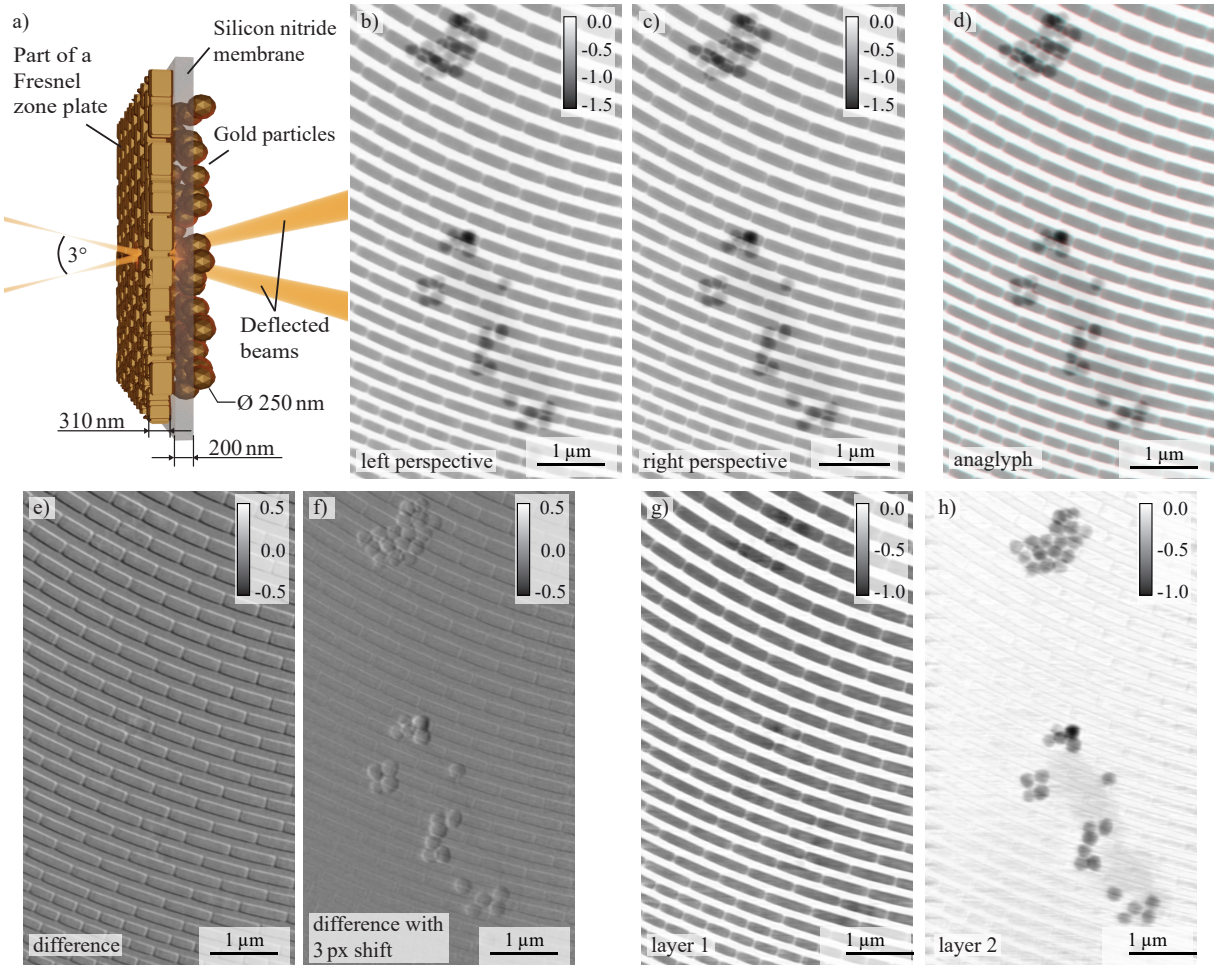

Figure 5.9: Two layers separated by a 200 nm thick membrane recovered from the left and right perspective. a) shows a schematic top view of the sample: A silicon nitride membrane with a Fresnel zone plate on one side and gold nanoparticles on the other side. b) and c) show the reconstructions of the left and right beam data sets. d) is an anaglyph of the two projections. e) shows the difference of the aligned reconstructions b) and c). The reconstructions are aligned in the second slice. f) shows the difference of the reconstructions with a shift of 3 px. The projections are here aligned in the first slice. g) and h) show the two layers recovered from the two projections b) and c) with an iterative algorithm based on a relative shift of the beams in the respective layers. Reprinted from [85].

The thickness of the FZP, which is also made of Au, can be deduced quantitatively from the ptychographic reconstruction itself, which shows an average phase shift of $-0.61\,\mathrm{rad}$ for the Au nanostructures. At the X-ray photon energy of 8 keV and using tabulated values for the refractive index decrement of $\delta_{\mathrm{Au}} = 4.77 \cdot 10^{-5}$ [130], this translates into an FZP thickness of 310 nm. Together with the 200 nm thick silicon nitride membrane and the 250 nm Au nanoparticles, the sample has a total thickness of about 760 nm. It is thus ideal for demonstrating the enhanced depth resolution of stereo X-ray ptychography.

To separate the Au nanoparticles from the FZP, the left and right projection t_1 and t_2, respectively, are modeled as the sum of two object layers l_1 and l_2 with a lateral shift S in one of the layers

$$\begin{pmatrix} t_1 \\ t_2 \end{pmatrix} = \begin{pmatrix} S & \mathbb{1} \\ \mathbb{1} & \mathbb{1} \end{pmatrix} \cdot \begin{pmatrix} l_1 \\ l_2 \end{pmatrix}. \tag{5.2}$$

We numerically solve the corresponding constrained convex optimization problem. The algorithm is set up so that features in the first (upstream, l_1) layer show a shift between the left and right perspectives, while features in the second (downstream, l_2) layer remain in place. The forward model is illustrated for a simplified two-layered sample in Fig. 5.10. More details on the algorithm are provided in the appendix B.2.

Since we assume that the displacements are constant over the entire field of view in each slice and shear is neglected, this approach is only valid for small angles and thin slices. For the presented the case, this simplification is well-justified by the very small viewing angles involved. The results are summarized in Fig. 5.9.

A difference image of the two aligned projections (see Fig. 5.9 e) reveals the contour of the FZP structures, while the Au nanoparticles are barely visible. Therefore, the layer comprising the Au nanoparticles is consistent in both projections. The distance between the FZP and the nanoparticle layer is approximately 480 nm. For an angle of 3.0° this corresponds to a relative shift of 25.1 nm or 3.1 px of the features of the first layer between the two projections. As the algorithm is limited to integer values thus far, a 3 px shift of the sample features was assumed in the optimization process. By shifting the right projection 3 px with respect to the left projection the FZP structure is aligned in both projections, and the difference image shows the contour of the Au nanoparticles (Fig. 5.9 f). Thus, the theoretical shift from the sample dimensions matches well with the actual shift in the projections. The two numerically retrieved slices are presented in Figs. 5.9g and h. The FZP nanostructures are clearly discernible in the first layer, while the Au nanoparticles are attributed to the second layer. This finding aligns with the qualitative impression highlighted by the corresponding anaglyph (see Fig. 5.9d). As the separation into only two layers is merely a rough approximation of the actual 3D representation of the sample volume, the disentangling of the Au nanoparticles from the FZP is not yet optimal and faint contributions from the other layer's content remain visible in the images. One could describe stereo ptychography as a case of limited angle tomography with a significant missing wedge. For this reason, a full 3D reconstruction of a volumetric sample is not possible from stereoscopic

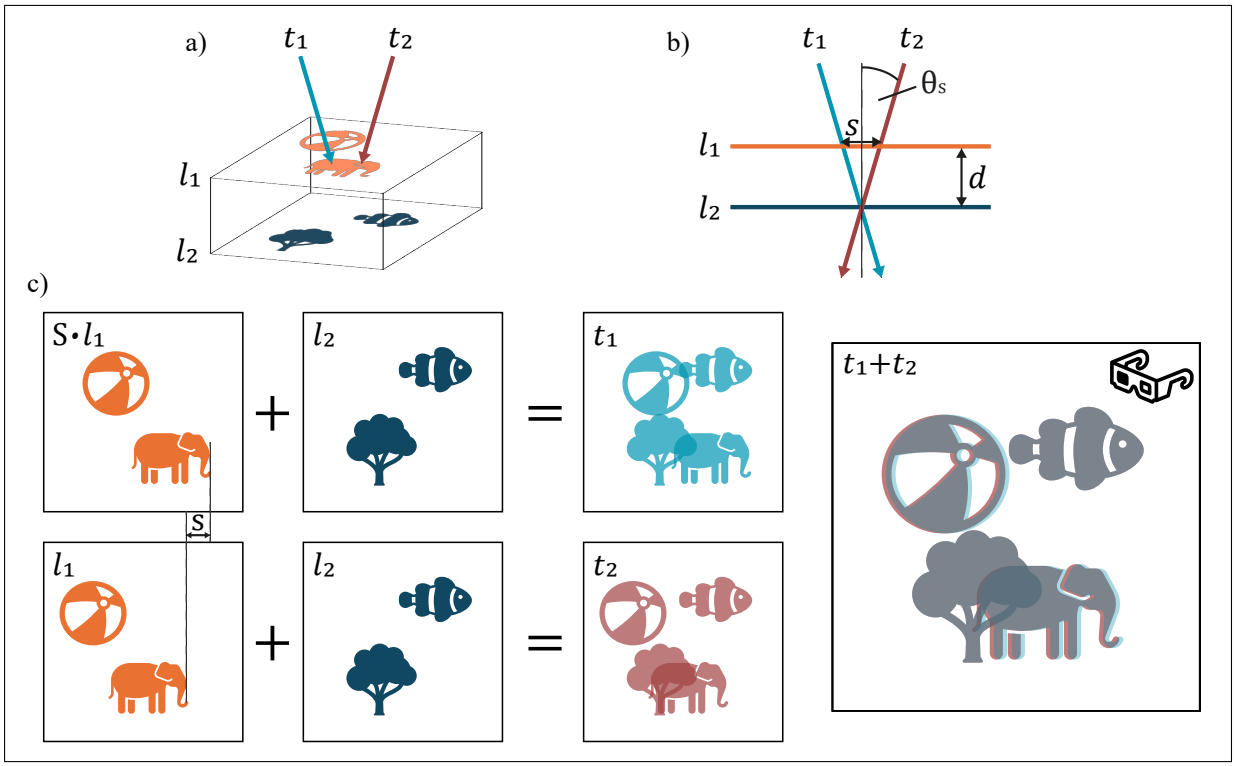

Figure 5.10: Illustration of the linear separation model. a) Two angled projections t_1 and t_2 of an object consisting of two layers l_1 and l_2 are taken. b) The projection images t_1 and t_2 are taken under different projection angles. For small angles $\theta_s \ll 1\,\text{rad}$, we neglect shearing and assume that the two projections differ only in a shift s of the first layer. c) The projection images t_1 and t_2 are each a sum of two different layers l_1 and l_2. A shift operator S is applied to the first layer l_1 in the first projection t_1. The sum of the two projections is shown as an anaglyph (shift was scaled for visual 3D effect in the anaglyph). Reprinted from [85].

images alone. Nevertheless, further enhancements to the algorithm may facilitate more precise layer separation. The outcomes illustrate that two sample layers with a distance of only 480 nm can be effectively distinguished through stereo X-ray ptychography. Since the recovery of the two layers is based on the individually reconstructed phase images, one could in principle also apply this concept to sequentially recorded projections.

To quantitatively recover slices from stereo X-ray projections, the sample should have a limited number of well-separated layers, two for the algorithm presented here. Prior knowledge of the layer distance is advantageous for slice recovery, but it can also be estimated from the shift of the layers visible in an anaglyph. The interlayer distance should be between the depth of field of a single beam and the depth resolution of the stereo setup. For optically thick objects the stereo-slice recovery could be applied to multi-slice reconstructions offering the opportunity to recover even more layers, which will be explored in the next section.

5.4.1 Stereo layer separation on multi-slice reconstructions

Thus far, we have demonstrated the separation of two layers from two stereo projections. Combining this method with the established multi-slice ptychography would open up the opportunity to distinguish more layers with a wider range of distances between them. In multi-slice ptychography, reconstructing multiple layers requires significant variation in the illumination function across the sample's cross section. On the other hand, stereo layer splitting relies on the stereo angle and can recover layers with even thinner spacing. Here, we combine the strengths of these two methods.

Method

The experiment was carried out using the same setup as described in Sec. 5.2.1. The photon energy was set to 7.84 keV, which moved the foci of the X-ray beams downstream. In this way, the intersection point of the beams is located in their focal plane. Table 5.1 lists the experimental and reconstruction parameters.

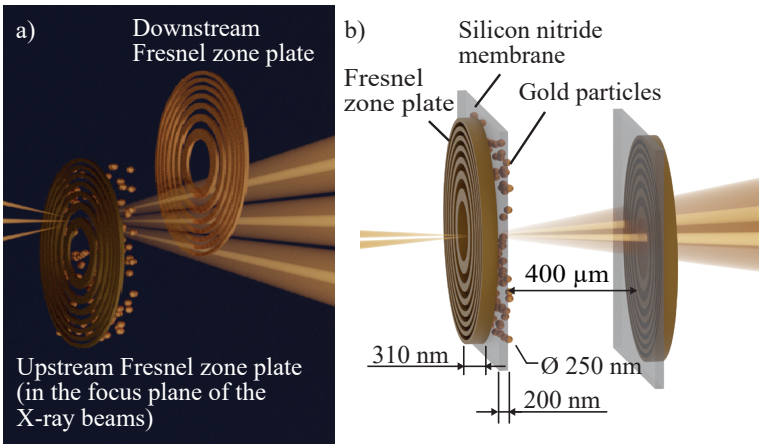

Figure 5.11: Sample used for stereo multi-slice ptychography. a) Top view of the Fresnel zone plates used as a sample. The upstream FZP is positioned at the intersection of the X-ray beams. The beams scan different areas of the downstream FZP. The subsequent analysis uses the two outer beams, which have the largest viewing angle. b) Dimensions of the sample consisting of two FZPs. The two FZPs are separated by 400 µm along the X-ray beam direction. The upstream FZP has a thickness of 310 nm and is separated by a 200 nm-thick silicon nitride membrane from the gold nanoparticles, which have a diameter of 250 nm. Adapted from [86].

Fig. 5.11 shows a sample consisting of two FZPs that was used to demonstrate the combination of stereo layer separation and multi-slice ptychography. Each FZP was positioned on a silicon nitride membrane with a 400 µm gap between them. Gold nanoparticles with a diameter of 250 nm were drop-casted on the backside of the 200 nm thick silicon nitride membrane of the upstream FZP to act as a third layer. The upstream FZP had a thickness of 310 nm. Thus, the middle of the upstream FZP and the nanoparticles were separated by 480 nm. The upstream FZP specimen is the same as the one described in Sec. 5.4. Here, the sample was extended by

Table 5.1: Experimental and reconstruction parameters

Parameter	
Photon energy	7.84 keV
Stereo angle	3.0°
Distance sample → detector	2.0 m
Layer distances	480 nm and 400 µm
Scan type	fly scan
Scan step size	49.5 nm
Field of view	5.0 µm × 5.0 µm
Exposure time per scan point	0.02 s
Reconstruction engine	3PIE [51]
Number of iterations	1000
Cropping area on detector	512 × 512 pixels
Position refinement [129] for each beam individually	starting at iteration 50
Upsampling [123]	3-times
Slice 1 – initialization	left perspective: 3. iteration right perspective: 1. iteration
Slice 2 – initialization	left perspective: 1. iteration right perspective: 3. iteration

the second, downstream FZP. The upstream FZP was placed in the focal plane of the X-ray beams. The beams were aligned in a way to intersect in the plane of the first FZP.

To separate the two FZPs, multi-slice ptychographic reconstructions of the left and right perspectives were performed. The reconstructions of the first slice were subsequently used to recover the FZP and nanoparticle layers from the stereo pair. The depth information encoded in the transverse shift of features in the two perspectives allows the two layers to be separated. For this purpose, the algorithm based on a Nesterov accelerated gradient descent, was used (see Sec. 5.4). A shift of 3 px in the first layer between the left and right perspectives was assumed for the layer separation. The algorithm ran, in this case, for 2000 iterations. At iteration $k = 1000$, the Nesterov momentum was set to zero for one iteration, to prevent over-accumulation of gradients.

Stereo multi-slice ptychography

In stereo imaging depth information is encoded as a transverse shift of features in the two perspectives. Scanning transmission X-ray microscopy images acquired with the left and right X-ray beams, shown in Fig. 5.12a and b, illustrate that the scanned area overlaps well on the upstream (right) FZP, while the downstream (left) FZP is shifted in the two perspectives. On the second FZP, the beams are separated in the transverse direction by 21 µm. This distance is close to the expected shift of 22 µm caused by the stereo angle of 3.0°. Fig. 5.12c shows an overlay of the two perspectives that visualizes this shift.

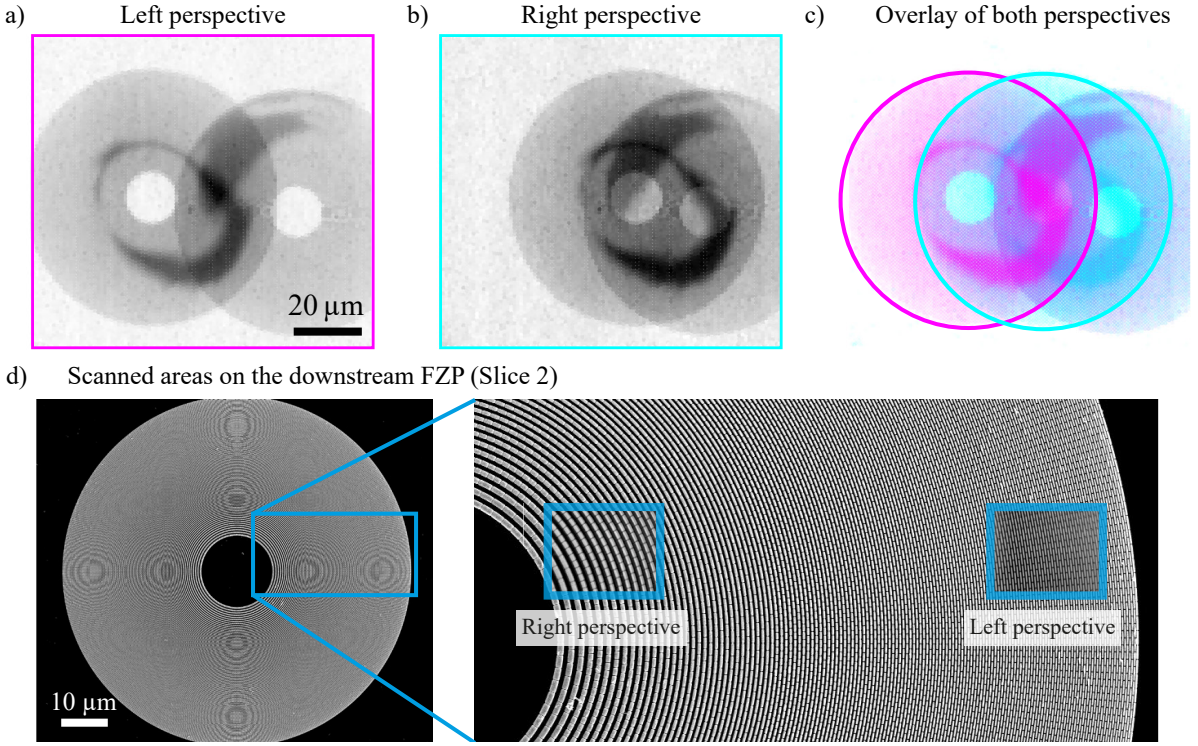

Figure 5.12: Scanning transmission X-ray microscopy images of the sample consisting of two Fresnel zone plates (FZP). a) Transmission image acquired with the left beam. The left beam is here defined as the one on the left side upstream of the intersection point of the two beams. b) Transmission image of the FZPs scanned with the right beam. c) Overlay of the transmission images of both beams, magenta corresponds to the left beam and cyan to the right beam. The upstream FZP, on the right side, is scanned in the same area by both beams. The downstream FZP is shifted by 21 µm due to the angle of 3° between the beams. d) Scanning electron microscopy image of a FZP with the same design parameters as the downstream FZP, indicating the areas scanned by the different nanofocused X-ray beams. The SEM image was taken by Mattias Åstrand. Reprinted from [86].

Multi-slice ptychography can be used to reconstruct the two FZPs as individual slices, the distance of 400 µm between them is sufficient for this purpose. Multi-slice reconstructions were performed on the diffraction patterns of each beam separately, yielding two individual slices for each perspective (see Fig. 5.13).

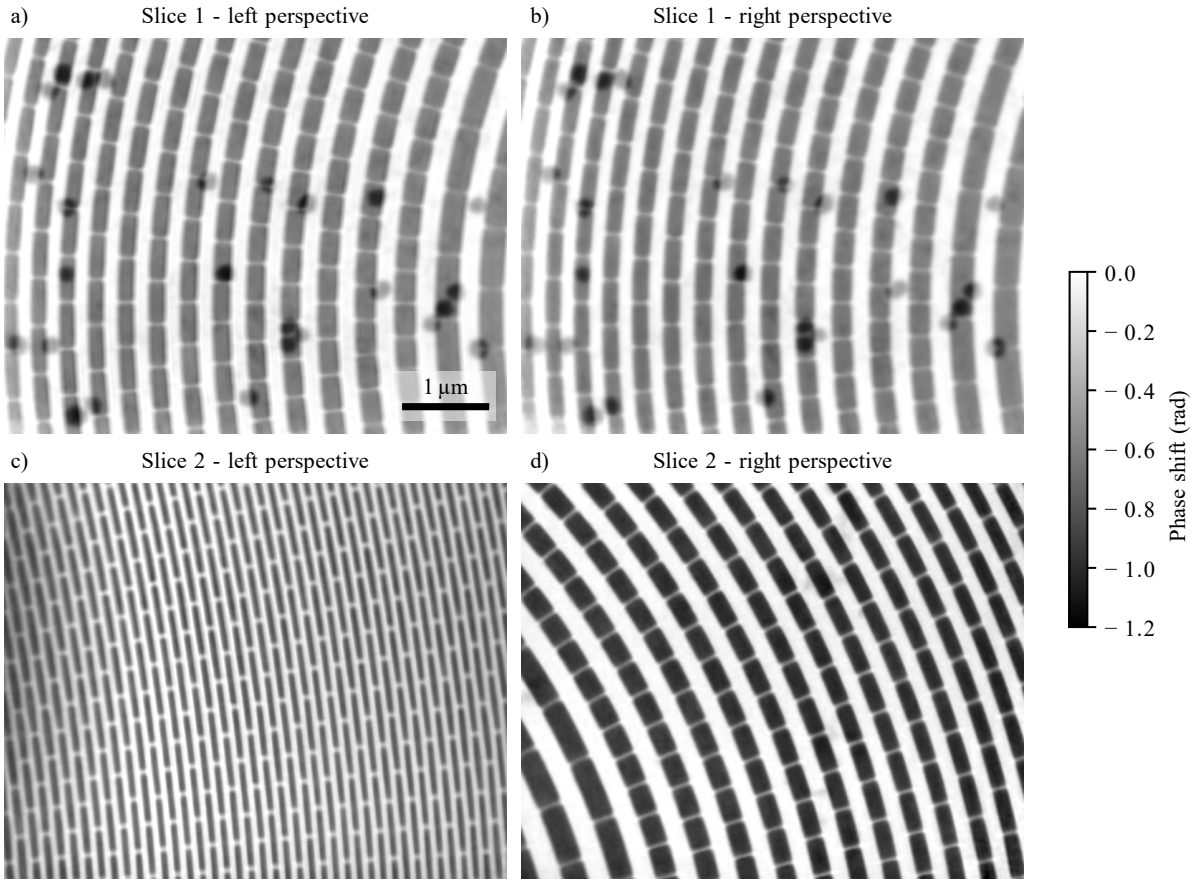

Figure 5.13: Multi-slice reconstruction of the left and right perspective. a) and b) The beams overlap in the first slice of both perspectives, which corresponds to the upstream FZP. c) The second slice of the left perspective shows the smaller features close to the outer edge of the zone plate. d) The second slice of the right perspective shows bigger features that are located closer to the center of the zone plate. Reprinted from [86].

The first slice demonstrates that both perspectives overlap to a high degree, displaying the same area of the upstream zone plate. It shows an area on the left side of the FZP, close to its center. The nanoparticles that were drop-casted onto the back of the membrane supporting the FZP are also visible. For this scan, the scanned area is not large enough for any overlap to be present in the second slice. With a layer separation of 400 µm and an inclination of 3° between the two nanofocused beams, the scanned areas in the second slice are separated by 21 µm. The second slice of the left perspective shows an area close to the outer edge of the FZP. The right perspective shows the larger zones located near the center of the FZP. The respective areas of the FZP visible in the second slice are highlighted in Fig. 5.12d.

The lateral resolution of the scan was determined by Fourier ring correlation [39,40] to be 23 nm for the first slice of the left beam and 25 nm for the right beam (see appendix Fig. B.3). Therefore, the depth of field for the multi-slice reconstruction using Eq. 3.8 with the constant $c = 5.2$ is 17 µm for the left beam and 20 µm for the right beam, small enough that multi-slice ptychography can be applied to each of the two perspectives. According to Eq. 5.1, layers with a distance

of 468 nm should be distinguishable by the additional stereoscopic effect. With a distance of 480 nm, the distance between the nanoparticle and the FZP layer of the first slice is very close to this theoretical limit. Therefore, this example is ideal for proving the validity of the depth resolution definition of stereo ptychography.

Stereo layer recovery from reconstructed slices

The left and right perspectives of the first slice are used to recover the individual FZP and nanoparticle layers. The result is visualized in Fig. 5.14. The upstream layer (l_1) shows the structure of the FZP, and the downstream layer (l_2) contains the nanoparticles. The distance between the two layers is 480 nm, which is very close to the theoretical layer separation limit. For this reason, the recovered objects contain slight contributions from the other layer. Combining multi-slice ptychography with stereo layer separation enabled the reconstruction of three individual layers. With this approach, the recovery of even more layers should be possible for more complex samples.

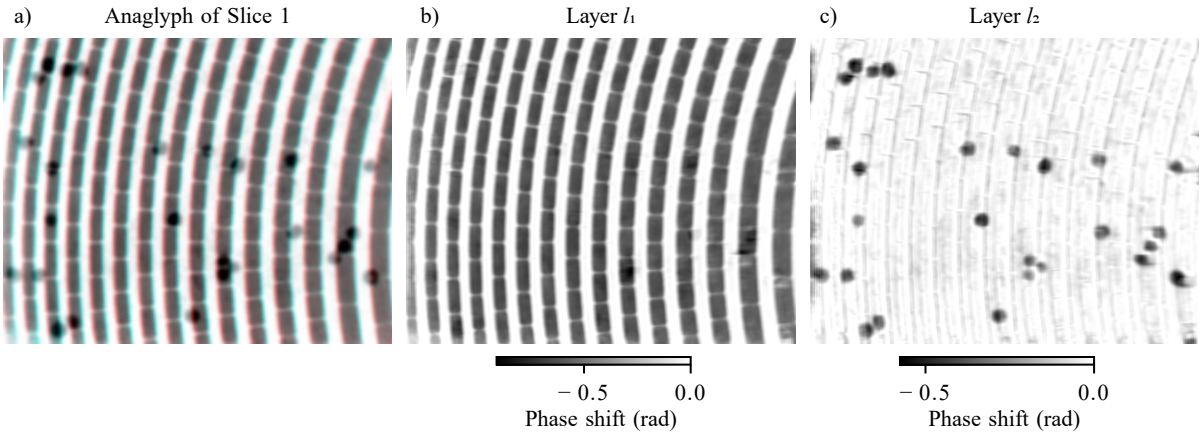

Figure 5.14: Stereo layer separation. The anaglyph (a) gives a qualitative depth impression of the sample. b) and c) show the reconstructed layers l_1 and l_2. The left and right perspective of the first slice were used to separate the FZP and nanoparticle layer based on the stereo effect. The upstream layer l_1 (b) shows the features of the FZP, whereas the downstream layer l_2 (c) shows the gold nanoparticles. Reprinted from [86].

5.5 In-situ stereo multi-slice ptychography

Achieving reproducible performance and functionality of complex nanomaterials remains critical, largely due to limited understanding of the underlying growth mechanisms. To address this challenge, scanning hard x-ray microscopy is a powerful tool for in-situ nanoimaging of complex chemical systems. It provides valuable morphological information, contributing towards achieving greater reproducibility and control over nanoparticles' properties. To study chemical reactions under realistic conditions and at relevant time scales, a good temporal resolution of the imaging method is crucial. Additionally, implementation of an in-situ chemical reactor, which provides

the needed reaction environment, often limits the accessible angular range that is necessary for full tomographic experiments [131]. Stereo ptychography allows to obtain 3D information from a single scan. In combination with multi-slice image reconstruction, this is a powerful tool to time-efficiently visualize chemical reactions in a bulky reaction environment.

Building on the experience from the previous ex-situ experiments, the stereo ptychography setup was employed to study the galvanic replacement reaction of cuprous oxide nanocubes with palladium under in-situ conditions.

5.5.1 Experiment

The in-situ reaction cell developed by Lukas Grote, described in Grote *et al.* (2023) [119], was modified by Sarah-Alexandra Hussak for the stereo setup. Only the inner container of the original cell was used. A holder for this inner container was 3D-printed and mounted on an adapter plate that also had a ball lens for position tracking with interferometers mounted, shown in Fig. 5.15a. In this modified reaction container, the distance between the entrance and exit polyimide foil (Kapton HN, DuPont de Nemours Inc.) was 1800 µm (see Fig. 5.15b). The inside of the entrance window was covered with pre-synthesized Cu_2O nanocubes. The in-situ cell was mounted on the scanning stage of PtyNAMi (see Fig. 5.15c). A tube inserted into the capillary of the cell connected it to a syringe pump, which was used to inject the reaction solution. The stereo ptychography setup, described in Sec. 5.2.1, was slightly modified compared to the ex-situ experiments. New FZPs with a focal length of 30 mm were used and the pinhole was placed on a rotation stage with a central hole for beam passage (SmarAct GmbH, Germany).

The Cu_2O nanocubes were pre-synthesized in the original in-situ cell following the procedure described in Grote *et al.* (2023) [119]. 1.4 mL Milli-Q ultrapure water with a resistivity of 18.2 MΩcm at 25 °C were filled into the reactor. At room temperature, a polytetrafluorethylene tube was inserted to dose 350 µL of a 10 mmolar aqueous H_2PdCl_4 solution using a syringe pump (PHD Ultra, Harvard Apparatus, USA). The injection rate was set to 100 µL h^{-1}. The galvanic replacement reaction is described by the following reaction equation

$$Cu_2O_{(s)} + PdCl^{2-}_{4(aq)} + 2H^{+}_{(aq)} \rightarrow Pd_{(s)} + 2Cu^{2+}_{(aq)} + 4Cl^{-}_{(aq)} + 1H_2O.$$

The sample was continuously scanned over a period of 3.5 h. An individual scan took 6 min covering a field of view of $5 \times 10\,\mu m^2$. The experimental parameters are summarized in Table 5.2. The left beam was not well aligned with the other two, and the OSA was cutting into it. For this reason, the right and direct beams were used for the subsequent analysis.

5.5.2 Recovery of a thin layer of interest from stereo pairs

After the experiment, multi-slice reconstructions of the scans with the 3PIE algorithm [51] were carried out. The entrance and exit window were recovered as individual slices. The reconstruction parameters can be found in Table 5.2. Aligned reconstructions of the first slice for the direct and

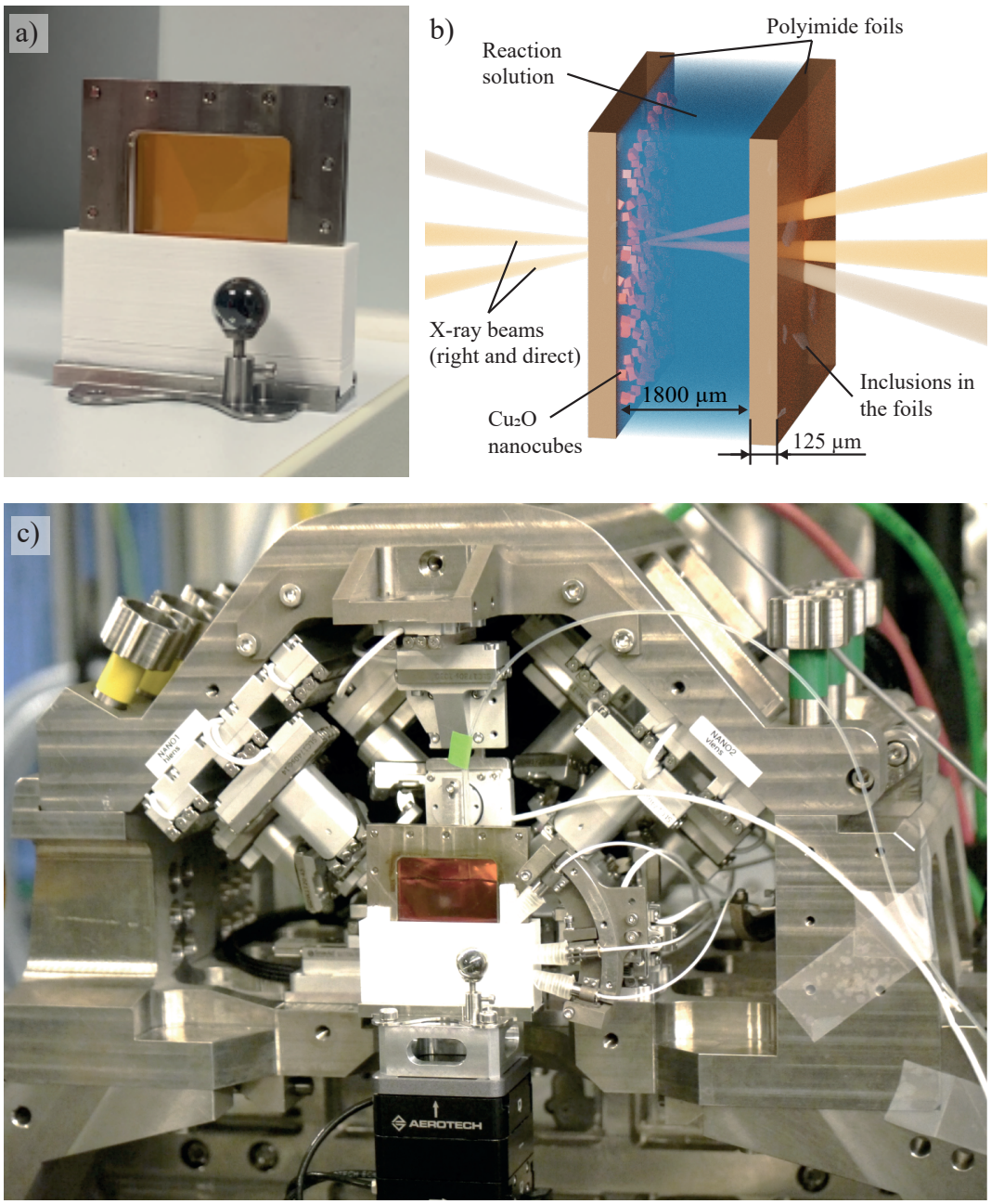

Figure 5.15: Modified in-situ cell for stereo ptychography. a) The inner container of the in-situ reactor described in [119] was placed in a new 3D printed holder. b) Schematic of the in-situ cell (not to scale). The Cu_2O nanocubes were located on the entry window, where the beams were overlapping. Only the right and direct beam (shown in brighter yellow) were used for the subsequent analysis, since the left beam was not well aligned with the others. c) The in-situ cell was mounted on the scanning stage at PtyNAMi. The inner container was clamped in the plastic holder with paper stripes.

right beam of a scan taken 12 min after start of the injection are shown in Fig. 5.16 a) and b). The resolution of this scan was determined to be 71 nm for the direct beam and 105 nm for the right beam (see appendix Fig. B.4).

Table 5.2: Experimental and reconstruction parameters

Parameter	
Photon energy	8.0 keV
Stereo angle	1.5°
Distance sample → detector	2.0 m
Scan type	Step scan with 40% jitter
Scan step size	196 nm
Field of view	5 µm(h) × 10 µm(v)
Exposure time per scan point	0.2 s
Reconstruction engine	3PIE [51]
Number of iterations	1000
Cropping area on detector	256 × 256 pixels
Position refinement [129] for each beam individually	Starting at iteration 50
Upsampling [123]	4-times
Slice 1 – initialization	Direct perspective: 1. iteration Right perspective: 30. iteration
Slice 2 – initialization	Direct perspective: 30. iteration Right perspective: 1. iteration

The two perspectives were aligned in a way that they overlap in the nanoparticle layer. The features that appear shifted in the anaglyph (Fig. 5.16c) are expected to be inclusions in the polyimide foil. Additives used as slipping agents in the production process [132,133] remain as inclusions in the polyimide foils, which compromise the clear observation of the layer of interest containing the nanoparticles. A light microscope image of these inclusions in the foils can be found in the appendix, Fig. C.4. The polyimide foils have a thickness of 125 µm, and the particles are spread in depth in these foils. For this reason, they cannot be attributed to a single second layer, besides the nanoparticle layer, as it was the case for the previous FZP samples. Additionally, the thickness of the inclusions themselves in some cases extends beyond the stereo depth resolution of 4 µm using Eq. 5.1. However, the distance between the nanoparticle layer and the inclusions is at the same time not sufficient to separate them in a multi-slice reconstruction.

The minimal slice separation for a single beam multi-slice reconstruction is 370 µm applying Eq. 3.8 with the constant $c = 5.2$.

A new method had to be sought to separate the studied nanoparticle layer from obscuring inclusions. The approach used here is based on the following constraints and assumptions:

1. The layer of interest is optically thin. The thickness is below the stereo depth resolution.
2. The phase shift in the reconstruction is the integral of the individual phase shifts of each layer in depth: $\phi_{\text{projection}} = \phi_{\text{layer1}} + \phi_{\text{layer2}} + \cdots$
3. The obscuring particles are sparse.
4. The particle size (horizontal dimension) is similar to or smaller than the transverse shift of the particle in the two projections introduced by the stereo angle.

In a stereo pair, the phase shift introduced by an, in the stereo sense, optically thin layer should be the same in both projections. If only few, relatively small particles obscure the image, a pragmatic approach to recover the layer of interest is to take the minimum value of the two aligned projections for each pixel.

The method was applied to the in-situ stereo scan, and the result is shown in Fig. 5.16f. The inclusions get removed from the combined perspective and a clearer image of the studied nanoparticles remains. By subtracting the corrected projection from the original reconstructions of the direct and right perspective, one can also recover the inclusions. They are visualized in a false colored overlay in Fig. 5.16d and e.

5.5.3 In-situ study of a galvanic replacement reaction

The galvanic replacement reaction of Cu_2O with Pd was studied for a duration of 3.5 h. First, multi-slice reconstructions of the scan series were carried out for the individual beams. Afterwards, the inclusions were removed from the reconstructions of the first slice with the approach described above and the result is shown in Fig. 5.17. The original reconstructions of both views can be found in the appendix Fig. B.6. In the second slice, the area scanned with the direct and right beam did not show any overlap, for this reason such an inclusion removal is not feasible. The reconstructions of the second slices of both views are shown in Fig. 5.18.

Over the first two hours of the reaction no significant changes were observed. Two hours after the start of the injection, the cubes seemed to disappear, and a grainy structure formed on the foil. Three hours after the start of the reaction, particles growing in the same spot as the cubes that had previously disappeared became visible. This observation is consistent for both perspectives and not a result of the post-processing corrections (see appendix Fig. B.6). Around the same time that the particles seemed to dissolve from the entrance window, particles growing on the exit window became apparent (Fig. 5.18).

Since the greatest morphological changes occurred two hours after the injection began, we will examine this time frame in greater detail with smaller time steps. Fig. 5.19 shows cropped phase

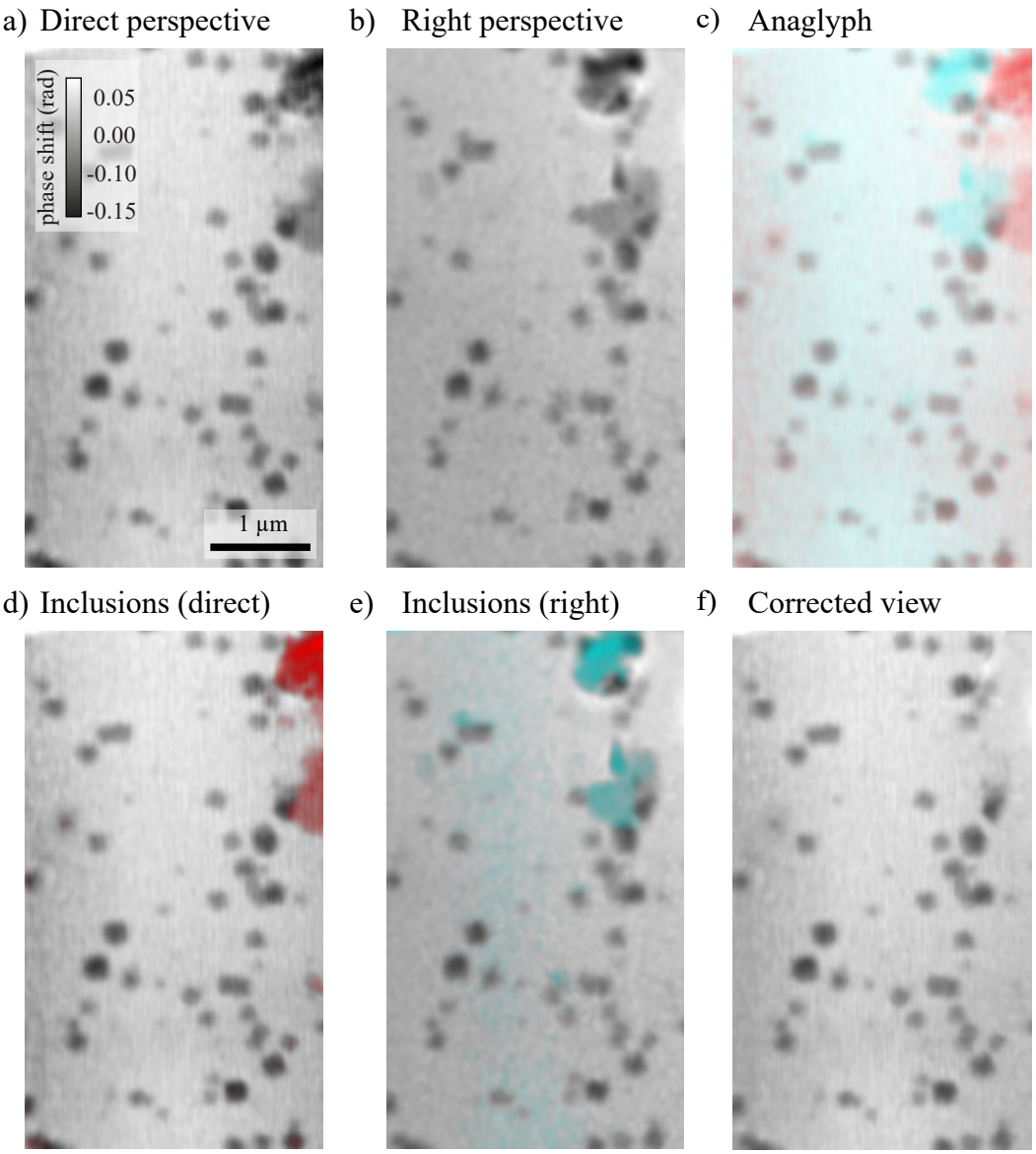

Figure 5.16: Example scan for the removal of inclusions in the polyimide foil from the layer of interest. a) and b) show the reconstruction of the entrance window of the reaction cell (first slice). c) is an anaglyph of the two projections. d) and e) visualize the inclusions (highlighted in red and cyan) in an overlay with the original reconstruction of the direct and right perspective. f) shows the corrected combined perspective without inclusions.

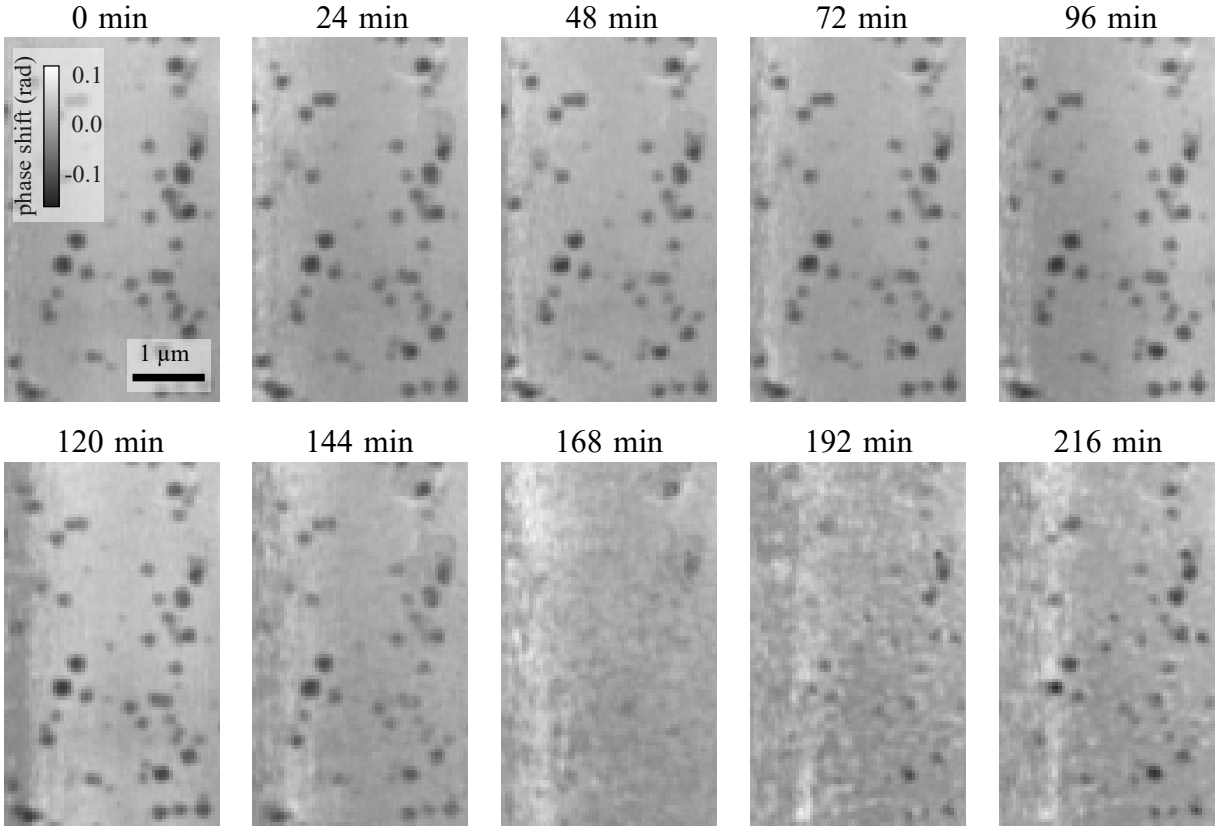

Figure 5.17: Entrance foil with Cu_2O nanocubes undergoing a galvanic replacement reaction with Pd. Inclusions in the polyimide foil were removed from the reconstructions.

images of the entrance and exit window in 6 min steps acquired with the direct beam. From 144 min onward, the background looked less flat. Some grainy or net-like structure seemed to grow on the foil. Around the same time, the particles gradually became less visible until they were practically invisible at 174 min. Later, the particles gradually "reappeared" at the same location, while the background structure remained unchanged. On the exit window, particles became visible after 132 min and grew continuously larger until the end of the measurement. The growth of particles on the exit window is likely caused by beam damage. Pd^{2+} ions can get reduced by hydrolysis products like H-radicals or solvated electrons and form Pd particles. This radiolytic synthesis of Pd has been extensively studied, mostly using γ-rays [75,77,134–136]. Scanning of the sample with multiple beams is necessary to achieve the improved depth sensitivity. However, this approach significantly increases the photon fluence on the sample compared to scanning with a single beam, which has a negative impact on radiation damage.

An analysis of the phase shift evolution of ten exemplary particles over the reaction time verifies the qualitative impression that the phase shift of the particles reduces from 120 min onward (see Fig. 5.20). The phase shift increased again around 174 min after the injection start. Around the same time the particles seemed to reappear in the reconstruction of the entrance window. A slight decrease in the phase shift would be expected for the reaction. The reconstructed phase

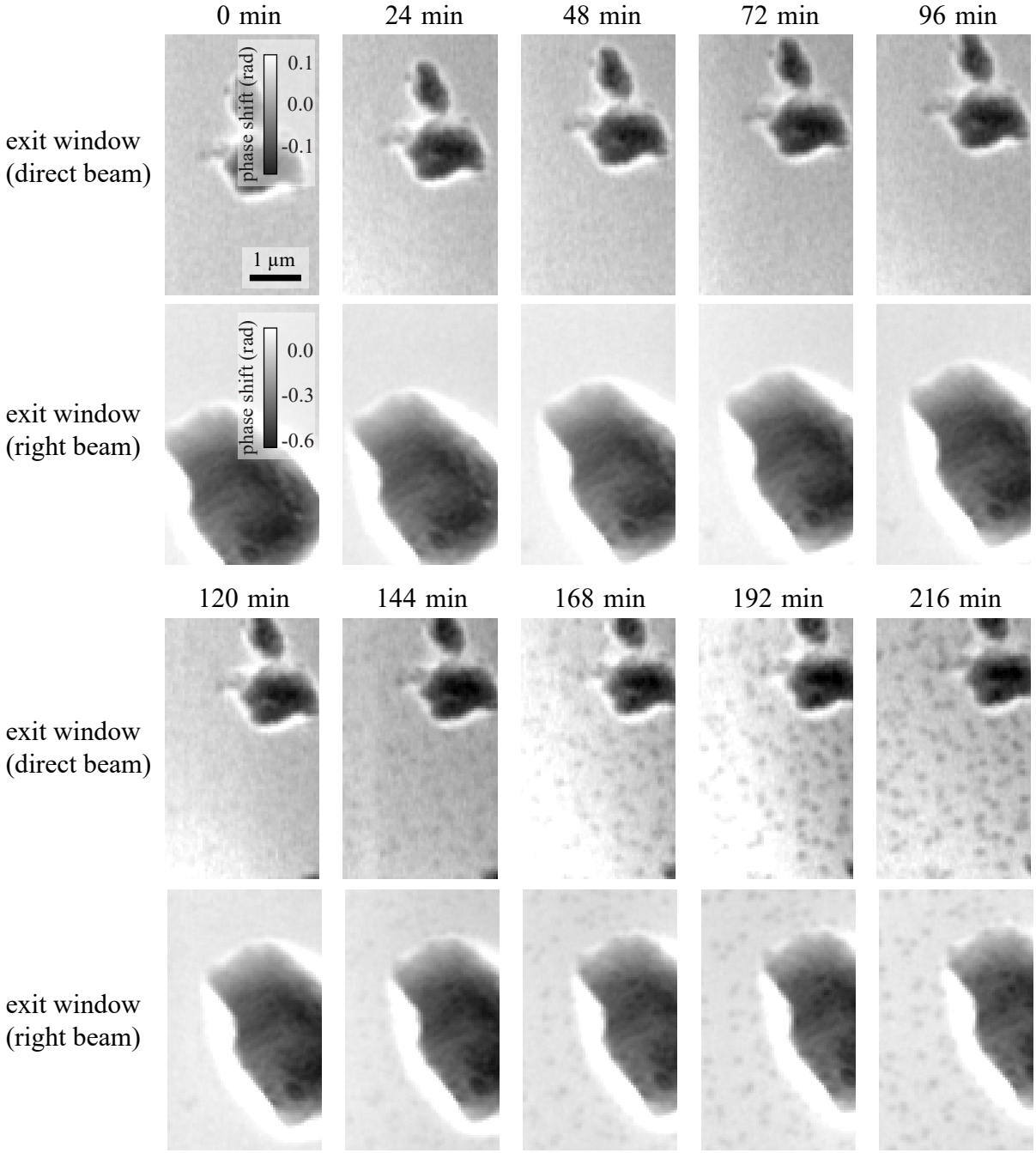

Figure 5.18: Stereo in-situ series – exit window. The two perspectives do not overlap on the exit window and show different parts of the foil. In the beginning, only the inclusions in the polyimide foil are visible. Particles growing on the backside of the in-situ cell become evident 144 min after the start of the injection.

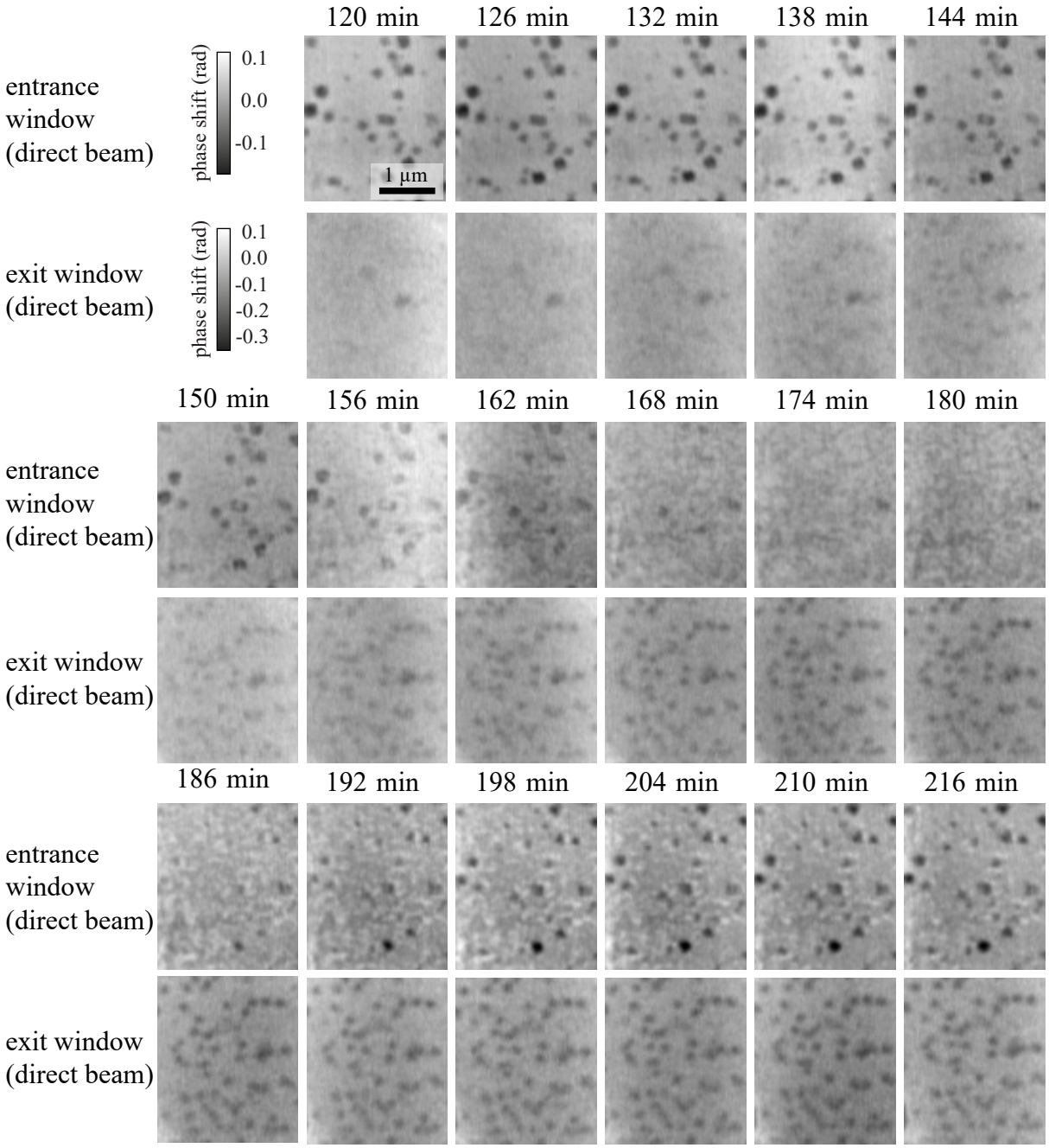

Figure 5.19: In-situ series between 2 h and 3.5 h in 6 min time steps. A smaller field of view was cropped out of the direct perspective to visualize the morphological changes on both windows in the most relevant time frame starting after two hours.

shift ϕ is directly related to the electron density

$$\phi = -\frac{2\pi n \delta M}{\lambda d^2 \rho}, \tag{5.3}$$

where n is the amount of substance, $1-\delta$ the real part of the refractive index, M the molar mass, λ the wavelength, d the pixel size, and ρ the density. Taking the stoichiometry of the reaction into account, one can calculate the expected phase shift at the end of the reaction. The relevant parameters are listed in Table 5.3. The wavelength and pixel size are constant over the in-situ series and for this reason not taken into account. Theoretically, the phase shift introduced by the Pd particles at the end of the reaction would be expected to be 67 % of the initial phase shift by the Cu_2O nanocubes.

Table 5.3: Expected phase shift evolution for the galvanic replacement of 1 mol Cu_2O by 1 mol Pd.

Parameter	**Cu_2O**	**Pd**
δ	$5.35 \cdot 10^{-6}$	$6.50 \cdot 10^{-6}$
ρ ($\frac{g}{cm^3}$)	8.96	12.02
n (mol)	1	1
M ($\frac{g}{mol}$)	143.09	106.42
ϕ (relative)	1.0	0.67
ϕ (mrad) (average)	-0.136 (measured)	-0.091 (expected) -0.105 (measured)

The phase shift introduced by the nanoparticles at the end of the reaction is close to the expected value. However, it is not usually expected that the particles "disappear" during the synthesis process. If one attributes the growth of Pd particles on the backside to radiolytic synthesis, it is unlikely that the galvanic replacement reaction on the entrance window is undisturbed by beam damage.

Examining the two windows with light microscopy after the reaction reveals that a significantly greater amount of substance grew on the surface in the scanned area. The brighter square that can be seen in Fig. 5.21a is in the area that was covered by faster overview fly scans. The inset shows a significantly thicker structure, which formed in the area that was continuously scanned during the synthesis. On the exit window (Fig. 5.21b) one can see three distinct spots, which likely correspond to the areas scanned by the three beams. The strongest growth occurred in the area of the direct beam. The least amount of substance can be seen where the foil was scanned by the left beam, which was partially blocked by the OSA. The color of the particles on the foils appears more golden than one would expect from Pd particles. This could be an optical illusion caused by the color of the light, or it could hint at the formation of a Pd-Cu alloy. The radiolytic synthesis of Cu-Pd particles has been shown before with γ-rays[134]. At the same time, the likelihood of Cu^{2+} diffusing to the window on the other side, resulting in a relevant

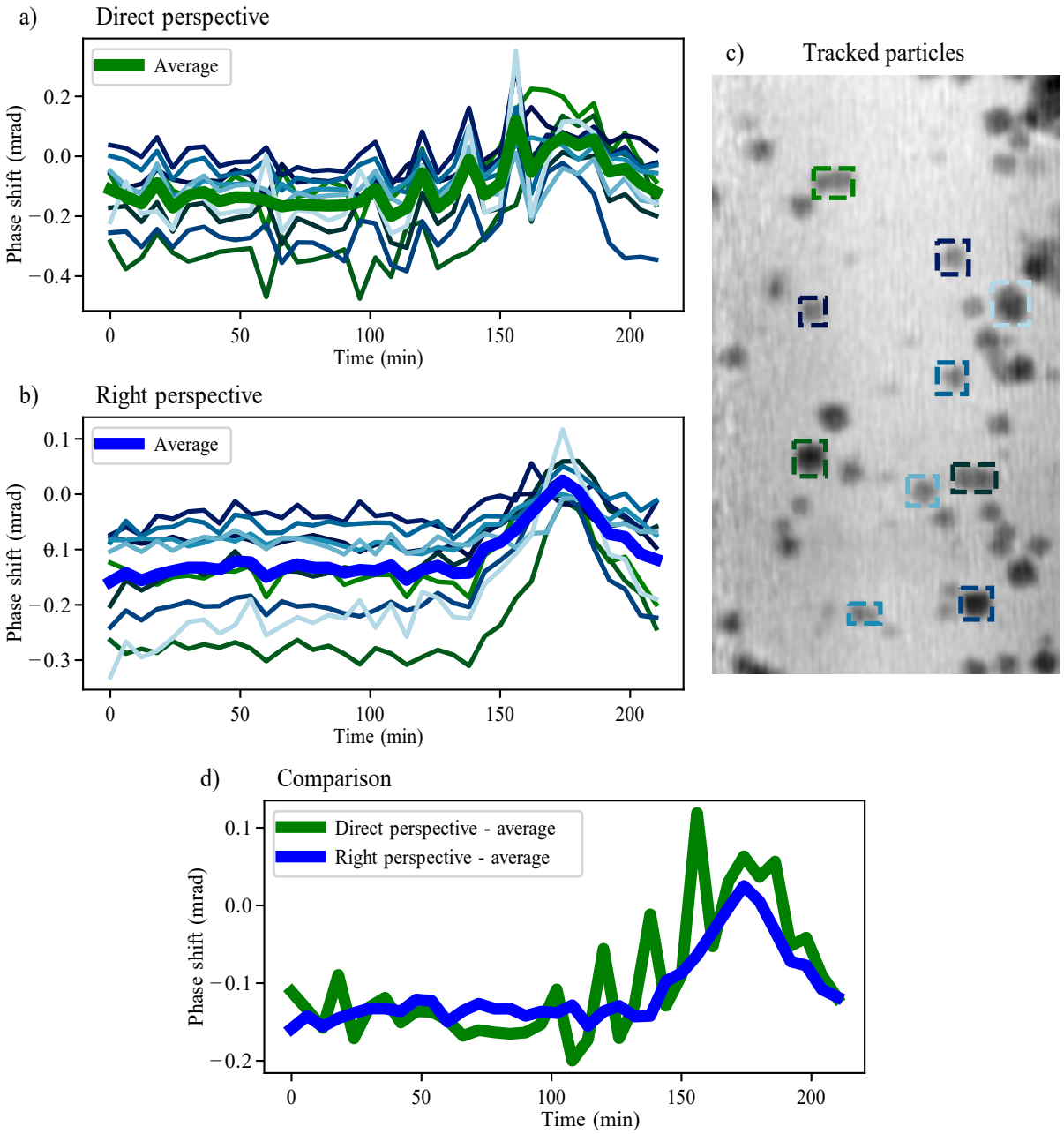

Figure 5.20: Evolution of the phase shift of exemplary cubes over the time frame of the in-situ series. a) shows the mean phase shift of the particles marked in c) in the direct perspective. b) depicts the mean phase shift of the same particles in the right perspective. In d) the average phase shifts over all tracked particles of the direct and right perspective are plotted.

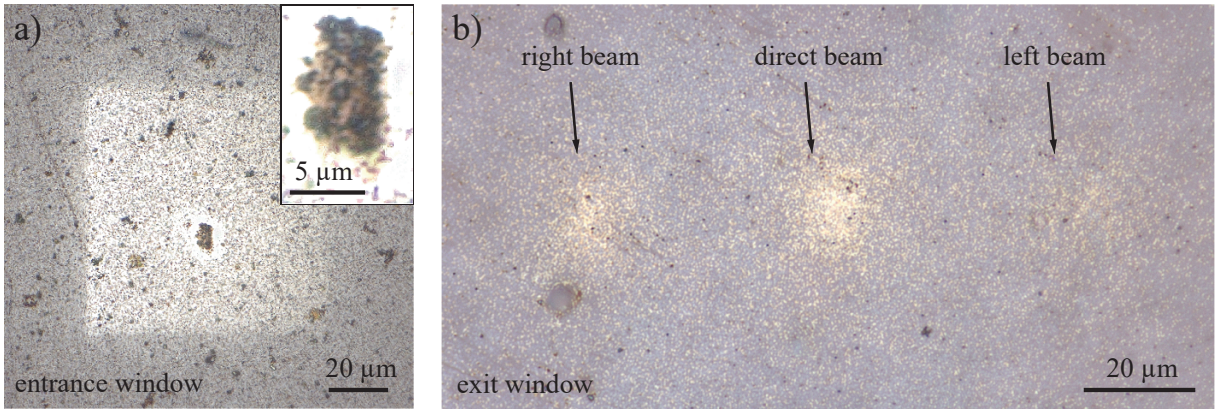

Figure 5.21: Light microscope images of the entrance and exit window. a) Entrance window showing the scanned area. The inset shows the area that was continuously scanned during the in-situ series. b) Exit window. It can be observed where the individual beams scanned the foil.

concentration for the formation of an alloy might not be high. Further analysis would be needed for a definitive answer.

The very thick structure that formed in the area studied during the reaction might in part explain why the particles seem to disappear. The grainy structure that can be seen on the entrance window from 162 min onward could be additional deposition of Pd on the foil. If Pd or a Cu-Pd alloy grows in between or on top of the particles undergoing galvanic replacement, this could lead to a decreased contrast of the particles. Further growth of them would then lead to their reappearance. Another factor could be that the injection solution is acidic (pH $\sim$ 4), and ionizing radiation can lead to a farther local acidification [59] of the reaction solution. In lab experiments carried out by Sarah-Alexandra Hussak, it was seen that Cu_2O nanocubes can get etched away under acidic conditions [137]. An acidic environment could, hence, lead to an increased dissolution of Cu^{2+}, which would result in a reduced phase shift. Further, OH-radicals formed through hydrolysis could open up a second redox pathway, as it was suggested for the galvanic replacement of Ag with Pd [138].

$$Cu_2O_{(s)} + 2\,OH\cdot + 2\,H^+_{(aq)} \longrightarrow 2\,Cu^{2+}_{(aq)} + H_2O$$

This decoupling of the oxidation of Cu from the reduction of $(PdCl_4)^{2-}$, could lead to an increased dissolution of Cu^{2+}.

Since the particles become visible again later on, it is unlikely that they completely disappeared before. It is more likely that they are simply below the resolution limit within this time frame. Since the in-situ reaction cell had to be modified for the stereo setup, the two windows were farther apart and less fixed in position than in previous experiments. If the propagation distance between the windows was not chosen correctly for the multi-slice reconstruction, features could become less visible. However, testing other propagation distances revealed that changing the propagation distance did not produce significantly different results.

Additionally, the photon energy was lower for this study – together with the longer beam path in the solution this led to a higher attenuation of the X-ray beam. Particles, too small to be actually resolved, growing in the solution and not on the windows could farther attenuate the beam. This would negatively impact the reconstruction quality. This list of possible explanations is certainly not exhaustive. For an accurate assessment, it would be advisable to repeat the measurement series with the original in-situ cell to check whether these results are reproducible.

The galvanic replacement reaction of Cu_2O nanocubes with Pd was for the first time studied with stereo X-ray ptychography. Simultaneous scanning with two beams allowed for a good correlation of the two acquired perspectives. Further, the time resolution was not compromised by an additional rotational step. Two perspectives of the sample were captured in 6 min. Inclusions in polyimide foils can be difficult to distinguish from particles of interest. These inclusions are widespread in the foils, making it difficult to avoid including them in the field of view. Using our new approach based on stereo perspectives, however, it is now possible to recover the nanoparticle layer by removing any obscuring inclusions or dirt particles.

5.6 Conclusion

These proof-of-principle experiments are the first demonstration of stereoscopic ptychography in the hard X-ray regime. By simultaneous scanning with multiple inclined nanobeams, in the presented example of a microchip, one is able to visually separate various electronic layers with a substantially improved depth resolution. With a total thickness of only 3.8 µm, the layered electronic structure highlights the sub-micron axial resolution of the stereoscopic hard X-ray microscope, which is far below the limits of multi-slice single-beam ptychography. This makes it comparable to high-performance, multi-layer X-ray optics [139], but with less restrictive experimental conditions and a larger working distance between the optics and the sample.

Stereo X-ray ptychography improves the depth of field by one order of magnitude in comparison to multi-slice ptychography using similar nanofocusing optics. It was shown that two sample layers with a distance of only 480 nm can be effectively distinguished through stereo X-ray ptychography. Phase images of the individual layers were recovered.

Further, stereo layer separation and multi-slice ptychography were combined to successfully reconstruct three layers of a test sample. The sample consisted of one FZP with nanoparticles on the backside of its membrane and a second FZP located 400 µm downstream of the first one. The two FZPs were separated in a multi-slice reconstruction. The layer containing the first FZP and the nanoparticle layer were subsequently recovered through layer separation based on the stereo projections of the first slice. Separating three layers with distances of 480 nm and 400 µm demonstrates that combining stereo X-ray ptychography and multi-slicing can provide depth information across different length scales.

For measurements that rely on shorter acquisition times, especially in-situ or operando studies, stereo ptychography has the unique potential to acquire a depth impression of a sample with a single scan. In-situ stereo ptychography was demonstrated at the example of a galvanic

replacement reaction of cuprous oxide nanocubes with palladium. Two perspectives of the reaction were captured simultaneously without compromising temporal resolution. With the presented approach using stereo pairs, dirt particles, inclusions, or other particles obscuring the view of the layer of interest can be effectively removed.

6 In-situ near-field ptychography

This chapter covers the first demonstration of in-situ X-ray near-field multi-slice ptychography. The results presented in this chapter are part of the publication "X-ray near-field multi-slice ptychography for in-situ imaging"[140]. Additional information on beam damage during the in-situ synthesis and the setup is provided beyond the content of the publication.

Karolina Stachnik and I share the first authorship for this paper. Karolina Stachnik and I conceived the experiment together with Jonas Voss, Christian G. Schroer, Dorota Koziej, and Andreas Schropp. The experiment was conducted by Karolina Stachnik, me, Jonas Voss, Mattias Åstrand, Lukas Grote, Andreas Schropp, Martin Seyrich, and Ulrich Vogt. Sven Niese and Peter Gawlitza manufactured the Multilayer Laue lenses and Sven Niese aligned them at the beamline. Karolina Stachnik and Felix Wittwer adapted the reconstruction algorithm. Karolina, I, Jonas Voss, Sarah-Alexandra Hussak, and Lukas Grote synthesized the samples for the experiment. Karolina Stachnik calculated the doses of each in-situ series. I carried out the ptychographic reconstructions, building on preliminary results from Jonas Voss. I prepared the manuscript for the publication together with Karolina Stachnik and Sarah-Alexandra Hussak. All authors reviewed the original manuscript for the publication.

6.1 Introduction

Ptychography has become the preferred method of high-spatial-resolution X-ray imaging at synchrotron radiation sources. Thus far, most of the research has focused on far-field ptychography (FFP). Regardless, near-field ptychography (NFP) has several advantages, such as requiring fewer scan points to image a large region with high spatial resolution[38].

It has been shown that the resolution in coherent diffractive imaging is inherently limited by the applied dose[141,142]. In their comparative study, Du *et al.* found no significant difference between near-field and far-field techniques in this regard[143]. For both, the photon fluence on the sample sets the limits for spatial resolution. However, NFP is far less sensitive to partial coherence than FFP[33,34]. This allows NFP to use larger fractions of the X-ray beam, resulting in a greater number of photons delivered to the scanned area within a comparable time unit. Considering the relationship between dose and resolution, NFP has the potential to offer faster scans for a given resolution and field of view.

When it comes to in-situ imaging, the limiting factor is often not the available photon flux, but rather the dose that a sample system can withstand before beam damage becomes apparent.

Beam-damage effects can significantly disturb the study of chemical reactions under in-situ conditions. Several factors influence the severity of radiation damage to the sample, such as sample composition, solvents, temperature, pH, photon energy, beam size, dose or dose rate [59,81]. The sensitivity of a sample to radiation damage is highly sample-dependent as are the measures that can be taken to reduce the degradation. The state of the art for X-ray studies of biological samples is cryocooling or the use of free-radical scavengers [144–146]. This is often not possible with in-situ or operando imaging, where specific temperatures and chemical environments are required to emulate realistic conditions.

NFP utilizes larger illumination sizes than FFP, which significantly reduces the dose rate per area. The dose can also be further decreased by performing NFP imaging at higher X-ray energies [147], since the phase shift does not decline with the same rate as the absorption at higher energies. The typical decrease in spatial coherence at higher photon energies at synchrotron radiation sources [33,148] can then be compensated for by using larger fractions of the beam. Given that NFP has generally weaker coherence requirements than FFP, this is a viable option. This makes NFP a compelling method for in situ imaging of chemical reactions. While the advantages listed above also apply to in-line holography, NFP has less stringent illumination requirements. In fact, the use of a highly structured illumination improves the reconstruction in NFP [38].

In our first demonstration of NFP for imaging nanoparticle growth, we use a reaction container with a size that exceeds the depth resolution of the microscope. We address this problem by exploiting near-field multi-slice ptychography, which enables imaging of optically thick objects by distinguishing between different sample layers. The combination of multi-slicing and NFP poses the particular challenge that the distances between the slices and the number of slices must be known precisely. This issue has been addressed through iterative refinement and demonstrated experimentally for optical wavelengths [149]. A first demonstration of near-field multi-slice ptychography with X-rays was reported [47] and the method was refined for imaging in the range of optical wavelengths [150]. In order to obtain an optimal resolution in the layer of interest, a high depth and lateral resolution of the imaging system is required, which can be achieved with high *NA*-lenses. At the same time, thick samples require the use of hard X-rays, where absorption is significantly lower. For this energy range ($> 10\,\mathrm{keV}$), multilayer Laue lenses (MLLs) provide the highest numerical aperture and the smallest focus size. In far-field multi-slice ptychography, MLLs enabled imaging with slice thicknesses of $10\,\mu\mathrm{m}$ and less [151,152].

In this chapter, in-situ near-field multi-slice ptychography with MLLs of the galvanic replacement reaction of cuprous oxide with gold is presented. In a first ex-situ experiment, we perform multi-slice NFP on a two-layer nanoparticle sample. In two in-situ studies, we demonstrate the capabilities of NFP for low dose rate and high spatial resolution imaging.

6.2 Multi-slicing for near-field ptychography

Near-field ptychography is a scanning phase-contrast imaging technique, which recovers the illumination and the sample transmission function from overlapping scan positions. Multi-slice

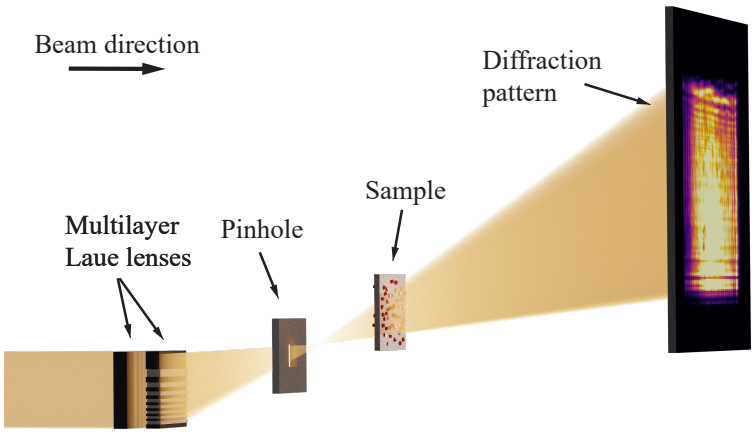

Figure 6.1: Schematic of the experimental setup. The x-ray beam is focused by a set of two MLLs to a focal spot of 30 nm (h) × 24 nm (v) in horizontal and vertical direction, respectively. A pinhole between the lenses and the focal spot acts as an order sorting aperture and cleans the beam. The sample is positioned at a distance between 0.63 mm and 3.00 mm downstream of the focus and scanned laterally across the beam. For each scan point, a diffraction pattern is recorded on a photon counting detector at a distance of 3.29 m behind the sample. Image is not to scale. Adapted from [140].

reconstructions extend the capabilities of ptychography to the imaging of optically thick specimens. It was initially used in FFP [51] and has recently been introduced for the near-field regime [47]. Multi-slice ptychography enables multiple layers of an optically thick sample to be recovered.

Although NFP is a lensless imaging technique that does not use an objective lens, the achievable depth resolution as described in Eq. 3.9 is directly related to the numerical aperture (NA) of the lens placed upstream of the sample. To achieve superior lateral and depth resolution, high-NA lenses should be used.

Many in-situ studies require bulky reaction environments. For this reason, a high penetration depth of the illuminating beam is required, which can be achieved by using hard X-rays. MLLs are the optics type with the highest NA in the hard X-ray range and were therefore utilized for this setup. A visualization of the used setup is shown in Fig. 6.1.

The experiment was carried out at the X-ray microscope PtyNAMi [122] available at beamline P06 at PETRA III. The photon energy was set to 18.0 keV with a channel cut monochromator. To accommodate the two multilayer Laue lenses, we used two hexapods which are components of the lens platform of the setup (shown in Fig. 6.2a). The horizontally focusing lens was placed 160 µm downstream of the vertically focusing one. The lenses created a square aperture of 40 µm×40 µm. The focused beam was cleaned from other diffraction orders by a rectangular pinhole (order sorting aperture) placed several millimeters downstream of the lenses. The sample was positioned on a piezo scanner between 0.63 mm and 3.00 mm downstream of the focal plane and diffraction patterns were recorded at a distance of 3.29 m behind the sample by the Eiger X 4M in-vacuum detector. The sample was scanned with a grid scan pattern. For each scan position, we introduced a random offset up to 30% of the step size to avoid perfect-grid artifacts [124]. The experimental parameters for each scan are summarized in Table 6.1.

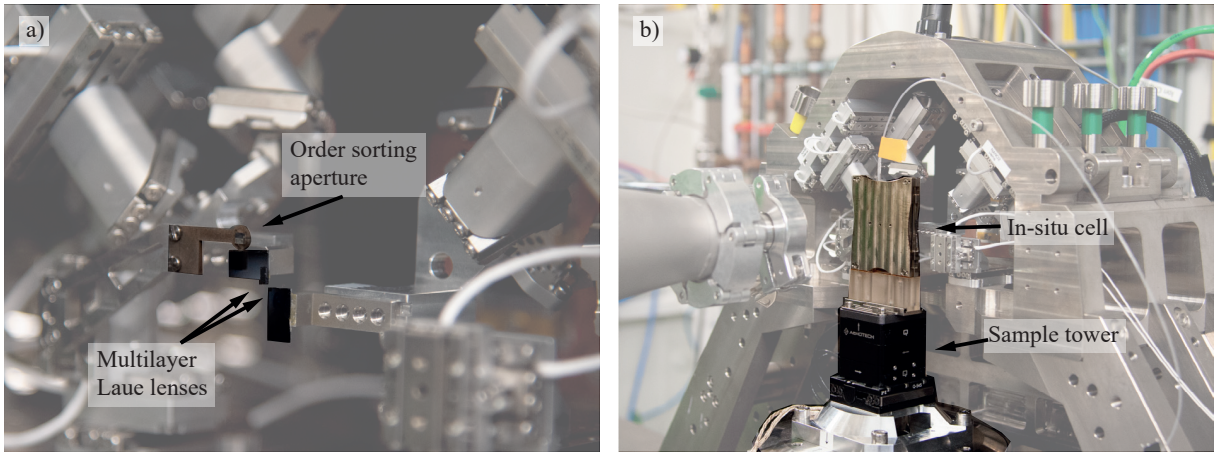

Figure 6.2: Experimental setup at PtyNAMi. a) Shows the MLLs mounted on the hexapods and the order sorting aperture. b) The in-situ cell is mounted on the scanning stages on the sample tower.

The focal length of the MLLs at the selected photon energy equaled 13.5 mm. The numerical aperture of the MLLs was $1.48 \cdot 10^{-3}$, which corresponds to a depth of focus of

$$\mathrm{DOF}_{\mathrm{MLL}} = \frac{\lambda}{NA^2} = \frac{68.88\,\mathrm{pm}}{(1.48 \cdot 10^{-3})^2} = 31.44\,\mu\mathrm{m}. \tag{6.1}$$

A far-field ptychographic scan of a Siemens star test pattern was used to characterize the focused X-ray beam. The corresponding beam caustic is shown in Fig. 6.3. The focal spot created by the horizontal and vertical focusing MLLs was determined to be 30 nm × 24 nm.

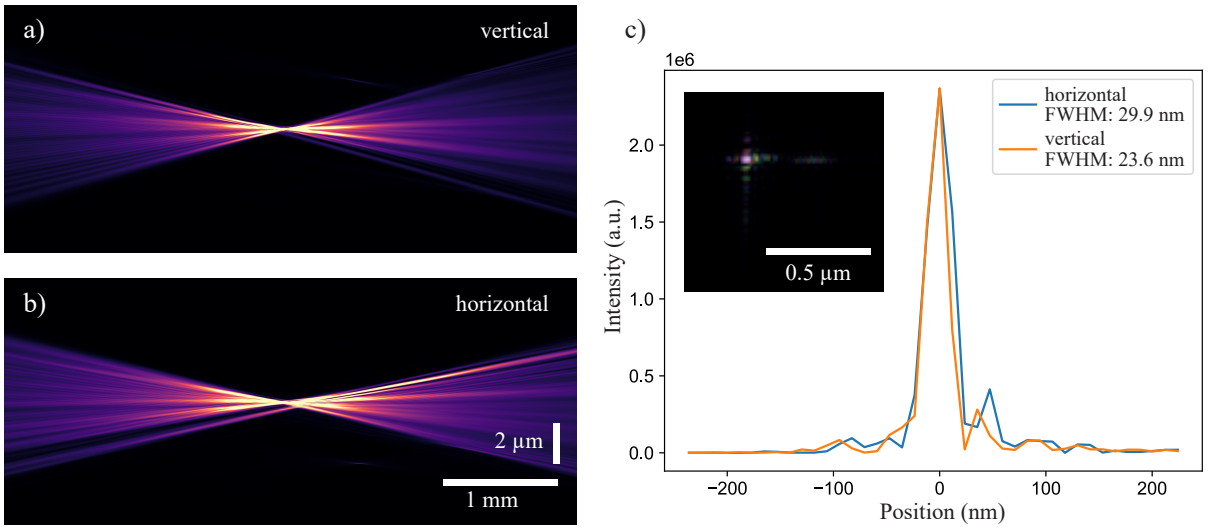

Figure 6.3: Characterization of the X-ray beam focused by multilayer Laue lenses. Beam caustic in vertical (a) and horizontal (b) direction. A slight astigmatism can be observed. c) The focus size (full width half maximum) was determined to be 29.9 nm × 23.6 nm. Inset shows the beam in the focal plane. Adapted from [140].

Parameter	Fig. 6.4	Fig. 6.5	Fig. 6.8
Photon energy (keV)	18.0	18.0	18.0
X-ray beam prefocusing (on / off)	on	off	on
Scanning area (µm^2)	10×10	10×10	8×8
Focus-to-sample distance (mm)	2.84	3.0	0.63
Grid-scan step size (nm)	323	196	157
Additive random jitter interval (%)	±30	±30	±30
Exposure time (s)	0.1	0.2	0.2
Sample-to-detector distance (m)	3.29	3.29	3.29
Detector pixel size (µm)	75	75	75

Table 6.1: Experimental parameters. Parameters used for the ptychograms shown in Figs. 6.4, 6.5, and 6.8.

For the in-situ series shown in Fig. 6.5 the MLLs were illuminated fully coherently. For the other measurements prefocusing compound reflective lenses located 56 m upstream of the MLLs were used. These reduced the coherence length at the MLL position to 15 µm in the horizontal and 85 µm in the vertical direction and led to a partially coherent illumination. In near field imaging, coherence over the first Fresnel zone width would be sufficient [35] and the coherence length for all measurements is well above this limit.

The scans were reconstructed using the ePIE [30] algorithm for the single-slice case and the 3PIE [51] algorithm for the multi-slice case (described in Sec. 3.5). In the reconstruction, the wavefield is propagated between the slices and between the sample and the detector using a Fresnel propagator. Details of the reconstruction parameters for each scan are summarized in Table 6.2.

In contrast to FFP, NFP is modeled with a cone beam geometry. For efficient image reconstruction, the cone beam is converted to an equivalent parallel-beam geometry, which is done by applying the Fresnel scaling theorem [153]. The pixel size and the propagation distance of each slice are scaled accordingly. This step requires the knowledge of the distance between the focus and the sample, measured during the experiment. In this work, the focus to sample distance and the distances between slices were refined interactively by performing reconstructions with the aforementioned distances varied by ±10% around the expected value. The values that produced a flat phase profile for the illumination and visually good results for the slices were chosen for the final reconstruction. In our experiment, the divergent MLL-beam had a size of 11.3 mm × 12.6 mm on the detector, with a propagation distance of 3.29 m between sample and detector. Using Eq. 3.9, it is found that the depth of field is $DOF \approx 275 \cdot \delta_r$. At a source size limited lateral resolution of $\delta_r = 30$ nm the achievable depth resolution with our setup is therefore $DOF = 8$ µm.

Parameter	Fig. 6.4c	Fig. 6.4e-f	Fig. 6.5c-h	Fig. 6.8b	Fig. 6.8c-f
Reconstruction mode	single-slice	multi-slice	multi-slice	single-slice	multi-slice
Number of slices	1	2	2	1	4
Focus → Slice 1 distance (mm)	2.84	2.84	3.0	0.63	0.63
Slice 1 pixel size (nm)	64.7	64.7	68.3	14.4	14.4
Slice 1 refinement delay (iterations)	–	100	50	–	15
Slice 1 → Slice 2 distance (mm)	–	0.225	1.0	–	0.125
Slice 2 pixel size (nm)	–	69.8	91.1	–	17.2
Slice 2 refinement delay (iterations)	–	0	0	–	30
Slice 2 → Slice 3 distance (mm)	–	–	–	–	1.2
Slice 3 pixel size (nm)	–	–	–	–	44.6
Slice 3 refinement delay (iterations)	–	–	–	–	5
Slice 3 → Slice 4 distance (mm)	–	–	–	–	0.0625
Slice 4 pixel size (nm)	–	–	–	–	46.0
Slice 4 refinement delay (iterations)	–	–	–	–	0
Cropping area on detector (pixels)	512×512	512×512	512×512	512×512	512×512
Reconstruction engine	ePIE [30]	3PIE [51]	3PIE [51]	ePIE [30]	3PIE [51]
Number of iterations	1000	1000	5000	1000	1000
Position refinement [129]	on	on	off	on	on

Table 6.2: Near-field ptychographic reconstruction parameters. Parameters for the single-slice and multi-slice reconstructions of Figs. 6.4, 6.5, and 6.8.

6.2.1 Implementation of the Fresnel scaling theorem

For near-field multi-slice ptychography in cone beam geometry, Fresnel scaling has to be implemented in the 3PIE[51] reconstruction algorithm. The cone beam is converted to an equivalent parallel beam geometry by scaling of the propagation distances and pixel sizes. The following adaptations were made:

The user defines the number of slices N and the real distances from one slice to the next $z_{n\to(n+1)}$. The algorithm begins by calculating the magnification from the slice closest to focus, $n = 0$, to the detector (index detector)

$$M_{0\to\text{detector}} = 1 + \frac{\text{z}_{0\to\text{detector}}}{z_{\text{focus}\to 0}}. \tag{6.2}$$

This magnification is used to calculate the object pixel size Δx_0 of the slice $n = 0$, as given by

$$\Delta x_0 = \frac{\Delta x_{detector}}{M_{0\to detector}}, \tag{6.3}$$

where $\Delta x_{detector}$ is the pixel size of the detector. For the propagation between slices, the inter-slice magnification between slices n and $n + 1$ is calculated for all slices

$$M_{n\to(n+1)} = 1 + \frac{z_{n\to(n+1)}}{z_{\text{focus}\to n}}. \tag{6.4}$$

From this, the effective propagation distance z_{eff} between the two slices follows

$$z_{\text{eff},n\to(n+1)} = \frac{z_{n\to(n+1)}}{M_{n\to(n+1)}}. \tag{6.5}$$

The object pixel size of a subsequent slice $n + 1$, Δx_{n+1}, is calculated by scaling the pixel size of the current slice n with the inter-slice magnification

$$\Delta x_{n+1} = \Delta x_n \cdot M_{n\to(n+1)}, \tag{6.6}$$

where the pixel size of the first slice Δx_0 is used as the starting point. The reconstruction algorithm works with discretized probe positions, calculated from the measured real-space scan positions and the pixel size. With the object pixel size changing from one slice to the next, the pixel-valued positions of the probe need to be calculated for each slice separately, even though the real-space positions are not changed.
Effectively, there are two changes to the 3PIE algorithm for the application in the near-field ptychography: Firstly, the near-field propagator is not only used in between slices but also for the propagation from the final slice to the detector and back. Secondly, the Fresnel scaling theorem is applied to all object pixel sizes, propagation distances and discretized probe positions.

6.2.2 Lateral resolution determination

The lateral resolution of the scans was determined using Fourier ring correlation [39,40]. For the Fourier ring correlation, the reconstructions were carried out using one half of the scan points of the original data set. The scan positions were split in a way that every second diffraction pattern was used, effectively mimicking a scanning step of twice the size in the vertical direction (fast scan axis). The half-bit criterion was used for the resolution determination since only half the diffraction patterns were used in each reconstruction. Details on the Fourier ring correlation for each scan are included in the appendix (Figs. C.1, C.2, and C.3).

6.3 Ex-situ near-field multi-slice ptychography

We first characterize our method by imaging cuprous oxide nanoparticles synthesized ex situ on both sides of a 225 µm-thick polyimide foil, as conceptually illustrated in Fig. 6.4a. We placed the front surface of our sample (slice 1) at a distance of 2.84 mm downstream of the X-ray focus. We scanned an area of $10 \times 10\,\mu m^2$ with a grid scan pattern of 31×31 scan points. The exposure time per scan point was 0.1 s. This geometry corresponds to an effective Fresnel number of $F = 412$ applying Eq. 6.8.

The reconstructed illuminating beam (Fig. 6.4b) shows a relatively flat phase profile (indicated by the colors), as it is expected in near-field imaging without a diffuser [38]. The grid-like structure visible in the amplitude of the illumination (indicated by the brightness) is caused by the layered structure of the MLLs. Structure in the illumination is in general beneficial for a robust reconstruction in ptychography [36,37] and even more important in NFP (see Sec. 3.3). For efficient phase retrieval, NFP relies on a structured illumination [34,38]. The structure is typically created using a diffuser, such as sandpaper, placed in front of the lens. The use of MLLs, whose slight imperfections produce an inherently structured wavefield, made a diffuser in this case unnecessary.

For the multi-slice reconstruction, the polyimide foil is a model specimen with two distinct planes of cuprous oxide cubes on either side of the foil, slice 1 and slice 2, as shown in Fig. 6.4a. A conventional NFP reconstruction of the foil, treating the sample as a single, optically thin object, is shown in Fig. 6.4c. The features on the upstream side of the foil are well resolved and sharp, while the cuprous oxide cubes on the back side appear blurred (see blue arrow in Fig. 6.4). This indicates that the single-slice approximation for the object is not sufficient to model the thicker sample. To resolve both sides of the foil, beam propagation effects between the different layers must be taken into account. With multi-slice NFP, the individual slices can be sharply recovered. Slice 1 (Fig. 6.4e) shows the particles located on the upstream side of the foil and slice 2 (Fig. 6.4f) the nanocubes on the downstream side. The pixelwise sum of the two slices, shown in Fig. 6.4d, exhibits sharp edges for all features of both layers. Due to the cone-beam geometry, the effective pixel sizes are not the same for the two object slices. The pixel size for slice 1, which is closer to the focus, is 64.7 nm and for slice 2 it is 69.8 nm. To create

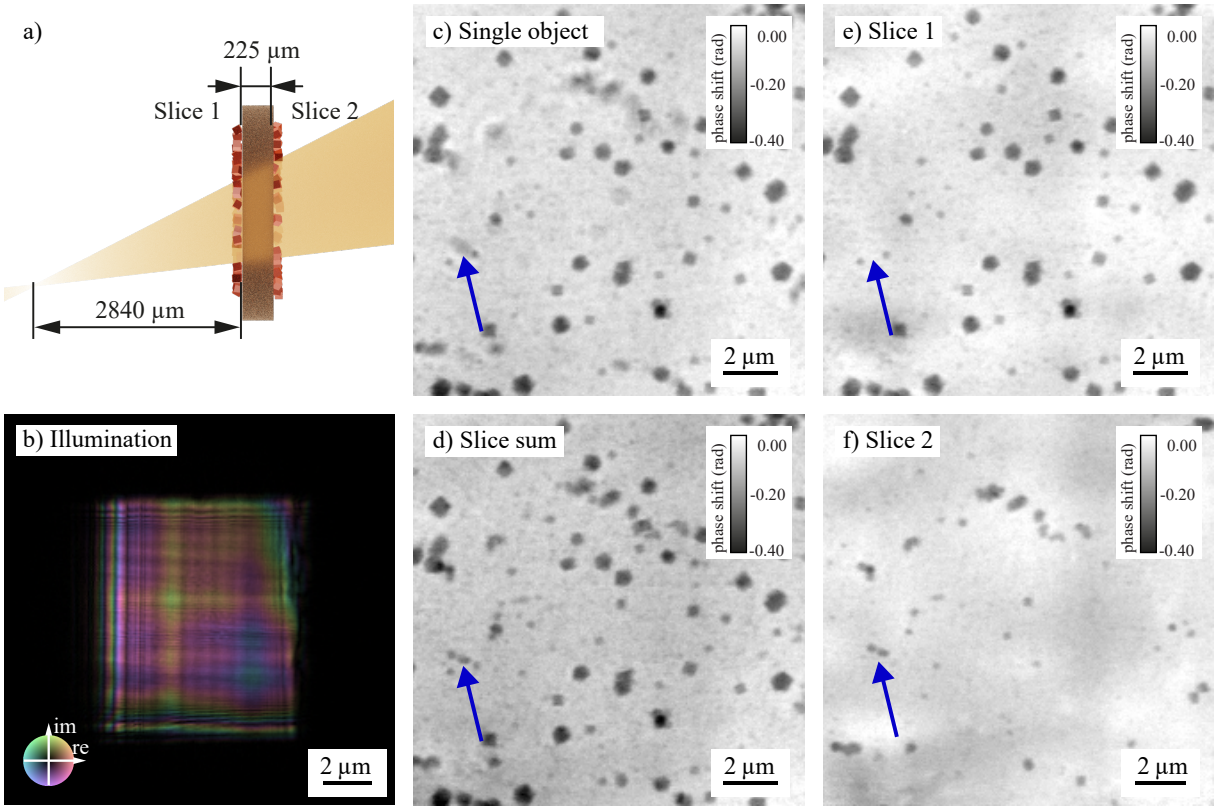

Figure 6.4: Near-field multi-slice ptychography of ex-situ cuprous oxide nanoparticles deposited on both sides of a polyimide foil. a) schematic of the sample placed 2840 µm downstream of the focus of the x-ray beam with the two particle layers separated by a 225 µm-thick polyimide foil. b) shows the corresponding reconstructed illumination with a size of 8.5 µm × 10.0 µm. c) reconstruction of the scan assuming a single optically thin object. d) summed phase of the multi-slice reconstruction shown in e) (first slice) and f) (second slice). The particles on the downstream side of the foil (slice 2) appear blurred in the single-slice reconstruction (see e. g. the blue arrow), while they are well resolved in the reconstruction of the second slice and in the sum of the slices. Adapted from [140].

the pixelwise slice sum in Fig. 6.4d as a parallel projection, we scaled the pixel size of slice 2 to match the pixel size of slice 1 using the scikit-image [126] resize function.

Background fluctuations (brighter and darker areas without any sharp edges) are apparent in the reconstructions of the slices and cancel out in the sum of the two. These low-frequency image artifacts are often present in multi-slice ptychography [46,90], typically caused by the short propagation distance between the slices. The maximum width between two points in one plane, for which interference effects can be observed after propagation over an effective distance z_{eff}, can be estimated by the first Fresnel zone radius r_F [14] (see also Sec. 2.1.3)

$$r_F = \sqrt{\lambda \cdot z_{\text{eff}}}, \tag{6.7}$$

where λ denotes the X-ray wavelength. This effectively limits the lowest spatial frequency that can be recovered for a given propagation distance.

In the multi-slice reconstructions, the scattering of the polyimide foil was neglected, and the wavefield propagated between the two slices. In reality, though, the polyimide foil introduces a phase shift. However, this effect is negligible at the used photon energy for a homogeneous foil of the given thickness. Applying Eq. 3.9 for a lateral resolution of $\delta_r = 102.6\,\text{nm}$, the DOF for this scan was equal to 27.5 µm while the reconstructed slices were separated by 225 µm, which is well above the DOF limit. Here, we demonstrated multi-slice NFP on an ex-situ model sample, in the next step we show its capabilities for in-situ imaging of chemical reactions.

6.4 In-situ near field ptychography of galvanic replacement

The galvanic replacement reaction of cuprous oxide nanocubes with gold was used as a model reaction for in-situ multi-slice NFP.

For this purpose, we adopted the synthetic procedure and the in-situ reactor reported by Grote *et al.*[119] A 125 µm thick polyimide foil (Kapton HN, DuPont de Nemours Inc.) containing previously grown Cu_2O nanocubes was used in the entrance position of the in-situ reactor, while the exit window was empty. 1.4 mL Milli-Q ultrapure water with a resistivity of 18.2 MΩcm at 25 °C was filled into the reactor. At room temperature, a polytetrafluorethylene tube was inserted to dose 400 µL of a 20 mmolar aq. $HAuCl_4$ solution using a syringe pump (PHD Ultra, Harvard Apparatus, USA). The injection rate was set to 66 µL/h for the high resolution series and 100 µL/h for the low dose rate series. The galvanic replacement reaction is described by the following reaction equation[54]

$$1.5Cu_2O_{(s)} + AuCl^-_{4(aq)} + 3H^+_{(aq)} \rightarrow Au_{(s)} + 3Cu^{2+}_{(aq)} + 4Cl^-_{(aq)} + 1.5H_2O$$

Benzyl alcohol ($\geq$ 99.0%), $Cu(acac)_2$ (99.99 %) and $HAuCl_4{\cdot}3H_2O$ ($\geq$ 99.9% trace metal basis) were purchased from Sigma-Aldrich, and ethanol (absolute) for washing from VWR. All chemicals were used without further purification.

6.4.1 Low dose rate in-situ near-field ptychography

We mounted our reaction cell for in-situ imaging of nanoparticle growth[119] at 3.0 mm behind the focal plane. The polyimide foil with the cuprous oxide cubes is placed on the upstream side of the reaction container. The downstream window is an empty polyimide foil, which is separated by 1 mm from the upstream window using a PTFE-frame between them. The resulting reaction container is enclosed in a metal casing. The reaction solution containing the gold precursor is injected between the two polyimide windows. The pre-synthesized cuprous oxide nanocubes are attached to a polyimide foil and, over the course of the reaction, the cuprous oxide is replaced by gold, as schematically shown in Figs. 6.5a and 6.5b. Further details on the reaction can be found in Grote *et al.*[119]

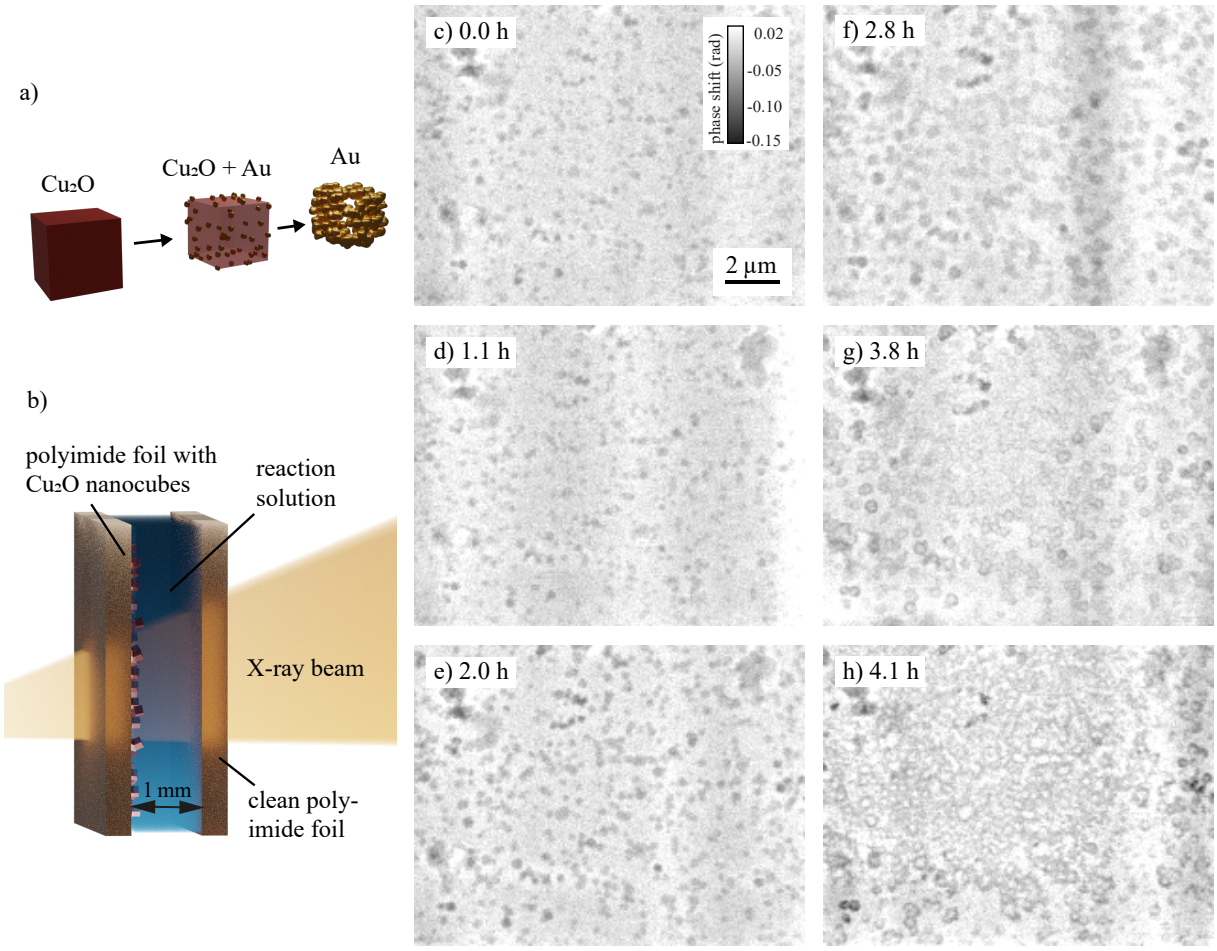

Figure 6.5: In-situ near-field multi-slicing ptychography of cuprous oxide nanocubes undergoing galvanic replacement reaction. a) Schematic of the galvanic replacement reaction. Gold particles form on the surface of the cuprous oxide cubes, Cu^{2+} dissolves over the course of the reaction and hollow gold nanocages form (adapted from [119]). b) Schematic of the reaction container. A polyimide foil with pre-synthesized cuprous oxide and a clean foil encapsulate the reaction solution with the gold precursor. c)-h) In-situ galvanic replacement reaction over 4.2 h. Multi-slice near-field reconstructions of the upstream window (phase shift). In the beginning (c) Cu_2O nanocubes are attached to the upstream polyimide foil. Over the first 2.8 h (c-f) a growth of the particles can be observed. A beam dump occurred between 3.0 h and 3.8 h after reaction start. At 3.8 h (g) hollow cages have formed, which seem to connect in the following (h). Adapted from [140].

The in-situ series of the galvanic replacement reaction of Cu_2O with Au was measured over 4.2 h. A single ptychographic scan spanned an area of 10 µm × 10 µm and required a total scan time of 9.6 min.

For this in-situ series, the *DOF* was 21 µm and the two reconstructed slices were separated by 1 mm. Scattering by the reaction solution was neglected and the distance between the two windows was modeled with a free-space propagator. In the post-processing step, a high-pass filter was applied to the reconstructed phase images of the upstream window to reduce low-frequency artifacts. We used the scikit-image[126] Butterworth filter with a cutoff frequency ratio of 0.018.

At the beginning of the reaction at 0.0 h (Fig. 6.5c), the upstream polyimide foil was covered with Cu_2O cubes with an edge length of 150 nm to 250 nm (see Fig. 6.7). The reaction solution containing the gold precursor (20 mM $HAuCl_4$) was slowly injected into the cell with a syringe pump. In the first phase of the reaction, Au particles formed on the surface of the nanocubes. In the second phase, the Au particles grew larger and fused together, Cu_2O was further oxidized and dissolved, and the cubes became less dense in their centers. The final stage of the reaction was the formation of hollow Au nanocages, similar like observed in FFP experiments reported by Grote *et al.*[119]

Between 0.0 h and 2.8 h (Figs. 6.5c-f), a growth of the particles could be observed. A beam dump between 3.0 h and 3.8 h after the start of the reaction did not allow data acquisition during this period. In the first scan after the beam dump (at 3.8 h) (Fig. 6.5g), the particles appeared hollow and in the subsequent scans, the hollow structures seemed to connect. The growth in the first phase can be attributed to Au particles forming on the Cu_2O surface. The galvanic replacement reaction progressed during the beam dump and at 3.8 h after the start of the reaction the hollow cages resembled the expected final result. The later Au deposition (Fig. 6.5h) can be attributed to beam damage. This is also evidenced by Au deposition on the downstream window of the reaction container (see Fig. 6.6), which is not the case in comparable ex-situ laboratory experiments.

For this in-situ series, the spatial resolution determined by Fourier-ring correlation was between 88 nm and 129 nm (see appendix Fig. C.2), which is comparable to the spatial resolution achieved in a similar experiment with FFP[119]. The average dose per projection was 0.36 MGy with a dose rate of 1.28 kGy/s, which corresponds to a reduction in dose by a factor of 2.5 for a given field of view and a reduction of the dose rate by more than two orders of magnitude compared to the FFP results. The dose and dose rate were calculated according to the procedure reported in[119]. The significantly reduced dose rate is a result of the large illumination. However, the cumulative dose is comparable and, therefore, so is the spatial resolution.

The growth and formation of the hollow cages was clearly observed. This study demonstrates the competitiveness of NFP for in-situ imaging with reduced dose rate and improved temporal resolution while maintaining high spatial resolution. NFP is an excellent method for radiation sensitive samples. However, beam damage is a complex process with many experimental parameters to consider, such as beam size, photon energy and more. Björling *et al.* describe

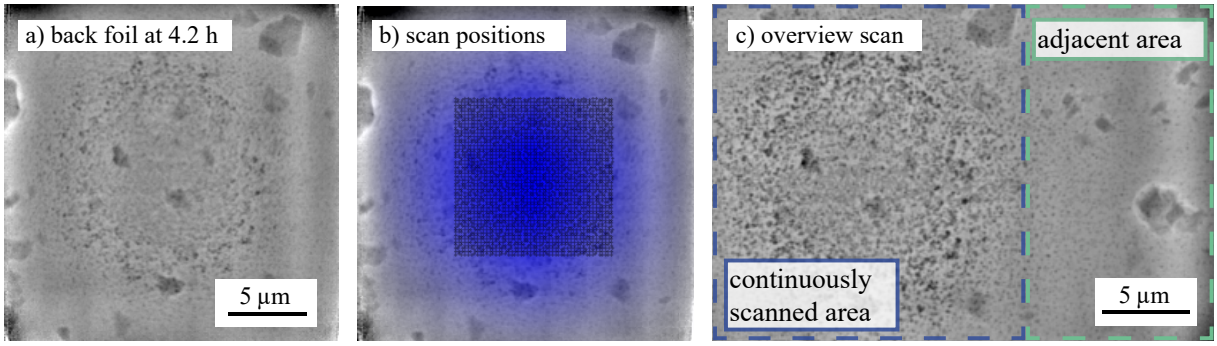

Figure 6.6: Beam damage in the in-situ series shown in Fig. 6.5. a) shows the initially empty back foil of the reaction container at 4.2 h. Normally, one would expect the foil to remain empty apart from the inclusions in the polyimide foil. b) indicates the scan positions with the black dots overlayed on the scan shown in a. The blue color indicates the intensity of the beam over the field of view. The beam intensity is calculated by summing up the amplitude of the illumination over all scan positions. c) is an overview scan at the end of the reaction. The left side of the scan was continuously scanned for the duration of the reaction. The right side was scanned only once for the overview scan. It is apparent that in the continuously scanned area of the sample a significant amount of gold grew. The right side remained mostly empty as it would be expected in experiments without X-ray beam exposure. Adapted from [140].

comprehensively the interplay between experimental parameters and free-radical formation in aqueous solutions [81].

The spatial resolution of the scans varied between 129 nm for the early scans, without significant beam damage, and 88 nm for the later scans, with significant beam damage. In addition to galvanic replacement, we observed a deposition of gold in the exposed areas of the sample. The increased size and thickness of the gold particles led to an increased phase shift and thus an increased X-ray optical contrast, thereby improving the spatial resolution of the reconstructions of later scans. The resolution of all scans was close to or below the size of two pixels. Therefore, they can be described as pixel-size-limited when the resolution is considered in terms of the Nyquist limit. In future experiments, the use of a detector with a smaller pixel size could improve the spatial resolution for similar temporal resolution and dose. Alternatively, an improved resolution could potentially be achieved by reducing the demagnified pixel size using a two-stage Fresnel propagator as described by Witte *et al.* [154]

Influence of beam damage on the galvanic replacement reaction

This in-situ experiment was aiming for low dose and low dose rate imaging of the galvanic replacement reaction to minimize radiation damage. But a comparison of areas on the polyimide foil, which were exposed to the X-rays with areas that were not exposed makes a difference in Au deposition evident. Fig. 6.7 shows the sample used for the low dose rate in-situ reaction before and after the galvanic replacement. Before the reaction Cu_2O cubes with an edge length of 150 nm to 250 nm were attached to the polyimide foil (Fig. 6.7a). The Cu_2O cubes in the unexposed area underwent a galvanic replacement reaction with Au, leading to the formation of hollow Au nanocages (Fig. 6.7b). In the area that was exposed to the X-ray beam, a layer of Au

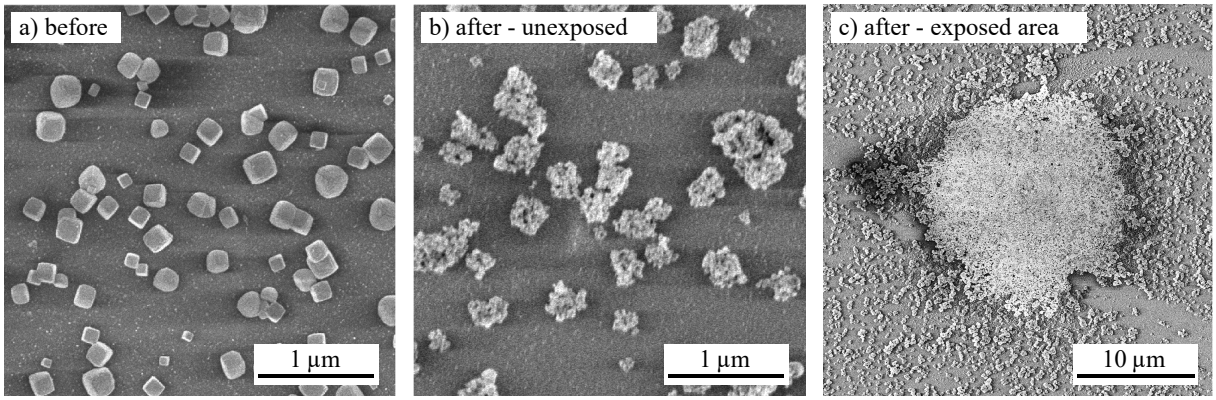

Figure 6.7: Scanning electron microscopy (SEM) images of the sample before and after the galvanic replacement reaction. a) Polyimide foil with attached Cu_2O cubes, which was used in the in-situ series shown in Fig. 6.5. b) An area of the same sample after the galvanic replacement reaction with Au that was not exposed to the X-ray beam. c) In the area that was continuously scanned a layer of Au formed. Images were acquired with a Regulus8220 SEM (Hitachi, Japan) at an acceleration voltage of 0.3 kV. The SEM images were taken by Karolina Stachnik and Sarah-Alexandra Hussak. Adapted from [140].

has formed (Fig. 6.7c). The additional Au deposition in the exposed area can be attributed to beam damage. Similarly, Au formation on the backside of the in-situ cell was observed exclusively within the scanned area, indicating beam-induced deposition (see Fig. 6.6).

The interaction of X-rays with the aqueous reaction solution causes hydrolysis, which leads to the formation of solvated electrons, $H\cdot$, and $OH\cdot$ radicals, and other reactive species (see Sec. 4.2.2). In a competing reaction to the galvanic replacement, the Au^{3+} ions can be reduced by solvated electrons and hydrogen radicals.

$$AuCl^-_{4(aq)} + 3e^-_{aq} \rightarrow Au^0 + 4Cl^-_{(aq)}$$
$$AuCl^-_{4(aq)} + 3H\cdot \rightarrow Au^0 + 3H^+ + 4Cl^-_{(aq)}$$

This side reaction can lead to additional deposition of Au on the two polyimide windows. Other products of hydrolysis, such as H_2O_2, could also act as reducing agents.

6.4.2 High resolution in-situ near-field ptychography

In a second in-situ series of the same reaction, our aim was to achieve imaging with an even higher spatial resolution. The reaction cell was moved to a position 630 µm downstream of the focal plane of the MLLs. By moving the sample closer to the focal plane, the magnification was increased by a factor of 4.75 to $M = 5223$ and the demagnified pixel size in the first slice therefore reduced by the same factor to 14.4 nm. The reaction was running for 1.0 h when the scan shown in Fig. 6.8 was recorded. The distance between the upstream and downstream window was 1.2 mm, slightly larger than in the previous experiment. However, this is within the assembly tolerances of the reaction container.

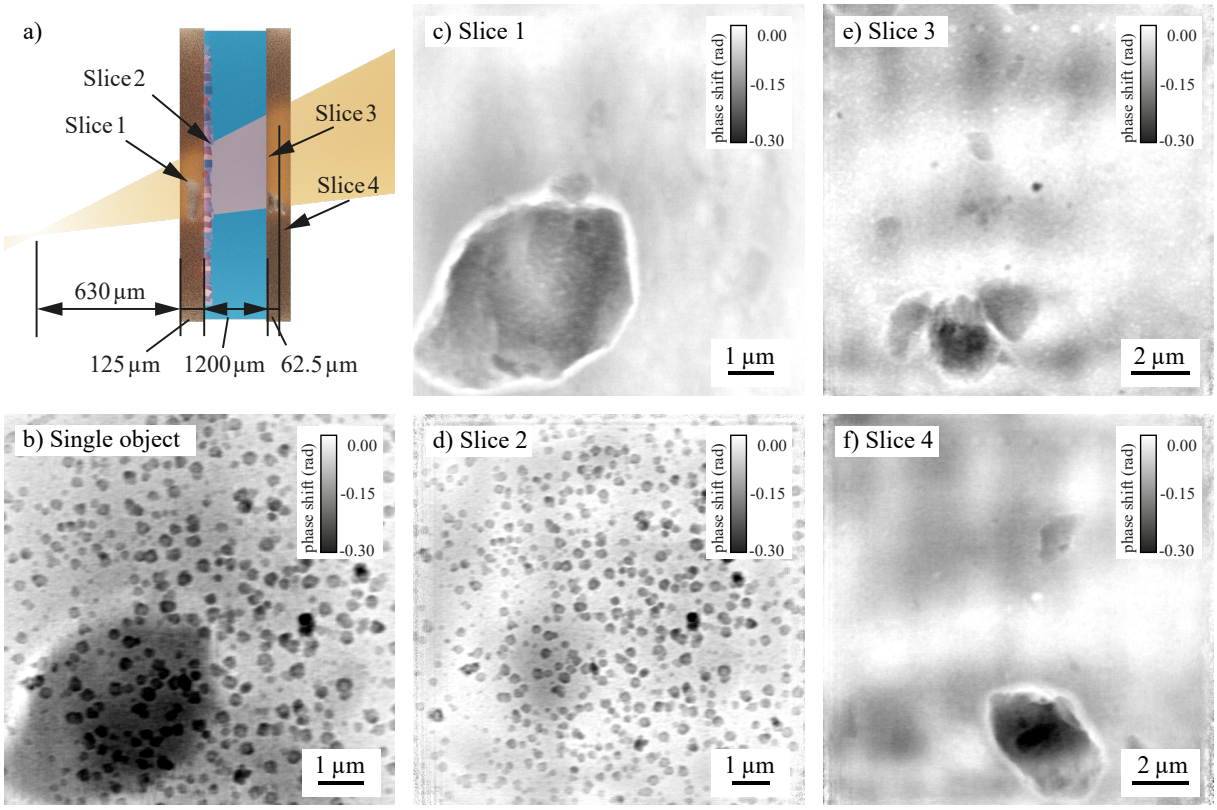

Figure 6.8: Imaging of nanoparticles growing in solution. a) shows a schematic longitudinal cross section of the chemical reactor with four distinct object planes (slices) in the direction of the X-ray beam. b) A conventional single-slice reconstruction of the chemical reactor with nanoparticles. Applying the multi-slice approach allows one to isolate four object planes corresponding to: c) the upstream reactor's window, d) the inner side of the upstream window with nanoparticles, e) the inner side of the downstream reactor's window, and f) the outer side of the downstream reactor's window. c), e), and f) show inclusions present in polyimide foils that otherwise obscure the view on the nanoparticles. Adapted from [140].

Fig. 6.8b shows a single-slice reconstruction, where the sample was treated as a single optically thin object. A big inclusion in the polyimide foil is clearly visible in the background in the lower left corner. The polyimide foils often contain inclusions from additives used as slipping agents in the production process[132,133] (see appendix Fig. C.4), which compromise the reconstruction of the layer of interest containing the nanoparticles.

To optimize the resolution of the plane of interest and to remove any inclusions obscuring the view on the nanoparticles, we recovered four distinct slices (Fig. 6.8c-f) in a multi-slice reconstruction. The two slices of the upstream window of the reaction cell (slice 1 and slice 2) are separated by 125 µm. The exit window is located 1200 µm downstream of the second slice and divided into two slices separated by 62.5 µm.

A distance of 630 µm between focal plane and sample may seem small to consider this measurement in the near-field imaging regime. The effective Fresnel number F for this scan is given by[38]

$$F = \frac{W^2}{\lambda z_{\text{eff}}} = 126.5, \tag{6.8}$$

with the extent of the illumination $W^2 = 2.2\,\mu\text{m} \times 2.5\,\mu\text{m}$, the wavelength $\lambda = 0.69\,\text{Å}$ and the effective propagation distance $z_{\text{eff}} = 630\,\mu\text{m}$. Even though the effective Fresnel number for this measurement is considerably larger than unity, the scan can still be analyzed with a far-field propagator between the last slice and the detector. However, the slice separation achieved with the near-field multi-slice reconstruction is superior to that of the far-field reconstruction (see Fig. 6.9). The contribution from other slices remaining in the plane of interest is significantly smaller, showing that the Fresnel approximation models the measurement more accurately in this case. The plane with the nanoparticles (slice 2, Fig. 6.8d) shows only a weak shadow of the large inclusion from slice 1 compared to the single-slice reconstruction. In order to correctly evaluate the reaction process, it is of great importance to obtain an undisturbed, quantitative image of the plane of interest, which we have achieved here in the multi-slice reconstruction. The large inclusions in slices 1, 3, and 4 are surrounded by a 'halo'. This is a well-known artifact for strongly phase-shifting features in phase-contrast imaging[155–158], resulting from the small modulation transfer of the low spatial frequencies.

The spatial resolution for slice 2, determined with Fourier ring correlation[39,40], is 30 nm. This is close to the theoretical limit given by the focal spot size of the MLLs and below the resolution limit of two times the pixel size, given by the Nyquist limit. The reconstruction can therefore be described as pixel-size-limited. The resolution for the other slices was 48 nm for the first slice, 84 nm for the third slice, and 130 nm for the fourth slice. The resolution of slice 1 is lower than slice 2 despite a smaller pixel size. This can be explained by a sparse sample plane for slice 1 with more than half of the scan points containing only little structural diversity and, hence, being more challenging to reconstruct. Details of the Fourier ring correlation analysis can be found in the appendix Fig. C.3. For these spatial resolutions, the slice thicknesses are all greater than the depth of field limit given by Eq. 3.9 (slice 1: 13 µm, slice 2: 8 µm, slice 3: 23 µm). Nevertheless,

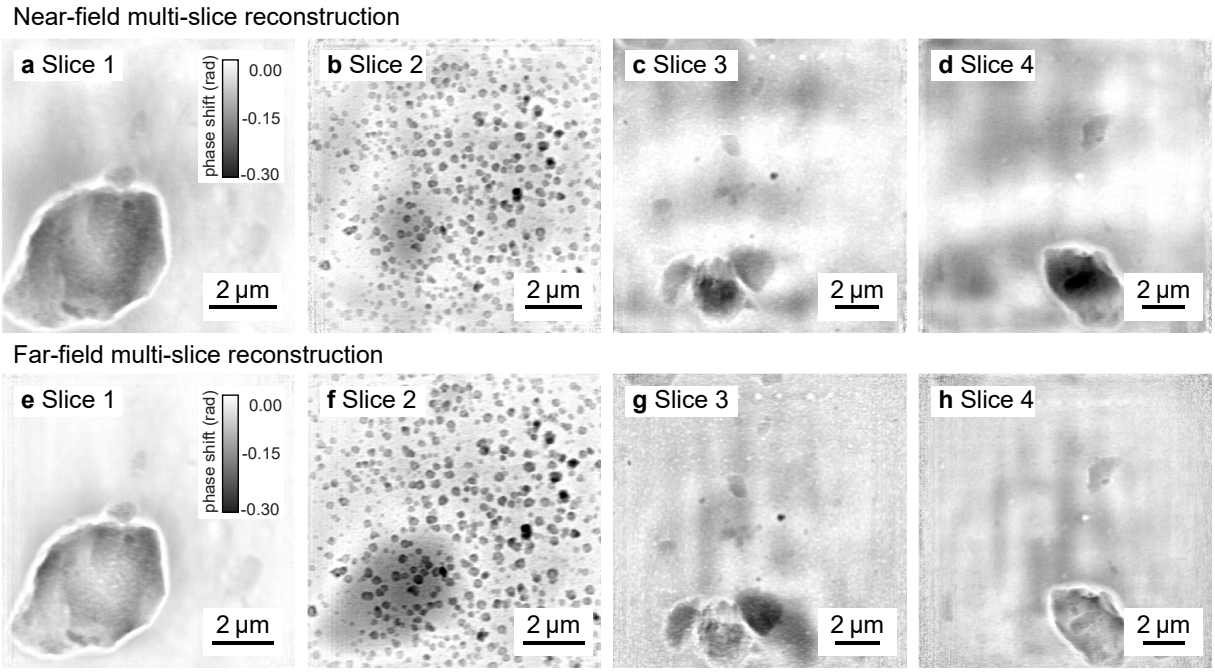

Figure 6.9: Comparison of a near-field and far-field multi-slice reconstruction. a) - d) Near-field reconstructions of the four slices. e) - h) Far-field reconstructions of the same scan. The far-field reconstructions were run with the same distances and number of iterations. Only few reconstruction parameters were adapted, all other parameters were the same as used for the near-field reconstruction. The far-field reconstruction was carried out with a three times virtually enlarged illumination [123] and the propagation between the last slice and the detector was modeled with a fast Fourier transform. The slices were initialized in a different order (starting iteration for slice 1: 20, slice 2: 0, slice3: 50, slice 4: 80). The illumination was initialized as a gaussian beam with a curved wavefront (spherical wave with a radius of 0.63 mm), whereas it was flat for the near field reconstruction. f) The big inclusion of slice 1 casts a big shadow in the second slice in the far field reconstruction, while there is only a very faint shadow in the near field reconstruction (b). The same effect can be seen in slice 3, where a shadow from the particle of slice 4 remains in the far-field reconstruction, but is considerably weaker in the near-field reconstruction. Adapted from [140].

the separation of slices 3 and 4 does not appear to be perfect. The dark particle in the center of slice 3 appears as a white shadow in slice 4. The slice thickness seems to be close to the practical reconstruction limit. Hu *et al.* already describe that the actual thickness of the slices in X-ray NFP often has to be significantly bigger than the theoretical limit given by Eq. 3.9 [47]. However, applying Eq. 3.8 with the constant $c = 1$ seems to overestimate the limit for slice separation ($DOF = 102.6\,\mu m$).

We found that, in the case of hard X-ray NFP, the experimental geometry must be known much more precisely than in the case of FFP experiments. The reconstruction is very sensitive to inaccuracies in defocus and interslice distance, as these have a strong impact on the effective Fresnel number.

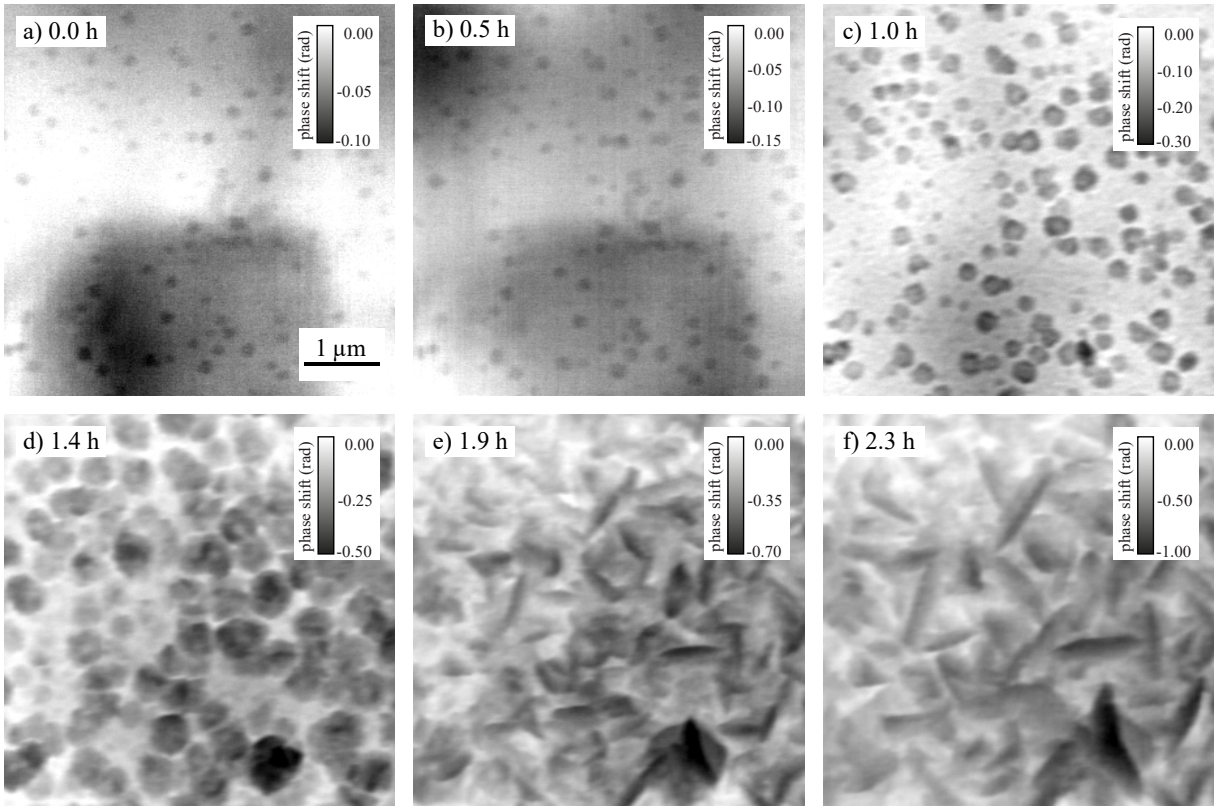

Figure 6.10: In-situ series corresponding to Fig. 6.8 a)-f) Show reconstructions of the inner side of the upstream window (slice 2) on which the Cu_2O nanocubes underwent a galvanic replacement reaction with Au. From d) onwards the reaction does not resemble the result of bench experiments anymore. The Au growth is much stronger than it would be seen in ex-situ experiments. Micrometer-long Au needles are visible on the polyimide foils at the end of the reaction (f). Adapted from [140].

Progression of beam damage induced Au growth

In the scans following the one shown in Fig. 6.8, beam damage overshadows the reaction progress. The increased photon flux in this high-resolution imaging series resulted in strongly increased growth of the Au particles compared to the expected result. The normal course of the reaction was overshadowed by beam induced growth of elemental Au on the foils (Fig. 6.10). This Au growth is driven by the reduction of $Au^{3+}_{(aq)}$ by solvated electrons or H-radicals and other reducing species, which are created through radiolysis by the X-ray beam. At 2.3 h after the reaction start, the entrance window is covered with gold. Micrometer-sized needles have formed. The average dose per projection was 5.86 MGy for this in-situ series. The scan after 2.3 h was the fifteenth scan after the start of the reaction, which corresponds to a cumulative dose at that point of 87.9 MGy. Compared to the low dose-rate series, the 16-times higher dose leads to significantly stronger growth of elemental gold through radiolytic synthesis on the polyimide foil.

In-situ imaging is a balancing act between spatial resolution and tolerable beam damage. Nevertheless, we have shown that NFP is competitive with FFP. Multi-slice NFP extends the

capabilities of the method to the imaging of optically thick specimens, making it attractive for in-situ imaging.

6.5 Conclusion

We demonstrated near-field multi-slice ptychography for in-situ imaging at high spatial resolution. This is the first in-situ X-ray NFP experiment with sub-50 nm spatial resolution.

In NFP, fewer scan points are needed for a given field of view compared to FFP, reducing the overhead time per scan to a minimum. Greater magnifications, which can be achieved by longer propagation distance, should enable larger illuminations without the loss of spatial resolution due to the large pixel size in the object plane in future experiments. Smaller detector pixels are another option to achieve smaller object pixel sizes. NFP with very large illuminations, brings the method closer to full-field imaging and thus offers a significant reduction in measurement time. This makes the method attractive and suitable for studying systems with much better time resolution.

With fully coherent flux at 4th generation synchrotron radiation sources, scan times of 1 min or less should be achievable for a field of view of comparable size to the results presented here.

MLLs have the highest *NA* for hard X-rays from all state-of-the-art X-ray optics, providing exceptionally small focus sizes in this photon energy regime. The MLLs allow NFP with large illuminations relatively close to the focus, making them ideal for compact setups like the one used here. The high *NA* of MLLs also leads to a shallow depth of field. In our experiment, this allowed multi-slice reconstructions with slices separated by 62.5 µm, which is the smallest distance demonstrated so far in X-ray NFP. Further, the intrinsic structure of MLL-based illumination eliminated the need for a diffuser, even for sparse samples such as nanoparticles.

We have shown that NFP is a competitive method for *in-situ* imaging applications that could find widespread application with fourth generation light sources, providing high temporal and spatial resolution.

For radiation-sensitive systems, in-situ near-field ptychography may be even a better choice than near-focus scanning with far-field ptychography. The dose rate can be significantly reduced with NFP. However, radiation damage is a process that involves the interaction of many factors, and aqueous systems are particularly challenging in this regard. Diffusion rates and concentrations of free radicals as a function of the size of the irradiating beam would need to be systematically studied. A combination of multiple measures might be needed for a reliable reduction of radiation damage in in-situ studies. The use of chemical inhibitors, such as radical scavengers, is worth exploring. The next chapter will compare different radical scavengers for reducing beam damage in X-ray studies of chemical reactions in aqueous solutions.

7 Radiation damage and use of scavengers in in-situ studies

This chapter examines the use of free radical scavengers to minimize beam damage during in-situ studies of galvanic replacement reactions using small-angle X-ray scattering and far-field multi-slice ptychography.

The small angle X-ray scattering experiment was conceived and conducted together with Jonas Voss, Maik Kahnt, and Cecilia Zito. Cecilia Zito further ran experiments in the laboratory beforehand to narrow down the list of potential scavengers. The imaging experiment was supported by Jonas Voss, Olga Vasylieva, Caterina Carus, Mattias Åstrand, Ulrich Vogt, and Andreas Schropp. The Cu_2O nanocube samples for the galvanic replacement reaction were pre-synthesized by Karolina Stachnik, Jonas Voss, and me. All data analysis of the experiments was carried out by me.

7.1 Introduction

In-situ studies of chemical reactions can provide valuable insights into reaction kinetics, intermediates, morphological evolution and more. Information not available in standard ex-situ methods, where particles might be washed away or agglomerate before their characterization, can be gathered. Further, products and intermediates are sometimes not stable over longer time and cannot be analyzed ex situ. But the in-situ measurement itself can potentially affect the synthesis. X-rays are a form of ionizing radiation, which can influence the sample system under study. The following chapter explores the use of radical scavengers to mitigate beam damage in in-situ studies of the galvanic replacement reaction of Cu_2O with Au.

When imaging the galvanic replacement reaction of Cu_2O nanocubes with Au in situ with X-rays, it can be seen that at first, the galvanic replacement reactions seem accelerated compared to bench experiments. At later stages, the Au nano-cages continue to grow beyond the expected size and in extreme cases a thick layer of gold grows on the polyimide foil in the illuminated area. The high resolution in-situ series described in Sec. 6.4 drastically illustrates how much the expected outcome of a reaction can be altered by the effect of ionizing radiation. This excessive growth of Au, beyond what is seen in ex-situ bench experiments, is what we define here as beam damage.

7.2 In-situ small angle X-ray scattering of Au nanoparticle growth

The radiolytic synthesis of Au particles in aqueous solutions with a gold precursor $(AuCl_4)^-_{(aq)}$ has been widely studied [61,71,73]. In these cases, the reaction solution was illuminated with ionizing radiation, mostly γ-rays, to cause the growth of Au particles.

$$AuCl^-_{4(aq)} + 3\,e^-_{(aq)} \longrightarrow Au^0 + 4\,Cl^-_{(aq)}$$
$$AuCl^-_{4(aq)} + 3\,H\cdot \longrightarrow Au^0 + 3\,H^+ + 4\,Cl^-_{(aq)}$$

In our case, this side reaction obstructs the clear observation of the reaction that we aim to study. For this reason, small angle X-ray scattering was used to monitor the growth of Au particles in the X-ray beam with different radical scavengers added. The X-ray beam was used both to measure and to cause the growth of the particles. In this first experiment only the radiolytic synthesis of the Au particles was studied. The most promising scavengers were subsequently tested in in-situ studies of the galvanic replacement reaction of Cu_2O nanocubes with Au.

7.2.1 Small angle X-ray scattering experiment

Propan-2-ol, ethanol and methanol were chosen as potential radical scavengers. They are applied to prevent beam damage in biological specimens [159–163]. In ex-situ tests in the laboratory the list of potential scavengers was narrowed down beforehand to those that did not significantly hinder the galvanic replacement reaction.

The SAXS experiment was carried out at the CoSAXS beamline at the fourth generation synchrotron light source MAX IV. The sample was placed at a distance of 36 m from the source in the experimental hutch [164]. With an Eiger2 4M detector (DECTRIS AG, Switzerland) at the end of a 18 m long vacuum tube, the beamline is optimized for good sampling of the relevant q-range in SAXS experiments. The experimental parameters are summarized in Table 7.1.

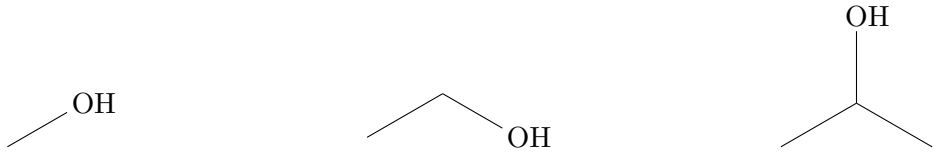

a) Methanol **b)** Ethanol **c)** Propan-2-ol

Figure 7.1: Structure of the tested scavengers

The in-situ reaction cell, described in more detail in [119], was assembled with two clean, empty polyimide windows (Kapton HN, DuPont de Nemours Inc.). Both windows were empty because the aim of this experiment was to study the radiolytic synthesis of gold in an aqueous solution, isolated from the influences of the galvanic replacement reaction. The cell was filled with 1.6 mL of Milli-Q ultrapure water with a resistivity of 18.2 MΩcm at 25 °C for the reference measurements. For the scavenger tests, 1.6 mL of the scavenger-water-solutions were filled in. The cell was then

Parameter	Reference	Scavenger tests
Scavenger	–	methanol, ethanol, propan-2-ol
Injection volume	100 µL	
Reaction solution	20 mmolar $HAuCl_4$	
Injection time	300 s	150 s
Photon energy	9.65 keV, 12.02 keV	9.65 keV
Exposure time	1 s × 1800 (0.1 µs break between exposures)	
Scan time	30 min	
Sample to detector distance	14.922 m	
Point of normal incidence on the detector (vertical, horizontal)	0.138 m, 0.020 m	
Detector rotation (x, y, z)	0 rad, 0 rad, 0 rad	

Table 7.1: Experimental parameters

mounted at the beamline, and a syringe pump was installed to infuse the reaction solution during the measurement. $HAuCl_4$ was used as an Au precursor. The reaction solution was prepared with a concentration of 20 mmolar $HAuCl_4$ in Milli-Q ultrapure water. The pH was adjusted to close to neutral with a 100 mmolar NaOH solution. The SAXS measurement and the injection were started at the same time. A volume of 100 µL of the reaction solution was infused with a syringe pump (PHD Ultra, Harvard Apparatus, USA) in the first minutes of the measurement and the reaction was monitored over 30 min. The exposure time was set to 1 s followed by a 0.1 µs break between exposures. The 2D-scattering data was azimuthally integrated for the data analysis. For a clear observation of the Au particle growth, any signal stemming from the in-situ cell windows and the aqueous solution had to be removed. The first ten seconds of each in-situ measurement were used for this background correction. In these initial ten seconds of the measurement the signal was attributed to the in-situ cell, the reaction solution, and other factors, but not the studied particle growth. The measured data was averaged over 10 s to reduce noise, which corresponds to a 10 × 1 s exposure.

7.2.2 Reference measurements without scavenger

SAXS measurements without any scavenger were performed at 9.65 keV and 12.02 keV, respectively. The measurement at 12.02 keV was performed slightly above the Au L_3 absorption edge, which is at 11.92 keV (see Fig. 7.2). The particle size evolution was determined with a Guinier analysis. The threshold for a small angle was set to $q < \frac{1.3}{R_g}$ in the analysis.

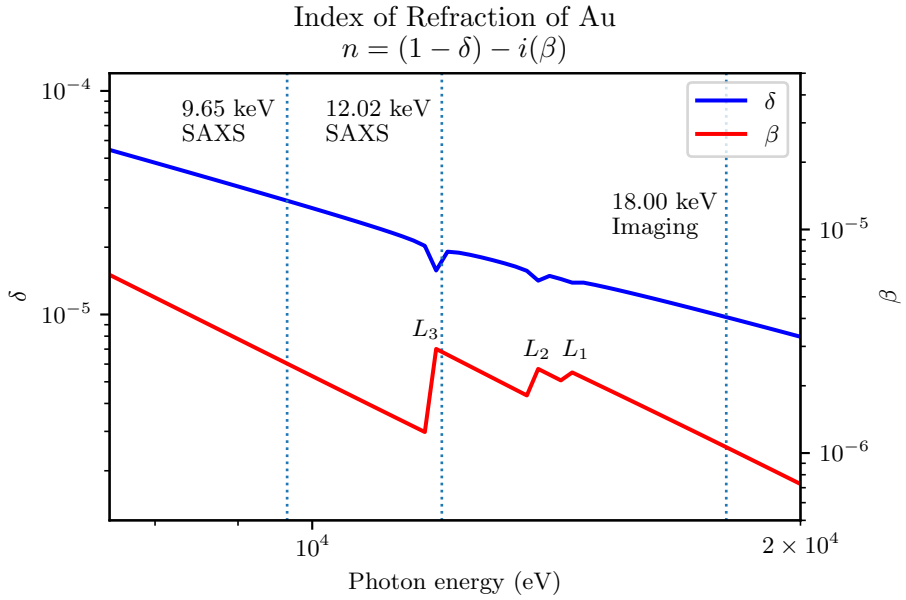

Figure 7.2: Refractive index of Au. Refractive index of Au for photon energies between 7.5 keV and 20.0 keV. Data was taken from Henke *et al.* [130]

Fig. 7.3 visualizes the normalized SAXS signal over time. No significant change was visible in the data over the first four minutes of the measurement. From four minutes onward, the growth of particles was clearly observed at both energies. The result of the particle size analysis is shown in Fig. 7.4.

In the measurement at 12.02 keV, the particles grow to a larger size than in the measurement at 9.65 keV. At 12.02 keV the particles reach a maximum radius of gyration of 54 nm after 30 min, at the same time at 9.65 keV the particles have a radius of gyration of 40 nm. Looking at the relative dose in both experiments, even though the measurement at 12.02 keV was conducted close to the L_3-absorption edge of Au, one can see that the dose was lower at the higher energy due to the reduced photon flux (see Table 7.2).

Photon energy		9.65 keV	12.02 keV
Photon flux		6×10^{10} photons/s	3×10^{10} photons/s
Attenuation length	Au	$0.25\,\mu m^{-1}$	$0.35\,\mu m^{-1}$
	H_2O	$5.7 \times 10^{-4}\,\mu m^{-1}$	$2.9 \times 10^{-4}\,\mu m^{-1}$
Relative Dose	Au	100 %	87.5 %
	H_2O	100 %	31.8 %

Table 7.2: Dose in the SAXS experiment

Considering only the water, this effect is even more pronounced – the dose at 12.02 keV is only a third of the dose at 9.65 keV. It might seem counter-intuitive that particles grow larger at lower dose, but these results are in line with observations on radiolytic synthesis of Au particles

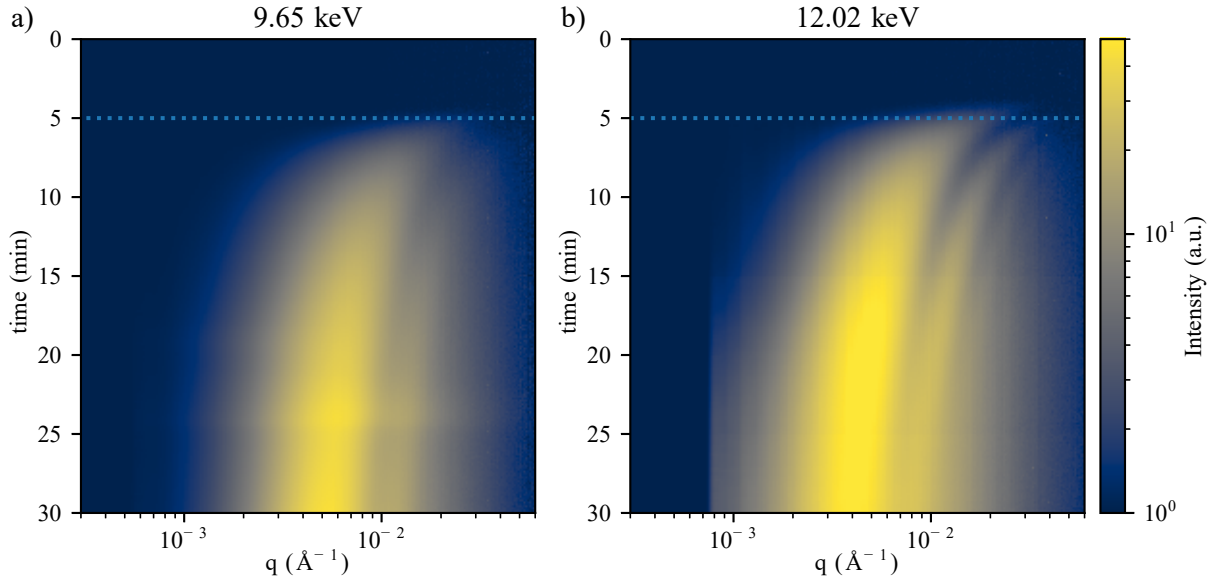

Figure 7.3: Reference SAXS without scavengers over time. a) and b) show the in-situ SAXS measurement normalized against the background at 9.65 keV and 12.02 keV, respectively. The intensity is encoded by the color. The injection was finished after 5 min, marked by the dashed line. At about the same time, first Au particles forming in the solution can be observed.

reported in the literature[71]. At higher dose smaller, more particles are expected to form, while at lower dose fewer, larger particles are to be expected. At higher dose and dose rate, the formation of more nuclei is expected, which leads to a faster local consumption of the metal precursor[71].

7.2.3 Comparison of scavengers

The scavenger tests were performed at 9.65 keV. The SAXS signal over time is shown in Fig. 7.5. The azimuthally integrated SAXS data without any background correction can be found in the appendix Fig. D.1. In the reference measurement without any scavenger, the growth of the Au particles was clearly visible. Shortly after the injection of the reaction solution finished at 2.5 min, a signal at high q was detected and particles of increasing size were measured in the following minutes. In the measurements with 10 vol.-% scavenger, for none of the alcohols significant changes beyond noise were detected. In the series with 3 vol.-%, propan-2-ol growth of particles became visible after ca. 3 min, but the signal was significantly weaker than in the reference measurement without a scavenger. For 3 vol.-% methanol, no changes were observed over the measured time frame. The result for 3 vol.-% ethanol lies in between propan-2-ol and methanol – there is a measurable signal, but it is weaker than for propan-2-ol.

The intensity over q with background normalization for all experimental conditions is plotted in Fig. 7.6. Here, the aforementioned trend becomes even more evident. The growth of Au particles in the beam seems to be reduced for all three scavengers. At lower volumetric concentrations, methanol completely prevented the growth of measurable particles, while some particle formation

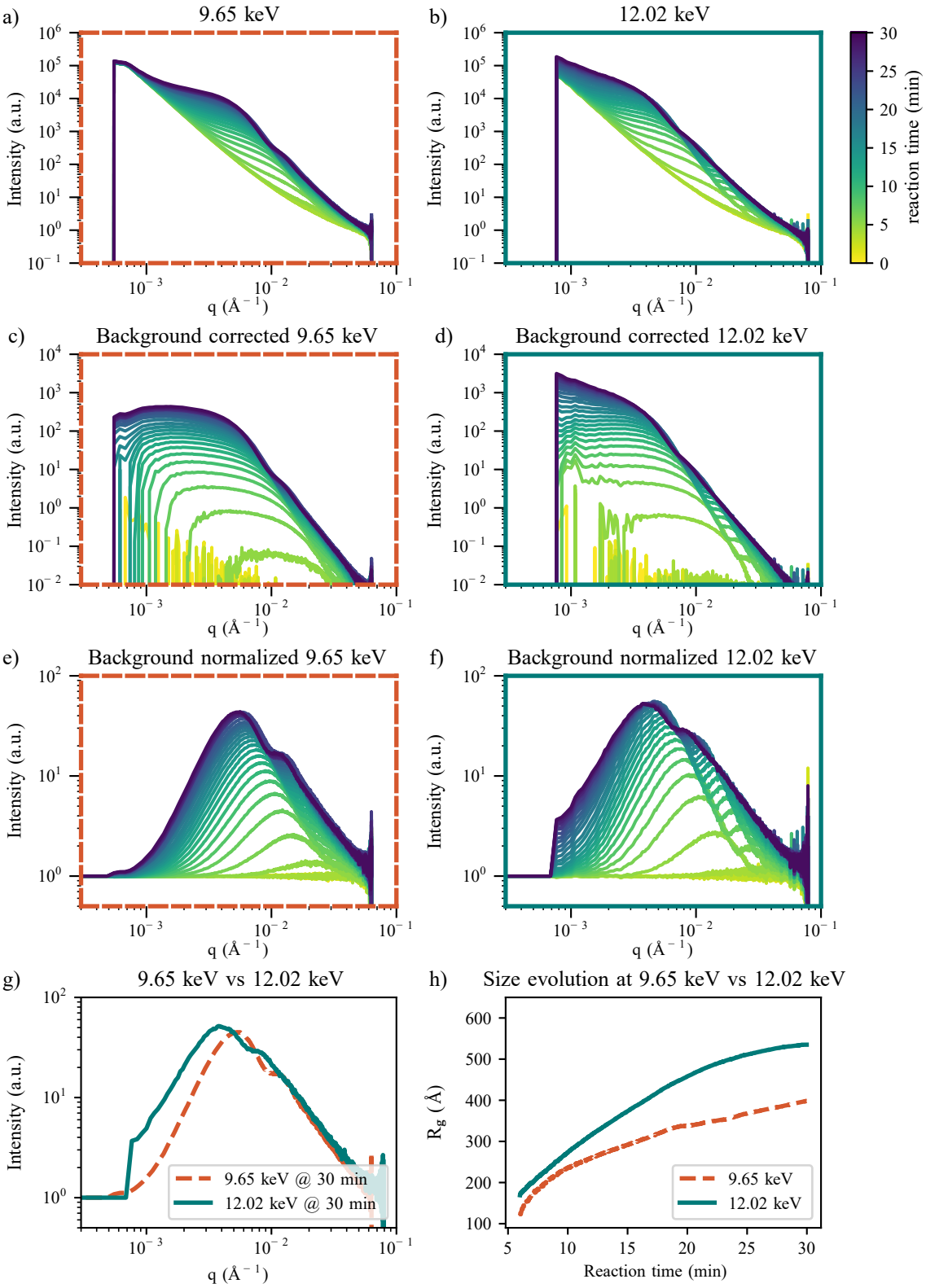

Figure 7.4: Reference SAXS without scavengers. a) and b) show the in situ SAXS measurement at 9.65 keV and 12.02 keV, respectively. The time is encoded by the color. c) and d) show the data with the background subtracted. e) and f) show the same measurements normalized against the first ten seconds of the measurement. A comparison of the two measurements after 30 min is shown in g). h) The particles size was calculated with a Guinier fit over the reaction time at both energies.

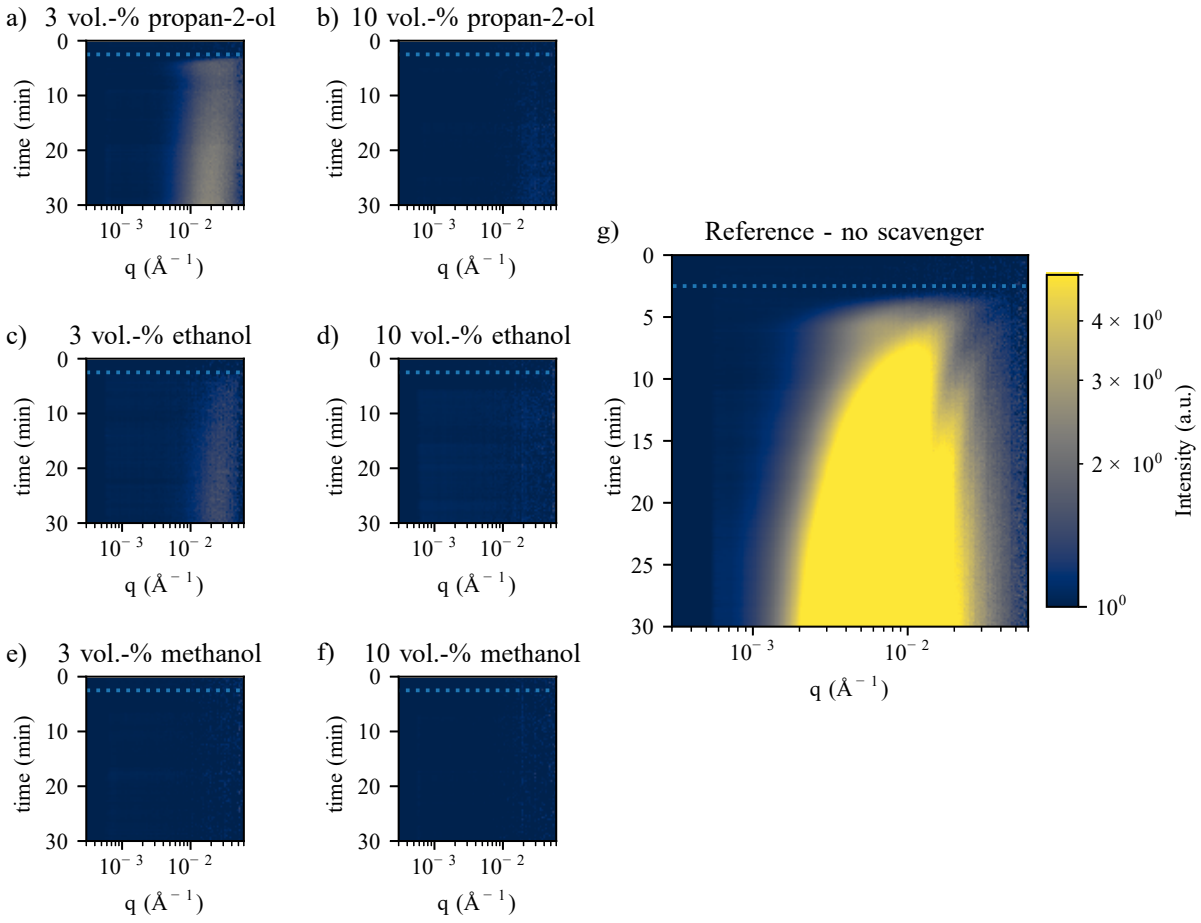

Figure 7.5: Scavenger comparison with SAXS over time. SAXS measurements of three different scavengers propan-2-ol a) and b), ethanol c) and d), and methanol e) and f) with a concentration of 3 vol.-% and 10 vol.-% each. The data was normalized against the respective background. g) shows the reference measurement without any scavenger. The intensity is encoded by the color. The injection was finished after 2.5 min, marked by the dashed line. At 10 vol.-% all scavengers prevent the growth of measurable particles. Methanol and ethanol show better performance at 3 vol.-% than propan-2-ol.

was observed for ethanol and even more so for propan-2-ol. Since the aim of this experiment was a qualitative comparison of scavengers in regard to their performance preventing the radiolytic synthesis of Au particles, an analysis of the particle size evolution was not attempted.

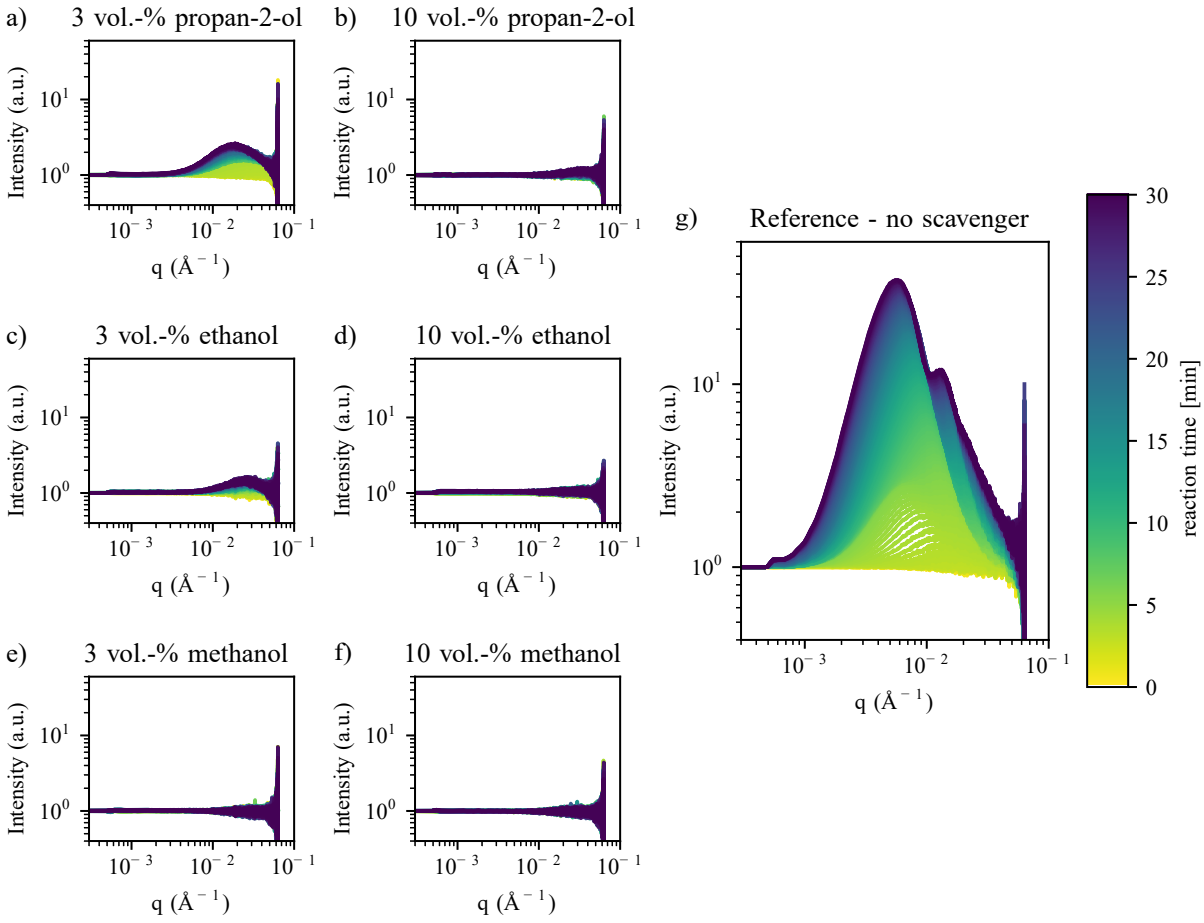

Figure 7.6: Scavenger comparison with SAXS. SAXS measurements of three different scavengers propan-2-ol a) and b), ethanol c) and d), and methanol e) and f) with a concentration of 3 vol.-% and 10 vol.-% each. g) shows the reference measurement without any scavenger. The data was normalized against the first ten seconds of the measurement. At 10 vol.-% all scavengers prevent the growth of measurable particles. Methanol and ethanol show better performance at 3 vol.-% than propan-2-ol.

7.3 In-situ far-field ptychography: Effect of beam damage and use of scavengers

In a second step the scavengers, which were evaluated with SAXS, were tested in a ptychographic far-field imaging experiment of the galvanic replacement reaction of cuprous oxide with gold.

$$1.5\,Cu_2O_{(s)} + AuCl_{4(aq)}^{-} + 3\,H_{(aq)}^{+} \rightarrow Au_{(s)} + 3\,Cu_{(aq)}^{2+} + 4\,Cl_{(aq)}^{-} + 1.5\,H_2O$$

7.3.1 Experiment

The experiment was carried out in the diffraction endstation (EH2) at the NanoMAX beamline at MAX IV [25]. The photon energy was set to 18.0 keV. The beamlines' standard KB mirror

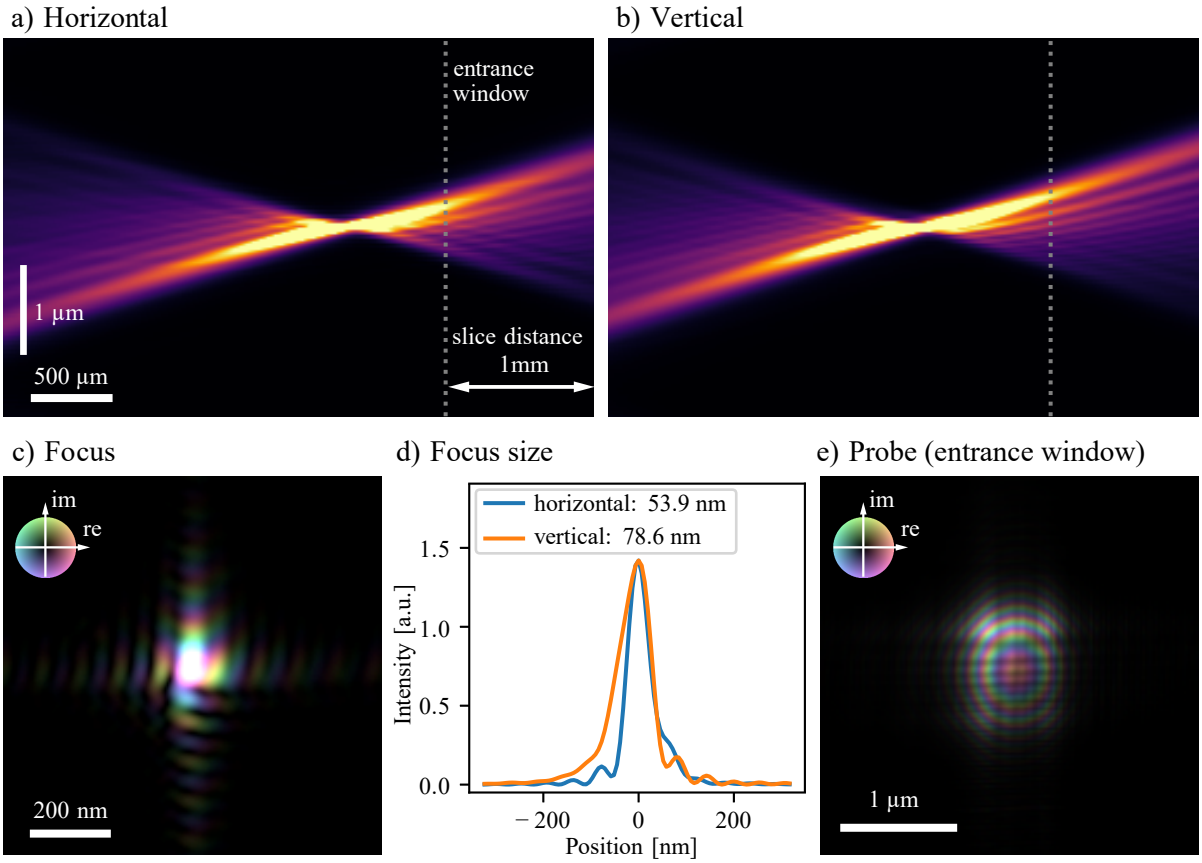

Figure 7.7: Beam characterization Horizontal (a) and vertical (b) beam caustic. The beam exhibits a slight astigmatism. The horizontal focus is shifted by 200 µm downstream with respect to the vertical one. c) shows the focal plane with the amplitude encoded by brightness and the phase indicated by hue. d) The focus size was determined to be 54 nm in horizontal and 79 nm in vertical direction (full width half maximum). e) shows the illuminating beam in the plane of the entrance window.

system was used, which created a focal spot size of $54 \times 79\,\mathrm{nm}^2$ at 47 m downstream of the source (Fig. 7.7).

A fermat spiral scanning pattern was chosen to avoid perfect grid artifacts in ptychography [124] (see Fig. 7.8). For all in-situ series, a 5 µm × 5 µm field of view was scanned with an average step size of 200 nm and an exposure time of 0.15 s. The entrance window of the in-situ cell was positioned 760 µm downstream of the X-ray beam focus. The illumination had a size of 1.1 µm (h) × 1.3 µm (v) in horizontal and vertical direction, respectively, in the sample plane.

The diffraction patterns were captured by an in-vacuum Eiger 1M detector (DECTRIS AG, Switzerland) located 3610 mm downstream of the sample.

In this experiment, in contrast to the SAXS experiment, concentrations of 1 M and 2 M of the scavengers were used. To enable a comparison of the results, a conversion from molar to volumetric concentrations is given in Table 7.3. A reference measurement without any scavenger was carried out and tests with 1 M methanol, 1 M ethanol, 1 M propan-2-ol, and 2 M propan-2-ol were performed under the same reaction conditions.

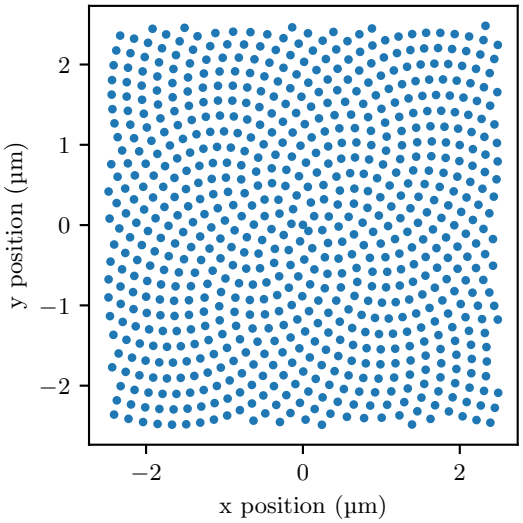

Figure 7.8: Fermat spiral scanning pattern. A fermat spiral scanning pattern was used for the scans to avoid perfect grid artifacts in the ptychographic reconstruction.

For this experiment we again employed, as in Ch. 6, the synthetic procedure and the in-situ reactor reported by Grote *et al.*[119] A polyimide foil with a thickness of 125 µm (Kapton HN, DuPont de Nemours Inc.) containing previously grown Cu_2O nanocubes was utilized as the entrance window of the in-situ reactor, while a clean foil was used for the exit window. The reactor was filled with 1.4 mL Milli-Q ultrapure water with a resistivity of 18.2 MΩcm at 25 °C. A syringe pump (PHD Ultra, Harvard Apparatus, USA) was used to dose a 20 mmolar aq. $HAuCl_4$ solution through a polytetrafluorethylene tube into the reactor. The injection rate was set to 200 µL h^{-1}, and the reaction was continuously scanned over two hours until the target volume of 400 µL was reached. The reaction was carried out at room temperature. Benzyl alcohol ($\geq$ 99.0%), $Cu(acac)_2$ (99.99 %) and $HAuCl_4 \cdot 3H_2O$ ($\geq$ 99.9% trace metal basis) were purchased from Sigma-Aldrich, and ethanol (absolute) for washing from VWR. All chemicals were used without further purification.

Scavenger	1 M	2 M	3 vol.-%	10 vol.-%
Methanol	4.05 vol.-%	8.10 vol.-% (not tested)	0.74 M	2.47 M
Ethanol	5.84 vol.-%	11.68 vol.-% (not tested)	0.51 M	1.71 M
Propan-2-ol	7.65 vol.-%	15.29 vol.-%	0.39 M	1.31 M

Table 7.3: Conversion volumetric concentration to molar and vice versa

The ptychograms of the in-situ series were reconstructed, modelling the entrance and the exit window as individual slices with 1 mm propagation distance between them. The 3PIE[51] reconstruction algorithm implemented in the in-house software *ptycho* was used for the data analysis. The reconstruction was run for 1000 iterations. An upsampling factor[123] of three was used and position refinement[129] was turned on after iteration 500, with intervals of every 50

iterations. The update weight α for the object was set to 1.0 and 0.5 was used for the weight β for the illumination function. The spatial resolution was determined at the example of the scan without any scavenger after 21 min with Fourier ring correlation to be 40 nm. In earlier scans, with lower phase shift, the spatial resolution is expected to be slightly worse.

7.3.2 In-situ ptychography of the galvanic replacement reaction of Cu_2O with Au using scavengers

For the galvanic replacement reaction of Cu_2O nanocubes with Au, a transition from solid cubes to hollow cages is expected[119] as it was already covered in Ch. 6 (see Fig. 6.5a). In areas which are not exposed to ionizing radiation, this morphological evolution can be observed (see Ch. 6 Fig. 6.7a and b). Fig. 7.9 shows the galvanic replacement reaction studied in-situ with different scavengers added.

Only the first hour of the reaction is displayed here, since severe growth induced by radiation damage overshadows any morphological changes stemming from the galvanic replacement reaction at later stages. The photon flux in this experiment was one order of magnitude higher than in the high-resolution near-field ptychography experiment, described in Sec. 6.4. The surface dose per scan was six times higher with a field of view of only 39 % of the size of the near-field scan. The parameters considered for the dose are listed in Table 7.4. The dose calculation was carried out by Karolina Stachnik.

Parameter	
Probe area	$1.6\,\mu m^2$
Flux per scan point	6.8×10^8 photons/s
Dose rate per scan point	5.53 MGy/s
Dose per scan	34.7 MGy
Number of scans	23
Cumulative dose	791 MGy

Table 7.4: Dose in the ptychography experiment

Considering the high dose, significant beam damage was expected in this in-situ measurement series. Without visible beam damage, it would have been difficult to evaluate the effect of scavengers on the degree of damage. A qualitative comparison of the five in-situ series indicates that methanol and ethanol at a concentration of 1 M do not mitigate radiation damage. Conversely, increased phase shift and larger particles, which we ascribe to beam damage, become evident at an earlier stage than in the reference measurement without any scavenger. Looking at the exit window, where one would not expect particles to attach or grow under ex-situ conditions, this impression is further confirmed (see Fig. 7.10). From 11 min onward, particles grow on the

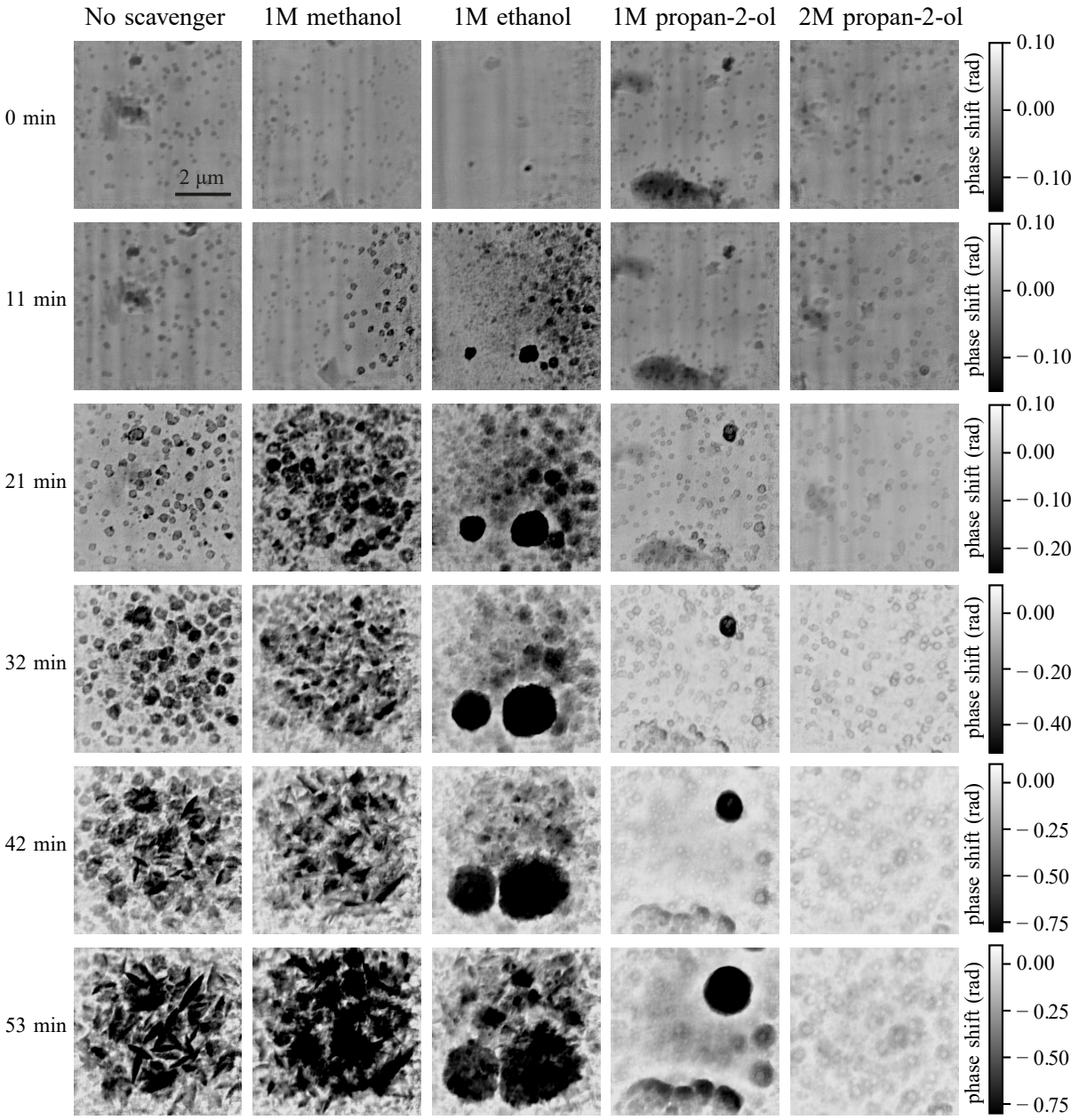

Figure 7.9: Scavenger comparison with far field ptychography. Comparison of three different scavengers ethanol, methanol, and propan-2-ol with a concentration of 1 M and, additionally, propan-2-ol with a concentration of 2 M. The left column shows the reference measurement without any scavenger.

backside of the reaction cell, quickly forming a thick layer, while this becomes visible for the reaction without any scavenger only between 21 min and 32 min onward.

The height profiles of the gold structures on the entrance and exit window of the in-situ cell after 2 h of the reaction were measured with laser-scanning microscopy. As visualized in Fig. 7.11, the structure on the front side grew considerably taller when methanol or ethanol were added to the solution than without a scavenger. This difference is less pronounced on the back side of the cell, but the structures are still slightly taller than in the reference case.

Propan-2-ol seems to have no negative impact on the progression of beam damage, while if any, only a mild positive effect can be observed for a concentration of 1 M (Fig. 7.9). In the reaction with 2 M propan-2-ol, the scan taken at 32 min after injection start is the closest to results of ex-situ experiments. After 53 min the particles grew larger than it would be the case if solely the galvanic replacement reaction took place, but in comparison to the other reaction conditions, it is the only one where the individual nanocages are still visible.

On the backside of the cell (Fig. 7.10) a similar trend can be observed, the reference without a scavenger and 1 M propan-2-ol look relatively similar, with a bit lower phase shift for 1 M propan-2-ol. 2 M propan-2-ol is the reaction where the least deposition on the back side is seen. The height profiles measured after 2 h of the reaction show a similar height for the reference and the 2 M propan-2-ol. However, the base level is less well defined in case of the 2 M propan-2-ol foil. If this were corrected for, the height would be below the one measured in the reference case. An evaluation of the front window of the 1 M propan-2-ol is not possible, because of a big scratch on the foil. On the back side of the reaction cell, the gold structure grew less tall for both propan-2-ol experiments than in the case without any scavenger.

An interesting effect can be observed on the entrance foil in the series with 1 M ethanol and 1 M propan-2-ol (Fig. 7.9). The growth of Au seems to be more pronounced in certain areas, where large round strongly phase shifting structures grow. The center of these large structures is already exhibiting a stronger phase shift in the early scans of the reaction series. These features in the early scans could be inclusions in the polyimide foil (see appendix Fig. C.4) close to or at the surface of the foil. Inclusions in the polyimide foils stem from additives added as slipping agents in the production process of the foils and are reported to be dicalcium phosphate [132] or calcium carbonate [133]. The particles could act as nucleation centers for Au and in the following lead to an increased Au deposition. The observations in this in-situ imaging experiment differ from the ones that one might have expected based on the in-situ SAXS results. This mismatch will be covered in the next section.

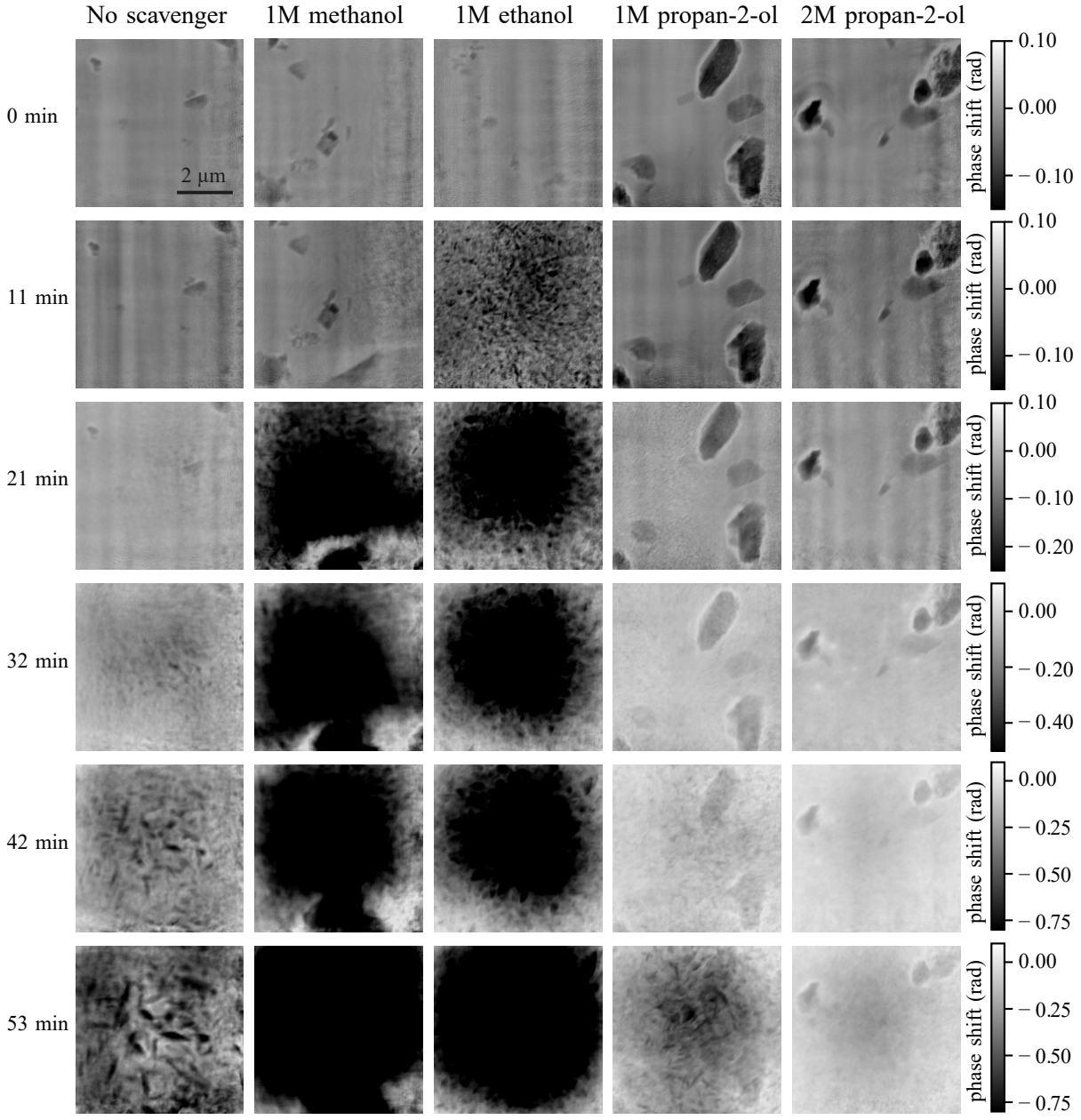

Figure 7.10: Comparison of Au deposition on the exit window for different scavengers. Backside of the reaction cell, which in ex-situ bench experiments would remain empty over the course of the reaction.

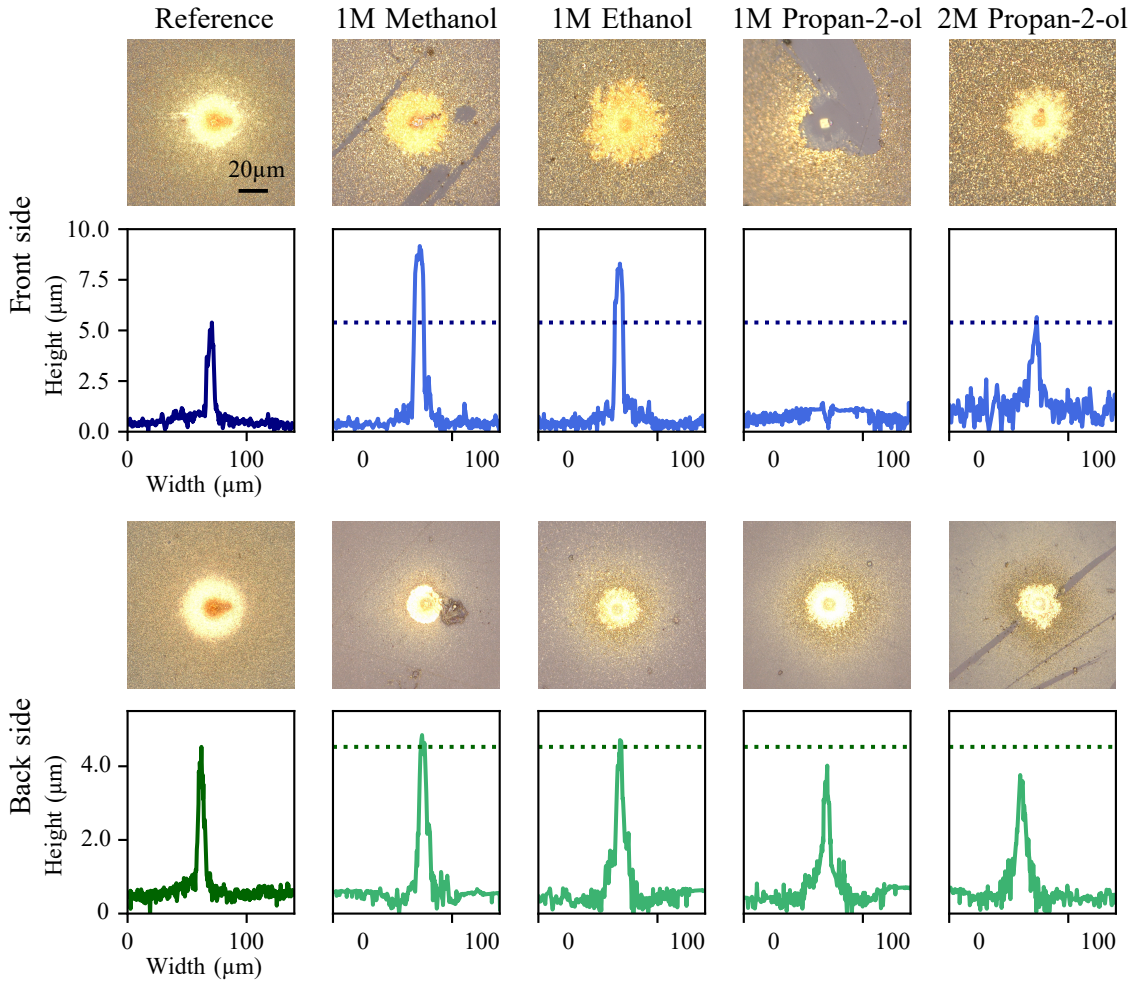

Figure 7.11: Comparison of the profile of the gold structures that grew during the in-situ series. The columns show light microscopy images of the front and back polyimide foils after the reaction with the respective scavenger and corresponding height profiles of the gold structure. The dashed line in the height profiles indicates the height of the structure in the reference measurement without any scavenger. For the methanol and ethanol reactions, the structure grew taller than in the reference reaction. The front side of the 1M propan-2-ol polyimide foil is severely scratched, which does not allow for acquisition of meaningful data on the height profile. The 2M propan-2-ol reaction resulted in a structure of similar height compared to the reference one on the front side. On the back side of the reaction cell, the height of the gold structure is decreased for the 1M propan-2-ol and even more decreased for the 2M propan-2-ol reaction. The height profiles and light microscopy images were acquired with a Keyence VK-X110 microscope.

7.4 Discussion

First, we will summarize the results from the SAXS and the ptychography experiment in Table 7.5. It stands out that methanol and ethanol performed very differently in the SAXS compared to the ptychographic experiment. While they effectively prevented the growth of Au particles in the SAXS experiment, an increased growth was witnessed in the ptychography experiment. The results for propan-2-ol, however, match well in both experiments.

Scavenger	SAXS	Ptychography
Methanol	+++	– –
Ethanol	++	– –
Propan-2-ol	+	+

Table 7.5: Qualitative evaluation of the performance of scavengers in their capability to minimize radiation induced growth of Au particles in the SAXS and ptychography experiment. A + symbolizes less growth of Au compared to the reference measurement without a scavenger, a – stands for increased growth.

Before discussing the performance of methanol and ethanol further, we should consider the differences between the two experiments:

- **Photon energy:** The SAXS experiment was carried out at a photon energy of 9.65 keV, the ptychography experiment at 18.0 keV.
- **Photon flux:** The photon flux was significantly higher in the SAXS experiment.
- **Focusing:** The beam was focused with KB-mirrors for the ptychography experiment, while no lenses were used in the SAXS experiment.
- **Detected signal:** SAXS data reveals the size evolution of particles in solution, while the ptychography experiment studied Au growth on the surface of the foils.
- **Detection limit:** In the SAXS data, particles of less than 20 nm diameter were detected, while the spatial resolution in the ptychography experiment of 40 nm would not have allowed for this.
- **Injection rate and volume:** In the SAXS experiment, 100 µL of the reaction solution were injected with an injection rate of 1200 $\mu L\,h^{-1}$. In the ptychographic experiment, the injection rate was set to 200 $\mu L\,h^{-1}$ and a total volume of 400 µL was injected.
- **Scavenger concentration:** In the SAXS experiment, the scavengers were tested with concentrations of 10 vol.-% and 3 vol.-%, while concentrations of 1 M and 2 M were used in the ptychography experiment.
- **Reaction:** The SAXS-experiment was designed as a pre-study to evaluate the capability of the scavengers to prevent radiolytic synthesis of Au from a reaction solution containing $HAuCl_4$. For this reason, two clean polyimide windows were used. In the ptychography experiment, one foil was covered with pre-synthesized Cu_2O nanocubes to evaluate the performance of the scavengers when studying a galvanic replacement reaction with Au.

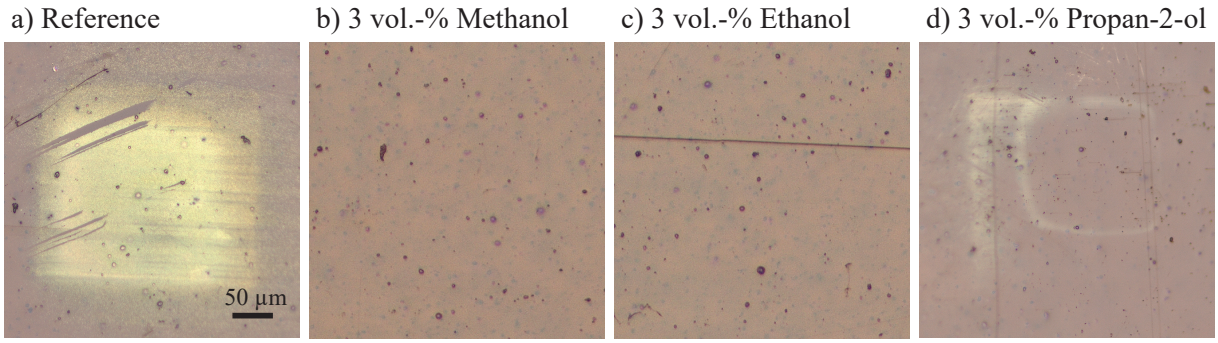

Figure 7.12: Entrance window of the in-situ cell in the SAXS experiment. a) shows the illuminated area of the foil used in the reference experiment without any scavenger. For the foils of the methanol b) and ethanol c) experiment it was impossible to locate an illuminated area. d) shows the entrance foil of the 3 vol.-% propan-2-ol measurement.

One possible explanation for the different results of the scattering and imaging experiments is that SAXS tracks homogeneous nucleation in the solution while ptychography studies heterogeneous nucleation and subsequent particle growth on the surface. To evaluate this option, we take a look at the polyimide foils that were mounted in the in-situ cell during the SAXS experiment with 3 vol.-% scavenger under the light microscope (see Fig. 7.12). On the foil from the measurement taken without a scavenger, Au deposition in the illuminated area is clearly visible. It was not possible to locate any formation of an Au layer on the foils from the methanol and ethanol trials. If, as in the imaging experiment, the growth on the surface was to increase compared to the reference, the area should be easily detectable. In case of 3 vol.-% propan-2-ol, some Au can be observed on the foil, but considerably less than in the reference case. This trend matches well with the results obtained from the SAXS data. Therefore, we can rule out this explanation for the contradictory results.

The next point that we will evaluate is the scavenger concentration. The concentrations were not exactly the same in both experiments. 1 M methanol corresponds to 4.05 vol.-% methanol (see Table 7.3), which is not far of the 3 vol.-% tested with SAXS. 1 M ethanol equals 5.84 vol.-% and 1 M propan-2-ol equals 7.65 vol.-%, both of them lie in between the 3 vol.-% and 10 vol.-% that were tested with SAXS. It is for this reason unlikely that these differences in scavenger concentration caused the different results.

Radiolysis has been reported for methanol, ethanol and propan-2-ol under γ-ray irradiation [165,166]. The difference in photon energy and photon flux might have influenced the probability of radiolysis for the different alcohols.

The other differences in the experiments cannot be evaluated this easily. A repetition of the experiment with fewer differences and further analysis would be needed to get to a definite answer.

Methanol and ethanol

Methanol and ethanol have been studied as scavengers with biological samples [159,161–163]. In biological systems, oxidizing agents are the ones more critical to beam damage and therefore OH· scavenging is most relevant in this case. Ethanol and methanol are both capable to effectively scavenge OH·, but less suited when it comes to H· and solvated electrons. For methanol under UV light, it was reported that also H· can be scavenged, but to a much smaller degree compared to OH· [167].

$$\mathrm{OH\cdot + H_3C{-}OH \longrightarrow HO{-}C^{\cdot}H_2 + H_2O}$$
$$\mathrm{H\cdot + H_3C{-}OH \longrightarrow HO{-}C^{\cdot}H_2 + H_2}$$

When we consider beam damage as any difference between the reaction process ex situ and the reaction under X-ray illumination, there are two main factors that have to be considered: Sutter *et al.* proposed for the galvanic replacement reaction of Ag with Pd that OH-radicals could lead to a direct oxidation of silver by OH-radicals circumventing the reduction of $(PdCl_4)^{2-}$ [138]. Transferring this to our reaction of Cu_2O with Au we get

$$\mathrm{Cu_2O_s + 2\,OH\cdot + 2\,H^+_{aq} \longrightarrow 2\,Cu^{2+}_{aq} + H_2O}$$

The result would be an increased dissolution of Cu^{2+}. The second part of the reaction, the reduction of Au^{3+}, can be impacted by radiation damage as well. Solvated electrons and H-radicals, products of the hydrolysis, can reduce Au^{3+}.

$$\mathrm{Au^{3+}_{aq} + 3\,e^-_{aq} \longrightarrow 3\,Au_s}$$
$$\mathrm{Au^{3+}_{aq} + 3\,H\cdot \longrightarrow 3\,Au_s + 3\,H^+}$$

The increased growth of Au that is seen on both foils of the reaction cell indicates that the reduction of gold ions by hydrolysis products is quite strong. However, ethanol and methanol are not well suited to scavenge solvated electrons and H-radicals. On the contrary, the scavenging of OH-radicals by them could lower the probability for recombination events and in this way facilitate this side reaction. In radiolytic synthesis of gold nanoparticles OH-scavengers are in some cases applied to increase the yield of the reaction [71]. To conclude, ethanol and methanol cannot be used to mitigate beam damage in in-situ experiments of the galvanic replacement reaction of Cu_2O with Au and the experimental X-ray imaging results confirm this. Further research is needed to explain their performance in the small angle X-ray scattering experiment.

Propan-2-ol

Like methanol and ethanol, propan-2-ol is mainly used as a hole scavenger. Propan-2-ol has been applied as a OH· scavenger in an in-situ liquid-cell TEM study of a galvanic replacement reaction of Ag with Pd, which reduced the, compared to bench experiments, accelerated oxidation of Ag [138].

Propan-2-ol primarily scavenges OH· and H· radicals.

$$\mathrm{OH\cdot + H_3C{-}CH(-OH){-}CH_3 \longrightarrow H_3C{-}C\cdot(-OH){-}CH_3 + H_2O}$$
$$\mathrm{H\cdot + H_3C{-}CH(-OH){-}CH_3 \longrightarrow H_3C{-}C\cdot(-OH){-}CH_3 + H_2}$$
$$\mathrm{OH\cdot + H_3C{-}C\cdot(-OH){-}CH_3 \longrightarrow H_3C{-}C(=O){-}CH_3 + H_2O}$$

During this process, acetone can be formed. Acetone is able to scavenge solvated electrons and $H\cdot$. radicals[62,168]

$$\mathrm{H\cdot + H_3C{-}C(=O){-}CH_3 \longrightarrow H_3C{-}C\cdot(-OH){-}CH_3}$$
$$\mathrm{H\cdot + H_3C{-}C(=O){-}CH_3 \longrightarrow H_3C{-}C(=O){-}C\cdot H_2 + H_2}$$
$$\mathrm{e^- + H_3C{-}C(=O){-}CH_3 \longrightarrow (H_3C{-}C(=O){-}CH_3)^-}$$

Solvated electrons and $H\cdot$ are the radical species most relevant for the beam damage that we try to omit. The combination of OH-radical and H-radical scavenging by propan-2-ol with the ability of electron scavenging of the formed acetone explains the effect of propan-2-ol addition seen in both experiments well. In future experiments, the use of acetone as a scavenger should be considered.

Interestingly, propan-2-ol has been reported to increase the yield in radiolytic synthesis of Au nanoparticles with γ-rays[71]. But for the radiolytic synthesis with X-ray radiation, Wang *et al.* reported a reduced yield[73]. Their experiment was carried out at a photon energy range comparable to the ones used in the presented SAXS and imaging experiment.

7.5 Conclusion

Methanol, ethanol and propan-2-ol were tested as radical scavengers. All three scavengers reduced the radiolytic synthesis of gold nanoparticles observed in a SAXS experiment at a photon energy of 9.65 keV. While methanol and ethanol were not suited to mitigate beam damage in an in-situ imaging experiment of Cu_2O with Au, the addition of propan-2-ol slowed the excessive growth of Au significantly down. In future experiments, acetone could be considered as a potential scavenger to study galvanic replacement reactions in aqueous solutions closer to ex-situ conditions. Due to its ability to scavenge both solvated electrons and H-radicals, acetone might be even better suited than propan-2-ol.

8 Summary and Outlook

In this study, we explored strategies to advance in situ hard X-ray imaging of chemical reactions. We developed methods to enhance the spatial and temporal resolution of in-situ X-ray imaging and examined measures to minimize radiation damage.

The development of stereo ptychography led to an improvement in depth sensitivity by more than one order of magnitude compared to single-beam ptychography. Two perspectives of the sample were obtained with a single scan by utilizing two inclined X-ray beams. In this way, a high temporal and lateral resolution was maintained. The combination of stereo X-ray ptychography and multi-slicing provides depth information across different length scales. Quantitative phase images can be recovered for layers separated by 480 nm as well as 400 µm. Studies that rely on short acquisition times, particularly in-situ or operando experiments, can greatly benefit from stereo ptychography. This technique has the unique ability to capture a three-dimensional impression of a sample in a single scan. With in-situ stereo ptychography, it was possible to remove particles that were obscuring a clear view of the nanoparticle growth from the reconstructions. These particles were too close to the layer of interest to remove them with established methods like multi-slicing.

The use of multilayer Laue lenses for near-field ptychography enabled in-situ imaging with a lateral resolution of 30 nm in the nanoparticle plane. Leveraging the high numerical aperture of multilayer Laue lenses (MLLs), the method achieves small focus sizes, a shallow depth of field, and needs fewer scan points, making it suitable for studying dynamic systems with improved temporal resolution. This demonstration of multi-slice near-field ptychography for in-situ imaging was the first of its kind, achieving unprecedented lateral and depth resolution in hard X-ray near-field multi-slice ptychography. For radiation-sensitive systems, in-situ near-field ptychography may be the superior option compared to near-focus scanning with far-field ptychography. In near-field ptychography, the extended illumination leads to a significantly reduced dose rate. However, this alone does not sufficiently reduce radiation damage, and a combination of measures might be needed.

Radical scavengers can eliminate products of hydrolysis caused by X-ray irradiation from reaction solutions and thus reduce radiation damage. Methanol, ethanol and propan-2-ol were tested and all three scavengers effectively reduced the yield of the radiolytic synthesis of gold nanoparticles observed in a small angle X-ray scattering experiment. However, methanol and ethanol were incapable of mitigating beam damage during an in-situ imaging experiment of the galvanic replacement reaction of Cu_2O with Au. The addition of propan-2-ol, on the other hand, significantly slowed the excessive growth of Au. Due to its ability to scavenge solvated

electrons and H-radicals, acetone could be considered as a potential scavenger to study galvanic replacement reactions in aqueous solutions closer to ex-situ conditions in future experiments.

With the rise of fourth-generation synchrotron radiation sources, the available coherent flux increases dramatically. To take full advantage of this, we need optimized X-ray imaging microscopy techniques.

The newly developed stereo ptychography opens up the opportunity to capture large areas of a sample (up to millimeters square) with multiple perfectly correlated perspectives at fourth-generation sources. Taking advantage of the higher coherence length, the individual lenses for each beam could be illuminated coherently. In this way, the beams could be modelled as a single illumination with a high numerical synthetic aperture, which could potentially also improve the lateral resolution. This would decouple the achievable resolution from any restrictions introduced by less performative X-ray lenses through a synthetic numerical aperture.

With the increased coherent photon flux at fourth generation sources, only very short exposure times are needed in high-resolution imaging. Overhead times in scans and usage of memory become even more relevant. Near-field ptychography perfectly addresses these needs. Fewer scan points are needed, resulting in a lower impact of overhead time for motor movement between scan points and fewer diffraction patterns that have to be saved. The use of multilayer Laue lenses allows for unprecedented spatial resolution in hard X-ray near-field imaging.

Radiation damage is now a relevant factor even for samples, which were so far considered radiation hard. In some cases, trade offs between desired spatial resolution and the dose that the sample can withstand have to be made. Wherever applicable cryocooling should be considered or chemical inhibitors, like radical scavengers, have to be introduced. In other cases, flow cells might sufficiently limit radiation damage, where radical species are continuously removed from the imaged area. Radiation-damage-free X-ray imaging might only be achievable with a diffraction before destruction approach, utilizing single shot techniques.

Fourth generation sources provide an opportunity to image chemical reactions with unprecedented spatial and temporal resolution. By accounting for beam-induced effects and taking the relevant measures, we can gain invaluable insights into the morphological evolution of nanoparticles.

Bibliography

[1] A. K. Pearce, T. R. Wilks, M. C. Arno, and R. K. O'Reilly, "Synthesis and applications of anisotropic nanoparticles with precisely defined dimensions," *Nature Reviews Chemistry*, vol. 5, pp. 21–45, 11 2020.

[2] Z. Zhang, R. Song, T. Cao, and W. Huang, "Morphology-dependent structures and catalytic performances of Au nanostructures on Cu_2O nanocrystals synthesized by galvanic replacement reaction," *Journal of Energy Chemistry*, vol. 25, pp. 1086–1091, 11 2016.

[3] H.-G. Liao, L. Cui, S. Whitelam, and H. Zheng, "Real-Time Imaging of Pt_3Fe Nanorod Growth in Solution," *Science*, vol. 336, pp. 1011–1014, 5 2012.

[4] J. J. D. Yoreo, "In-situ liquid phase TEM observations of nucleation and growth processes," *Progress in Crystal Growth and Characterization of Materials*, vol. 62, pp. 69–88, 6 2016.

[5] W. Wang, H. Yan, U. Anand, and U. Mirsaidov, "Visualizing the Conversion of Metal–Organic Framework Nanoparticles into Hollow Layered Double Hydroxide Nanocages," *Journal of the American Chemical Society*, vol. 143, pp. 1854–1862, 2 2021.

[6] N. Ortiz Peña, D. Ihiawakrim, S. Creţu, G. Cotin, C. Kiefer, S. Begin-Colin, C. Sanchez, D. Portehault, and O. Ersen, "In situ liquid transmission electron microscopy reveals self-assembly-driven nucleation in radiolytic synthesis of iron oxide nanoparticles in organic media," *Nanoscale*, vol. 14, pp. 10950–10957, 2022.

[7] E. A. Sutter and P. W. Sutter, "In situ liquid cell electron microscopy of Ag–Au galvanic replacement reactions," *Nanoscale*, vol. 9, pp. 1271–1278, 2017.

[8] J. W. Goodman, *Introduction to Fourier Optics*. Roberts and Company Publishers, 3 ed., 2005.

[9] C. Jacobsen, *X-ray microscopy*. Cambridge University Press, 1 2019.

[10] J. Als-Nielsen and D. McMorrow, *Elements of Modern X-Ray Physics*. John Wiley & Sons, 2000.

[11] P. Willmott, *An introduction to synchrotron radiation : techniques and applications*. John Wiley & Sons, Inc., 2019.

[12] E. Hecht, *Optik*. De Gruyter, 7 ed., 2018.

[13] R. F. Mould, *A century of x-rays and radioactivity in medicine : with emphasis on photographic records of the early years*. Institute of Physics Publishing, 1993.

[14] A. Pogany, D. Gao, and S. W. Wilkins, "Contrast and resolution in imaging with a microfocus x-ray source," *Rev. Sci. Instrum.*, vol. 68, pp. 2774–2782, 7 1997.

[15] M. Berger, J. Hubbell, S. Seltzer, J. Chang, J. Coursey, R. Sukumar, D. Zucker, and K. Olsen, "XCOM: Photon Cross Sections Database," *NIST Standard Reference Database 8 (XGAM)*, 2010.

[16] C. M. Jeffries, J. Ilavsky, A. Martel, S. Hinrichs, A. Meyer, J. S. Pedersen, A. V. Sokolova, and D. I. Svergun, "Small-angle X-ray and neutron scattering," *Nature Reviews Methods Primers*, vol. 1, p. 70, 10 2021.

[17] A. G. Kikhney and D. I. Svergun, "A practical guide to small angle X-ray scattering (SAXS) of flexible and intrinsically disordered proteins," *FEBS Letters*, vol. 589, pp. 2570–2577, 9 2015.

[18] T. Li, A. J. Senesi, and B. Lee, "Small Angle X-ray Scattering for Nanoparticle Research," *Chemical Reviews*, vol. 116, pp. 11128–11180, 9 2016.

[19] C. J. Gommes, S. Jaksch, and H. Frielinghaus, "Small-angle scattering for beginners," *Journal of Applied Crystallography*, vol. 54, pp. 1832–1843, 12 2021.

[20] W. C. Röntgen, *Eine neue Art von Strahlen. Vorläufige Mittheilung*. Verlag und Druck der Stahel'schen K. Hof- und Universitäts-Buch- und Kunsthandlung, 2 ed., 1896.

[21] G. E. Ice, J. D. Budai, and J. W. L. Pang, "The Race to X-ray Microbeam and Nanobeam Science," *Science*, vol. 334, pp. 1234–1239, 12 2011.

[22] P. Kirkpatrick and A. V. Baez, "Formation of Optical Images by X-Rays," *Journal of the Optical Society of America*, vol. 38, p. 766, 9 1948.

[23] J. Yamada, S. Matsuyama, I. Inoue, T. Osaka, T. Inoue, N. Nakamura, Y. Tanaka, Y. Inubushi, T. Yabuuchi, K. Tono, K. Tamasaku, H. Yumoto, T. Koyama, H. Ohashi, M. Yabashi, and K. Yamauchi, "Extreme focusing of hard X-ray free-electron laser pulses enables 7 nm focus width and 1022 W cm2 intensity," *Nature Photonics*, vol. 18, pp. 685–690, 7 2024.

[24] G. Martínez-Criado, J. Villanova, R. Tucoulou, D. Salomon, J.-P. Suuronen, S. Labouré, C. Guilloud, V. Valls, R. Barrett, E. Gagliardini, Y. Dabin, R. Baker, S. Bohic, C. Cohen, and J. Morse, "ID16B: a hard X-ray nanoprobe beamline at the ESRF for nano-analysis," *Journal of Synchrotron Radiation*, vol. 23, pp. 344–352, 1 2016.

[25] U. Johansson, D. Carbone, S. Kalbfleisch, A. Björling, M. Kahnt, S. Sala, T. Stankevic, M. Liebi, A. R. Fernandez, B. Bring, D. Paterson, K. Thånell, P. Bell, D. Erb, C. Weninger,

Z. Matej, L. Roslund, K. Åhnberg, B. N. Jensen, H. Tarawneh, A. Mikkelsen, and U. Vogt, "NanoMAX: the hard X-ray nanoprobe beamline at the MAX IV Laboratory," *Journal of Synchrotron Radiation*, vol. 28, pp. 1935–1947, 2021.

[26] I. Mohacsi, I. Vartiainen, B. Rösner, M. Guizar-Sicairos, V. A. Guzenko, I. McNulty, R. Winarski, M. V. Holt, and C. David, "Interlaced zone plate optics for hard X-ray imaging in the 10 nm range," *Scientific Reports*, vol. 7, p. 43624, 3 2017.

[27] S. Bajt, M. Prasciolu, H. Fleckenstein, M. Domaracký, H. N. Chapman, A. J. Morgan, O. Yefanov, M. Messerschmidt, Y. Du, K. T. Murray, V. Mariani, M. Kuhn, S. Aplin, K. Pande, P. Villanueva-Perez, K. Stachnik, J. P. Chen, A. Andrejczuk, A. Meents, A. Burkhardt, D. Pennicard, X. Huang, H. Yan, E. Nazaretski, Y. S. Chu, and C. E. Hamm, "X-ray focusing with efficient high-NA multilayer Laue lenses," *Light: Science & Applications*, vol. 7, pp. 17162–17162, 11 2017.

[28] W. Zhang, J. L. Dresselhaus, H. Fleckenstein, M. Prasciolu, M. Zakharova, N. Ivanov, C. Li, O. Yefanov, T. Li, D. Egorov, I. D. G. Aquino, P. Middendorf, S. Bajt, and H. Chapman, "Nanometer-resolution hard X-ray near-field ptychography with multilayer Laue lenses," *EPJ Web of Conferences*, vol. 335, p. 01015, 9 2025.

[29] H. Yumoto, T. Koyama, A. Suzuki, Y. Joti, Y. Niida, K. Tono, Y. Bessho, M. Yabashi, Y. Nishino, and H. Ohashi, "High-fluence and high-gain multilayer focusing optics to enhance spatial resolution in femtosecond X-ray laser imaging," *Nature Communications*, vol. 13, p. 5300, 9 2022.

[30] A. M. Maiden and J. M. Rodenburg, "An improved ptychographical phase retrieval algorithm for diffractive imaging," *Ultramicroscopy*, vol. 109, pp. 1256–1262, 9 2009.

[31] Z. Hu, Y. Zhang, and A. Maiden, "Computational optical sectioning via near-field multi-slice ptychography," *Optics Letters*, vol. 49, p. 4839, 9 2024.

[32] M. K. Stockmar, *Ptychographic phase retrieval for the near-field regime with applications in x-ray nano-tomography.* PhD thesis, Technische Universität München, 2015.

[33] W. Xu, S. Ning, and F. Zhang, "Numerical and experimental study of partial coherence for near-field and far-field ptychography," *Opt. Express*, vol. 29, pp. 40652–40667, Nov 2021.

[34] R. M. Clare, M. Stockmar, M. Dierolf, I. Zanette, and F. Pfeiffer, "Characterization of near-field ptychography," *Opt. Express*, vol. 23, no. 15, pp. 19728–19742, 2015.

[35] P. Cloetens, R. Barrett, J. Baruchel, J.-P. Guigay, and M. Schlenker, "Phase objects in synchrotron radiation hard x-ray imaging," *Journal of Physics D: Applied Physics*, vol. 29, pp. 133–146, 1 1996.

[36] M. Odstrčil, M. Lebugle, M. Guizar-Sicairos, C. David, and M. Holler, "Towards optimized illumination for high-resolution ptychography," *Optics Express*, vol. 27, p. 14981, 5 2019.

[37] M. Guizar-Sicairos, M. Holler, A. Diaz, J. Vila-Comamala, O. Bunk, and A. Menzel, "Role of the illumination spatial-frequency spectrum for ptychography," *Physical Review B*, vol. 86, p. 100103, 9 2012.

[38] M. Stockmar, P. Cloetens, I. Zanette, B. Enders, M. Dierolf, F. Pfeiffer, and P. Thibault, "Near-field ptychography: phase retrieval for inline holography using a structured illumination," *Scientific Reports*, vol. 3, no. 1, p. 1927, 2013.

[39] N. Banterle, K. H. Bui, E. A. Lemke, and M. Beck, "Fourier ring correlation as a resolution criterion for super-resolution microscopy," *Journal of Structural Biology*, vol. 183, pp. 363–367, 9 2013.

[40] M. van Heel and M. Schatz, "Fourier shell correlation threshold criteria," *Journal of Structural Biology*, vol. 151, pp. 250–262, 9 2005.

[41] L. Liu, J. Du, B. Zhuang, M. Gong, J. Liu, H. Gu, and S. Liu, "Pushing the resolution limit of coherent diffractive imaging," *Light: Science & Applications*, vol. 14, p. 298, 8 2025.

[42] T. Latychevskaia, "Lateral and axial resolution criteria in incoherent and coherent optics and holography, near- and far-field regimes," *Applied Optics*, vol. 58, p. 3597, 5 2019.

[43] U. Kubitscheck, *Fluorescence Microscopy*. Wiley, 4 2013.

[44] M. Stockmar, M. Hubert, M. Dierolf, B. Enders, R. Clare, S. Allner, A. Fehringer, I. Zanette, J. Villanova, J. Laurencin, P. Cloetens, F. Pfeiffer, and P. Thibault, "X-ray nanotomography using near-field ptychography," *Opt. Express*, vol. 23, no. 10, pp. 12720–12731, 2015.

[45] C. Jacobsen, "Relaxation of the Crowther criterion in multislice tomography," *Opt. Lett.*, vol. 43, pp. 4811–4814, Oct 2018.

[46] E. H. R. Tsai, I. Usov, A. Diaz, A. Menzel, and M. Guizar-Sicairos, "X-ray ptychography with extended depth of field," *Opt. Express*, vol. 24, no. 25, pp. 29089–29108, 2016.

[47] Z. Hu, Y. Zhang, P. Li, D. Batey, and A. Maiden, "Near-field multi-slice ptychography: quantitative phase imaging of optically thick samples with visible light and X-rays," *Opt. Express*, vol. 31, pp. 15791–15809, May 2023.

[48] J. M. Rodenburg and H. M. L. Faulkner, "A phase retrieval algorithm for shifting illumination," *Applied Physics Letters*, vol. 85, pp. 4795–4797, 11 2004.

[49] P. Thibault, M. Dierolf, O. Bunk, A. Menzel, and F. Pfeiffer, "Probe retrieval in ptychographic coherent diffractive imaging," *Ultramicroscopy*, vol. 109, pp. 338–343, 3 2009.

[50] P. Thibault and M. Guizar-Sicairos, "Maximum-likelihood refinement for coherent diffractive imaging," *New Journal of Physics*, vol. 14, 6 2012.

[51] A. M. Maiden, M. J. Humphry, and J. M. Rodenburg, "Ptychographic transmission microscopy in three dimensions using a multi-slice approach," *Journal of the Optical Society of America A*, vol. 29, p. 1606, 8 2012.

[52] M. H. Oh, T. Yu, S.-H. Yu, B. Lim, K.-T. Ko, M.-G. Willinger, D.-H. Seo, B. H. Kim, M. G. Cho, J.-H. Park, K. Kang, Y.-E. Sung, N. Pinna, and T. Hyeon, "Galvanic Replacement Reactions in Metal Oxide Nanocrystals," *Science*, vol. 340, pp. 964–968, 5 2013.

[53] M. D. Susman, R. Popovitz-Biro, A. Vaskevich, and I. Rubinstein, "pH-Dependent Galvanic Replacement of Supported and Colloidal Cu 2 O Nanocrystals with Gold and Palladium," *Small*, vol. 11, pp. 3942–3953, 8 2015.

[54] J. M. Lowe and R. H. Coridan, "Mechanistic control of a galvanic replacement reaction on cuprous oxide," *Nanoscale Advances*, vol. 1, pp. 1343–1350, 2019.

[55] B. D. Anderson and J. B. Tracy, "Nanoparticle conversion chemistry: Kirkendall effect, galvanic exchange, and anion exchange," *Nanoscale*, vol. 6, pp. 12195–12216, 2014.

[56] Y. Sun and Y. Xia, "Alloying and Dealloying Processes Involved in the Preparation of Metal Nanoshells through a Galvanic Replacement Reaction," *Nano Letters*, vol. 3, pp. 1569–1572, 11 2003.

[57] X. Xia, Y. Wang, A. Ruditskiy, and Y. Xia, "25th Anniversary Article: Galvanic Replacement: A Simple and Versatile Route to Hollow Nanostructures with Tunable and Well-Controlled Properties," *Advanced Materials*, vol. 25, pp. 6313–6333, 11 2013.

[58] C. M. Cobley and Y. Xia, "Engineering the properties of metal nanostructures via galvanic replacement reactions," *Materials Science and Engineering: R: Reports*, vol. 70, pp. 44–62, 11 2010.

[59] W. Bras, D. A. A. Myles, and R. Felici, "When x-rays alter the course of your experiments," *Journal of Physics: Condensed Matter*, vol. 33, p. 423002, 10 2021.

[60] L. Young, E. T. Nienhuis, D. Koulentianos, G. Doumy, A. M. March, S. H. Southworth, S. B. Clark, T. M. Orlando, J. A. LaVerne, and C. I. Pearce, "Photon-In/Photon-Out X-ray Free-Electron Laser Studies of Radiolysis," *Applied Sciences*, vol. 11, p. 701, 1 2021.

[61] E. Gachard, H. Remita, J. Khatouri, B. Keita, L. Nadjo, , and J. Belloni, "Radiation-induced and chemical formation of gold clusters," *New Journal of Chemistry*, vol. 22, pp. 1257–1265, 1998.

[62] A. Abedini, A. R. Daud, M. A. A. Hamid, N. K. Othman, and E. Saion, "A review on radiation-induced nucleation and growth of colloidal metallic nanoparticles," 2013.

[63] Y. Guang, I. Bykova, Y. Liu, G. Yu, E. Goering, M. Weigand, J. Gräfe, S. K. Kim, J. Zhang, H. Zhang, Z. Yan, C. Wan, J. Feng, X. Wang, C. Guo, H. Wei, Y. Peng, Y. Tserkovnyak,

X. Han, and G. Schütz, "Creating zero-field skyrmions in exchange-biased multilayers through X-ray illumination," *Nature Communications*, vol. 11, p. 949, 2 2020.

[64] H. Wallander and J. Wallentin, "Simulated sample heating from a nanofocused X-ray beam," *Journal of Synchrotron Radiation*, vol. 24, pp. 925–933, 9 2017.

[65] A. J. Warren, D. Axford, and R. L. Owen, "Direct measurement of X-ray-induced heating of microcrystals," *Journal of Synchrotron Radiation*, vol. 26, pp. 991–997, 7 2019.

[66] N. Laanait, E. B. R. Callagon, Z. Zhang, N. C. Sturchio, S. S. Lee, and P. Fenter, "X-ray–driven reaction front dynamics at calcite-water interfaces," *Science*, vol. 349, pp. 1330–1334, 9 2015.

[67] B. M. Weon, J. S. Lee, J. H. Je, and K. Fezzaa, "X-ray-induced water vaporization," *Physical Review E*, vol. 84, p. 032601, 9 2011.

[68] J. Belloni, J.-L. Marignier, and M. Mostafavi, "Mechanisms of metal nanoparticles nucleation and growth studied by radiolysis," *Radiation Physics and Chemistry*, vol. 169, p. 107952, 4 2020.

[69] K. Čubová and V. Čuba, "Synthesis of inorganic nanoparticles by ionizing radiation – a review," *Radiation Physics and Chemistry*, vol. 169, p. 108774, 4 2020.

[70] A. Abedini, A. A. A. Bakar, F. Larki, P. S. Menon, M. S. Islam, and S. Shaari, "Recent Advances in Shape-Controlled Synthesis of Noble Metal Nanoparticles by Radiolysis Route," *Nanoscale Research Letters*, vol. 11, p. 287, 12 2016.

[71] L. F. de Freitas, G. Varca, J. dos Santos Batista, and A. B. Lugão, "An Overview of the Synthesis of Gold Nanoparticles Using Radiation Technologies," *Nanomaterials*, vol. 8, p. 939, 11 2018.

[72] M. Toro-González, D. M. Clifford, M. C. Molina, C. E. Castano, and J. V. Rojas, "New concept of radiolytic synthesis of gold nanoparticles in continuous flow," *Radiation Physics and Chemistry*, vol. 188, p. 109614, 11 2021.

[73] C. H. Wang, C. C. Chien, Y. L. Yu, C. J. Liu, C. F. Lee, C. H. Chen, Y. Hwu, C. S. Yang, J. H. Je, and G. Margaritondo, "Structural properties of 'naked' gold nanoparticles formed by synchrotron X-ray irradiation," *Journal of Synchrotron Radiation*, vol. 14, pp. 477–482, 10 2007.

[74] A. Yamaguchi, I. Okada, T. Fukuoka, I. Sakurai, and Y. Utsumi, "Synthesis of metallic nanoparticles through X-ray radiolysis using synchrotron radiation," *Japanese Journal of Applied Physics*, vol. 55, p. 055502, 5 2016.

[75] A. SARKANY, Z. PAPP, I. SAJO, and Z. SCHAY, "Unsupported Pd nanoparticles prepared by γ-radiolysis of PdCl," *Solid State Ionics*, vol. 176, pp. 209–215, 1 2005.

[76] P. Abellan, L. R. Parent, N. A. Hasan, C. Park, I. Arslan, A. M. Karim, J. E. Evans, and N. D. Browning, "Gaining Control over Radiolytic Synthesis of Uniform Sub-3-nanometer Palladium Nanoparticles: Use of Aromatic Liquids in the Electron Microscope," *Langmuir*, vol. 32, pp. 1468–1477, 2 2016.

[77] T. Redjala, G. Apostolecu, P. Beaunier, M. Mostafavi, A. Etcheberry, D. Uzio, C. Thomazeau, and H. Remita, "Palladium nanostructures synthesized by radiolysis or by photoreduction," *New Journal of Chemistry*, vol. 32, p. 1403, 2008.

[78] H. Oyanagi, Y. Orimoto, K. Hayakawa, K. Hatada, Z. Sun, L. Zhang, K. Yamashita, H. Nakamura, M. Uehara, A. Fukano, and H. Maeda, "Nanoclusters Synthesized by Synchrotron Radiolysis in Concert with Wet Chemistry," *Scientific Reports*, vol. 4, p. 7199, 11 2014.

[79] H. Remita and I. Lampre, "Synthesis of Metallic Nanostructures Using Ionizing Radiation and Their Applications," *Materials*, vol. 17, p. 364, 1 2024.

[80] J. Grand, S. R. Ferreira, V. de Waele, S. Mintova, and T. M. Nenoff, "Nanoparticle Alloy Formation by Radiolysis," *The Journal of Physical Chemistry C*, vol. 122, pp. 12573–12588, 6 2018.

[81] A. Björling, L. A. B. Marçal, R. M. Arán-Ais, and J. Solla-Gullón, "Chemical Limits on X-ray Nanobeam Studies in Water," *The Journal of Physical Chemistry C*, vol. 127, pp. 13877–13885, 7 2023.

[82] R. Sanishvili, D. W. Yoder, S. B. Pothineni, G. Rosenbaum, S. Xu, S. Vogt, S. Stepanov, O. A. Makarov, S. Corcoran, R. Benn, V. Nagarajan, J. L. Smith, and R. F. Fischetti, "Radiation damage in protein crystals is reduced with a micron-sized X-ray beam," *Proceedings of the National Academy of Sciences*, vol. 108, pp. 6127–6132, 4 2011.

[83] J. L. Dickerson and E. F. Garman, "The potential benefits of using higher X-ray energies for macromolecular crystallography," *Journal of Synchrotron Radiation*, vol. 26, pp. 922–930, 7 2019.

[84] D. Madsen, C. L. Thomsen, J. Thøgersen, and S. R. Keiding, "Temperature dependent relaxation and recombination dynamics of the hydrated electron," *The Journal of Chemical Physics*, vol. 113, pp. 1126–1134, 7 2000.

[85] S. Röper, S.-A. Hussak, K. Stachnik, D. Koziej, M. Åstrand, U. Vogt, C. Carus, J. Dora, J. Hagemann, M. Seyrich, C. G. Schroer, and A. Schropp, "Stereo hard X-ray ptychography," *Optics Express*, vol. 33, p. 22755, 6 2025.

[86] S. Röper, S.-A. Hussak, K. Stachnik, D. Koziej, M. Åstrand, U. Vogt, C. Carus, J. Dora, J. Hagemann, M. Seyrich, C. G. Schroer, and A. Schropp, "Stereo hard X-ray ptychography

with multislicing," in *X-Ray Nanoimaging: Instruments and Methods VII* (B. Lai and Y. S. Chu, eds.), p. 2, SPIE, 9 2025.

[87] M. Dierolf, A. Menzel, P. Thibault, P. Schneider, C. M. Kewish, R. Wepf, O. Bunk, and F. Pfeiffer, "Ptychographic X-ray computed tomography at the nanoscale," *Nature*, vol. 467, no. 7314, pp. 436–440, 2010.

[88] M. Holler, M. Guizar-Sicairos, E. H. R. Tsai, R. Dinapoli, E. Müller, O. Bunk, J. Raabe, and G. Aeppli, "High-resolution non-destructive three-dimensional imaging of integrated circuits," *Nature*, vol. 543, pp. 402–406, 2017.

[89] M. Holler, M. Odstrcil, M. Guizar-Sicairos, M. Lebugle, E. Müller, S. Finizio, G. Tinti, C. David, J. Zusman, W. Unglaub, O. Bunk, J. Raabe, A. F. J. Levi, and G. Aeppli, "Three-dimensional imaging of integrated circuits with macro- to nanoscale zoom," *Nature Electronics*, vol. 2, no. 10, pp. 464–470, 2019.

[90] M. Kahnt, L. Grote, D. Brückner, M. Seyrich, F. Wittwer, D. Koziej, and C. G. Schroer, "Multi-slice ptychography enables high-resolution measurements in extended chemical reactors," *Scientific Reports*, vol. 11, p. 1500, Jan 2021.

[91] M. Holler, A. Diaz, M. Guizar-Sicairos, P. Karvinen, E. Färm, E. Härkönen, M. Ritala, A. Menzel, J. Raabe, and O. Bunk, "X-ray ptychographic computed tomography at 16 nm isotropic 3D resolution," *Scientific Reports*, vol. 4, p. 3857, 2014.

[92] S. Gleber, C. Knöche, J. Thieme, D. Rudolph, and G. Schmahl, "3-D computer reconstruction of X-ray microscopy objects from stereo images," *Journal de Physique IV (Proceedings)*, vol. 104, pp. 639–642, 3 2003.

[93] S.-C. Gleber, J. Sedlmair, M. Bertilson, O. von Hofsten, S. Heim, P. Guttmann, H. M. Hertz, P. Fischer, and J. Thieme, "X-ray stereo microscopy for investigation of dynamics in soils," *Journal of Physics: Conference Series*, vol. 186, p. 012104, 9 2009.

[94] T. Kimura, Y. Takeo, K. Sakurai, N. Furuya, S. Egawa, G. Yamaguchi, Y. Matsuzawa, T. Kume, H. Mimura, M. Shimura, H. Ohashi, I. Matsuda, and Y. Harada, "Soft X-ray ptychography system using a Wolter mirror for achromatic illumination optics," *Optics Express*, vol. 30, p. 26220, 7 2022.

[95] K. Shimomura, A. Suzuki, M. Hirose, and Y. Takahashi, "Precession X-ray ptychography with multislice approach," *Physical Review B - Condensed Matter and Materials Physics*, vol. 91, p. 214114, 6 2015.

[96] K. Shimomura, M. Hirose, and Y. Takahashi, "Multislice imaging of integrated circuits by precession X-ray ptychography," *Acta Crystallographica Section A: Foundations and Advances*, vol. 74, pp. 66–70, 1 2018.

[97] C. Chang, X. Pan, H. Tao, C. Liu, S. P. Veetil, and J. Zhu, "3D single-shot ptychography with highly tilted illuminations," *Optics Express*, vol. 29, p. 30878, 9 2021.

[98] D. Goldberger, J. Barolak, C. G. Durfee, and D. E. Adams, "Three-dimensional single-shot ptychography," *Optics Express*, vol. 28, p. 18887, 6 2020.

[99] M. Hoshino, K. Uesugi, J. Pearson, T. Sonobe, M. Shirai, and N. Yagi, "Development of an X-ray real-time stereo imaging technique using synchrotron radiation," *Journal of Synchrotron Radiation*, vol. 18, pp. 569–574, 7 2011.

[100] W. Voegeli, K. Kajiwara, H. Kudo, T. Shirasawa, X. Liang, and W. Yashiro, "Multibeam X-ray optical system for high-speed tomography," *Optica*, vol. 7, p. 514, 5 2020.

[101] W. Voegeli, H. Takayama, X. Liang, T. Shirasawa, E. Arakawa, H. Kudo, and W. Yashiro, "Multibeam X-ray tomography optical system for narrow-energy-bandwidth synchrotron radiation," *Applied Physics Express*, vol. 17, p. 032002, 3 2024.

[102] E. M. Asimakopoulou, V. Bellucci, S. Birnsteinova, Z. Yao, Y. Zhang, I. Petrov, C. Deiter, A. Mazzolari, M. Romagnoni, D. Korytar, Z. Zaprazny, Z. Kuglerova, L. Juha, B. Lukić, A. Rack, L. Samoylova, F. Garcia-Moreno, S. A. Hall, T. Neu, X. Liang, P. Vagovic, and P. Villanueva-Perez, "Development towards high-resolution kHz-speed rotation-free volumetric imaging," *Optics Express*, vol. 32, p. 4413, 1 2024.

[103] J. Duarte, R. Cassin, J. Huijts, B. Iwan, F. Fortuna, L. Delbecq, H. Chapman, M. Fajardo, M. Kovacev, W. Boutu, and H. Merdji, "Computed stereo lensless X-ray imaging," *Nature Photonics*, vol. 13, pp. 449–453, 7 2019.

[104] D. Fainozzi, M. Ippoliti, F. Bille, D. D. Angelis, L. Foglia, C. Masciovecchio, R. Mincigrucci, M. Pancaldi, E. Pedersoli, C. M. Günther, B. Pfau, M. Schneider, C. V. K. Schmising, S. Eisebitt, G. Kourousias, F. Bencivenga, and F. Capotondi, "Three-dimensional coherent diffraction snapshot imaging using extreme-ultraviolet radiation from a free electron laser," *Optica*, vol. 10, p. 1053, 8 2023.

[105] P. Villanueva-Perez, B. Pedrini, R. Mokso, P. Vagovic, V. A. Guzenko, S. J. Leake, P. R. Willmott, P. Oberta, C. David, H. N. Chapman, and M. Stampanoni, "Hard X-ray multi-projection imaging for single-shot approaches," *Optica*, vol. 5, p. 1521, 12 2018.

[106] P. Villanueva-Perez, V. Bellucci, Y. Zhang, S. Birnsteinova, R. Graceffa, L. Adriano, E. M. Asimakopoulou, I. Petrov, Z. Yao, M. Romagnoni, A. Mazzolari, R. Letrun, C. Kim, J. C. P. Koliyadu, C. Deiter, R. Bean, G. Giovanetti, L. Gelisio, T. Ritschel, A. Mancuso, H. N. Chapman, A. Meents, T. Sato, and P. Vagovic, "Megahertz X-ray Multi-projection imaging," *arXiv:2305.11920*, 5 2023.

[107] V. Bellucci, M.-C. Zdora, L. Mikeš, Š. Birnšteinová, P. Oberta, M. Romagnoni, A. Mazzolari, P. Villanueva-Perez, R. Mokso, C. David, M. Makita, S. Cipiccia, J. Uličný, A. Meents,

A. P. Mancuso, H. N. Chapman, and P. Vagovič, "Hard X-ray stereographic microscopy for single-shot differential phase imaging," *Optics Express*, vol. 31, p. 18399, 5 2023.

[108] S. Flenner, A. Kubec, C. David, I. Greving, and J. Hagemann, "Dual-beam X-ray nano-holotomography," *Journal of Synchrotron Radiation*, vol. 31, pp. 916–922, 7 2024.

[109] T. Li, M. Kahnt, T. L. Sheppard, R. Yang, K. V. Falch, R. Zvagelsky, P. Villanueva-Perez, M. Wegener, and M. Lyubomirskiy, "X-Ray Multibeam Ptychography at up to 20 keV: Nano-Lithography Enhances X-Ray Nano-Imaging," *Advanced Science*, vol. 11, p. 2310075, 8 2024.

[110] M. Hirose, T. Higashino, N. Ishiguro, and Y. Takahashi, "Multibeam ptychography with synchrotron hard X-rays," *Optics Express*, vol. 28, p. 1216, 1 2020.

[111] M. Lyubomirskiy, F. Wittwer, M. Kahnt, F. Koch, A. Kubec, K. V. Falch, J. Garrevoet, M. Seyrich, C. David, and C. G. Schroer, "Multi-beam X-ray ptychography using coded probes for rapid non-destructive high resolution imaging of extended samples," *Scientific Reports*, vol. 12, p. 6203, 4 2022.

[112] Y. Yao, Y. Jiang, J. A. Klug, M. Wojcik, E. R. Maxey, N. S. Sirica, C. Roehrig, Z. Cai, S. Vogt, B. Lai, and J. Deng, "Multi-beam X-ray ptychography for high-throughput coherent diffraction imaging," *Scientific Reports*, vol. 10, p. 19550, 11 2020.

[113] F. Wittwer, M. Lyubomirskiy, F. Koch, M. Kahnt, M. Seyrich, J. Garrevoet, C. David, and C. G. Schroer, "Upscaling of multi-beam x-ray ptychography for efficient x-ray microscopy with high resolution and large field of view," *Applied Physics Letters*, vol. 118, p. 171102, 4 2021.

[114] J. Deng, C. Preissner, J. A. Klug, S. Mashrafi, C. Roehrig, Y. Jiang, Y. Yao, M. Wojcik, M. D. Wyman, D. Vine, K. Yue, S. Chen, T. Mooney, M. Wang, Z. Feng, D. Jin, Z. Cai, B. Lai, and S. Vogt, "The Velociprobe: An ultrafast hard X-ray nanoprobe for high-resolution ptychographic imaging," *Review of Scientific Instruments*, vol. 90, p. 083701, aug 2019.

[115] J. Reinhardt, R. Hoppe, G. Hofmann, C. D. Damsgaard, J. Patommel, C. Baumbach, S. Baier, A. Rochet, J.-D. Grunwaldt, G. Falkenberg, and C. G. Schroer, "Beamstop-Based Low-Background Ptychography to Image Weakly Scattering Objects," *Ultramicroscopy*, vol. 173, pp. 52–57, 2017.

[116] R. N. Wilke, M. Priebe, M. Bartels, K. Giewekemeyer, A. Diaz, P. Karvinen, and T. Salditt, "Hard X-ray imaging of bacterial cells: nano-diffraction and ptychographic reconstruction," *Opt. Express*, vol. 20, no. 17, pp. 19232–19254, 2012.

[117] S. Baier, C. D. Damsgaard, M. Scholz, F. Benzi, A. Rochet, R. Hoppe, T. Scherer, J. Shi, A. Wittstock, B. Weinhausen, J. B. Wagner, C. G. Schroer, and J.-D. Grunwaldt, "In situ

Ptychography of Heterogeneous Catalysts using Hard X-rays: High Resolution Imaging at Ambient Pressure and Elevated Temperature," *Microscopy and Microanalysis*, vol. 22, no. 1, pp. 178–188, 2016.

[118] L. Grote, M. Seyrich, R. Döhrmann, S. Y. Harouna-Mayer, F. Mancini, E. Kaziukenas, I. Fernandez-Cuesta, C. A. Zito, O. Vasylieva, F. Wittwer, M. Odstrčzil, N. Mogos, M. Landmann, C. G. Schroer, and D. Koziej, "Imaging Cu2O nanocube hollowing in solution by quantitative in situ X-ray ptychography," *Nature Communications*, vol. 13, no. 1, p. 4971, 2022.

[119] L. Grote, S.-A. Hussak, L. Albers, K. Stachnik, F. Mancini, M. Seyrich, O. Vasylieva, D. Brückner, M. Lyubomirskiy, C. G. Schroer, and D. Koziej, "Multimodal imaging of cubic Cu2O@Au nanocage formation via galvanic replacement using X-ray ptychography and nano diffraction," *Scientific Reports*, vol. 13, no. 1, p. 318, 2023.

[120] H. Ohlin, T. Frisk, M. Åstrand, and U. Vogt, "Miniaturized Sulfite-Based Gold Bath for Controlled Electroplating of Zone Plate Nanostructures," *Micromachines*, vol. 13, p. 452, 3 2022.

[121] M. Åstrand, T. Frisk, H. Ohlin, and U. Vogt, "Understanding dose correction for high-resolution 50 kV electron-beam lithography on thick resist layers," *Micro and Nano Engineering*, vol. 16, p. 100141, 2022.

[122] A. Schropp, R. Döhrmann, S. Botta, D. Brückner, M. Kahnt, M. Lyubomirskiy, C. Ossig, M. Scholz, M. Seyrich, M. E. Stuckelberger, P. Wiljes, F. Wittwer, J. Garrevoet, G. Falkenberg, Y. Fam, T. L. Sheppard, J.-D. Grunwaldt, and C. G. Schroer, "PtyNAMi: ptychographic nano-analytical microscope," *Journal of Applied Crystallography*, vol. 53, pp. 957–971, 8 2020.

[123] F. Wittwer, R. Hoppe, F. Seiboth, J. Reinhardt, M. Scholz, and C. G. Schroer, "Ptychography with a Virtually Enlarged Illumination," *Microscopy and Microanalysis*, vol. 24, pp. 46–47, 2018.

[124] M. Odstrčil, M. Holler, and M. Guizar-Sicairos, "Arbitrary-path fly-scan ptychography," *Optics Express*, vol. 26, p. 12585, 5 2018.

[125] F. Wittwer, J. Hagemann, D. Brückner, S. Flenner, and C. G. Schroer, "Phase retrieval framework for direct reconstruction of the projected refractive index applied to ptychography and holography," *Optica*, vol. 9, p. 295, mar 2022.

[126] S. van der Walt, J. L. Schönberger, J. Nunez-Iglesias, F. Boulogne, J. D. Warner, N. Yager, E. Gouillart, and T. Yu, "scikit-image: image processing in Python," *PeerJ*, vol. 2, p. e453, 6 2014.

[127] J. Hagemann, A.-L. Robisch, D. R. Luke, C. Homann, T. Hohage, P. Cloetens, H. Suhonen, and T. Salditt, "Reconstruction of wave front and object for inline holography from a set of detection planes," *Opt. Express*, vol. 22, no. 10, pp. 11552–11569, 2014.

[128] C. Homann, T. Hohage, J. Hagemann, A.-L. Robisch, and T. Salditt, "Validity of the empty-beam correction in near-field imaging," *Phys. Rev. A*, vol. 91, p. 013821, 2015.

[129] A. Schropp, R. Hoppe, V. Meier, J. Patommel, F. Seiboth, H. J. Lee, B. Nagler, E. C. Galtier, B. Arnold, U. Zastrau, J. B. Hastings, D. Nilsson, F. Uhlen, U. Vogt, H. M. Hertz, and C. G. Schroer, "Full spatial characterization of a nanofocused x-ray free-electron laser beam by ptychographic imaging," *Scientific Reports*, vol. 3, p. 1633, 2013.

[130] B. Henke, E. Gullikson, and J. Davis, "X-Ray Interactions: Photoabsorption, Scattering, Transmission, and Reflection at E = 50-30,000 eV, Z = 1-92," *Atomic Data and Nuclear Data Tables*, vol. 54, pp. 181–342, 7 1993.

[131] Y. Fam, T. L. Sheppard, J. Becher, D. Scherhaufer, H. Lambach, S. Kulkarni, T. F. Keller, A. Wittstock, F. Wittwer, M. Seyrich, D. Brueckner, M. Kahnt, X. Yang, A. Schropp, A. Stierle, C. G. Schroer, and J.-D. Grunwaldt, "A versatile nanoreactor for complementary in situ X-ray and electron microscopy studies in catalysis and materials science," *Journal of Synchrotron Radiation*, vol. 26, pp. 1769–1781, 9 2019.

[132] I. J. Arnquist, C. Beck, M. L. di Vacri, K. Harouaka, and R. Saldanha, "Ultra-low radioactivity Kapton and copper-Kapton laminates," *Nuclear Instruments and Methods in Physics Research Section A: Accelerators, Spectrometers, Detectors and Associated Equipment*, vol. 959, p. 163573, 4 2020.

[133] Y. Fang, J. G. D. Hester, W. Su, J. H. Chow, S. K. Sitaraman, and M. M. Tentzeris, "A bio-enabled maximally mild layer-by-layer Kapton surface modification approach for the fabrication of all-inkjet-printed flexible electronic devices," *Scientific Reports*, vol. 6, p. 39909, 12 2016.

[134] S.-D. Oh, M.-R. Kim, S.-H. Choi, J.-H. Chun, K.-P. Lee, A. Gopalan, C.-G. Hwang, K. Sang-Ho, and O. J. Hoon, "Radiolytic synthesis of Pd–M (M=Ag, Au, Cu, Ni and Pt) alloy nanoparticles and their use in reduction of 4-nitrophenol," *Journal of Industrial and Engineering Chemistry*, vol. 14, pp. 687–692, 9 2008.

[135] J. Belloni, M. Mostafavi, H. Remita, J.-L. Marignier, , and M.-O. Delcourt, "Radiation-induced synthesis of mono- and multi-metallic clusters and nanocolloids," *New Journal of Chemistry*, vol. 22, pp. 1239–1255, 1998.

[136] S. Kapoor, M. Kumar, and C. Gopinathan, "Pulse and gamma radiolytic studies on the formation of Cd, Pd and Cu clusters in aqueous solutions," *Radiation Physics and Chemistry*, vol. 50, pp. 465–469, 11 1997.

[137] S.-A. Hussak, *Tuning nanomaterial syntheses for in situ ptychographic X-ray microscopy.* University of Hamburg, 2020.

[138] E. Sutter, K. Jungjohann, S. Bliznakov, A. Courty, E. Maisonhaute, S. Tenney, and P. Sutter, "In situ liquid-cell electron microscopy of silver–palladium galvanic replacement reactions on silver nanoparticles," *Nature Communications*, vol. 5, p. 4946, 9 2014.

[139] S. Bajt, M. Prasciolu, H. Fleckenstein, M. Domaracky, H. N. Chapman, A. J. Morgan, O. Yefanov, M. Messerschmidt, Y. Du, K. T. Murray, V. Mariani, M. Kuhn, S. Aplin, K. Pande, P. Villanueva-Perez, K. Stachnik, J. P. J. Chen, A. Andrejczuk, A. Meents, A. Burkhardt, D. Pennicard, X. Huang, H. Yan, E. Nazaretski, Y. S. Chu, and C. E. Hamm, "X-ray focusing with efficient high-NA multilayer Laue lenses," *Light-Science & Applications*, vol. 7, p. 17162, 2018.

[140] S. Röper, K. Stachnik, J. Voss, S.-A. Hussak, M. Åstrand, L. Grote, F. Wittwer, M. Seyrich, S. Niese, P. Gawlitza, U. Vogt, C. G. Schroer, D. Koziej, and A. Schropp, "X-ray near-field multi-slice ptychography for in-situ imaging," *Scientific Reports*, vol. 15, p. 32150, 9 2025.

[141] Q. Shen, I. Bazarov, and P. Thibault, "Diffractive imaging of nonperiodic materials with future coherent X-ray sources," *J. of Synchrotron Radiat.*, vol. 11, no. 5, pp. 432–438, 2004.

[142] A. Schropp and C. G. Schroer, "Dose requirements for resolving a given feature in an object by coherent x-ray diffraction imaging," *New Journal of Physics*, vol. 12, p. 035016, 3 2010.

[143] M. Du, D. Gürsoy, and C. Jacobsen, "Near, far, wherever you are: simulations on the dose efficiency of holographic and ptychographic coherent imaging," *Journal of Applied Crystallography*, vol. 53, pp. 748–759, 6 2020.

[144] S. H. Shahmoradian, E. H. R. Tsai, A. Diaz, M. Guizar-Sicairos, J. Raabe, L. Spycher, M. Britschgi, A. Ruf, H. Stahlberg, and M. Holler, "Three-Dimensional Imaging of Biological Tissue by Cryo X-Ray Ptychography," *Scientific Reports*, vol. 7, p. 6291, 7 2017.

[145] Y. Kadoma and S. Fujisawa, "A Comparative Study of the Radical-scavenging Activity of the Phenolcarboxylic Acids Caffeic Acid, p-Coumaric Acid, Chlorogenic Acid and Ferulic Acid, With or Without 2-Mercaptoethanol, a Thiol, Using the Induction Period Method," *Molecules*, vol. 13, pp. 2488–2499, 10 2008.

[146] T. R. Stachowski, M. E. Snell, and E. H. Snell, "A SAXS-based approach to rationally evaluate radical scavengers – toward eliminating radiation damage in solution and crystallographic studies," *Journal of Synchrotron Radiation*, vol. 28, pp. 1309–1320, 9 2021.

[147] M. R. Howells, T. Beetz, H. N. Chapman, C. Cui, J. M. Holton, C. J. Jacobsen, J. Kirz, E. LIMA, S. Marchesini, H. Miao, D. Sayre, D. A. Shapiro, J. C. H. Spence, and D. Starodub, "An assessment of the resolution limitation due to radiation-damage in X-ray diffraction

microscopy," *Journal of Electron Spectroscopy and Related Phenomena*, vol. 170, pp. 4–12, Mar. 2009.

[148] A. Björling, S. Kalbfleisch, M. Kahnt, S. Sala, K. Parfeniukas, U. Vogt, D. Carbone, and U. Johansson, "Ptychographic characterization of a coherent nanofocused X-ray beam," *Optics Express*, vol. 28, p. 5069, 2 2020.

[149] A. Pan and B. Yao, "Three-dimensional space optimization for near-field ptychography," *Opt. Express*, vol. 27, pp. 5433–5446, Feb 2019.

[150] Z. Hu, Y. Zhang, and A. Maiden, "Computational optical sectioning via near-field multi-slice ptychography," *Opt. Lett.*, vol. 49, pp. 4839–4842, Sep 2024.

[151] H. Öztürk, H. Yan, Y. He, M. Ge, Z. Dong, M. Lin, E. Nazaretski, I. K. Robinson, Y. S. Chu, and X. Huang, "Multi-slice ptychography with large numerical aperture multilayer Laue lenses," *Optica*, vol. 5, no. 5, pp. 601–607, 2018.

[152] X. Huang, H. Yan, Y. He, M. Ge, H. Öztürk, Y.-L. L. Fang, S. Ha, M. Lin, M. Lu, E. Nazaretski, I. K. Robinson, and Y. S. Chu, "Resolving 500 nm axial separation by multi-slice X-ray ptychography," *Acta Crystallographica Section A Foundations and Advances*, vol. 75, pp. 336–341, 3 2019.

[153] D. M. Paganin, *Coherent X-Ray Optics*. Oxford University Press, 1 ed., 2006.

[154] S. Witte, A. Pelekanidis, and K. Eikema, "Propagators with user-defined object-plane pixel size for ptychography," *Optica Open*, 1 2025.

[155] F. Zernike, "How I discovered phase contrast," *Science*, vol. 121, pp. 345–349, 1955.

[156] H. Chang, P. Enfedaque, J. Zhang, J. Reinhardt, B. Enders, Y.-S. Yu, D. Shapiro, C. G. Schroer, T. Zeng, and S. Marchesini, "Advanced denoising for X-ray ptychography," *Opt. Express*, vol. 27, pp. 10395–10418, 2019.

[157] C. Ozsoy-Keskinbora, C. B. Boothroyd, R. E. Dunin-Borkowski, P. A. van Aken, and C. T. Koch, "Hybridization approach to in-line and off-axis (electron) holography for superior resolution and phase sensitivity," *Scientific Reports*, vol. 4, p. 7020, 2014.

[158] M. E. Kandel, M. Fanous, C. Best-Popescu, and G. Popescu, "Real-time halo correction in phase contrast imaging," *Biomedical Optics Express*, vol. 9, p. 623, 2 2018.

[159] V. Múčka, P. Bláha, V. Čuba, and J. Červenák, "Influence of various scavengers of •OH radicals on the radiation sensitivity of yeast and bacteria," *International Journal of Radiation Biology*, vol. 89, pp. 1045–1052, 12 2013.

[160] E. G. Allan, M. C. Kander, I. Carmichael, and E. F. Garman, "To scavenge or not to scavenge, that is STILL the question," *Journal of Synchrotron Radiation*, vol. 20, pp. 23–36, 1 2013.

[161] V. Múčka, J. Červenák, D. Reimitz, V. Čuba, P. Bláha, and B. Neužilová, "Effects of irradiation conditions on the radiation sensitivity of microorganisms in the presence of OH-radical scavengers," *International Journal of Radiation Biology*, vol. 94, pp. 1142–1150, 12 2018.

[162] G. Miller and J. Raleigh, "Action of some Hydroxyl Radical Scavengers on Radiation-induced Haemolysis," *International Journal of Radiation Biology and Related Studies in Physics, Chemistry and Medicine*, vol. 43, pp. 411–419, 1 1983.

[163] J. S. Miller and D. G. Cornwell, "The role of cryoprotective agents as hydroxyl radical scavengers," *Cryobiology*, vol. 15, pp. 585–588, 10 1978.

[164] T. S. Plivelic, A. E. Terry, R. Appio, K. Theodor, and K. Klementiev, "X-ray tracing, design and construction of an optimized optics scheme for CoSAXS, the small angle x-ray scattering beamline at MAX IV laboratory," *AIP Conference Proceedings*, vol. 2054, p. 030013, 01 2019.

[165] J. V. Belloni, M. Mostafavi, and T. Douki, *Radiation Chemistry*. EDP Sciences, 11 2020.

[166] J. J. J. Myron and G. R. Freeman, "THE RADIOLYSIS OF ETHANOL: III. LIQUID PHASE," *Canadian Journal of Chemistry*, vol. 43, pp. 381–394, 2 1965.

[167] G. Heit, A. Neuner, P.-Y. Saugy, and A. M. Braun, "Vacuum-UV (172 nm) Actinometry. The Quantum Yield of the Photolysis of Water," *The Journal of Physical Chemistry A*, vol. 102, no. 28, pp. 5551–5561, 1998.

[168] S. Nehari and J. Rabani, "THE REACTION OF H ATOMS WITH OH - IN THE RADIATION CHEMISTRY OF AQUEOUS SOLUTIONS," *The Journal of Physical Chemistry*, vol. 67, pp. 1609–1613, 8 1963.

[169] P. L. Combettes and J.-C. Pesquet, *Proximal Splitting Methods in Signal Processing*, pp. 185–212. Springer, 2011.

[170] Y. Nesterov, "A method for solving the convex programming problem with convergence rate $O(1/k^2)$," in *Dokl akad nauk Sssr*, vol. 269, p. 543, 1983.

List of publications

S. Röper, S.-A. Hussak, K. Stachnik, D. Koziej, M. Åstrand, U. Vogt, C. Carus, J. Dora, J. Hagemann, M. Seyrich, C. G. Schroer, and A. Schropp, "Stereo hard X-ray ptychography", *Optics Express*, vol. 33, p. 22755, 6 2025.

S. Röper, S.-A. Hussak, K. Stachnik, D. Koziej, M. Åstrand, U. Vogt, C. Carus, J. Dora, J. Hagemann, M. Seyrich, C. G. Schroer, and A. Schropp, "Hard X-ray stereo ptychography with multi-slicing", in X-Ray Nanoimaging: Instruments and Methods VII, p. 1362202, *Proc. SPIE*, 9 2025.

S. Röper, K. Stachnik, J. Voss, S.-A. Hussak, M. Åstrand, L. Grote, F. Wittwer, M. Seyrich, S. Niese, P. Gawlitza, U. Vogt, C. G. Schroer, D. Koziej, and A. Schropp, "X-ray near-field multi-slice ptychography for in-situ imaging", *Scientific Reports*, vol. 15, p. 32150, 9 2025.

Appendices

A Declaration of hazardous substances

Table A.1 lists all potentially hazardous substances that were used in this work and the corresponding hazard (H) and precautionary (P) statements according to the Globally Harmonized System of Classification and Labelling of Chemicals (GHS).

Table A.1: Particularly relevant hazardous substances used in the project and their hazard characteristics and safety advice. EU-GHS-standard.

Substance	Pictograms		H and P statements
Benzyl alcohol		**Warning**	H314, H317, P260, P280, P301+P330+P331, P303+P361+P353, P305+P351+P338
Copper(II) acetyl-acetonate		**Warning**	H315, H319, H335, P280, P305+P351+P338
Hydrochloric acid 37%		**Danger**	H290, H314, H335, P260, P280, P303+P361+P353, P305+P351+P338, P390, P403+P233, P501
Sodium hydroxide		**Danger**	H290, H314, P260, P280, P301+P330+P331, P303+P361+P353, P305+P351+P338
Palladium(II) chloride		**Danger**	H302, H332, H319, P280, P304+P340, P305+P351+P338
Tetrachloroauric(III) acid trihydrate		**Danger**	H302, H332, H319, P280, P304+P340, P305+P351+P338
Ethanol (absolute)		**Danger**	H225, H319, P210, P233, P240, P241, P242, P305+P351+P338
Methanol		**Danger**	H225, H301+H311+H331, H370, P210, P233, P280, P301+P310, P303+P361+P353, P304+P340+P311
Propan-2-ol		**Danger**	H225, H319, H336 P210, P233, P305+P351+P338

B Stereo ptychography

B.1 Resolution determination

In Fig. B.1 the resolution analysis by Fourier ring correlation [39,40] for all three projections of the microchip is shown. The resolution was determined to be 14 nm for the central beam and for the deflected left and right beam 10 nm and 12 nm, respectively. Fig. B.2 shows the Fourier ring correlation for the single-slice nanoparticle-FZP sample (Fig. 5.9). The spatial resolution is 13 nm for both projections.

The Fourier ring correlation for the multi-slice nanoparticle-FZP sample (Fig. 5.13). The spatial resolution is 23 nm for the left and 25 nm for the right projection.

An exemplary Fourier ring correlation for the first slice in the stereo in-situ series using the scan acquired 12 min after the start of the reaction (Fig. 5.16). The spatial resolution is 71 nm for the direct and 105 nm for the right projection.

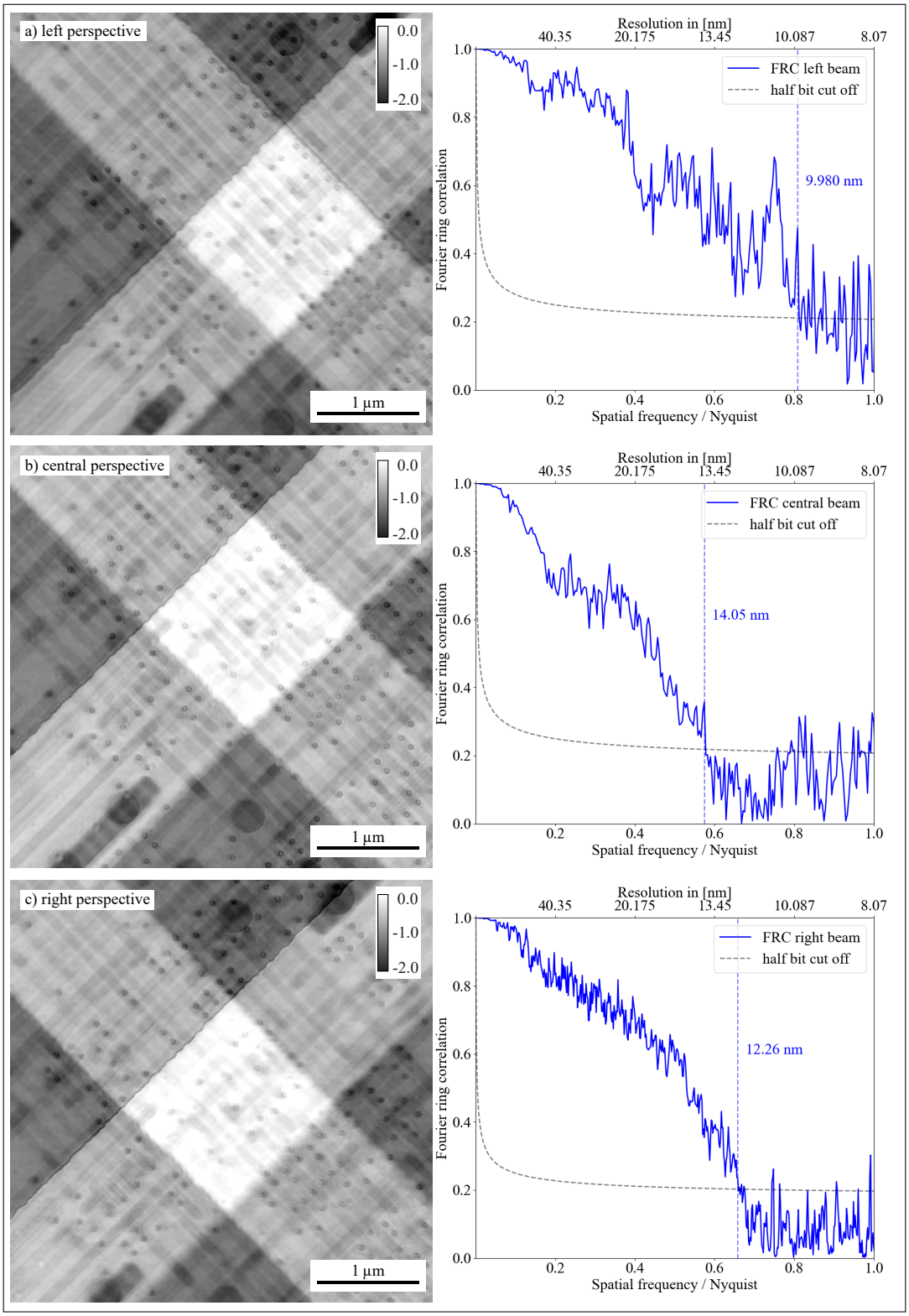

Figure B.1: Fourier ring correlation analysis of the microchip. a) The resolution of the left projection was determined to be 10 nm with a 512 px × 512 px part cropped from the middle of the reconstruction. b) The resolution for the undeflected, central beam was calculated analog to the left beam to be 14 nm. c) The right perspective has a spatial resolution of 12 nm. Reprinted from [85].

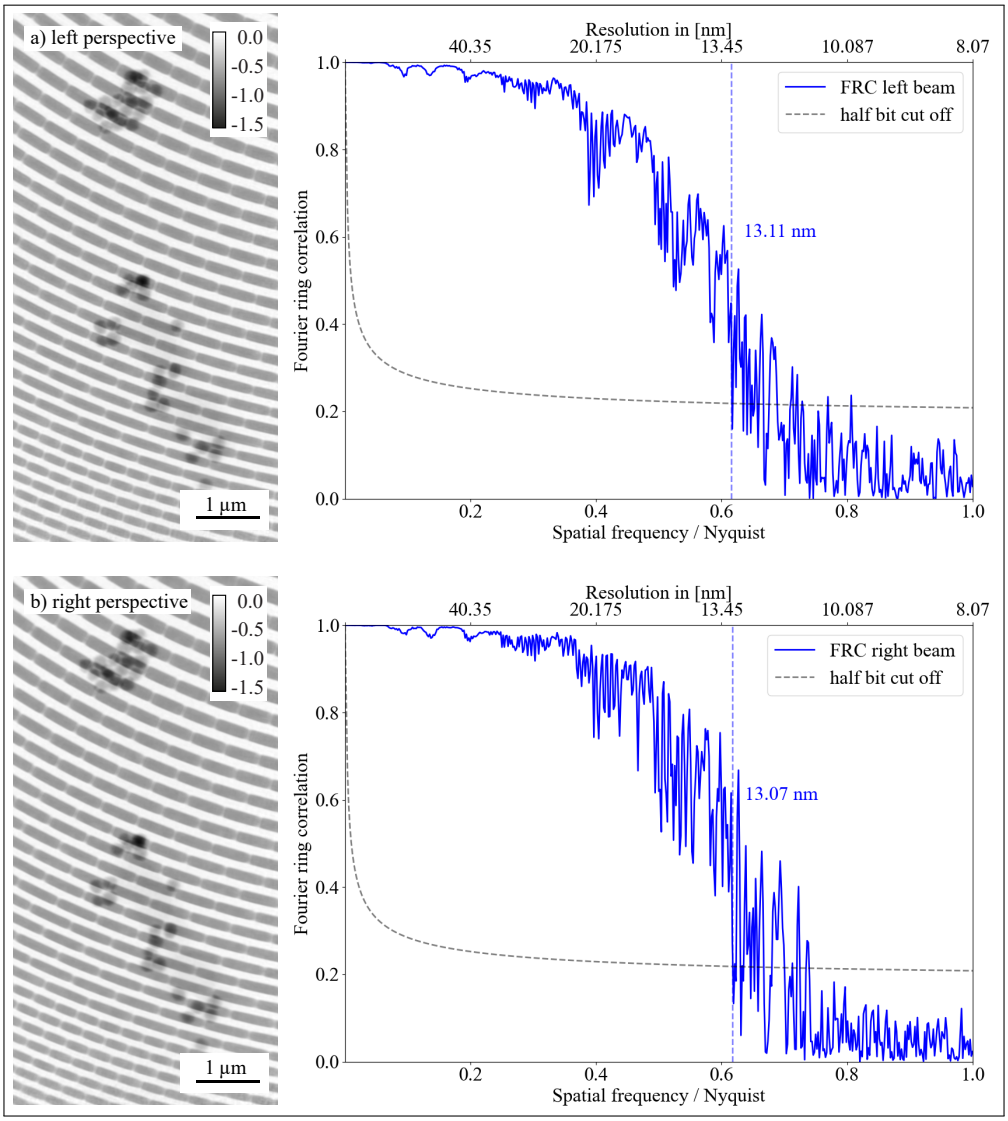

Figure B.2: Fourier ring correlation analysis of the Au nanoparticles on a FZP. a) Resolution determination for the left perspective with a 512 px × 1024 px part cropped from the reconstruction. b) shows the Fourier ring correlation for the right perspective. The resolution for both projections was determined to be 13 nm. Reprinted from [85].

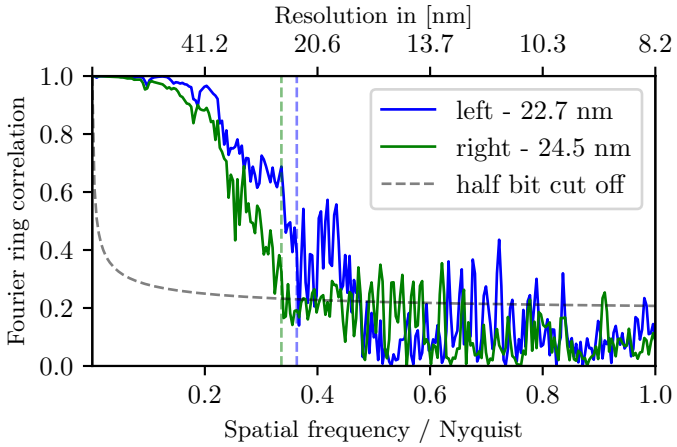

Figure B.3: Determination of the lateral resolution of the first slice with Fourier ring correlation. The resolution of the left and right perspective for the first slice was determined to be 22.7 nm and 24.5 nm, respectively. Reprinted from [86].

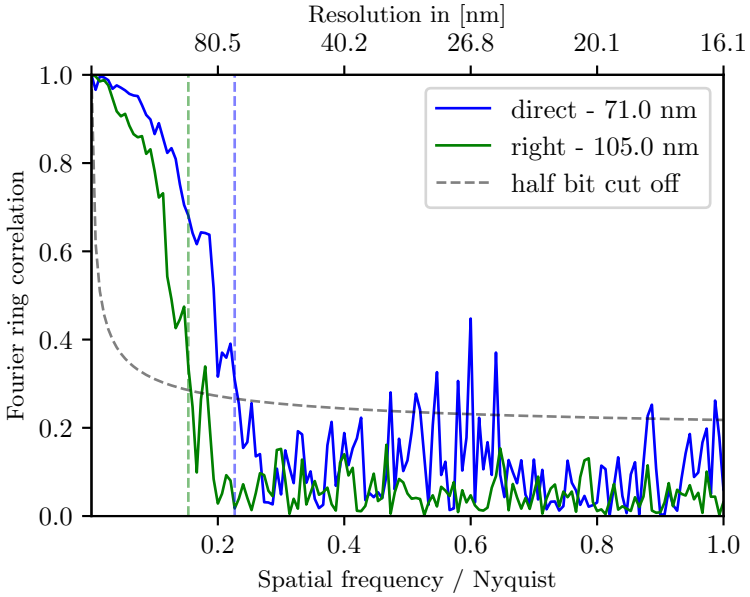

Figure B.4: Resolution determination using Fourier ring correlation of the in-situ scan used for the thin layer recovery. The resolution of the first slice of the direct perspective was determined to be 71 nm and of the right perspective 105 nm.

B.2 Iterative algorithm to separate two distinct layers based on an X-ray stereo pair

The described algorithm was developed jointly by Johannes Dora and Caterina Carus and adapted for the individual samples by me. The description of the algorithm is taken from the supplementary material of Röper et al. (2025)[85].

We separate object layers using the individual left and right perspective phase images obtained by the extended ptychographic iterative engine (ePIE)[30]. To separate two object layers l_1 and l_2 from two reconstructed phase images t_1 and t_2 we applied a simplified linear forward model.

We assume that the object can be represented by two layers and the measured stereo images by two symmetric projections. The two phase images can then be described by projecting the volume in directions that differ in the viewing angle θ_s. For small angles $\theta_s \ll 1\,\mathrm{rad}$, we neglect shearing effects in the projections, leaving us only with a simple displacement of the first layer. This shift s in pixels is given by the trigonometric function

$$s = \frac{2d\tan(\theta_s)}{\Delta x}, \tag{A.1}$$

where d is the layer distance and, Δx is the pixel size. We get two linear equations with

$$t_1 = S(l_1) + l_2 \tag{A.2}$$

$$t_2 = l_1 + l_2 \tag{A.3}$$

for each projection respectively, where S is the shift operation for the first layer. We summarize the two equations as

$$t = Al, \tag{A.4}$$

with

$$\begin{pmatrix} t_1 \\ t_2 \end{pmatrix} = \begin{pmatrix} S & \mathbb{1} \\ \mathbb{1} & \mathbb{1} \end{pmatrix} \cdot \begin{pmatrix} l_1 \\ l_2 \end{pmatrix} \tag{A.5}$$

and recover an approximation $\hat{l}$ of the two object layers by solving a corresponding constrained convex optimization problem

$$\hat{l} = \underset{l}{\operatorname{argmin}}\, F(l) + \mathcal{X}_+(l), \tag{A.6}$$

where $F(l)$ is a data consistency term

$$F(l) := \frac{1}{2}\|Al - t|_2^2, \tag{A.7}$$

and $\mathcal{X}_+(l)$ is the indicator function, which enforces the non-negativity of l with

$$\mathcal{X}_+(l) := \begin{cases} 0 & \text{if } l \in \mathbb{R}_+^N \\ +\infty & \text{else} \end{cases}, \tag{A.8}$$

where N is the number of image pixels. We minimize the target function Eq. A.6 with a forward-backward splitting approach, which is extended by a Nesterov accelerated gradient [169,170]. The Gradient of $F(l)$ can be calculated straight forward and yields

$$\nabla F(l) = A^T(Al - t), \tag{A.9}$$

where matrix A is real valued and A^T is the transposed of A. The Nesterov accelerated gradient at iteration k is then given by the recursion

$$\nabla G(l_k) = \gamma \nabla G(l_{k-1}) + \eta \nabla F(l_k - \gamma \nabla G(l_{k-1})), \tag{A.10}$$

where η is the update step of the gradient descent and γ is the Nesterov momentum. The implementation of the non-negativity constraint is also straight forward and can be realized by a projection $\mathcal{P}_{\mathcal{X}_+}(l)$ onto $\mathbb{R}_+^N$ with

$$\mathcal{P}_{\mathcal{X}_+}(l) := \max(l, 0). \tag{A.11}$$

The full algorithm is shown in Alg. B.5. Since the input projection images here are retrieved phase images and thus always negative valued, we inverted the input images. After reconstruction, we inverted the slices to recover the quantitative phase values.
The algorithm was initialized with an empty array and ran for $k_{\max} = 400$ iterations. The update rate was set to $\eta = 0.40$ and the Nesterov momentum to $\gamma = 0.15$. At iteration $k = 200$, the Nesterov momentum was set to 0 for one iteration, to prevent over-accumulation of the gradients.

Input: Projections t, maximum number of iterations $k_{\max}$, update rate η, Nesterov momentum γ
Output: Separated layers $\hat{l}$

$g_0 \leftarrow 0$
$k \leftarrow 0$
while $k < k_{max}$ **do**
  $y \leftarrow l_k - \gamma g_k$
  $g_{k+1} \leftarrow \gamma g_k + \eta A^T(Ay - t)$
  $l_{k+1} \leftarrow \max(l_k - g_{k+1}, 0)$
  $k \leftarrow k + 1$
end
$\hat{l} \leftarrow l_{k_{\max}}$
return $\hat{l}$

Figure B.5: Forward-backward splitting approach with a Nesterov accelerated gradient for the separation of stereoscopic layers under small projection angles.

B.3 In situ stereo ptychography

Fig. B.6 shows the uncorrected direct and right perspectives of the galvanic replacement reaction of Cu_2O with Pd.

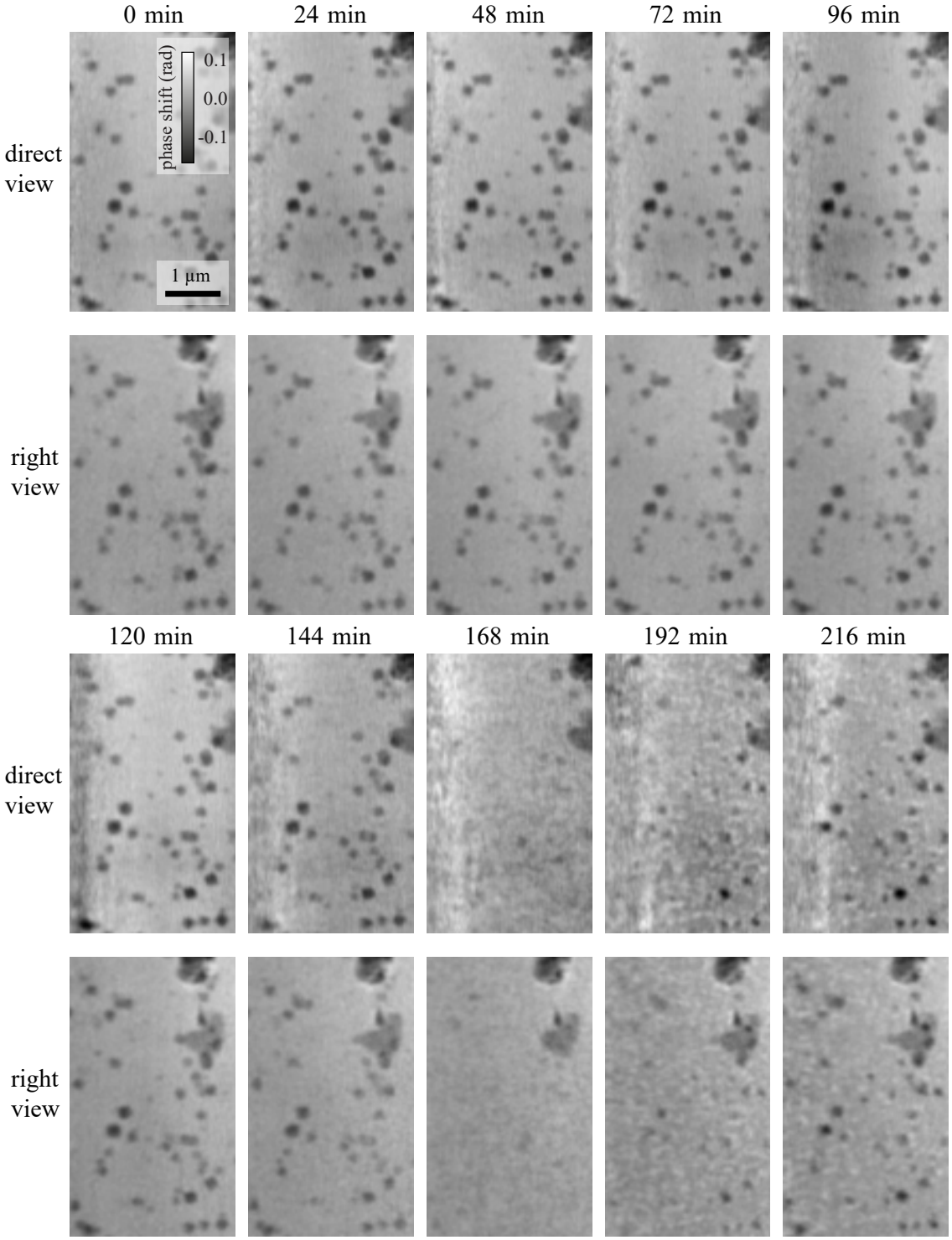

Figure B.6: Stereo in-situ series. Slice 1 (entrance window) of the multi-slice reconstructions of the ptychograms acquired with the direct and right beam.

C Near-field ptychography

C.1 Fourier ring correlation

For each multi-slice reconstruction, the resolution was determined with Fourier ring correlation [39,40]. For each scan, the resolution of the layer(s) of interest was close to or below two pixels. The spatial resolution in this experiment can, therefore, be called pixel size limited. The evaluation for the reconstructions shown in Fig. 6.4 are shown in Fig C.1, for Fig. 6.5 in Fig. C.2, and for Fig. 6.8 in Fig. C.3.

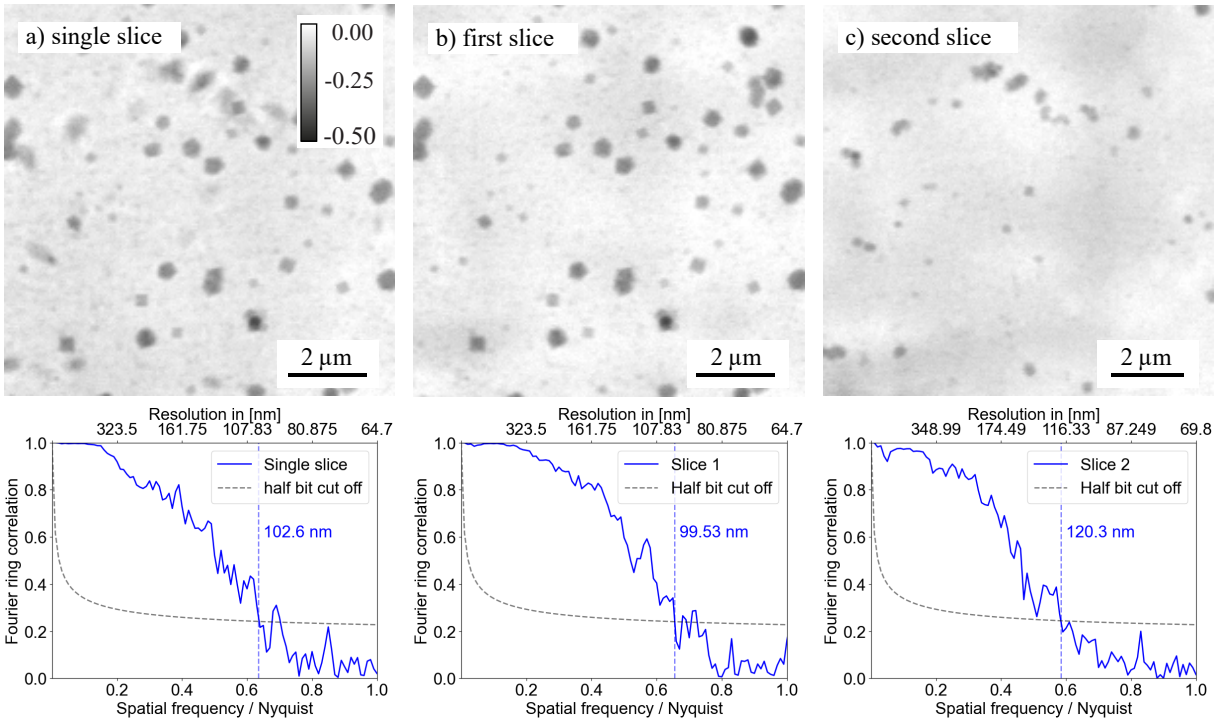

Figure C.1: Spatial resolution determination for Cu_2O cubes on both sides of a 225 μm thick foil. a) Ptychographic reconstructions of the object as a single slice. The gray scale indicates the phase shift in radians. For the Fourier ring correlation, the reconstructions were carried out using one half of the scan points of the original data set. The dotted line in the bottom plot shows the half-bit cut off. The resolution is determined to be 103 nm for the single slice. The resolution for the first slice was calculated to be 100 nm b) and 120 nm for the second slice c). This corresponds to 1.4 px and 1.7 px, respectively. Considering that the spatial resolution, taking into account the Nyquist criterion, can not be better than two pixels, we conclude that the achieved resolution is for both slices pixel size limited. Adapted from [140].

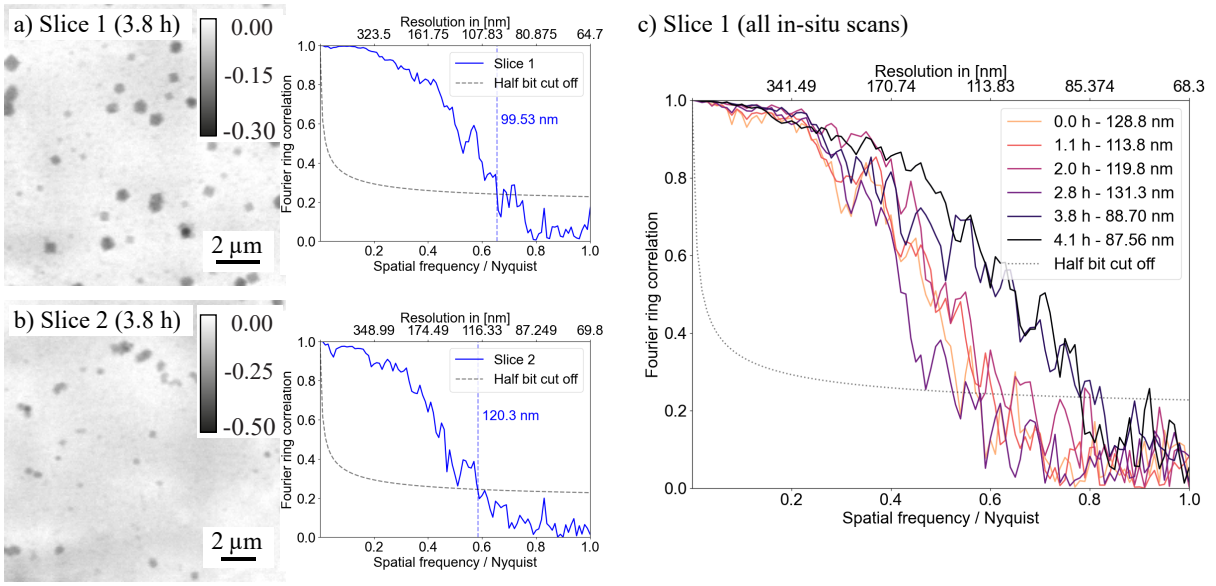

Figure C.2: Spatial resolution determination for the in-situ series. a) Exemplary ptychographic reconstruction of the first slice of the scan taken after 3.8 h of the reaction start. Each image was reconstructed using one half of the scan points of the original data set. The gray scale indicates the phase shift in radians. The resolution is determined to be 88.7 nm, which corresponds to 1.3 px. The resolution can, therefore, be seen as pixel size limited. b) The resolution of the second slice of the same scan was determined to be 293 nm. c) Overview of the spatial resolution of the first slice for each scan of the in-situ series. The resolution improved over the course of the reaction starting with 129 nm (1.9 px) to 88 nm (1.3 px) at the end of the reaction. Adapted from [140].

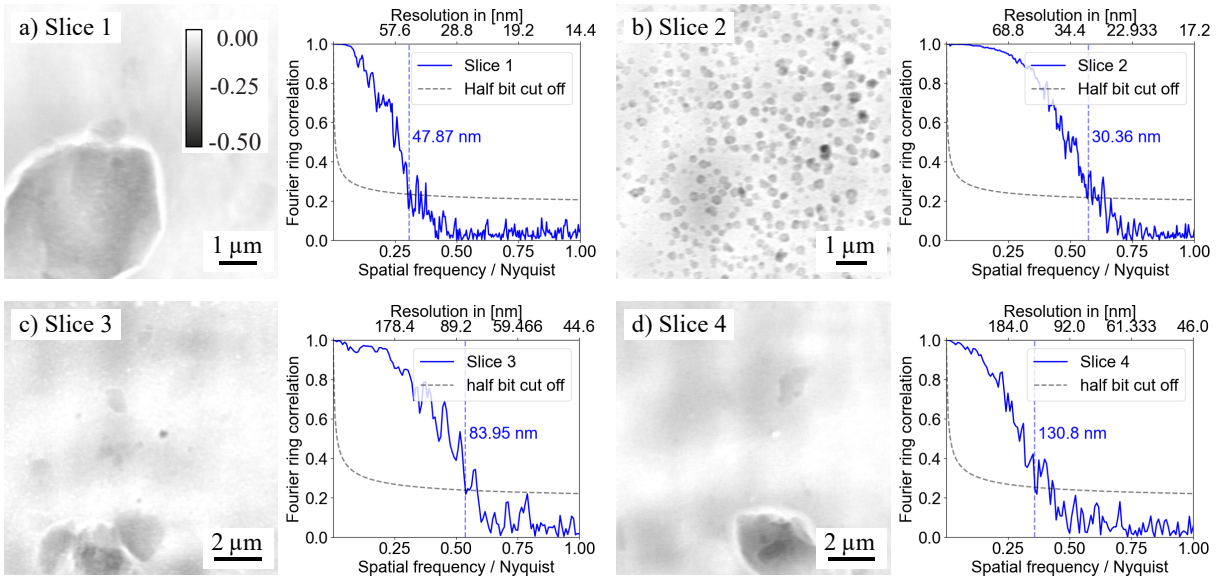

Figure C.3: Spatial resolution determination for the reconstructions of the in-situ cell. a) Multi-slice reconstruction of the object. The gray scale indicates the phase shift in radians. For the Fourier ring correlation, the reconstructions were carried out using one half of the scan points of the original data set. The dotted line in the bottom plot shows the half-bit cut off. The resolution is determined to be 48 nm for the first slice. The spatial resolution for the second slice b) was calculated to be 30 nm, for the third slice c) 84 nm, and for the fourth slice d) 131 nm. Adapted from [140].

C.2 Inclusions in the polyimide foils

The polyimide foils, used as the substrate for the synthesis, often contain inclusions. These inclusions are most likely a slip additive introduced during the production process of the foils. The inclusions are reported to be dicalcium phosphate [132] or calcium carbonate [133]. Fig. C.4 shows light microscope images of a polyimide foil of the same type that was used for the synthesis.

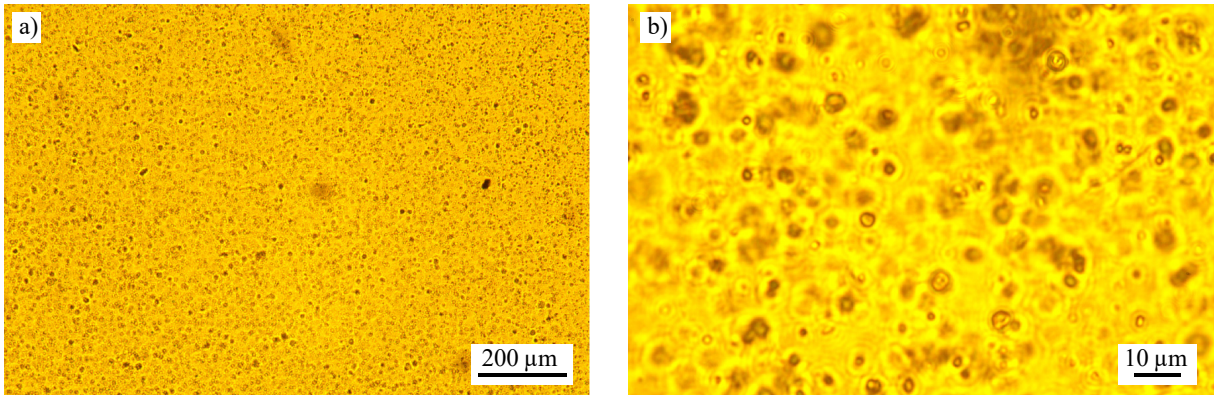

Figure C.4: Inclusions in the polyimide foil. a) A light microscope image shows that dicalcium phosphate inclusions are widespread over the entire polyimide foil. b) Inclusions are present in different depths of the foil with varying sizes between 1 µm and 8 µm. Particles embedded deeper in the foil than the depth resolution appear blurred. The microscopy images were taken by Sarah-Alexandra Hussak. Adapted from [140].

D Radiation damage and use of scavengers in in-situ studies

D.1 In-situ small angle X-ray scattering

Fig. D.1 shows the azimuthally integrated SAXS data from the scavenger tests without any background correction.

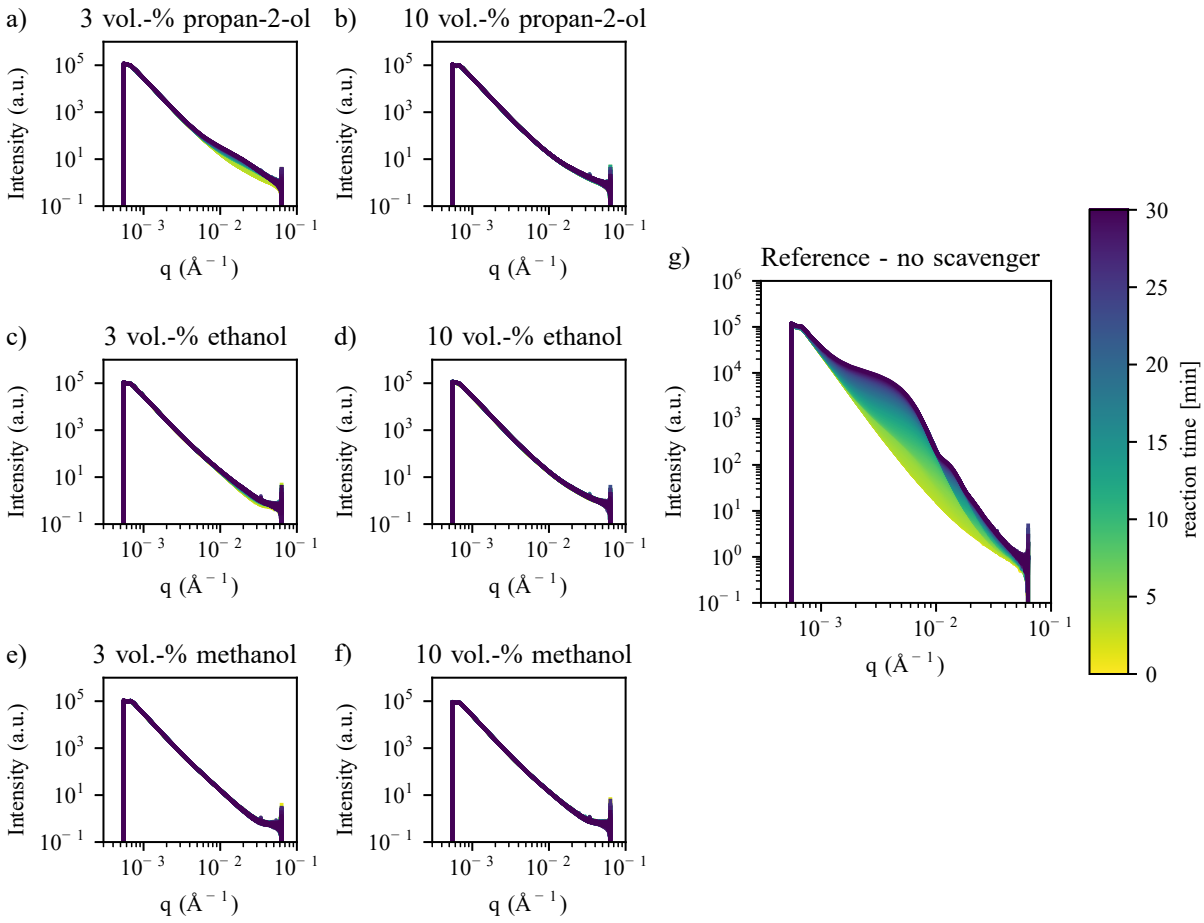

Figure D.1: Comparison of different scavengers with SAXS. Three different alcohols isopropanol (a and b), ethanol (c and d), and methanol (e and f) were introduced to the reaction solution as scavengers with a concentration of 3 vol −% and 10 vol −% each. g) shows the reference measurement without any scavenger.

D.2 In-situ X-ray imaging

The resolution in the in-situ experiments was determined with Fourier ring correlation at the example of the reference measurement without any scavenger 21 min after the start of the reaction (Fig. D.2).

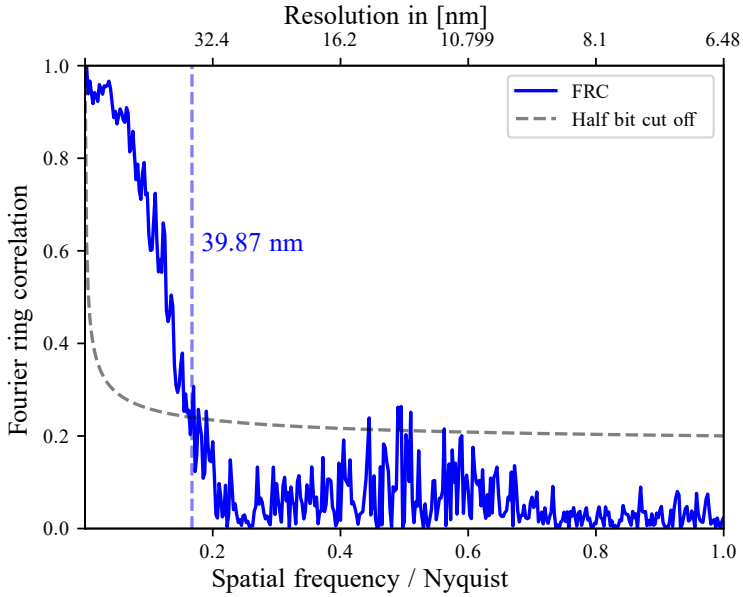

Figure D.2: Resolution determination at the example of the scan taken after 21 min in the reference reaction series. The spatial resolution of the slice showing the nanoparticles was determined with Fourier ring correlation to be 40 nm.

Acknowledgments

Many people have in one way or another supported and accompanied me on this journey, called a PhD. First, I would like to express my gratitude to my supervisors, Prof. Dorota Koziej and Prof. Christian Schroer, for welcoming me into their groups and for their guidance throughout my PhD program. I would like to thank Dorota for providing new perspectives in our discussions and for offering me the opportunity to continue my research when I officially moved to her group. Christian's positive attitude and encouragement helped me believe in myself and my results again whenever I was struggling.

I thank Dr. Andreas Schropp for introducing me to the wonderful world of X-ray imaging. His expertise and guidance were crucial to the success of our many beam times together. He fostered an environment that allowed me to freely explore my ideas.

I would like to express my gratitude to Jun.-Prof. Peter Modregger, who showed a deep interest in my research and immediately agreed to be the second reviewer of this thesis when I asked him. Further, I would like to thank the other members of the examination committee for their interest in my research and their efforts.

The support of all XStereoVision project members was invaluable. I thank Ulrich Vogt for the many fruitful discussions we had and for his valuable and prompt feedback on the numerous proposals and reports. The YoungXStereo team, namely Karolina Stachnik, Mattias Åstrand, Sarah-Alexandra Hussak, Caterina Carus, Jonas Voss, and Lukas Grote, made this time truly enjoyable, and I am happy to consider them not only colleagues but friends as well. Together, we shared the frustration, desperation, and joy encountered during beam times and data analysis, as well as some delicious pizza.

I would like to thank everyone I had the pleasure of sharing an office with: Philipp Paetzold, Silvio Achilles, Vahid Rahmani, Shahin Sepanlou, and Mirko Pollok. Thank you for the great atmosphere, casual chitchat, and advice – or more often, chocolate.

To all the members of the FS-PETRA group, I am very thankful for the friendly and open atmosphere. I would specifically like to thank Christina Ossig, Johannes Hagemann, Martin Seyrich, and Felix Wittwer for sharing their knowledge and helpful advice with me. My PhD studies would not have been the same without Johannes Dora, Thea Engler, Chaitali Sow, Samaneh Ehteram, and Johannes Grün. Thank you for the support, relaxing coffee breaks, and discussions, not all of which were work-related.

The engineering team played a crucial role in the success of the stereo experiments. I acknowledge the tremendous support of Ralph Döhrmann, Stephan Botta, Patrik Wiljes, and Mathias Bohn.

I would like to thank all the members of the Koziej Lab for their kindness and helpful advice. In particular, I would like to thank Cecilia Zito and Olga Vasylieva for their support in the preparation and conduction of the experiments in Sweden.

The support of the beamline staff was the cornerstone of our successful experiments. I would like to thank Jan Garrevoet, Gerald Falkenberg, Dennis Brückner, Vanessa Galbierz, and the rest of the P06 beamline team, as well as Maik Kahnt, Sebastian Kalbfleisch, Ann Terry, and Antara Pal at MAX IV.

Finally, I would like to thank my family and friends for their invaluable support. Robert, your reassurance and celebration of my accomplishments mean a lot to me. Thank you for always believing in me.

Eidesstattliche Erklärung

Hiermit versichere ich an Eides statt, die vorliegende Dissertationsschrift selbst verfasst und keine anderen als die angegebenen Quellen und Hilfsmittel benutzt zu haben. Sofern im Zuge der Erstellung der vorliegenden Dissertationsschrift generative Künstliche Intelligenz (gKI) basierte elektronische Hilfsmittel verwendet wurden, versichere ich, dass meine eigene Leistung im Vordergrund stand und dass eine vollständige Dokumentation aller verwendeten Hilfsmittel gemäß der Guten wissenschaftlichen Praxis vorliegt. Ich trage die Verantwortung für eventuell durch die gKI generierte fehlerhafte oder verzerrte Inhalte, fehlerhafte Referenzen, Verstöße gegen das Datenschutz- und Urheberrecht oder Plagiate.

Ort, Datum

Sina Röper